INTERSATELLITE CLOCK SYNCHRONIZATION AND ABSOLUTE RANGING FOR GRAVITATIONAL WAVE DETECTION IN SPACE

Von der QUEST-Leibniz-Forschungsschule der
Gottfried Wilhelm Leibniz Universität Hannover

zur Erlangung des akademischen Grades

Doktor der Naturwissenschaften
– Dr. rer. nat. –

genehmigte Dissertation von

M. Sc. Kohei Yamamoto

2023

Referent:	apl. Prof. Dr. Gerhard Heinzel
Korreferent:	Prof. Dr. Oliver Gerberding
Korreferent:	associate Prof. Dr. Kiwamu Izumi
Tag der Promotion:	28.08.2023

ABSTRACT

The Laser Interferometer Space Antenna (LISA) is a European Space Agency (ESA) large-scale space mission, aiming to detect gravitational waves (GWs) in the observation band of 0.1 mHz to 1 Hz. The constellation is formed by three spacecrafts (SCs), exchanging laser beams with each other. The detector adopts heterodyne interferometry with MHz frequency offsets. GW signals are then encoded in optical beatnote phases, and the phase information has to be extracted by a core device called phasemeter (PM). Unequal and time-varying orbital motions introduce an overwhelming laser noise coupling that impedes the LISA performance levels of $10\,\mu\text{cycle}/\sqrt{\text{Hz}}$. Thereby, the post-processing technique called time-delay interferometry (TDI) time-shifts phase signals to synthesize virtual equal-arm interferometers. TDI requires absolute-ranging information, as its input, to the accuracy of 1 m rms, which will be provided by monitors like pseudo-random noise ranging (PRNR) and time-delay interferometry ranging (TDIR). An additional challenge is independent clocks on each SC that time-stamp PM data. This, alongside TDI, requires the synchronization of the onboard clocks in post-processing.

This thesis reports on the experimental demonstrations of such key components for LISA. This is done by extending the scope of the hexagonal optical testbed at the Albert Einstein Institute (AEI): the "Hexagon". The first part of the thesis focuses on clock synchronization, utilizing the TDIR-like algorithm. With representative technologies both in devices and data analysis, this shows a new benchmark performance of LISA clock synchronization, achieving a $1\,\mu\text{cycle}/\sqrt{\text{Hz}}$ mark above 60 mHz and a TDIR accuracy of 1.84 m in range. This part also includes the first-ever verification of three noise couplings stemming from TDI and clock synchronization in an optical experiment.

The second part of the thesis evolves the Hexagon further with PRNR. It commences with a review of the latest development using a transmission/reception loopback on a single hardware platform. This is followed by the research on the impact of the pseudo-random noise (PRN) modulation on phase tracking. This reveals that the codes, used at best knowledge so far, hinder the carrier phase extraction from achieving the $1\,\mu\text{cycle}/\sqrt{\text{Hz}}$ mark with realistic data encoded for intersatellite data communication. Some adaptations of PRN codes are proposed, and it is shown that these offer enough suppression of the noise coupling into phase tracking. After phase tracking is confirmed to be compatible with PRN modulations, PRNR itself is investigated. The key novelty of this thesis in terms of PRNR is the study of its absolute-ranging feature, while previous research on this technology focused on stochastic noise properties. This requires the resolution of PRNR ambiguity and the correction of ranging biases. There suggests that the PRNR estimate, alongside some calibrations, can constantly function as *absolute* ranging with sub-meter accuracy.

Keywords: GRAVITATIONAL WAVE, LASER INTERFEROMETRY, LISA, PHASEMETER, CLOCK SYNCHRONIZATION, ABSOLUTE RANGING

KURZZUSAMMENFASSUNG

LISA (Laser Interferometer Space Antenna) ist eine groß angelegte Weltraummission der Europäischen Weltraumorganisation (ESA) mit dem Ziel, Gravitationswellen (GWs) im Beobachtungsband von 0.1 mHz bis 1 Hz zu entdecken. Die Konstellation besteht aus drei Satelliten (SC), die untereinander Laserstrahlen austauschen. Der Detektor verwendet Heterodyn-Interferometrie mit MHz-Frequenzversatz. Die GW-Signale werden dann in optischen Schwebungsphasen kodiert und die Phaseninformation muss von einem zentralen Gerät, dem Phasenmeter (PM), extrahiert werden. Ungleiche und zeitlich veränderliche Abstände zwischen den SCs führen zu einer enormen Laserrauschkopplung, die die LISA-Leistungsniveaus von 10 µcycle/$\sqrt{\text{Hz}}$ beeinträchtigt. Die Nachbearbeitungstechnik namens Time-Delay Interferometrie (TDI) verschiebt die Phasensignale zeitlich, um virtuelle Interferometer mit gleichen Armlängen zu synthetisieren. TDI benötigt absolute Entfernungen mit einer Genauigkeit von 1 m rms, die von Techniken wie Pseudo-Random Noise Ranging (PRNR) und Time-Delay Interferometrie Ranging (TDIR) geliefert werden. Eine weitere Herausforderung sind unabhängige Uhren auf jedem SC, die die PM-Daten mit einem Zeitstempel versehen. Dies erfordert neben TDI auch die Synchronisierung der Borduhren in der Nachbearbeitung.

In dieser Arbeit wird über die experimentellen Nachweise solcher Schlüsselkomponenten für LISA berichtet. Dies geschieht durch die Erweiterung des hexagonalen optischen Aufbaus am Albert Einstein Institut (AEI): dem "Hexagon". Der erste Teil der Arbeit konzentriert sich auf die Uhrensynchronisation unter Verwendung eines TDIR-ähnlichen Algorithmus. Mit repräsentativen Technologien sowohl bei den Geräten als auch bei der Datenanalyse wird eine neue Benchmark-Leistung der LISA-Uhrensynchronisierung gezeigt, wobei die 1 µcycle/$\sqrt{\text{Hz}}$-Marke über 60 mHz und eine TDIR-Genauigkeit von 1.84 m in der Distanz erreicht wird. Dieser Teil umfasst auch die allererste Verifizierung in einem optischen Experiment von drei Rauschkopplungen, die von TDI und Uhrensynchronisation verursacht werden.

Im zweiten Teil der Arbeit wird das Hexagon mit PRNR weiterentwickelt. Er beginnt mit einem Überblick über die neueste Entwicklung bei der eine Übertragungs-/Rezeptionsschleife auf einer einzigen Hardwareplattform verwendet wird. Darauf folgt die Untersuchung der Auswirkungen der Pseudo-Random-Noise (PRN)-Modulation auf die Phasenauslesung. Dabei zeigt sich, dass die bisher nach bestem Wissen und Gewissen verwendeten Codes verhindern, dass die extrahierte Trägerphase bei realistischen, für die Kommunikation zwischen SCs kodierten Daten, die Marke von 1 µcycle/$\sqrt{\text{Hz}}$ erreicht. Es werden einige Anpassungen von PRN-Codes vorgeschlagen, und es wird gezeigt, dass diese eine ausreichende Unterdrückung der Rauschkopplung bei der Phasenauslesung bieten. Nachdem bestätigt wurde, dass die Phasenauslesung mit PRN-Modulationen kompatibel ist, wird PRNR selbst untersucht. Die wichtigste Neuerung dieser Arbeit in Bezug auf PRNR ist die Untersuchung der absoluten Entfernungen, während sich frühere Forschungen zu dieser Technologie auf die stochastischen Rauscheigenschaften von PRNR konzentrierten. Dies erfordert die Auflösung der PRNR-Mehrdeutigkeit und die Korrektur von Entfernungsfehlern. Es gibt Hinweise darauf, dass die PRNR-Schätzung zusammen mit einigen Kalibrierungen konstant als absolu-

te Entfernungsmessung mit einer Genauigkeit von weniger als einem Meter funktionieren kann.

Schlagwörter: Gravitationswellen, Laserinterferometrie, LISA, Phasenmeter, Uhrensynchronisation, absolute Entfernungsmessung

CONTENTS

Abstract iii
Kurzzusammenfassung iii
List of Figures ix
List of Tables xii
Acronyms xiii

I INTRODUCTION

1 THE LASER INTERFEROMETER SPACE ANTENNA 3
1.1 Science . . . 3
1.2 Mission overview . . . 3
1.3 Performance . . . 7
2 PHASEMETER 15
2.1 Hardware overview . . . 15
2.2 Digital phase-locked loop (DPLL) . . . 16
2.3 Delay-locked loop (DLL) . . . 19
2.4 Filtering and decimation . . . 21
2.5 Timer model . . . 22
2.6 Frequency distribution . . . 24
3 THE HEXAGON 29
3.1 Three-signal test . . . 29
3.2 The Hexagon interferometer . . . 30
3.3 Relation between LISA and the Hexagon . . . 31
3.4 Experimental topologies . . . 34
3.5 Significance for the mission . . . 36

II INTERSATELLITE CLOCK SYNCHRONIZATION

4 CLOCK SYNCHRONIZATION IN THE HEXAGON 41
4.1 Setup . . . 41
4.2 Model . . . 43
4.3 Result . . . 47
4.4 Tone-assisted TDIR . . . 54
4.5 Summary and Outlook . . . 58

III INTERSATELLITE ABSOLUTE RANGING

5 PSEUDORANDOM NOISE RANGING AND DATA COMMUNICATION 63
5.1 Design overview . . . 63
5.2 PRN code . . . 64
5.3 Technology description . . . 65
6 IMPACT ON PHASE TRACKING 73
6.1 BPSK in the view of phase tracking . . . 73
6.2 Adapting PRN codes . . . 75
6.3 Experimental demonstration . . . 78
6.4 Summary . . . 80
7 ABSOLUTE RANGING IN THE HEXAGON 83
7.1 Setup . . . 84
7.2 Model . . . 84

7.3 Demonstration . . . 89
7.4 Data communication . . . 104
7.5 Summary and Outlook . . . 106

IV APPENDIX

A NOVEL OPTICAL HEAD DESIGN FOR DEEP FREQUENCY MODULATION INTERFEROMETRY 111
A.1 Deep frequency modulation interferometry . . . 111
A.2 Optical head design . . . 112
A.3 Structural analysis: ghost beams . . . 113
A.4 Structural analysis: manufacturing tolerance . . . 114
A.5 Noise budget . . . 116
A.6 Performance enhancement . . . 116
A.7 Combination of TM interferometers . . . 118
A.8 Thermal noise reduction with reference interferometers . . . 118

B NEW TOPOLOGY OF ON-AXIS LASER RAGING INTERFEROMETRY 121
B.1 Optical bench design . . . 121
B.2 Layout . . . 122
B.3 Characteristics . . . 122
B.4 Comparison with former designs . . . 123
B.5 Optical simulation . . . 124
B.6 Simulation protocol . . . 126
B.7 Results . . . 127

C OPTICAL NOISE IN HETERODYNE INTERFEROMETRY 131
C.1 Phase noise categorization . . . 131
C.2 Balanced detection . . . 133

D PILOT TONE FREQUENCY 135
D.1 Impact on PLL . . . 135
D.2 Impact on DLL . . . 136
D.3 Timing fidelity . . . 138

E NOISE COUPLINGS IN CLOCK SYNCHRONIZATION 141
E.1 Aliasing effect . . . 141
E.2 Lagrange interpolation error . . . 142
E.3 Flexing-filtering coupling . . . 143

F LASER LOCK WITH A PHASEMETER 145
F.1 Analytical form . . . 145
F.2 Demonstration . . . 148

G DECIMATION ARTIFACTS 153

Bibliography 155

Acknowledgments 163

LIST OF FIGURES

Figure 1.1 GW detector sensitivities and target sources 4
Figure 1.2 LISA constellation and orbit 4
Figure 1.3 Simplified schematic of LISA interferometers 6
Figure 1.4 Simulated interspacecraft interferometer signal with one QPR segment 8
Figure 1.5 Simulated interspacecraft interferometer signal with two QPRs 8
Figure 1.6 LISA laser frequency noise 10
Figure 1.7 Comparison of clock stability in timing 12
Figure 1.8 LISA strain sensitivity 13
Figure 2.1 PM hardware overview 15
Figure 2.2 Schematic of DPLL implemented on PM 17
Figure 2.3 Sideband PLL with frequency feed-forward 18
Figure 2.4 Sideband PLL with phase feed-forward 18
Figure 2.5 Raw outputs of total frequencies from different sideband PLL topologies 19
Figure 2.6 Schematic of a PRN signal chain 20
Figure 2.7 Compound band-pass filter for a PRN modulation. . . 20
Figure 2.8 Simulated PLL Q value with a PRN modulation 20
Figure 2.9 DLL design overview 21
Figure 2.10 PM decimation chain 21
Figure 2.11 Transfer functions of FIR filters 22
Figure 2.12 Conceptual schematic of the entire FDS 25
Figure 3.1 The Hexagon interferometer 29
Figure 3.2 Simplified topology of LISA simulated by the Hexagon 35
Figure 3.3 The Hexagon topologies 36
Figure 3.4 Diagram of one of the LISA on-ground processing pipelines 38
Figure 4.1 Schematic of the experimental setup to demonstrate clock synchronization 42
Figure 4.2 Conceptual diagram of the clock tone transfer 43
Figure 4.3 Two differential clock signals in time 47
Figure 4.4 Performance of a three-signal test using clock synchronization 48
Figure 4.5 TDIR precision in a three-signal test 49
Figure 4.6 Noise couplings to a three-signal test with clock synchronization 49
Figure 4.7 Aliased noise in the time domain 51
Figure 4.8 Flexing-filtering couplings in a three-signal test 51
Figure 4.9 Compensation for distortions of onboard FIR filters with inverse filters 52
Figure 4.10 Improvement of the three-signal performance with the inverse filter 53
Figure 4.11 Transformation of the local timing reference in a three-signal test. 54

Figure 4.12 Limit of the timing accuracy with tone-assisted TDIR due to the flexing-filtering coupling . . . 56
Figure 4.13 Clock synchronization with tone-assisted TDIR . . . 57
Figure 4.14 Clock synchronization with tone-assisted TDIR, zooming in on the tone . . . 58
Figure 5.1 Overview of the FPGA architecture from the perspective of PRN ranging and data communication . . . 63
Figure 5.2 Simplified diagram of two DLL instances . . . 64
Figure 5.3 Diagram of the current nominal PRN code parameters for LISA . . . 66
Figure 5.4 Data encoding on PRN code . . . 69
Figure 5.5 Comparison of BER with and without RS coding . . . 70
Figure 5.6 BER with and without RS coding as a function of C/N_0 71
Figure 6.1 Normalized ASDs of heterodyne beatnotes with different PRN codes and random data encoded . . . 76
Figure 6.2 Simulated PRN mainlobe additive noise . . . 77
Figure 6.3 Auto correlations of different PRN codes . . . 78
Figure 6.4 PRN sidelobe additive noise . . . 78
Figure 6.5 Electrical setup to probe the PRN mainlobe additive noise . . . 79
Figure 6.6 Measured PRN mainlobe additive noise with different codes . . . 80
Figure 6.7 Measured PRN sidelobe additive noise with different sideband offset . . . 80
Figure 7.1 Schematic of the bidirectional ranging in the Hexagon. 84
Figure 7.2 Round-trip ranging, combining PRNR observables at two PMs . . . 91
Figure 7.3 PRNR prior calibration . . . 93
Figure 7.4 Bias-corrected received PRNR estimate against TDIR with extra cable insertions . . . 94
Figure 7.5 Sinusoidal modulation of a heterodyne beatnote frequency and its impact on PRNR . . . 95
Figure 7.6 Clock synchronization with PRNR, under different bias treatments . . . 96
Figure 7.7 Coupling of the in-band PRNR noise to clock synchronization via time-stamping . . . 97
Figure 7.8 Different combinations of PRNR observables at two PMs 97
Figure 7.9 Simulated DLL error signals with different beatnote signal amplitudes . . . 98
Figure 7.10 Simulated coupling from a heterodyne amplitude to a PRNR bias via PLL . . . 99
Figure 7.11 Comparison of the amplitude coupling to PRNR biases between different code pairs . . . 101
Figure 7.12 Clock synchronization with the bit-balanced 4-1 pair, under different bias treatments . . . 101
Figure 7.13 Measured impact of ICC on PRNR bias estimations in round-trip measurements . . . 102
Figure 7.14 Injected GW signal from MBHB . . . 103
Figure 7.15 Ranging with the existence of a GW signal from MBHB 104
Figure 7.16 Structure of encoded data sequence . . . 105

Figure 7.17 Measured raw data errors without RS coding 106
Figure 7.18 Projection of measured data errors to a theory 107
Figure A.1 SEDI optical head layout 113
Figure A.2 Ghost beams in the SEDI setup 114
Figure A.3 Critical manufacturing tolerances are divided into two categories 114
Figure A.4 Prism sensitivity to manufacturing imperfections in the xy plane 115
Figure A.5 Prism sensitivity to perpendicularity imperfections . . 115
Figure A.6 Performance of the SEDI inertial sensor 117
Figure A.7 Conceptual schematic of the two-side configuration of optical heads 118
Figure A.8 Influence of an arbitrary correlation in temperature noise on the performance of the dual-OH setup 120
Figure B.1 LRI optical bench layout 123
Figure B.2 LRI OB as modelled in IFOCAD and drawn in OPTOCAD125
Figure B.3 Amplitude and phase of the "flat-top" RX beam 126
Figure B.4 LRI ideal simulation 129
Figure B.5 LRI thermal analysis 130
Figure D.1 Dependency of the PT impact on carrier PLL on their frequencies 136
Figure D.2 Disturbance of a lsb-lsb beatnote due to the aliased PT signal 137
Figure D.3 PT frequencies at a PLL error point 137
Figure D.4 Demonstration of the impact of a PT signal on PRN ranging 138
Figure D.5 CFDS performance-critical-chain timing fidelity with a 37.5 MHz PT signal 139
Figure F.1 Block diagram of laser lock loop. Red for optical signals, blue for analog electrical signals, and black for digital signals. 146
Figure F.2 Open-loop transfer functions of the frequency-lock loops148
Figure F.3 Performance of the laser frequency-lock loop 149
Figure F.4 Experimental demonstration of the laser lock system implemented on Red Pitaya 149
Figure F.5 Demonstration of beatnote frequency noise injection . . 150
Figure F.6 Demonstration of various drifts of beatnote frequencies 151
Figure G.1 Decimation-artifact-free PRN range 154

LIST OF TABLES

Table 3.1 Hexagon topologies used in experiments in the thesis . 36
Table 5.1 Current nominal parameters of PRN codes for LISA . . 65
Table 6.1 Different PRN code types 76
Table 7.1 Nominal parameters for bidirectional ranging experiments 90
Table 7.2 Summary of PRNR bias modulations and clock synchronization performances 102
Table 7.3 Data communication results under the normal-light condition with code interference 105
Table A.1 Geometrical parameters relevant to the structural analysis and noise investigations 112
Table A.2 Parameters of the SEDI simulation setup 113
Table A.3 Amplitude of the displacement noise of two interferometers in a single OH due to the main noise sources . 116
Table B.1 Comparison of optical parameters between two configurations of the proposed LRI OB design, the GRACE-FO LRI OB, and two modified versions of the GRACE-FO LRI OB 124

ACRONYMS

AA	anti-aliasing
AC	alternating current
ADC	analog-to-digital converter
AEI	Albert Einstein Institute
ANU	Australian National University
AOI	angle of incidence
AR	anti-reflective
ASD	amplitude spectrum density
AWGN	additive white Gaussian noise
BEE	backend electronics
BER	bit error rate
BPSK	binary phase-shift keying
BS	beam splitter
CBE	current best estimate
CFDS	clock frequency distribution system
CIC	cascaded integrator comb
CNES	Centre National d'Exploration Spatiale
CNR	carrier-to-noise ratio
C/N_0	carrier-to-noise-density ratio
DAC	digital-to-analog converter
DC	direct current
DECIGO	DECi-hertz Interferometer Gravitational-wave Observatory
DLL	delay-locked loop
DFMI	deep frequency modulation interferometry
DPLL	digital phase-locked loop
DPMI	deep phase modulation interferometry
DSB	double sideband
DWS	differential wavefront sensing
EBB	elegant bread board
E_b/N_0	energy-per-bit-to-noise-density ratio
EGSE	electrical ground support equipment
EMRI	extreme-mass-ratio inspiral
EOM	electro-optical modulator
ESA	European Space Agency
FDM	frequency distribution module
FDS	frequency distribution system
FIOS	fiber injector optical subassembly
FIR	finite impulse response
FMC	FPGA mezzanine card
FPGA	field programmable gate array
FSM	fast steering mirror
DLR	German Aerospace Center

GPS	global positioning system
GRS	gravitational reference sensor
GRACE	Gravity Recovery and Climate Experiment
GRACE-FO	Gravity Recovery and Climate Experiment Follow-On
GW	gravitational wave
HR	highly-reflective
ICC	interfering code cancellation
IIR	infinite impulse response
IPTA	International Pulsar Timing Array
KAGRA	Kamioka Gravitational Wave Detector
KF	Kalman filter
LIGO	Laser Interferometer Gravitational-Wave Observatory
LISA	Laser Interferometer Space Antenna
LO	local oscillator
LPS	longitudinal pathlength signal
LRI	laser ranging interferometry
lsb	lower sideband
LUT	lookup table
LVDS	low voltage differential signaling
MBHB	massive black hole binary
MEM	mode expansion method
MOC	mission operation center
MOSA	moving optical sub-assembly
MZI	Mach-Zehnder interferometer
NASA	National Aeronautics and Space Administration
NCO	numerically controlled oscillator
NGGM	next generation gravity mission
NPRO	non-planar ring oscillator
OB	optical bench
OBC	onboard computer
OCXO	oven-controlled crystal oscillator
OMS	optical metrology system
OH	optical head
PA	phase accumulator
PD	photo detector
PDH	Pound-Drever-Hall
PF	particle filter
PI	proportional integral
PIR	phase increment register
PLL	phase-locked loop
PM	phasemeter
PMS	phase measurement system
PR	photo receiver
PRN	pseudo-random noise
PRNR	pseudo-random noise ranging
PSD	power spectrum density
PT	pilot tone

PZT	piezoelectric transducer
QPD	quadrant photo-diode
QPR	quadrant photo-receiver
RF	radio-frequency
RIN	relative intensity noise
RMS	root-mean-square
RS	Reed Solomon
RX	receiving
RP	reference point
SC	spacecraft
SG	signal generator
SEDI	single-element dual-interferometer
SEPD	single-element photo detector
SMBHB	super massive black hole binary
SNR	signal-to-noise ratio
SSB	single sideband
TDI	time-delay interferometry
TDIR	time-delay interferometry ranging
TDOBS	tilt-dynamics optical bench simulator
TIA	trans-impedance amplifier
TM	test mass
TTL	tilt-to-length
TX	transmitting
UGF	unity-gain frequency
USO	ultra stable oscillator
usb	upper sideband
VCXO	voltage-controlled crystal oscillator
VFDS	VCXO frequency distribution system
VHDL	very high-speed integrated circuit hardware description language
XOR	exclusive-or

Part I

INTRODUCTION

1 THE LASER INTERFEROMETER SPACE ANTENNA

LISA is a large-scale mission led by ESA. This GW detector in space shifts the observation band from 10 Hz to 1 kHz, achieved by ground-based detectors, to lower frequencies from 0.1 mHz to 1 Hz.

Section 1.1 introduces target science outcomes by this space-borne GW detector, which is followed by the technical overview of the mission in Section 1.2. After that, Section 1.3 wraps up this chapter by bringing up primary noise sources in LISA, which are the scope of this thesis, and analyzing their impacts on the LISA detector sensitivity to motivate the work in this thesis.

1.1 SCIENCE

The first detection of a GW by two Laser Interferometer Gravitational-Wave Observatory (LIGO) detectors in 2015 was the dawn of gravitational wave astronomy [1]. It has been followed by more detections achieved by an international collaboration established with Virgo [2, 3, 4, 5, 6]. Also, Kamioka Gravitational Wave Detector (KAGRA) recently joined the detector network [7]. The target observation band of these ground-based detectors is 10 Hz to 1 kHz, being limited by seismic and gravity gradient noise below 10 Hz.

LISA, being a gravitational-wave detector in space, will avoid the mentioned limitations, targeting the observation band from 0.1 mHz to 1 Hz. Such mHz regime is rich in GWs from a system with heavier astronomical bodies: massive black hole binarys (MBHBs), extreme-mass-ratio inspiral (EMRI), etc [8].

International Pulsar Timing Array (IPTA) recently opened a complementary window into the GW landscape by observing an isotropic GW background in the nHz regime [9, 10, 11, 12]. super massive black hole binarys (SMBHBs) seem to be a primary candidate of the source, while more exotic cosmological and astrophysical sources cannot be excluded.

Figure 1.1 summarizes the design sensitivities of different observatories, together with target GW sources. In addition to possible sources depicted in the figure, there are expected to exist unresolvable white dwarf binaries around the bottom of the LISA curve. The compact binary inspirals in the observation band of the ground-based detectors could also be detected by LISA at their earlier stages.

1.2 MISSION OVERVIEW

The instrumental overview of the mission to achieve scientific outcomes in Section 1.1 is provided in this section.

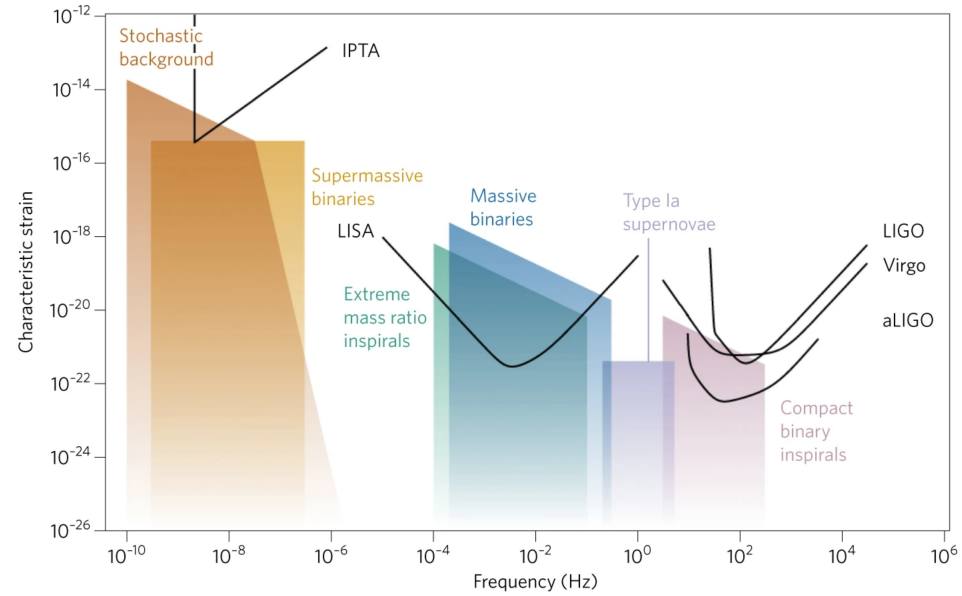

FIGURE 1.1: GW detector sensitivities and target sources, from [13].

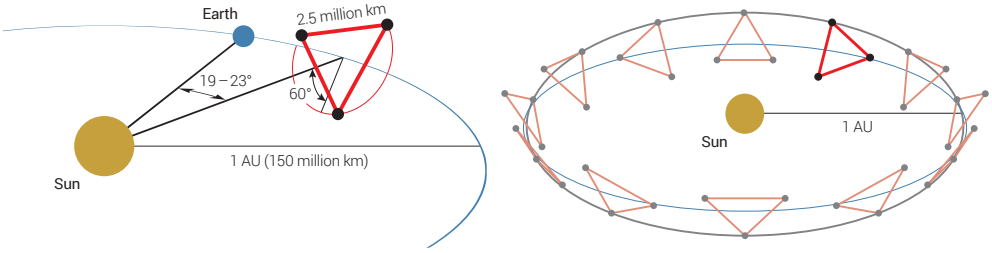

FIGURE 1.2: LISA constellation (left) and orbits (right), from [14].

1.2.1 *Constellation*

LISA constellation comprises three SC, forming a quasi-equilateral triangle with 2.5 million kilometer arm lengths. Trailing the Earth, the constellation revolves around the Sun, being tilted by 60° to the ecliptic plane. Each pair of two SC configures a bidirectional laser link, and a received beam, with power in the order of 100 pW due to diffraction loss, is interfered with a local beam, with the order of 1 mW of power. The LISA constellation and orbits are illustrated in Figure 1.2.

By convention, a round trip is counted as "two links". Hence, LISA comprises six links in total.

Relative positions of the three SC are not actively controlled in LISA and keep drifting. This is called *constellation flight*. Correspondingly, orbital variations will lead to armlength drifts of $10\,\mathrm{m\,s^{-1}}$, which causes MHz drifts of laser beam frequencies due to the Doppler effect. To handle such MHz frequency drifts, LISA adopts heterodyne interferometry by locking the local beam to the received beam with a MHz offset frequency.

Contrary, in *formation flight*, SC separation is locked over the mission duration. This will be adopted by the DECi-hertz Interferometer Gravitational-wave Observatory (DECIGO) where a pair of SC configures an optical cavity.

1.2.2 *Challenges and treatments*

The ground-based observatories are based on an equal-arm Michelson interferometer insensitive to inherent laser frequency noises. LISA follows the same philosophy by combining two bidirectional links, i.e., four links at least; however, separations of different pairs of SC differ by order of 10^8 m due to the constellation flight introduced in Section 1.2.1. Such unequal arm lengths cause a large coupling of laser frequency noise into the interferometric phase readout.

To mitigate this overwhelming noise source, a virtual interferometer insensitive to laser frequency noise can be synthesized in postprocessing by a technique named TDI [15]. Interferometric phase signals are extracted by a PM. Each SC accommodates two PM instances, one per laser link, with a common system clock called ultra stable oscillator (USO). Hence, four PMs (i.e., the minimum required) record the input phase signals, and TDI requires shifting the PM signals by precise time intervals related to the light travel times along the arms, ideally in a common clock frame. This raises a necessary technology, i.e., *intersatellite absolute ranging* to monitor the light travel times as inputs to TDI. This is achieved via phase modulation of a beam with a binary sequence called PRN code. This technology is one of the main scopes of this thesis and will be investigated in Part III.

The aforementioned ideal situation of clock frames is impeded by the uncertain relation of sample times between different SC due to the independent clocks, which exhibit offsets and drifts, and the light travel delays between the SC. On top, differential clock jitter in the mHz measurement band directly couples into phase sensing precision. This brings up another technology, i.e., *intersatellite clock synchronization*, to adjust time stamps of all phase signals to a common time frame in postprocessing. This is achieved via another phase modulation with a GHz sinusoidal signal originating from USO. This will be discussed mainly in Part II.

The two key ingredients for TDI above are the scopes in this thesis. Other technical challenges and treatments in LISA will be summarized for completeness below.

Each SC hosts a free-falling test mass (TM). The microscopic relative displacement of these TMs needs to be with $10\,\mathrm{pm}/\sqrt{\mathrm{Hz}}$ precision per TM pair to accomplish the science in Section 1.1. However, it is technically not feasible to keep a distance between an optical bench (OB) and a TM with such pico-meter accuracy. Hence, a TM-to-TM link must be broken into three: the TM-to-OB, the OB-to-OB, and the OB-to-TM. The first and third are called TM interferometers, while the second is an interspacecraft interferometer. GW signals are embedded in the interspacecraft interferometer. Combining those interferometers in postprocessing, the SC relative motion to the TM can be canceled.

Not for all degrees of freedom, but only for the longitudinal axis.

Intersatellite laser links in LISA have lengths around 2.5 million kilometer as mentioned. The $\mathrm{pm}/\sqrt{\mathrm{Hz}}$ precision is designed to be limited by shot noise (around intermediate to high frequencies), which couples to phase detection with the square root of the received beam power. Hence, a telescope must point to a distant SC with the precision of around $10\,\mu\mathrm{rad}$ [16, 17]. Considered together with the constellation flight where SC relative positions keep drifting, each SC hosts two moving optical sub-assembly (MOSA), each of which comprises one OB, one laser source, one TM, and is attached to one phase measurement system (PMS). This, in turn, requires the third and final type of interferometer, the so-called reference interferometer, to beat the two local laser beams and be used to cancel their relative noises in postprocessing.

All three types of interferometers, introduced above, are illustrated in Figure 1.3, together with other key components on the OB.

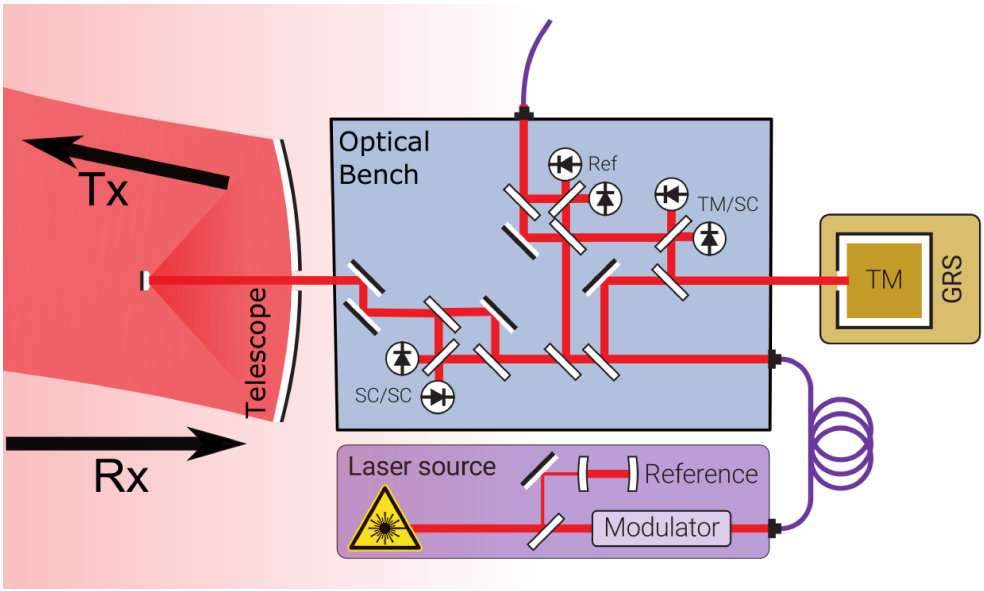

FIGURE 1.3: Simplified schematic of LISA interferometers, from [18].

1.2.3 *Interferometric signals*

Interferometric signals in LISA will be expressed in a general form in this section.

A beam i with a clock-sideband and PRN modulations is written,

$$\begin{aligned} E_i(t) &= |E_i| \cdot \exp\left(j(\omega_i + \delta\omega_i(t))t + jm_{\text{sb}} \sin \omega_{\text{sb},i}(t + \delta\tau_i(t)) + jm_{\text{prn}}c_i(t)\right) \\ &\approx |E_i| \cdot \exp\left(j(\omega_i + \delta\omega_i(t))t + jm_{\text{prn}}c_i(t)\right) \\ &\quad \cdot \left(J_0(m_{\text{sb}}) + J_1(m_{\text{sb}})e^{j\omega_{\text{sb},i}(t+\delta\tau_i(t))} - J_1(m_{\text{sb}})e^{-j\omega_{\text{sb},i}(t+\delta\tau_i(t))}\right), \end{aligned} \tag{1.1}$$

where the first, second, and third terms are called a carrier, a upper sideband (usb) and a lower sideband (lsb); ω_i and $\delta\omega_i$ are a central frequency of a beam and an inherent beam frequency noise, respectively; m_{sb} and m_{prn} are modulation depths of a clock-sideband and PRN modulations, respectively; ω_{sb} is a clock-sideband modulation frequency; $\delta\tau_i(t)$ is a clock timing noise, according to a given reference time frame; c_i is a PRN binary code, i.e., -1 or 1; J_0 and J_1 are Bessel functions of the first kind.

A heterodyne interferometer mixes two electromagnetic fields, with a frequency offset, at a combining beamsplitter. Intersatellite light travel times are not explicitly formulated for the arbitrary expression of interferometric signals in LISA [1]. The interference part, to be tracked by a PM [2], is given by a real number of

$$\begin{aligned} E_0(t) \cdot E_1^*(t) = |E_0||E_1| \cdot \exp &\left(j(\omega_{\text{het}} + \delta\omega_{\text{het}}(t))t + jm_{\text{prn}}(c_0(t) - c_1(t))\right) \\ &\cdot \left(J_0^2(m_{\text{sb}}) + J_1^2(m_{\text{sb}})e^{j\Delta\omega_{\text{sb}}t + j\delta\theta_{\text{sb}}(t)}\right. \\ &\left. + J_1^2(m_{\text{sb}})e^{-j\Delta\omega_{\text{sb}}t - j\delta\theta_{\text{sb}}(t)}\right), \end{aligned} \tag{1.2}$$

1 This does not lose generality because the delayed field can be redefined at the time of t via $(t + \Delta t) \to t$ where Δt is the delay.

2 Only MHz sinusoidal signals are written in Eq. (1.2) because other interference components in the GHz regime are out of the photodetection bandwidth.

where a heterodyne frequency $\omega_{\text{het}}(= \nu_{\text{het}}/2\pi)$, a heterodyne beatnote frequency noise $\delta\omega_{\text{het}}(= \delta\nu_{\text{het}}(t)/2\pi)$, a clock beatnote offset $\Delta\omega_{\text{sb}}(= \Delta\nu_{\text{sb}}/2\pi)$, and a differential clock phase $\delta\theta_{\text{sb}}$ were defined as follows,

$$\omega_{\text{het}} = \omega_0 - \omega_1, \tag{1.3}$$
$$\delta\omega_{\text{het}}(t) = \delta\omega_0(t) - \delta\omega_1(t), \tag{1.4}$$
$$\Delta\omega_{\text{sb}} = \omega_{\text{sb},0} - \omega_{\text{sb},1}, \tag{1.5}$$
$$\delta\theta_{\text{sb}}(t) = \omega_{\text{sb},0}\delta\tau_0(t) - \omega_{\text{sb},1}\delta\tau_1(t). \tag{1.6}$$

A perfect heterodyne efficiency was assumed Eq. (1.2). The first, second, and third terms in Eq. (1.2) are a carrier-carrier beatnote, a usb-usb beatnote, and a lsb-lsb beatnote.[3] A resulting alternating current (AC) signal in photocurrent is given by

A parameter to evaluate the geometrical overlap of two beams

$$I_{\text{ifo}}(t) = 2\gamma\,\text{Re}(E_0(t)\cdot E_1^*(t)) + \delta I(t), \tag{1.7}$$
$$\delta I(t) = \delta I_{\text{shot}}(t) + \delta I_{\text{RIN}}(t) + \delta I_{\text{PR}}(t), \tag{1.8}$$
$$\delta I_{\text{shot}}(t) = \sqrt{2q\gamma(|E_0|^2 + |E_1|^2)}, \tag{1.9}$$
$$\delta I_{\text{RIN}}(t) = \gamma(n_{\text{RIN},0}|E_0|^2 + n_{\text{RIN},1}|E_1|^2), \tag{1.10}$$

where γ is a photo receiver (PR) responsivity [A/W] and $\delta I(t)$ is an additive noise, which is broken into a shot noise (δI_{shot}) [19], a laser relative intensity noise (RIN) (δI_{RIN}) [20], and a PR electronic noise (δI_{PR}) [19]. Appendix C categorizes some optical phase noises not discussed here. The interference part I_{ifo} can be broken down to three heterodyne beatnotes, which can be expressed in voltage by,

$$V_c(t) = A_c\cdot\cos\left((\omega_{\text{het}} + \delta\omega_{\text{het}}(t))t + m_{\text{prn}}(c_0(t) - c_1(t))\right), \tag{1.11}$$
$$V_{\text{usb}}(t) = A_{\text{sb}}\cdot\cos\left((\omega_{\text{het}} + \Delta\omega_{\text{sb}} + \delta\omega_{\text{het}}(t))t + \delta\theta_{\text{sb}}(t) + m_{\text{prn}}(c_0(t) - c_1(t))\right), \tag{1.12}$$
$$V_{\text{lsb}}(t) = A_{\text{sb}}\cdot\cos\left((\omega_{\text{het}} - \Delta\omega_{\text{sb}} + \delta\omega_{\text{het}}(t))t - \delta\theta_{\text{sb}}(t) + m_{\text{prn}}(c_0(t) - c_1(t))\right), \tag{1.13}$$

where

$$A_c = 2\gamma|E_0||E_1|J_0^2(m_{\text{sb}})\cdot G_{\text{TIA}}, \tag{1.14}$$
$$A_{\text{sb}} = 2\gamma|E_0||E_1|J_1^2(m_{\text{sb}})\cdot G_{\text{TIA}}. \tag{1.15}$$

G_{TIA} is a trans-impedance amplifier (TIA) gain [V/A]. Notice that many contents are absorbed into electromagnetic fields E_i in the formulation above such that E_i has a dimension of $\sqrt{\text{W}}$.

The speed of light, the vacuum permittivity, the refractive index, and the field integration at a PR

Figure 1.4 and Figure 1.5 show that the signal spectra of the interspacecraft interferometer in LISA with one quadrant photo-receiver (QPR) segment and two entire QPRs in balanced-detection mode, respectively.

1.3 PERFORMANCE

Section 1.1 introduced the LISA frequency band for the discussed observation target. The LISA sensitivity to GWs is further discussed in this section.

3 Through this thesis, they also are naively called "carrier beatnote", "usb beatnote" (or "upper-sideband beatnote"), and "lsb beatnote" (or "lower-sideband beatnote"). The latter two will also be referred to as "sideband beatnotes".

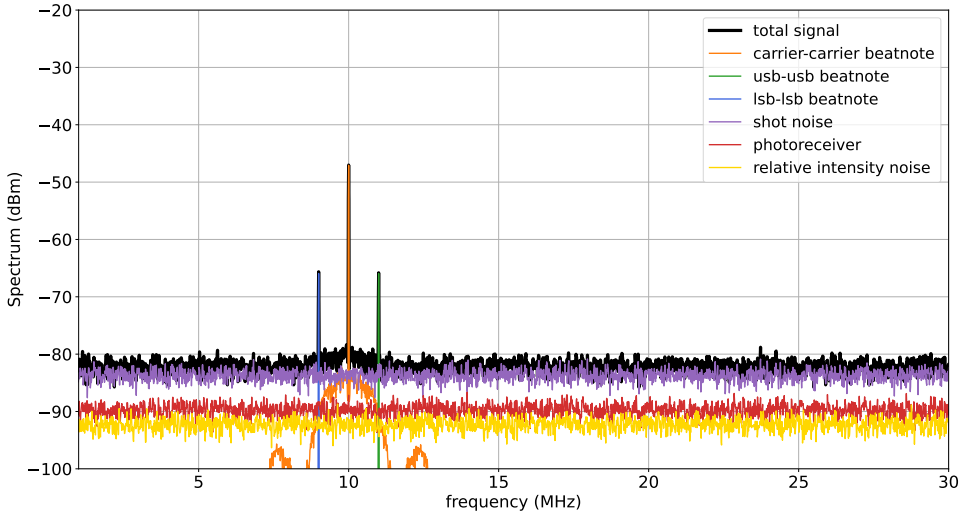

FIGURE 1.4: Simulated interspacecraft interferometer signal with one QPR segment.

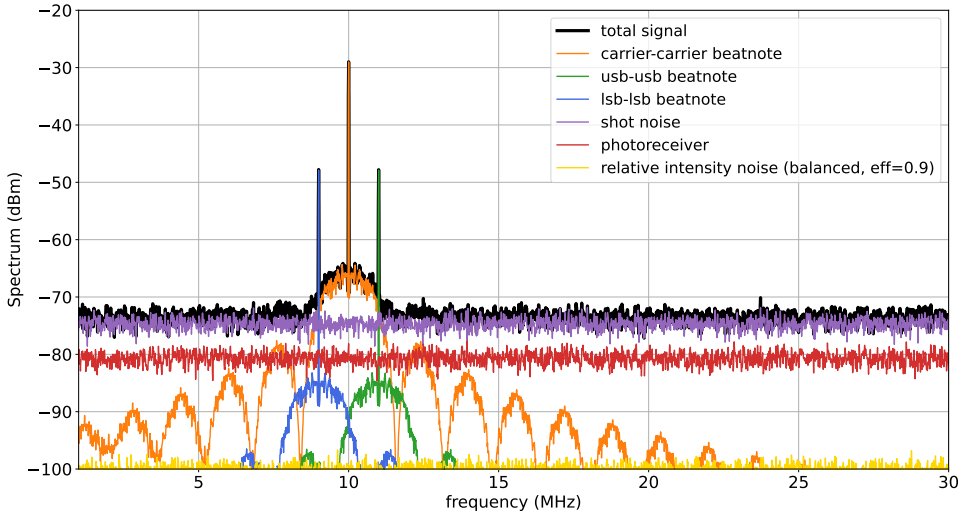

FIGURE 1.5: Simulated interspacecraft interferometer signal with two QPRs. A balanced detection scheme, discussed in Appendix C, is assumed to suppress the RIN noise floor with the balancing efficiency of 0.9.

1.3.1 *Noises*

The two primary noises in the scope of this thesis are introduced in this section: laser frequency noises and onboard clock noises. As mentioned, the former and latter are the noise sources to be suppressed by *intersatellite absolute ranging* and *intersatellite clock synchronization*.

1.3.1.1 *Laser frequency noise*

If not treated by TDI, a laser frequency noise is the overwhelming noise source due to the unequal-arm interferometers on board, which is unacceptable to meet the LISA design sensitivity even with the stabilization with an onboard reference cavity.

Single laser noise: According to [21], the upper bounds of requirements on free-running and stabilized laser frequency noises in amplitude spectrum density (ASD) are given in the range from 0.1 mHz to 1 MHz by,

$$\sqrt{S_\nu^{\text{free,req}}(f)} = 3.75\,\text{Hz}/\sqrt{\text{Hz}} \cdot \sqrt{1 + (8\,\text{kHz}/f)^2}, \tag{1.16}$$

$$\sqrt{S_\nu^{\text{stab,req}}(f)} = \begin{cases} \sqrt{S_\nu^{\text{stab,low}}(f)} = 30\,\text{Hz}/\sqrt{\text{Hz}} \cdot \sqrt{1 + (2\,\text{mHz}/f)^4} \\ \sqrt{S_\nu^{\text{stab,high}}(f)} = \sqrt{S_\nu^{\text{free,req}}(f)}, \end{cases} \tag{1.17}$$

where $\sqrt{S_\nu^{\text{stab,low}}(f)}$ and $\sqrt{S_\nu^{\text{stab,high}}(f)}$ are defined in the frequency ranges between 0.1 mHz and 1 Hz and between 1 Hz and 1 MHz, respectively.

The "LISA laser frequency noises" in this thesis are correspondingly formulated by,

$$\sqrt{S_\nu^{\text{free}}(f)} = \sqrt{S_\nu^{\text{free,req}}(f)}, \tag{1.18}$$

$$\sqrt{S_\nu^{\text{stab}}(f)} = \left(\sqrt{\frac{1}{S_\nu^{\text{stab,low}}(f)} + \frac{1}{S_\nu^{\text{stab,high}}(f)}} \right)^{-1}, \tag{1.19}$$

where the cavity-stabilized frequency noise was tailored for a smooth curve without the discontinuity at 1 Hz in Eq. (1.17) by extrapolating the low- and high-frequency requirements over the frequency range. The single-laser frequency noises with and without the onboard stabilization are plotted in solid curves on the top panel in Figure 1.6.

Beatnote noise: The actual input signal to PM is not a single laser beam but an optical beatnote. Hence, the input noise is the beatnote noise instead of the original beam frequency noise in Eqs. (1.18) and (1.19). The beatnote dynamics are not uniform in the constellation and highly depend on which PM is under discussion. The following conditions need to be taken into account to derive the beatnote frequency noise based on the beam noises,

- **Local laser lock:** If two interfering beams are locally locked, the beatnote noise is highly suppressed down to the residual error of the laser-lock loop,

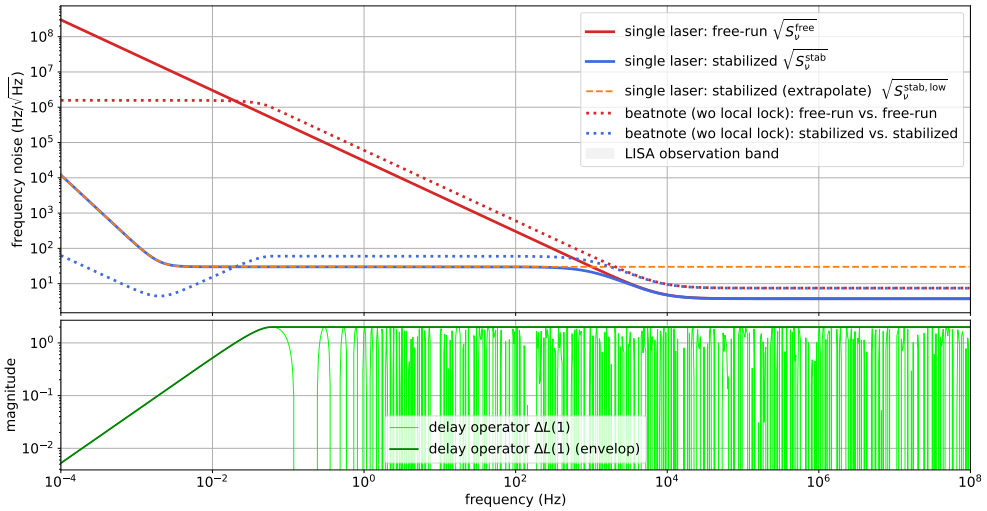

FIGURE 1.6: LISA laser frequency noise. **Top:** the laser and beatnote frequency noises under different conditions. **Bottom:** the delay factor $\Delta L(1)$ from Eq. (1.20). The beatnote noises on the top are based on the envelope of the delay factor $\Delta L(1)$ in solid green on the bottom.

- **Effective delay:** The effective time delay between two interfering beams breaks their coherence. The main contribution must be an intersatellite light travel time.

The conditions are determined by LISA frequency plan, designed by Gerhard Heinzel [22]. The laser transponder lock in the first point is discussed in detail in Appendix F, while the impact of the second point is discussed here. In case the two beams have the same frequency noise level, a resulting beatnote noise can be derived by applying the following operator to the common frequency noise in ASD,

$$\begin{aligned}\Delta L(n) &= |1 - \mathbf{D}^n| \\ &= 2\sin(\pi f n \Delta\tau), \qquad (1.20)\\ \mathbf{D} &= \exp(-i2\pi f \Delta\tau), \qquad (1.21)\end{aligned}$$

where the effective time delay between the beams is denoted by $\Delta\tau$, which corresponds to 8.3 s with the one-way intersatellite separation of 2.5×10^9 m, and n is the number of such an intersatellite delay between the beams. The delay factor $\Delta L(1)$ and its envelope are plotted on the bottom in Figure 1.6. Lastly, the beatnote noises based on the single laser noise in Eqs. (1.18) and (1.19) and $\Delta L(1)$ without the local laser lock are plotted on the top in Figure 1.6: dotted-red is the beatnote noise between the free-running lasers, and dotted blue is the one between the stabilized lasers. The latter is the worst case in the science mode in three senses: no local laser lock, a requirement-driven curve instead of current best estimate (CBE) of laser stability, and an envelope of a delay factor. To simulate such a noisiest PM input noise in a lab, a white noise floor in the dotted-blue, i.e., $60\,\text{Hz}/\sqrt{\text{Hz}}$, is normally injected via the laser lock system (see Appendix F) in experiments in this thesis.

1.3.1.2 *Clock noise*

Each of three SC in the LISA constellation accommodates a single clock, so-called USO. The three USOs run independently, and any onboard measurements are time-stamped by USOs. This raises an issue when the data from different SC must be combined to perform TDI. Due to clock desynchronization, the timestamps of phase signals to be combined have large initial offsets

and time-varying slow drifts due to deterministic relative trends, often called clock bias. In addition, stochastic clock jitter affects the detector sensitivity directly in the observation band [23], which has a significant entry to a noise budget.

To synchronize the timestamps to a reference time frame and also remove the in-band clock jitter in on-ground data processing, electro-optical modulator (EOM) imprints the local USO signal on a transmitted beam phase by investing around 15 % of a beam power for the sidebands. A clock frequency is up-converted from MHz to GHz to enhance the timing-jitter coupling into the phase to relax a requirement on phase readout. As a result, the beam interference at beam splitter (BS) generates sideband-sideband beatnotes in addition to the primary carrier-carrier beatnotes. The phases of these additional beatnotes are also tracked by PM (see Section 2.2.2) to extract the differential clock signals for clock synchronization in post-processing.

Nominally from 80 MHz to 2.4 GHz; see Section 2.6 for details.

Three types of clocks in this thesis are listed below, together with their models in power spectrum density (PSD) of timing jitter $S_\tau(f)$,

- "Atomic USO": an atomic clock as a state-of-the-art space-qualified clock. The measurement is from a cold-atom space clock, namely PHARAO, from Centre National d'Exploration Spatiale (CNES) [4] [23, 24]. Model: $S_\tau(f) = 10^{-32} + 10^{-28} \cdot \left(1/f + 1/f^3\right)$.
- "EGSE USO": an oven-controlled crystal oscillator (OCXO) used for a test campaign of electrical ground support equipment (EGSE) at the AEI [25]. This would be a CBE of a flight model for LISA in this thesis. Model: $S_\tau(f) = 3.6 \times 10^{-33} + 1.6 \times 10^{-27}/f + 10^{-26}/f^4$.
- "Hexagon USO": a commercial signal generator (SG), referring to an internal OCXO, used for the Hexagon experiment, introduced in Chapter 3, in this thesis. Model: $S_\tau(f) = 2 \cdot 10^{-31} + 10^{-27}/f + 10^{-22}/f^3$.

Figure 1.7 compares the stability of the three clocks in ASD of timing jitter. The in-band stability directly affects the detector sensitivity, as mentioned. In contrast, the high-frequency stability around MHz has a significant impact on phase-locked loop (PLL) on PM tracking a differential clock signal; see Section 2.2.2. The Atomic USO and EGSE USO are both coupled to voltage-controlled crystal oscillator (VCXO) with PLL. The bumps around 10 Hz to 100 Hz in both clocks are attributable to the transition from the original clock to VCXO.

1.3.2 *Design sensitivity*

The current official LISA sensitivity curve can be found in [26]. The design sensitivity is normally decomposed into two contributions: optical metrology

4 Peter Wolf, personal communication, used with permission from CNES

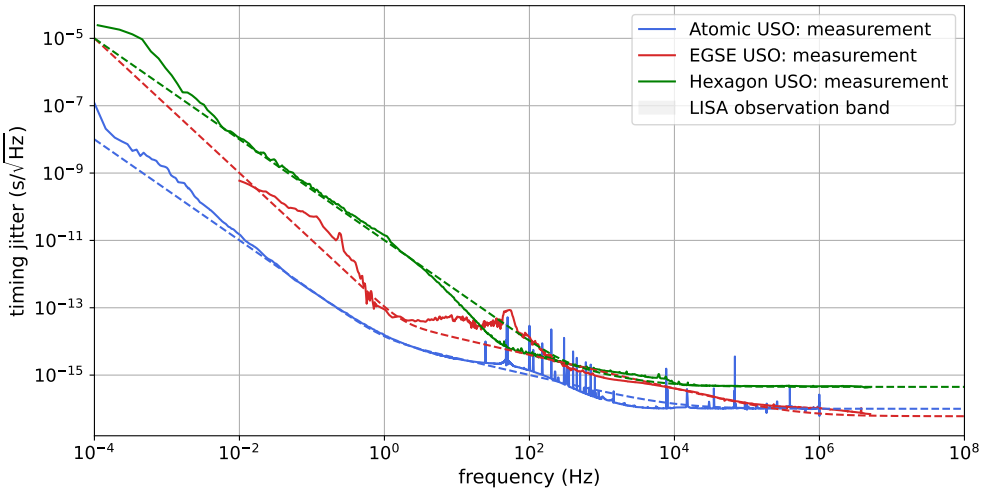

FIGURE 1.7: Comparison of clock stability in timing. Dashed curves are models for each USO. Measurement credit: Atomic USO, Peter Wolf, personal communication, used with permission from CNES. EGSE USO, Daikang Wei. Hexagon USO, Sergio Lozano Althammer.

system (OMS) noises and TM acceleration noises. The requirement levels of them are given by,

$$\sqrt{S_{\mathrm{OMS}}}(f) = 15\,\mathrm{pm}/\sqrt{\mathrm{Hz}}\sqrt{1+\left(\frac{2\times10^{-3}}{f}\right)^4}, \tag{1.22}$$

$$\sqrt{S_{\mathrm{acc}}}(f) = 3\,\mathrm{fms}^{-2}/\sqrt{\mathrm{Hz}}\sqrt{1+\left(\frac{0.4\times10^{-3}}{f}\right)^2}\sqrt{1+\left(\frac{f}{8\times10^{-3}}\right)^4}. \tag{1.23}$$

The acceleration noise level has been demonstrated in space with LISA pathfinder [27, 28]. Any noises in the scope of this thesis, including the laser frequency noise and clock noise mentioned above, are absorbed into the OMS noise $\sqrt{S_{\mathrm{OMS}}}$. The $1\,\mathrm{pm}/\sqrt{\mathrm{Hz}}$ mark with a safety margin taken into account is commonly assigned to each contribution.

The total detector noise can be derived by properly combining $\sqrt{S_{\mathrm{OMS}}}$ and $\sqrt{S_{\mathrm{acc}}}$, taking TDI into account [26]. Finally, the strain sensitivity is defined by the total detector noise over the GW response. The LISA strain sensitivity is shown in solid black in Figure 1.8 together with the OMS and acceleration noises. The sensitivity curve was computed based on a Python script used for [26], provided by Antoine Petiteau.

By convention, the antenna pattern function in the GW response is averaged over sky localization and GW polarizations to compute the sensitivity.

In addition, the coupling of the laser frequency noise (pink) and the in-band clock jitter (green) is also plotted in case they are not treated by TDI and clock synchronization, respectively. The pre-TDI laser noise level is computed by substituting the stabilized frequency noise Eq. (1.19) into the noise model of an unequal-arm Michelson [29]. Because it is unknown yet what clock will fly, the clock noise is plotted by an area bounded by the "Atomic USO" and the "EGSE USO" from Section 1.3.1.2.

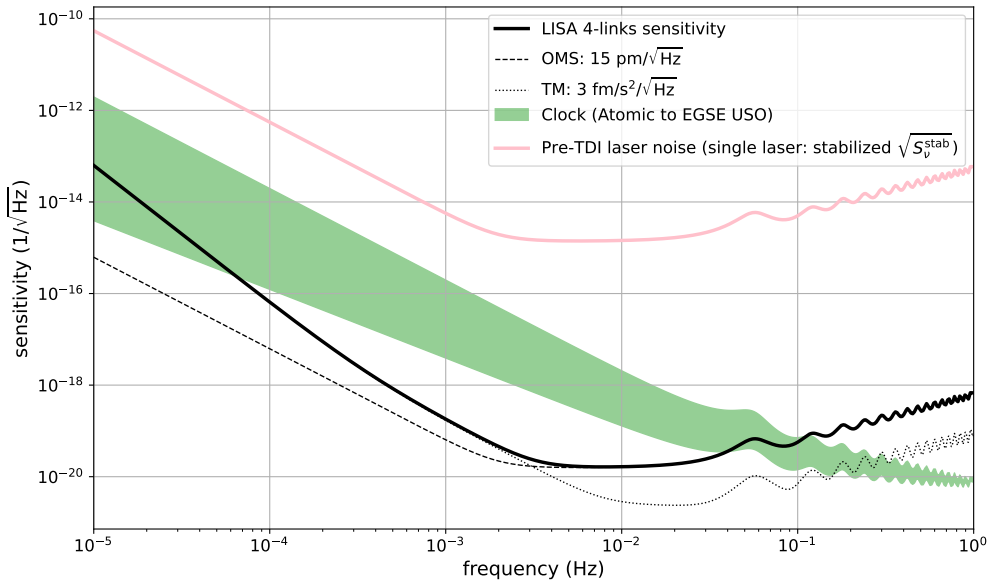

FIGURE 1.8: LISA strain sensitivity. The clock noise area is bounded by the Atomic USO and the EGSE USO.

2

PHASEMETER

As the name suggests, the main goal of PMs is to extract the phase of an input optical beatnote, converted to a voltage by PRs in advance. However, LISA requires this pivotal device to be more multifunctional, evolving from just a "phasemeter". This chapter provides a quick look at key functionalities in the scope of this thesis. In addition, the model of PM signals from [29] is recalled, based on which experiments later will be formulated.

2.1 HARDWARE OVERVIEW

A SC in LISA acts as a receiver and a transmitter because it configures bi-directional links with the distant counterpart. Correspondingly, a PM features functionalities from both perspectives.

Figure 2.1 illustrates the hardware realization. Red is an input optical beatnote signal. Blue shows electrical signals, containing the heterodyne beatnote signal detected by a PR and clock-related synthetic signal lines: the 80 MHz system clock driving an analog-to-digital converter (ADC) and a field programmable gate array (FPGA), GHz-clock sideband signals for clock-tone transfer, a PRN code for absolute ranging, and a pilot tone (PT) signal at the frequency of f_{PT} for the suppression of ADC jitter, which could hinder us from achieving the $1\,\mathrm{pm}/\sqrt{\mathrm{Hz}}$ requirement on the phase-extraction accuracy via a PM. All these synthetic signals are derived from an original onboard clock named USO via frequency distribution system (FDS) (see Section 2.6). Black represents digital signal lines: The beatnote signal (and the PT signal) is digitized by the ADC and delivered to the FPGA programmed in very high-speed integrated circuit hardware description language (VHDL) where plentiful digital signal processing occurs. Multiple PLLs (see Section 2.2) operate to extract signal phases and frequencies, while a delay-locked loop (DLL) (see Section 2.3) runs for intersatellite absolute ranging and data communication.

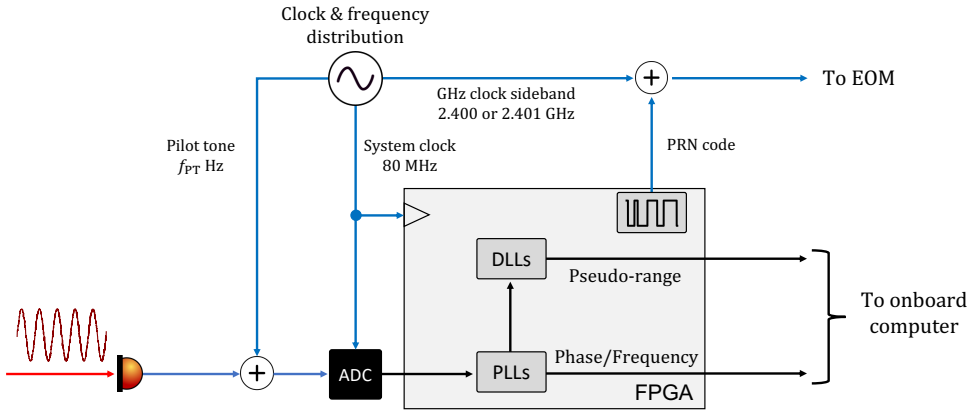

FIGURE 2.1: PM hardware overview. Red is an input optical signal; blue is an electrical signal; black is a digital signal.

2.2 DIGITAL PHASE-LOCKED LOOP (DPLL)

The core functionality of PM is, under the name, to extract the phase and frequency of an incoming beatnote signal. This is achieved by digital phase-locked loop (DPLL) implemented on FPGA. A quick overview of the DPLL design by Oliver Gerberding [30] will be provided here. In addition, Section 2.2.2 includes the author's modification of sideband PLL.

2.2.1 *Basic design*

The block diagram of DPLL is shown in Figure 2.2, together with curves to show how signals at different points look. The input beatnote signal with a MHz heterodyne frequency is mixed with a local sinusoidal signal in quadrature, i.e., with a 90° phase offset. After passing through a low-pass filter, implemented by a simple infinite impulse response (IIR) filter removing a second harmonic, a loop servo generates a control signal from the loop error. The servo comprises a gain stage and a proportional integral (PI) controller. After being integrated, the control signal is plugged into a lookup table (LUT) of a sinusoidal signal. The integration and LUT constitute so-called numerically controlled oscillator (NCO) together with registers corresponding to frequency and phase signals (see below). Finally, the sinusoidal signal, acting as a local copy of the input beatnote, is fed back to the mixer. An open-loop transfer function of this PLL is formulated in the z domain [31],

This also eliminates a pilot-tone signal introduced in Section 2.6.2.

$$G_{\mathrm{PLL}}(z) = \frac{A_{\mathrm{het}}\pi}{2} \cdot F_{\mathrm{PLF}} \cdot 2^{-C_p} \cdot \left(k_p + \frac{k_i}{z-1}\right) \cdot \left(\frac{1}{z-1}\right) \cdot z^{-D}, \tag{2.1}$$

$$F_{\mathrm{PLF}}(z) = \left(\frac{k_{\mathrm{PLF}}}{z-(1-k_{\mathrm{PLF}})}\right)^{N_{\mathrm{PLF}}}, \tag{2.2}$$

$$F_{\mathrm{PD}}(z) = A_{\mathrm{het}}/4. \tag{2.3}$$

Implemented by a series of a simple low-cost IIR filters.

A_{het} is an amplitude of the heterodyne beatnote; F_{PLF} is a transfer function of the PLL low-pass filter, parameterized by k_{PLF} and N_{PLF}; 2^{-C_p} is an attenuation at the gain stage with a bit growth by C_p; k_p and k_i are PI gains; z^{-D} is a digital-signal-processing delay with the number of registers of D. The phase detector response F_{PD} was defined separately for later in this thesis. In addition, a closed-loop transfer function $H_{\mathrm{PLL}}(z)$ and an error function $E_{\mathrm{PLL}}(z)$ are defined,

$$H_{\mathrm{PLL}}(z) = \frac{G_{\mathrm{PLL}}(z)}{1+G_{\mathrm{PLL}}(z)}, \tag{2.4}$$

$$E_{\mathrm{PLL}}(z) = \frac{1}{1+G_{\mathrm{PLL}}(z)}. \tag{2.5}$$

From this feedback loop, three signals are picked off for readout; a quadrature signal (or just "Q value"), a frequency signal (corresponding to "phase increment register (PIR)"), and a phase signal (corresponding to "phase accumulator (PA)") [1]. In addition, the input heterodyne signal can be mixed separately with its local copy "in phase" to recover a signal amplitude (or just

1 Physical interpretations of signals in a loop can be deduced from a LUT. A LUT defines its input as a phase in cycles. This is a simple integration of the servo output; hence, the servo output is a frequency signal normalized by the system clock rate of 80 MHz.

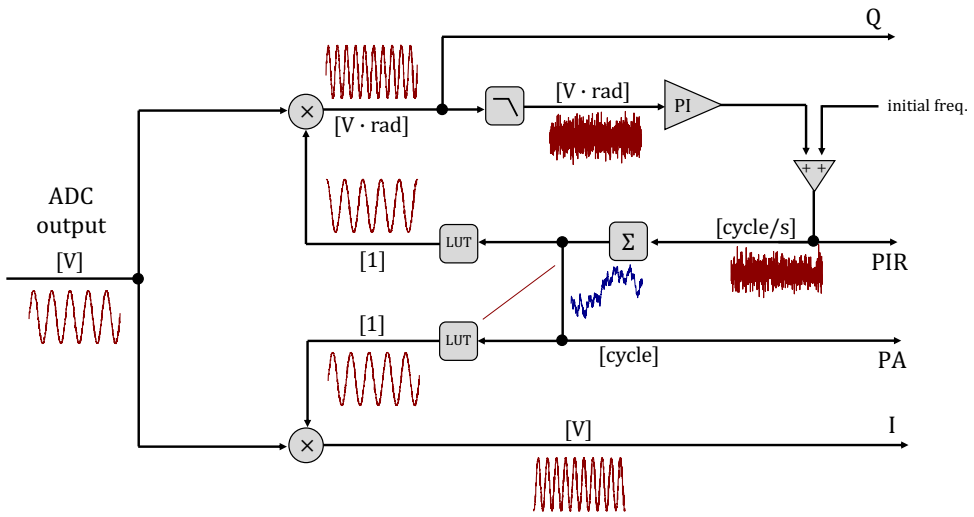

FIGURE 2.2: Schematic of DPLL implemented on a PM. After a low-pass filter, a servo includes a gain stage and a PI controller. "[1]" denotes dimensionless values. Dark-red curves visualize how signals look at different points (signal magnitudes are inconsistent). Only the PA value shows its detrended curve in blue in addition.

"I value"), as also depicted in Figure 2.2. The primary signal is nominally the frequency because it is free from a dramatic slope, appearing in phase due to the MHz heterodyne frequency, and, hence, easy to handle in post-processing. However, the frequency signal lacks an integration constant beneficial for absolute ranging. Hence, the phase will also be downlinked to the Earth at a lower rate to keep such information. This is called "phase anchor". The Q and I values are for diagnostics: the I value is especially helpful in estimating ranging biases as discussed later in Part III.

FPGA handles multiple PLL based on this basic design,

- *carrier PLL*: this tracks phases of carrier-carrier beatnotes, i.e., main science beatnotes where GW signals are embedded. One instance per PM channel. Nominal bandwidth: $\mathcal{O}(10\,\mathrm{kHz})$ to $\mathcal{O}(100\,\mathrm{kHz})$.
- *sideband PLL*: this tracks phases of sideband-sideband beatnotes to extract differential onboard clock signals. One instance per quadrant photo-diode (QPD), i.e., per four PM channels. Nominal bandwidth: $\mathcal{O}(10\,\mathrm{Hz})$ to $\mathcal{O}(100\,\mathrm{Hz})$.
- *PT PLL*: this tracks phases of PT signals, added to science signals before ADC, to probe ADC jitter. One instance per PM channel. Nominal bandwidth: $\mathcal{O}(1\,\mathrm{kHz})$.

Only the sideband PLL has a unique feature in addition to the basic architecture in Figure 2.2, which is the focus of the next section.

2.2.2 *Sideband PLL*

As introduced in Chapter 1, LISA requires the synchronization of independent clocks on different SC. For this purpose, differential clock signals need to be monitored onboard to be used for their synchronization in post-processing. This is achieved by encoding the clocks in beam phases via EOM, generating sideband-sideband beatnotes in addition to carrier-carrier beatnotes at BS, and tracking their phases with dedicated PLL.

The dedicated PLL is called sideband PLL. The sideband-sideband beatnote contains any carrier phase signals (including a laser noise, GW signals, etc.),

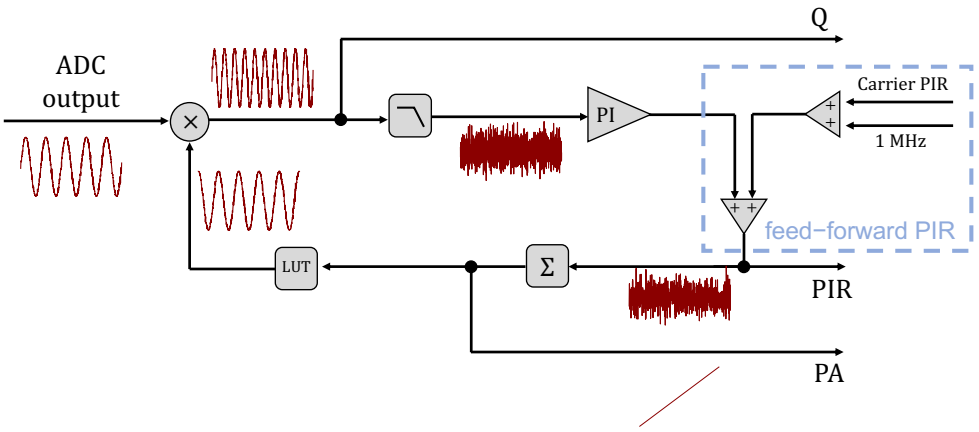

FIGURE 2.3: Sideband PLL with frequency feed-forward. The frequency readout is located after the feed-forward; hence, it contains all information, including the redundant. This can be restricted to the target clock signal by shifting the readout.

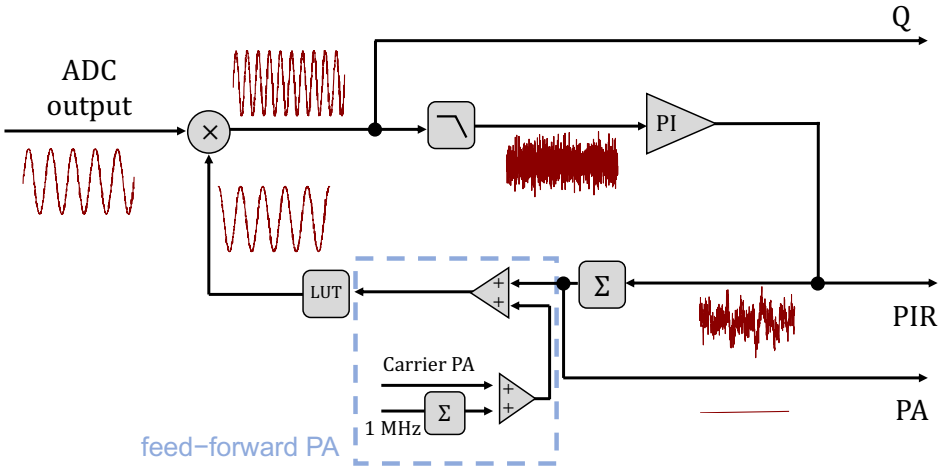

FIGURE 2.4: Sideband PLL with phase feed-forward. Both the frequency and phase contain the target clock signal, eliminating redundant information.

an offset frequency nominally at 1 MHz, and the target signal composed of desynchronized clocks and residual Doppler effects. The carrier signal is feed-forwarded from the carrier PLL [30] to track only the target signal. This allows us to reduce a loop bandwidth, above which shot noise is rejected; hence, it helps an acquisition and improves the phase-tracking robustness.

Notably, the outputs from sideband PLL contain all frequency and phase contributions, regardless of the feed-forward scheme, including the redundant information from the carrier beatnote. This is because the readout point is located after the feed-forward point[2]. Another option shown in Figure 2.4 has been implemented by the author to restrict the outputs of sideband PLL to the target signals. This design feed-forwards the carrier and 1 MHz phase instead of frequency and shifts the phase readout point before the feed-forward[3].

Raw frequency signals from each PLL with the two topologies are compared in Figure 2.5. The carrier-carrier beatnote frequency was set at 24.9 MHz. The old design, from Figure 2.3, shown on the left column, provides the outputs of sideband PLLs with all contributions, including carrier-carrier beatnote dynamics and 1 MHz offset. Frequency fluctuations are, as expected,

2 This is the most straightforward implementation in VHDL and even allows reusing the code of the carrier PLL; the sum of the carrier frequency and 1 MHz can be plugged to the initial frequency port in Figure 2.2.

3 To restrict the frequency output to the target clock signal, it is enough to change the frequency readout to the point before the frequency feed-forward in Figure 2.3. However, the phase feed-forward can also restrict the phase output, which is cleaner when processing phase anchor for ranging.

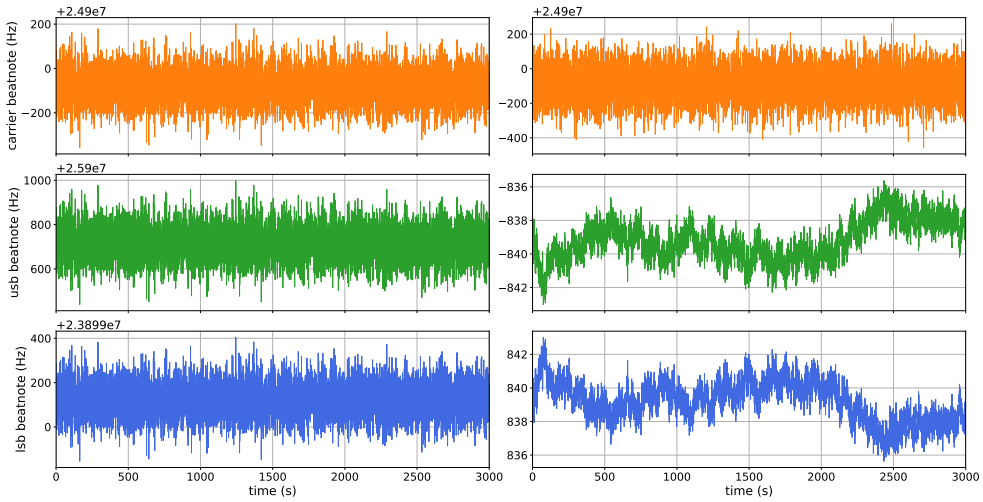

FIGURE 2.5: Raw outputs of total frequencies from different sideband PLL topologies (all are real measurements). **Left:** the old topology with frequency feed-forward. **Right:** the new topology with phase feed-forward.

dominated by carrier frequency noise. The new design, from Figure 2.4, shown on the right column, properly restricts the outputs of sideband PLLs to the target differential clock signals. The upper and lower sideband PLLs show opposite polarities, following the differential clock terms $\delta\theta_{\text{sb}}$ in Eq. (1.2).

2.3 DELAY-LOCKED LOOP (DLL)

TDI needs pseudo-range, a combination of a physical intersatellite light travel time and a desynchronized clock contribution. In LISA, the pseudo-range is obtained via multiple monitors. One of them is PRNR [32, 33], which is achieved by an additional feedback loop implemented on PM, i.e., DLL. In addition to the ranging, the PRN modulation also achieves *intersatellite data communication* with PM data superimposed on it. The intersatellite communication allows ground communication with only one of three SC, which in turn relaxes the rate of the antenna re-pointing, around ten days [14].

This section aims to clarify a PRN signal chain through the FPGA architecture and introduce only the basic information of DLL. DLL will be revisited later in Chapter 5 with more technology descriptions and formulations.

2.3.1 *PRN signal chain*

In PRNR, a beam phase is modulated with binary signals called PRN code at the transmitter side, in addition to the GHz clock modulations. A receiver compares the received code with its local copy by computing their correlation. The pseudo-range is derived as a time shift between the phase of the received code and a local counter driving the local copy and a transmitted code, which maximizes the correlation.

The receiver extracts the PRN signal from the Q value of a carrier PLL. The modulation signal exists at the PLL error point since its parameters are selected so that the binary chip rate is above the PLL bandwidth and not tracked by the loop. After this picked-off signal passes through a dedicated low-pass filter, it is plugged into the input of DLL.

This signal chain is illustrated in Figure 2.6, while Figure 2.7 shows transfer functions to allow the PRN signal extraction; the PLL error function ($E_{\text{PLL}}(z)$) and a pre-DLL low-pass filter (F_{DLF}). F_{DLF} needs a corner frequency high

Instead of a single PLL, the length error given by a mean value of four segments (or even eight segments) will be used to maximize signal-to-noise ratio (SNR), based on the PLL design proposed by [34]. A single PLL might not be enough for DLL to track a code, graphically shown in Figures 1.4 and 1.5.

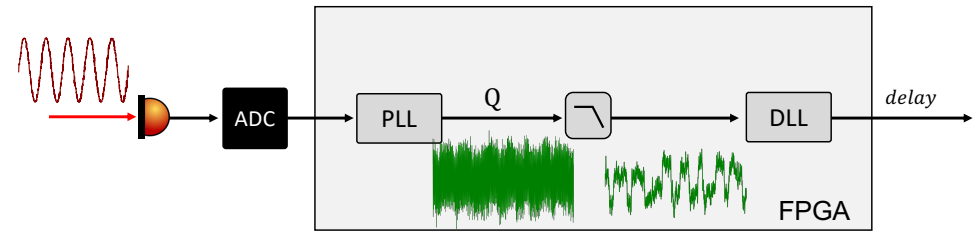

FIGURE 2.6: Schematic of a PRN signal chain. Filtered by the pre-DLL low-pass filter, the PLL Q value is plugged into DLL, which outputs a delay estimate.

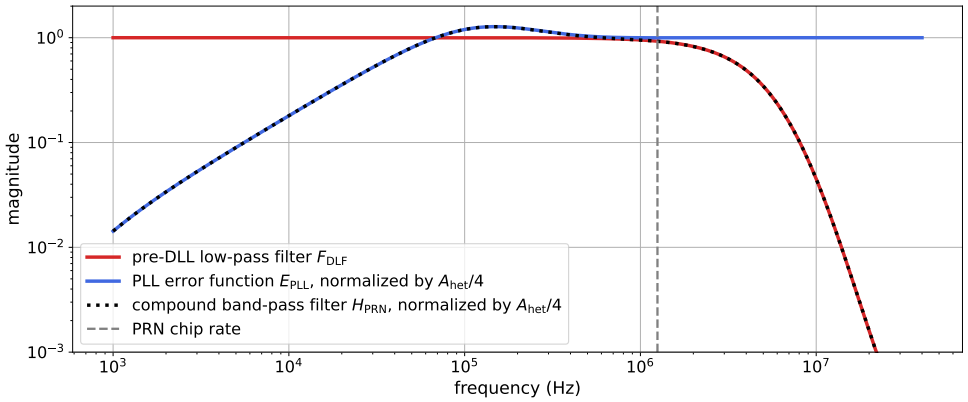

FIGURE 2.7: Compound band-pass filter for a PRN modulation. The phase detector response F_{PD} from Eq. (2.3) normalizes the flat levels.

enough to maintain the PRN code, which requires a steep slope to eliminate heterodyne second harmonics and a PT signal.

Figure 2.8 shows a simulation to visualize different contributions to the Q value before and after the low-pass filter. The heterodyne second harmonics dominate the raw Q value. The pre-DLL low-pass filter F_{DLF} eliminates the harmonics and shot noise contributions above its corner frequency. Time shifts due to the group delay of F_{DLF} can also be recognized.

2.3.2 *Design overview*

The PRN signal after the low-pass filter F_{DLF} comes in DLL where a pseudo-range is estimated.

Figure 2.9 is the loop overview, including the data-decoding paths. DLL operation can be categorized into two steps: *acquisition* and *tracking*.

Acquisition mode: This first stage aims to acquire an instant pseudo-range

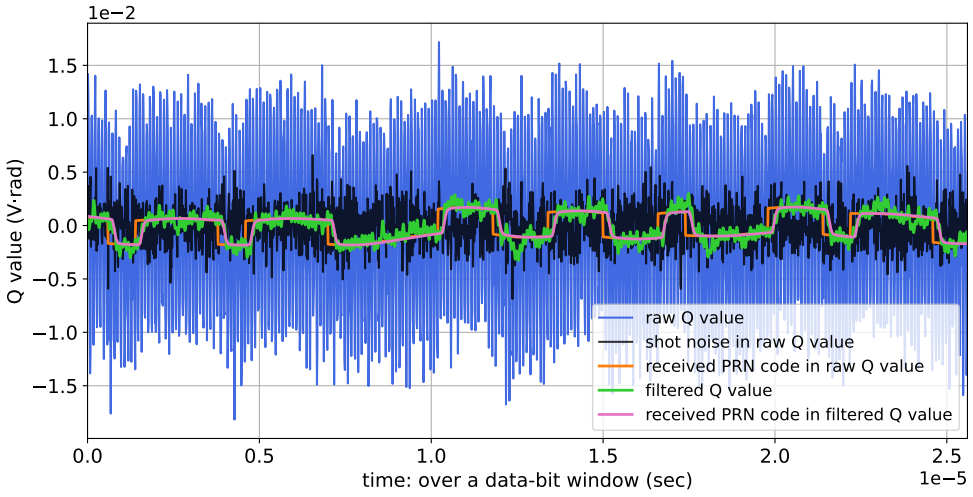

FIGURE 2.8: Simulated PLL Q value with a PRN modulation (no interfering PRN code), without a PT signal. A raw PLL Q value (blue) is dominated by heterodyne second harmonics. Heterodyne frequency is 5 MHz, a PRN modulation depth is 0.1 rad, the order of a pre-DLL IIR filter is 8, and other optical parameters are for a long-arm interferometer.

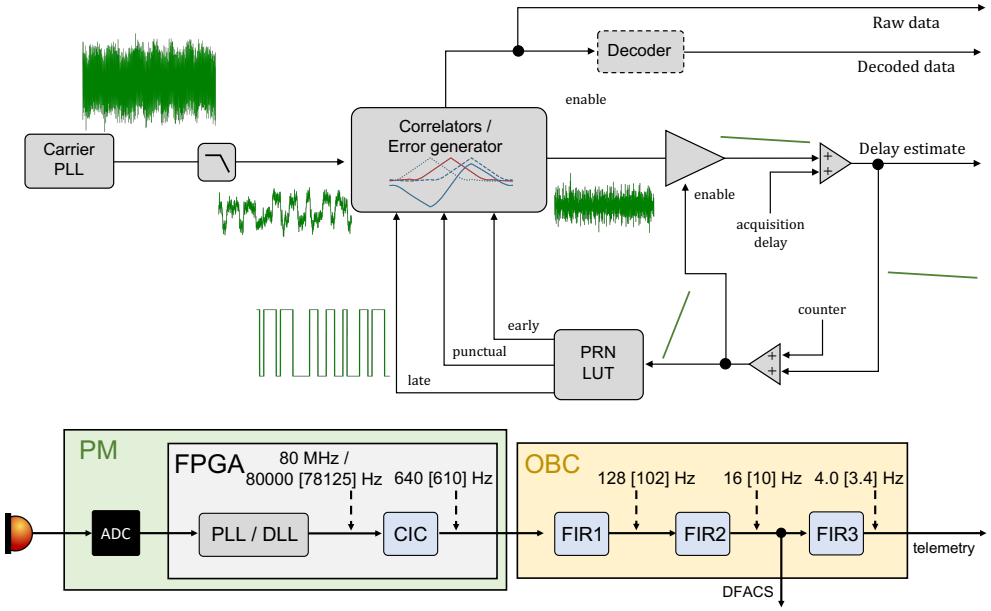

FIGURE 2.9: DLL design overview, including the data decoder chain. It is under discussion where the decoder shall be implemented (FPGA or onboard computer (OBC)). Green curves visualize how signals look at each point (signal magnitudes are inconsistent).

FIGURE 2.10: PM decimation chain. Blue blocks represent decimation stages with the names of accompanied anti-aliasing filters. Values for the implementation in this thesis are, if different, shown in square parenthesis.

with the loop open by turning off the servo, to close the loop with a reasonable initial estimate in the next step. The address driving a PRN LUT scans the entire code length and finds an address in phase with the received signal. The acquisition of such an in-phase address is based on a peak detection of the correlation between the received signal and its local copy, the so-called "punctual" signal. The naming distinguishes it from the other two local signals generated by the PRN LUT in the following mode.

Tracking mode: A feedback control is established by closing the loop in this mode. To obtain an error signal from such a binary signal, the local PRN LUT generates two more local copies shifted by half of a PRN chip from the punctual signal in the opposite directions (so-called "early" and "late" signals). The loop error is computed by a difference between the "early" and "late" correlations with the received PRN signal. A nominal bandwidth of the loop is $\mathcal{O}\,(100\,\mathrm{Hz})$.

2.4 FILTERING AND DECIMATION

PLL in Section 2.2 operates at the system clock of 80 MHz, while DLL in Section 2.3 runs at the data-bit rate around 80 kHz. The high-rate scientific outputs from these feedback loops need to be decimated to a few Hz for further scientific analysis and telemetry. On top, the decimation should be accompanied by a dedicated anti-aliasing filter to avoid aliased noises in the observation band.

The whole decimation is separated into multiple stages. The first decimation stage is implemented with a cascaded integrator comb (CIC) filter on FPGA. The CIC filter is computationally cheap and compatible with FPGA, which has limited resources. However, the suppression of the filter is moderate. Thereby, the filter is often followed by finite impulse response (FIR) filters with dramatic attenuations, which is the case also on the LISA PM.

Signals decimated to the intermediate rate with the CIC filter are sent to an OBC, and then, the OBC decimates the signals to the final rate of a

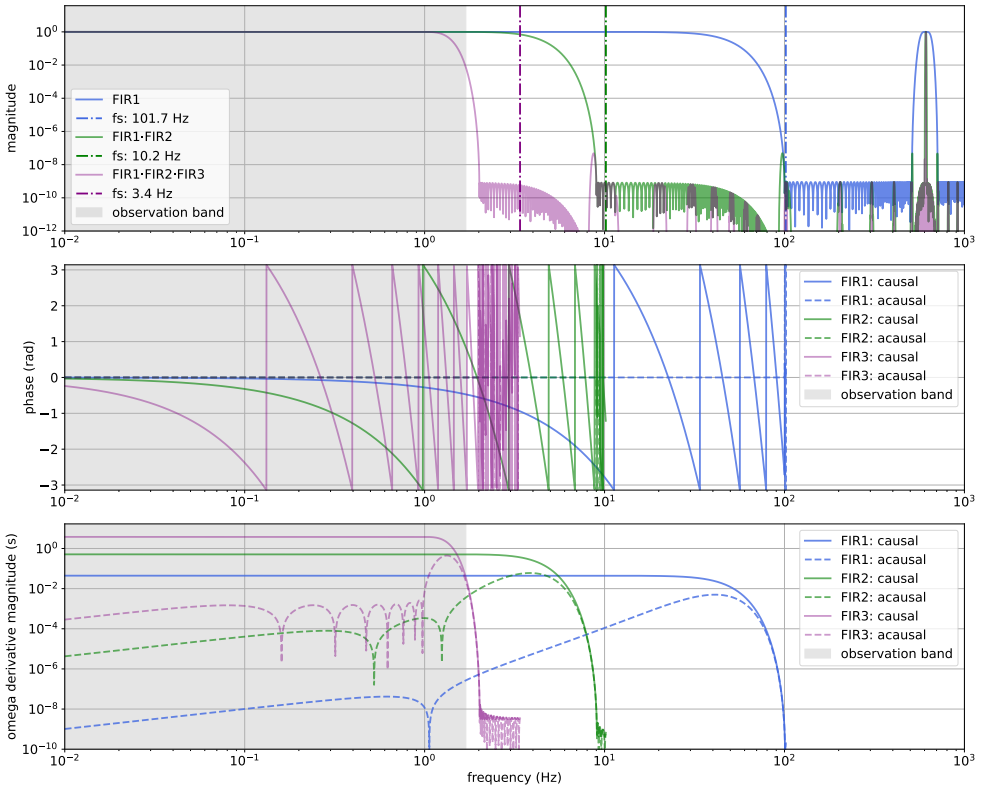

FIGURE 2.11: Transfer functions of FIR filters. **Top:** the magnitudes of the total filters down to a particular stage. **Middle:** the phases of the causal and acausal versions. **Bottom:** the absolute values of the frequency derivatives of the causal and acausal versions. Sampling frequencies follow the values for this thesis (i.e., square parenthesis in Figure 2.10.)

few Hz with multiple FIR-filter stages. Figure 2.10 shows a schematic of the end-to-end PM decimation chain. The data rates in the figure would not be final for LISA [4]. Note that this decimation chain introduces artifacts in case a digital signal ramps and reaches bounds determined by the number of bits, which occurs to heterodyne phases from PLL and PRN delay estimates from DLL. See Appendix G for the method to overcome this issue.

To wrap up this section, transfer functions of anti-aliasing filters are shown in Figure 2.11. The figures also show the frequency derivatives of transfer functions in addition to the usual magnitudes and phases. The frequency derivatives determine so-called flexing-filtering couplings, modeled in Appendix E.3 and experimentally verified in Chapter 4. They are usually dominated by group delays in real FIR filters implemented on hardware, which are always causal. Contrary to it, a virtual filter in which a group delay is subtracted is called an "acausal filter", where the frequency derivative of the magnitude is the only residual.

All PMSs nominally share the same filter stages after PLLs. Relative group delays between carrier signals on different PMSs are zeroed in this case, and the entry to the flexing-filtering coupling converges on the acausal case.

2.5 TIMER MODEL

Modeling the time-stamping of PM signals by a driving clock is essential in case a setup is composed of multiple PMs and their data need to be combined, as is the point for clock synchronization in LISA and the Hexagon experiment introduced in Chapter 3. Hence, in the following, the timer model described in [29] is recalled and slightly adapted for the rest of this thesis. When PM signals are formulated with the following timer model in this thesis, it is commonly assumed, if no particular remark, that the measured frequencies

4 The current nominal for LISA is 640 Hz, 128 Hz, 16 Hz, and 4 Hz, while values for any experiments in this thesis are 610 Hz, 102 Hz, 10 Hz, and 3.4 Hz.

are the PM outputs, i.e., the low-rate data around a few Hz after the down-sampling, introduced in Section 2.4, from the 80 MHz sampling frequency. Imperfections in the down-sampling process are studied separately, as done in Appendix E.

The timing noise of the secondary clock i relative to the primary clock m is denoted as $q_i(\tau)$, while the overall clock time $\tau_i^{\tau_m}(\tau)$ at a given reference clock time τ is modeled as

While a LISA model in [29] considers a SC proper time as a reference, one of the clocks driving PMs is normally selected as a primary (= reference) clock in this thesis, except for Section 2.6.

$$\begin{aligned}\tau_i^{\tau_m}(\tau) &= \tau + \delta\tau_i(\tau) \\ &= \tau + q_i(\tau) + \delta\tau_{i,0},\end{aligned} \tag{2.6}$$

since

$$\delta\tau_i(\tau) \coloneqq q_i(\tau) + \delta\tau_{i,0}, \tag{2.7}$$

with $\delta\tau_{i,0}$ as the constant initial time offset between the clocks. We call $\delta\tau_i(\tau)$ timer deviation. The superscript τ_m explicitly shows that this function is according to the clock m. The primary clock naturally satisfies $\tau_m^{\tau_m}(\tau) = \tau$.

To transform variables sampled by the clock i to the primary clock time frame, the inverse of Eq. (2.6) is needed, i.e., the primary clock time according to a time of the clock i. The following implicit equation can express this,

$$\tau_m^{\tau_i}(\tau) = \tau - \delta\tau_i(\tau_m^{\tau_i}(\tau)), \tag{2.8}$$

which utilized a chain rule,

$$\tau_m^{\tau_i}(\tau_i^{\tau_m}(\tau)) = \tau. \tag{2.9}$$

Phase measurements ϕ^{τ_i} sampled according to one of the clocks i are simply shifted in time according to Eq. (2.8),

$$\begin{aligned}\phi^{\tau_i}(\tau) &= \phi^{\tau_m}(\tau_m^{\tau_i}(\tau)) \\ &= \phi^{\tau_m}(\tau - \delta\tau_i(\tau_m^{\tau_i}(\tau))).\end{aligned} \tag{2.10}$$

As stated above, the PM output is used in terms of frequencies related to the phase by a time derivative. This gives

$$\begin{aligned}\nu^{\tau_i}(\tau) &= \frac{d\phi^{\tau_i}(\tau)}{d\tau} \\ &= \nu^{\tau_m}(\tau_m^{\tau_i}(\tau)) \cdot \frac{d\tau_m^{\tau_i}(\tau)}{d\tau} \\ &= \frac{\nu^{\tau_m}(\tau_m^{\tau_i}(\tau))}{1 + \dot{q}_i(\tau_m^{\tau_i}(\tau))},\end{aligned} \tag{2.11}$$

for expressing a frequency measured according to the clock i relative to the same frequency measured by the reference clock, since

$$\begin{aligned}\frac{d\tau_m^{\tau_i}(\tau)}{d\tau} &= 1 - \frac{d\delta\tau_i(\tau_m^{\tau_i})}{d\tau_m^{\tau_i}} \cdot \frac{d\tau_m^{\tau_i}(\tau)}{d\tau} \quad \because \text{ Eq. (2.8)} \\ &= 1 - \dot{q}_i(\tau_m^{\tau_i}(\tau)) \cdot \frac{d\tau_m^{\tau_i}(\tau)}{d\tau} \quad \because \text{ Eq. (2.7)} \\ \therefore \frac{d\tau_m^{\tau_i}(\tau)}{d\tau} &= \frac{1}{1 + \dot{q}_i(\tau_m^{\tau_i}(\tau))}.\end{aligned} \tag{2.12}$$

In this timer model, the primary clock time frame τ_m is not necessarily a physical clock. Any user-defined reference can be used for this time frame. For the rest of this thesis, any phase or frequency signal without a superscript is implicitly according to a given global time frame. This will mainly apply to signals before an ADC sampling. To transform the signal to a time frame defined by a physical clock via an ADC, the time-stamping operator is introduced,

$$\phi^{\tau_i}(\tau) = \mathbf{T}_i \phi(\tau), \tag{2.13}$$
$$\nu^{\tau_i}(\tau) = \dot{\mathbf{T}}_i \nu(\tau), \tag{2.14}$$

where $\dot{\mathbf{T}}_i$ includes the multiplicative factor in Eq. (2.11) in addition to time shifts.

2.6 FREQUENCY DISTRIBUTION

Onboard synthetic signals at different frequencies have been mentioned up to this point: the 80 MHz clock driving an ADC and a FPGA, GHz sideband signals at 2.400 GHz and 2.401 GHz for intersatellite clock-tone transfer, and a PT signal at the frequency of f_{PT} for the suppression of ADC jitter. And all these frequencies must be synchronized to an original USO at dozens MHz. This is achieved by a PM sub-module called FDS. This section first overviews the local frequency distribution by uncovering the "oscillator" in Figure 2.1. Secondly, this frequency distribution will be formulated to clarify what the naive term "clock" in Section 2.5 represents in this system. It ends with the reasonable nomination of the PT signal for a local timing reference.

This refers to inherent timing noise of ADC itself, independent from the noise of a clock driving it.

2.6.1 *Design*

Figure 2.12 shows the latest design of the entire FDS in the top, composed of two boards: a VCXO frequency distribution system (VFDS) for 80 MHz clock synthesis from the original USO at the frequency of f_{USO} [5] and a clock frequency distribution system (CFDS) for the synthesis of GHz-clock sideband signals and the PT signal. The latter would also generate the 1 MHz electrical reference between the sideband signals as a monitor of their relative noise [6]. The bottom shows the design for experiments in this thesis, from [35, 36]. This design contains only separate frequency-divider chains for the PT signal and the system clock from an input 2.400 GHz. Another modulation signal at 2.400 GHz$\pm$1 MHz and the 1 MHz reference signal are generated by a separate USO and an external mixer, respectively. See Chapter 3 and Part II for the detail.

The fundamental limit of intersatellite clock synchronization is set by relative timing noises between a transmitter's actual local timing reference and a timing a receiver monitors as the transmitter's timing reference: the received

5 f_{USO} is conventionally 10 MHz. In contrast, the latest study proposed $3 \cdot 2^{24}$ Hz to avoid a frequency within the heterodyne band of 5 MHz to 25 MHz, allow easier FPGA processing using the power of two, and accommodate needs from gravitational reference sensor (GRS).

6 This is for diagnostics because sideband-sideband beatnotes of reference interferometers contain the complete information of relative noises between the two local GHz sidebands, including, e.g., the contribution from a laser amplifier following EOM.

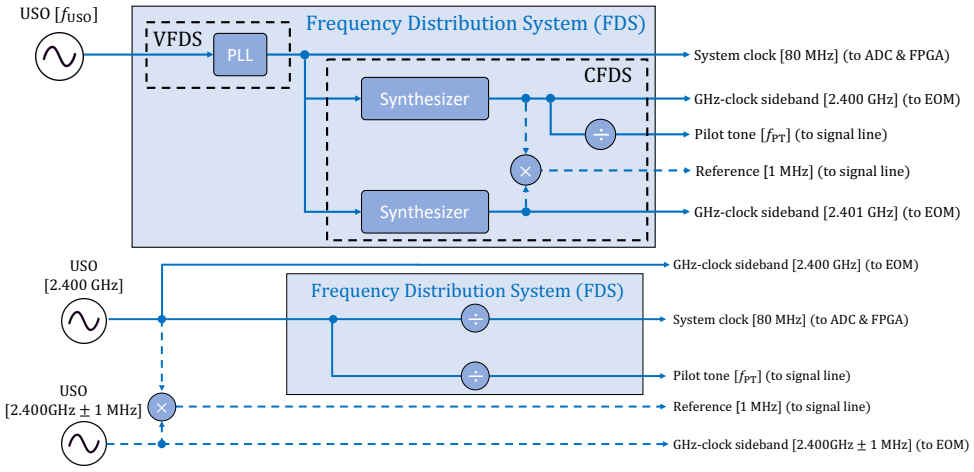

FIGURE 2.12: Conceptual schematic of the entire FDS. **Top:** latest design. **Bottom:** design used for experiments in this thesis. Square brackets show the frequencies of signals, while parentheses show their destinations.

GHz-clock sideband. The required timing stability between the two signals is, based on the usual $1\,\mathrm{pm}/\sqrt{\mathrm{Hz}}$ mark, expressed by,

$$\begin{aligned} 1\,\mathrm{pm}/\sqrt{\mathrm{Hz}} &\approx 1\,\mu\mathrm{cycle}/\sqrt{\mathrm{Hz}} \quad (\because \lambda_0 = 1064\,\mathrm{nm}) \\ &= 40\,\mathrm{fs}/\sqrt{\mathrm{Hz}} \quad (\because \max(f_{\mathrm{het}}) = 25\,\mathrm{MHz}), \end{aligned} \tag{2.15}$$

where λ_0 is a beam wavelength and f_{het} is a heterodyne frequency.

Hence, it is critical to clarify the local timing reference out of the different USO-originated signals and assign the stringent requirement on the phase fidelity between the GHz-clock sideband and the selected signal as the reference.

2.6.2 *Formulation*

Section 2.5 denoted the local timing reference by τ_i. However, as shown in Figure 2.12, multiple USO-synchronized signals with different timing fidelity exist. This section applies the timer model to the local frequency distribution and the PT correction of a science phase signal to define an optimal local timer for the timing reference τ_i for the rest of this thesis. In the following formulation, signals will be written according to the 2.400 GHz sideband signal τ_{GHz}, which is monitored by a distant SC. This choice of reference frame is exceptional and only happens in this section. Such analysis from the perspective of the distant SC efficiently characterizes the local signals and derives the best selection of the local timing reference.

First, the PT-signal timing, the 80 MHz-clock timing, and the actual ADC timing are written, neglecting delays between them,

$$\tau_{\mathrm{PT}}^{\tau_{\mathrm{GHz}}}(\tau) = \tau + q_{\mathrm{PT}}^{\epsilon}(\tau), \tag{2.16}$$

$$\tau_{\mathrm{CLK}}^{\tau_{\mathrm{GHz}}}(\tau) = \tau + q_{\mathrm{CLK}}^{\epsilon}(\tau), \tag{2.17}$$

$$\tau_{\mathrm{ADC}}^{\tau_{\mathrm{GHz}}}(\tau) = \tau + q_{\mathrm{CLK}}^{\epsilon}(\tau) + q_{\mathrm{ADC}}^{\epsilon}(\tau). \tag{2.18}$$

The superscript ϵ explicitly represents that the error terms only contain stochastic components. Notice that the errors are relative to the reference frame, i.e., the 2.400 GHz sideband signal. Referring to Figure 2.12, this conceptually means $q_{\mathrm{PT}}^{\epsilon}$ is the frequency-division chain, $q_{\mathrm{CLK}}^{\epsilon}$ is the synthesizer, and $q_{\mathrm{ADC}}^{\epsilon}$ is the ADC jitter relative to the GHz signal.

A PT frequency signal at the central frequency of f_{PT} is, in this timer set, computed via Eq. (2.16),

$$\begin{aligned}\nu_{\mathrm{PT}}^{\tau_{\mathrm{GHz}}}(\tau) &= f_{\mathrm{PT}} \frac{d\tau_{\mathrm{PT}}^{\tau_{\mathrm{GHz}}}(\tau)}{d\tau} \\ &= f_{\mathrm{PT}} \left(1 + \dot{q}_{\mathrm{PT}}^{\epsilon}(\tau)\right). \end{aligned} \tag{2.19}$$

A heterodyne beatnote signal ν_{het} and the PT signal ν_{PT} are sampled by the ADC $\tau_{\mathrm{ADC}}(\tau)$ following Eq. (2.11),

$$\nu_{\mathrm{het}}^{\tau_{\mathrm{ADC}}}(\tau) = \frac{\nu_{\mathrm{het}}^{\tau_{\mathrm{GHz}}}(\tau_{\mathrm{GHz}}^{\tau_{\mathrm{ADC}}}(\tau))}{1 + \dot{q}_{\mathrm{CLK}}^{\epsilon}(\tau_{\mathrm{GHz}}^{\tau_{\mathrm{ADC}}}(\tau)) + \dot{q}_{\mathrm{ADC}}^{\epsilon}(\tau_{\mathrm{GHz}}^{\tau_{\mathrm{ADC}}}(\tau))}, \tag{2.20}$$

$$\begin{aligned}\nu_{\mathrm{PT}}^{\tau_{\mathrm{ADC}}}(\tau) &= \frac{\nu_{\mathrm{PT}}^{\tau_{\mathrm{GHz}}}(\tau_{\mathrm{GHz}}^{\tau_{\mathrm{ADC}}}(\tau))}{1 + \dot{q}_{\mathrm{CLK}}^{\epsilon}(\tau_{\mathrm{GHz}}^{\tau_{\mathrm{ADC}}}(\tau)) + \dot{q}_{\mathrm{ADC}}^{\epsilon}(\tau_{\mathrm{GHz}}^{\tau_{\mathrm{ADC}}}(\tau))} \\ &= \frac{f_{\mathrm{PT}}\left(1 + \dot{q}_{\mathrm{PT}}^{\epsilon}(\tau_{\mathrm{GHz}}^{\tau_{\mathrm{ADC}}}(\tau))\right)}{1 + \dot{q}_{\mathrm{CLK}}^{\epsilon}(\tau_{\mathrm{GHz}}^{\tau_{\mathrm{ADC}}}(\tau)) + \dot{q}_{\mathrm{ADC}}^{\epsilon}(\tau_{\mathrm{GHz}}^{\tau_{\mathrm{ADC}}}(\tau))}. \end{aligned} \tag{2.21}$$

Eq. (2.19) was used in the second line of Eq. (2.21). The PT correction can be performed by combining $\nu_{\mathrm{het}}^{\tau_{\mathrm{ADC}}}(\tau)$ and $\nu_{\mathrm{PT}}^{\tau_{\mathrm{ADC}}}(\tau)$ from the equations,

$$\begin{aligned}\nu_{\mathrm{het,corr}}^{\tau_{\mathrm{ADC}}}(\tau) &= \nu_{\mathrm{het}}^{\tau_{\mathrm{ADC}}}(\tau) \cdot \frac{f_{\mathrm{PT}}}{\nu_{\mathrm{PT}}^{\tau_{\mathrm{ADC}}}(\tau)} \\ &= \frac{\nu_{\mathrm{het}}^{\tau_{\mathrm{GHz}}}(\tau_{\mathrm{GHz}}^{\tau_{\mathrm{ADC}}}(\tau))}{1 + \dot{q}_{\mathrm{PT}}^{\epsilon}\left(\tau_{\mathrm{GHz}}^{\tau_{\mathrm{ADC}}}(\tau)\right)} \\ &\approx \frac{\nu_{\mathrm{het}}^{\tau_{\mathrm{GHz}}}(\tau_{\mathrm{GHz}}^{\tau_{\mathrm{PT}}}(\tau))}{1 + \dot{q}_{\mathrm{PT}}^{\epsilon}\left(\tau_{\mathrm{GHz}}^{\tau_{\mathrm{PT}}}(\tau)\right)} \\ &= \nu_{\mathrm{het}}^{\tau_{\mathrm{PT}}}(\tau), \end{aligned} \tag{2.22}$$

where the third line is based on the fact that the heterodyne frequency drifts very slowly, and the cross-term between its time derivative and the stochastic timer component is negligible. This enables the interchangeable use of different local timers in time arguments. The fourth line suggests that the ADC-digitized signal corrected by the PT signal $\nu_{\mathrm{het,corr}}^{\tau_{\mathrm{ADC}}}(\tau)$ is equal to the heterodyne signal according to τ_{PT} to the first order approximation.

Eq. (2.22) results in two conclusions:

- *Proper local timing reference*: the PT timer τ_{PT} is a suitable local timing reference represented by τ_i in the timer model in Section 2.5, assuming all beatnotes are already corrected by the PT signals,
- *Performance critical chain*: nominating the PT signal for the local timing reference, the performance of intersatellite clock synchronization is limited by its relative noise to the 2.400 GHz-clock signal τ_{GHz}, i.e., $\dot{q}_{\mathrm{PT}}^{\epsilon}$ in Eq. (2.16). This corresponds to the divider chain in Figure 2.12.

The PT correction plans to be performed on board to save the data amount of the downlink from SC to the Earth. Notice that the relative noise between 2.400 GHz and 2.401 GHz can be corrected via a sideband-sideband beatnote in the reference interferometer in post-processing as a part of TDI; hence, not performance critical. In addition, a local SC hosts two PMS, and correspondingly two FDS, as mentioned in Section 1.2.2. One FDS generates the

2.400 GHz, while the other generates the 2.401 GHz; see the caption of Figure 2.12. Considering the fixed division ratio of the divider chain, PT signals for both PMS need to be generated from the 2.400 GHz. Hence, the CFDS instance at 2.401 GHz receives the 2.400 GHz from the other and frequency-divides it to generate the PT signal for the PMS. As a result, two local PT signals exist, and their relative noise must be below the requirement of Eq. (2.15).

3 THE HEXAGON

LISA requires the PM to detect the phase of an optical heterodyne beatnote with the accuracy of $1\,\mathrm{pm}/\sqrt{\mathrm{Hz}}$ in space. It is necessary to develop a reliable test method to test the core device under such a stringent requirement. As a PM optical testbed, the "Hexagon" interferometer was first proposed by Gerhard Heinzel; see Figure 3.1 for his drawing in 2009 and the picture of the constructed testbed, taken by Daniel Penkert.

The scope of this experiment was extended, as summarized in [37], beyond the test of a stand-alone PM, implementing three independent PMs and optical phase modulations with GHz-clock and PRN-code signals. This extended topology can be considered as a miniature-scale LISA in a lab. It helps test several critical technologies required for the mission's success from the perspective of both devices and data processing. Such an extended experiment is the main scope of this thesis, which will be discussed in the following parts; Parts II and III.

This chapter first recalls the original motivation of this experiment in Section 3.1, which will be followed by the introduction of the interferometer and the extension of the experiment in Section 3.2. Section 3.3 clarifies the link between LISA and the extended experiment, and possible experimental topologies, which will be referred to for the rest of the thesis, are listed in Section 3.4. Section 3.5 wraps up this chapter with a summary of the significance of the Hexagon for the LISA mission.

3.1 THREE-SIGNAL TEST

Three test methods are often considered to test a phase extraction via a PM: a single-channel absolute test, a split test, and a three-signal test. They are well summarized in [38], but also recalled briefly here.

A "single-channel absolute test" compares a PM single-channel output with an applied phase signal. In this way, any distortion of the PM phase extraction can be observed in principle. However, this scheme requires a distortion of the phase reference below the accuracy under which the PM needs to be

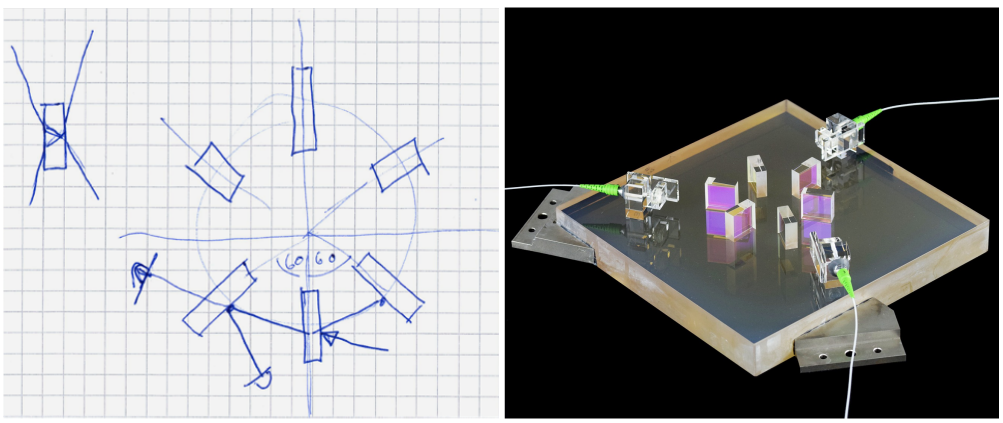

FIGURE 3.1: The Hexagon interferometer. **Left:** a drawing by Gerhard Heinzel in 2009. **Right:** a photograph by Daniel Penkert.

tested, i.e., $1\,\mathrm{pm}/\sqrt{\mathrm{Hz}}$. This stringent requirement inclines us to perform the following two methods.[1]

Apart from the single-channel absolute test, possible experimental setups evaluate PM against itself. The most accessible scheme would be a so-called "split test", which splits a single sinusoidal signal into the number of PM channels under test. In post-processing, differences between the channels can be computed, and residual phase errors reveal distortions of phase extractions. This test is often performed to evaluate PMs; however, this scheme cannot detect common-mode errors like non-linear behavior, which must also be investigated.

As a test topology to overcome this issue, a "three-signal test" was first studied in [39]. This scheme generates three intermediate phases by mixing three initial phase signals pairwise. Three PM channels operate with different signal dynamics; hence, common-mode errors can be detected when three extracted phase signals are linearly combined appropriately in post-processing. This test can be performed in different domains, with digital, electrical, or optical signals. The digital test is convenient to implement [39], but cannot probe a PM analog front end or other devices in the metrology chain, like PRs. The former can be included with electrical signals, while electric mixers are not stable enough to test PM linearity at $1\,\mathrm{pm}/\sqrt{\mathrm{Hz}}$ level [40]. The optical test would be the most suitable option for a three-signal experiment as a test method of the LISA PM.

3.2 THE HEXAGON INTERFEROMETER

The Hexagon interferometer, or just "the Hexagon", is an optical testbed for the LISA PM, implementing the optical three-signal test. This interferometer generates three beatnotes pairwise from three beam sources, phase-locked to each other with MHz frequency offsets. Section 3.2.1 explains how this scheme is achieved in this experiment. After that, the scope of this experiment will be extended beyond the test of a stand-alone PM in Section 3.2.2.

3.2.1 *Optical bench*

The Hexagon OB is composed of three fiber injectors, six BSs, and six PRs. The experiment is named after its hexagonal OB formed by the six BSs. The BSs can be categorized into two kinds; the first BS after each fiber injector splits a beam into two, and the second BS combines them to provide optical beatnotes for PRs.

To reproduce LISA-like heterodyne bandwidth, all three lasers are frequency-locked to each other with MHz offsets in an optical preparation table. See Appendix F for the detail of the laser lock.

1 At the AEI Hannover, there is an effort to develop a device, called "MOSA simulator", to enable this absolute test under the LISA requirement.

3.2.2 *Extending the scope*

The Hexagon was presented above as a testbed for the LISA PM with the optical three-signal test. The extension of the scope of this experiment was first proposed in [37].

The idea is to simulate the *interspacecraft interferometers* in LISA by implementing three PMs driven by independent clocks. Although the Hexagon can not simulate the LISA-like intersatellite light travel time, the metrology chain of the interferometers can be reproduced and tested with this update, which contains optical clock-tone transfer, PRNR, and data communication. In addition, proper data processing is required to reach the LISA performance level with the three-phasemeter three-signal test; otherwise, independent PM outputs are desynchronized. Hence, such an experimental topology also enables testing some of the critical techniques of LISA data analysis in addition to the core devices.

The insight into possible setups is given by mapping LISA to the Hexagon, considering its technical limitation, in Section 3.3. This is followed by Section 3.4 that lists experimental topologies in the Hexagon, which will be referred to for the rest of this thesis. In Parts II and III, the aforementioned intersatellite technologies will be investigated using an optimal topology for each technology.

3.3 RELATION BETWEEN LISA AND THE HEXAGON

The ultimate goal of the Hexagon is to study critical devices and data analysis techniques for LISA with a representative configuration; however, without long-arm entities featured. To achieve it, this section aims to map LISA to the Hexagon and to clarify their link. Notations of LISA interferometric signals follow [41].

3.3.1 *Carrier-carrier beatnotes*

The first step is to write down expressions of interferometric signals in LISA. Only carrier frequencies at laser sources are considered, and any secondary noises are neglected. Under these conditions, the TM and reference interferometers degenerate because the same pair of beams form them; see Figure 1.3.

Fiber reciprocity, PM and PR noises, SC motion relative to TM, etc.

- $\mathrm{tmi}_{ij}(\tau) = \mathrm{rfi}_{ij}(\tau)$: No test mass.

Hence, two interspacecraft interferometers $\mathrm{isi}_c(\tau)$ and two reference interferometers $\mathrm{rfi}_c(\tau)$ will be considered per SC. These four interferometers in SC i in units of frequency are expressed as,

$$\mathrm{isi}_{ij,c}(\tau) = \dot{\mathbf{D}}_{ij}\nu_{ji}^{\tau_i}(\tau) - \nu_{ij}^{\tau_i}(\tau), \tag{3.1}$$

$$\mathrm{isi}_{ik,c}(\tau) = \dot{\mathbf{D}}_{ik}\nu_{ki}^{\tau_i}(\tau) - \nu_{ik}^{\tau_i}(\tau), \tag{3.2}$$

$$\mathrm{rfi}_{ij,c}(\tau) = \nu_{ik}^{\tau_i}(\tau) - \nu_{ij}^{\tau_i}(\tau), \tag{3.3}$$

$$\mathrm{rfi}_{ik,c}(\tau) = -\mathrm{rfi}_{ij,c}(\tau), \tag{3.4}$$

where ν_{ij} is a single beam frequency on an OB in SC i, linked to a distant SC j; the subscript c represents a carrier-carrier beatnote; $\dot{\mathbf{D}}$ is a delay operator applied to a beam frequency, representing intersatellite light travel times; the superscript τ_i explicitly shows that these interferometric signals are sampled according to the onboard clock on SC i.

To reduce LISA to the Hexagon, the following conditions need to be imposed,

- $\dot{\mathbf{D}}_{ij} = \mathbb{1}$: The Hexagon does not simulate the intersatellite distances,
- $\mathrm{rfi}_{ij,c}(\tau) = \mathrm{rfi}_{ik,c}(\tau) = 0$: The Hexagon has only one laser per SC.

These conditions simplify Eqs. (3.1) to (3.4),

$$\mathrm{isi}_{ij,c}(\tau) = \nu_j^{\tau_i}(\tau) - \nu_i^{\tau_i}(\tau), \tag{3.5}$$
$$\mathrm{isi}_{ik,c}(\tau) = \nu_k^{\tau_i}(\tau) - \nu_i^{\tau_i}(\tau), \tag{3.6}$$
$$\nu_i^{\tau_i}(\tau) = \nu_{ik}^{\tau_i}(\tau) = \nu_{ij}^{\tau_i}(\tau). \tag{3.7}$$

Eq. (3.7) relabels the degenerate lasers $\nu_{ij}^{\tau_i}(\tau)$ and $\nu_{ik}^{\tau_i}(\tau)$ with the single index same as the SC.

This reduction ends up with six interspacecraft interferometers listed in the following,

$$\text{SC 1} \begin{cases} \mathrm{isi}_{12,c}(\tau) = \nu_2^{\tau_1}(\tau) - \nu_1^{\tau_1}(\tau), & \text{(3.8a)} \\ \mathrm{isi}_{13,c}(\tau) = \nu_3^{\tau_1}(\tau) - \nu_1^{\tau_1}(\tau), & \text{(3.8b)} \end{cases}$$

$$\text{SC 2} \begin{cases} \mathrm{isi}_{23,c}(\tau) = \nu_3^{\tau_2}(\tau) - \nu_2^{\tau_2}(\tau), & \text{(3.9a)} \\ \mathrm{isi}_{21,c}(\tau) = \nu_1^{\tau_2}(\tau) - \nu_2^{\tau_2}(\tau), & \text{(3.9b)} \end{cases}$$

$$\text{SC 3} \begin{cases} \mathrm{isi}_{31,c}(\tau) = \nu_1^{\tau_3}(\tau) - \nu_3^{\tau_3}(\tau), & \text{(3.10a)} \\ \mathrm{isi}_{32,c}(\tau) = \nu_2^{\tau_3}(\tau) - \nu_3^{\tau_3}(\tau). & \text{(3.10b)} \end{cases}$$

Two complementary PRs per beatnote with relative π phase shift enable the Hexagon to generate these six signals. For example, Eqs. (3.8a) and (3.9b) have such π phase shift, but they are sampled according to different clocks. This means that one of the two complementary signals can be connected to a PM driven by clock 1, while the other is connected to the one driven by clock 2. And the same applies to the other two optical beatnotes.

It would also be an option to drop complementary signals, e.g., Eqs. (3.8a), (3.9a) and (3.10a). This is most straightforward for a three-signal measurement with three independent PMs, not expected to spoil the representativeness of the Hexagon much. The pairs of PRs on both ends of the intersatellite links become essential, especially in case intersatellite separations $\dot{\mathbf{D}}_{ij}$ are time-variant [2]. Due to the abovementioned conditions, this is not considered in the Hexagon. Nevertheless, such a bidirectional link between PMs would be helpful in functional tests of ranging (see Chapter 7). Different experimental topologies are summarized in Section 3.4.

2 In LISA, measuring beatnotes on both SC is important also because beam powers are significantly lost at a telescope.

3.3.2 *Sideband-sideband beatnotes*

Neglecting any secondary noises as Section 3.3.1 did, sideband-sideband beatnotes in the interspacecraft and reference interferometers are given by:

$$\mathrm{isi}_{ij,\mathrm{sb}}(\tau) = \mathrm{isi}_{ij,c}(\tau) + \dot{\mathbf{D}}_{ij} f_{ji} \left(1 + \dot{q}_j(\tau)\right) - f_{ij} \left(1 + \dot{q}_i(\tau)\right), \tag{3.11}$$

$$\mathrm{isi}_{ik,\mathrm{sb}}(\tau) = \mathrm{isi}_{ik,c}(\tau) + \dot{\mathbf{D}}_{ik} f_{ki} \left(1 + \dot{q}_k(\tau)\right) - f_{ik} \left(1 + \dot{q}_i(\tau)\right), \tag{3.12}$$

$$\mathrm{rfi}_{ij,\mathrm{sb}}(\tau) = \mathrm{rfi}_{ij,c}(\tau) + f_{ik} \left(1 + \dot{q}_i(\tau)\right) - f_{ij} \left(1 + \dot{q}_i(\tau)\right), \tag{3.13}$$

$$\mathrm{rfi}_{ik,\mathrm{sb}}(\tau) = -\mathrm{rfi}_{ij,\mathrm{sb}}(\tau), \tag{3.14}$$

where the subscript sb represents a sideband-sideband beatnote; $\dot{q}_i$ is a relative noise of the clock i according to a reference time frame in units of fractional frequency (see Eq. (2.7) for a timer model); f_{ij} is a constant GHz modulation frequency. In LISA, this frequency is limited to 2.400 GHz or 2.401 GHz.

On top of the two LISA-to-Hexagon conditions imposed in Section 3.3.1, another condition on this modulation frequency needs to be set,

- $f_{ij} = f_{ik}$: The Hexagon has only one modulation frequency per SC.

All three conditions considered, Eqs. (3.11) to (3.14) are reduced to

$$\mathrm{isi}_{ij,\mathrm{sb}}(\tau) = \mathrm{isi}_{ij,c}(\tau) + f_j \left(1 + \dot{q}_j(\tau)\right) - f_i \left(1 + \dot{q}_i(\tau)\right), \tag{3.15}$$

$$\mathrm{isi}_{ik,\mathrm{sb}}(\tau) = \mathrm{isi}_{ik,c}(\tau) + f_k \left(1 + \dot{q}_k(\tau)\right) - f_i \left(1 + \dot{q}_i(\tau)\right), \tag{3.16}$$

$$f_i = f_{ij} = f_{ik}. \tag{3.17}$$

Reference interferometers vanish, as explained before. Eq. (3.17) relabels the degenerate modulation frequencies f_{ij} and f_{ik} with the single index used for the SC.

This reduction leads to six interspacecraft interferometers listed in the following,

$$\text{SC 1} \begin{cases} \mathrm{isi}_{12,\mathrm{sb}}(\tau) = \mathrm{isi}_{12,c}(\tau) + f_2 \left(1 + \dot{q}_2(\tau)\right) - f_1 \left(1 + \dot{q}_1(\tau)\right), & \text{(3.18a)} \\ \mathrm{isi}_{13,\mathrm{sb}}(\tau) = \mathrm{isi}_{13,c}(\tau) + f_3 \left(1 + \dot{q}_3(\tau)\right) - f_1 \left(1 + \dot{q}_1(\tau)\right), & \text{(3.18b)} \end{cases}$$

$$\text{SC 2} \begin{cases} \mathrm{isi}_{23,\mathrm{sb}}(\tau) = \mathrm{isi}_{23,c}(\tau) + f_3 \left(1 + \dot{q}_3(\tau)\right) - f_2 \left(1 + \dot{q}_2(\tau)\right), & \text{(3.19a)} \\ \mathrm{isi}_{21,\mathrm{sb}}(\tau) = \mathrm{isi}_{21,c}(\tau) + f_1 \left(1 + \dot{q}_1(\tau)\right) - f_2 \left(1 + \dot{q}_2(\tau)\right), & \text{(3.19b)} \end{cases}$$

$$\text{SC 3} \begin{cases} \mathrm{isi}_{31,\mathrm{sb}}(\tau) = \mathrm{isi}_{31,c}(\tau) + f_1 \left(1 + \dot{q}_1(\tau)\right) - f_3 \left(1 + \dot{q}_3(\tau)\right), & \text{(3.20a)} \\ \mathrm{isi}_{32,\mathrm{sb}}(\tau) = \mathrm{isi}_{32,c}(\tau) + f_2 \left(1 + \dot{q}_2(\tau)\right) - f_3 \left(1 + \dot{q}_3(\tau)\right). & \text{(3.20b)} \end{cases}$$

These six sideband-sideband beatnotes can be generated by the Hexagon using the same logic as applied to Eqs. (3.8a) to (3.10b).

Note that this reduction results in two additional technical constraints:

- Selection of modulation frequencies: The Hexagon needs to apply three different frequencies, i.e., f_1, f_2, and f_3. Otherwise, some sideband-sideband beatnotes lack an RF frequency offset from their carrier-carrier counterparts, become indistinguishable from them, and contaminate their readout. For example, in Eq. (3.18a), $\mathrm{isi}_{12,\mathrm{sb}}(\tau)$ has the

same RF frequency as $\mathrm{isi}_{12,c}(\tau)$ with $f_1 = f_2 = 2.400\,\mathrm{GHz}$ and $f_3 = 2.401\,\mathrm{GHz}$. Hence, the Hexagon nominally adopts modulation frequencies of 2.400 GHz, 2.401 GHz and 2.399 GHz, which result in a 2 MHz, instead of 1 MHz, frequency offset in one of the three sideband-sideband beatnotes.

- 1 MHz electrical signal: LISA FDS, described in Section 2.6, is based on the assumption that all SC share the same GHz frequency, nominally 2.400 GHz, from which a PT frequency is derived with frequency dividers with 1 µcycle phase fidelity. To represent this scheme, three "SCs" in the Hexagon also need to have 2.400 GHz. This apparently contradicts the first point of this constraint list. Hence, to compensate for the difference in modulation noise between 2.400 GHz and 2.401 GHz or 2.399 GHz, such two secondary "SCs" generate a 1 MHz signal from the two GHz signals using an electric mixer, which is also measured by PM.

This description is based on the FDS design for this thesis, illustrated on the bottom of Figure 2.12, where the 80 MHz system clock is generated from the GHz-clock signal. However, once the latest version, on the top of Figure 2.12, is implemented in the experiment, the 1 MHz reference would not be necessary because all PMs can maintain 80 MHz for the system clock.

3.3.3 *Simplified LISA simulated by the Hexagon*

The simplified topology of LISA, which the Hexagon can simulate, will be illustrated to wrap up this section. The main conditions to map and reduce LISA to the Hexagon described in the previous sections are listed in the following,

LISA-to-Hexagon conditions:

- $\mathrm{tmi}_{ij}(\tau) = \mathrm{rfi}_{ij}(\tau)$: No test mass,
- $\dot{\mathbf{D}}_{ij} = \mathbb{1}$: The Hexagon does not simulate the intersatellite distances,
- $\mathrm{rfi}_{ij,c}(\tau) = \mathrm{rfi}_{ik,c}(\tau) = 0$: The Hexagon has only one laser per SC,
- $f_{ik} = f_{ik}$: The Hexagon has only one modulation frequency per SC.

Grasping these conditions is essential to deduce what the Hexagon can or cannot demonstrate.

From the mathematical point of view, simple inteferometric signals Eqs. (3.8a) to (3.10b) and Eqs. (3.18a) to (3.20b) were derived from these *LISA-to-Hexagon conditions*.

The visual counterpart is illustrated in Figure 3.2. For the sake of simplicity, the complementary signals are omitted as described at the end of Section 3.3.1. The optical path lengths are static and rather short, $L_{12} \approx L_{23} \approx L_{31} \ll 1\,\mathrm{m}$.

3.4 EXPERIMENTAL TOPOLOGIES

Different experimental topologies using the Hexagon interferometer are described in this section, which will be referred to throughout the rest of this thesis. The notation of the topologies is mainly based on the number of PMs and the number of signals: "XPMYS" represents a setup with X PMs and Y signals. "Signal" basically refers to an optical beatnote: "2S" means two beatnotes, generated from two beams, at the complementary outputs of a combining BS, and "3S" represents three optical beatnotes generated pairwise from three beams. Hence, the optical beatnotes, referred to as "2S", share

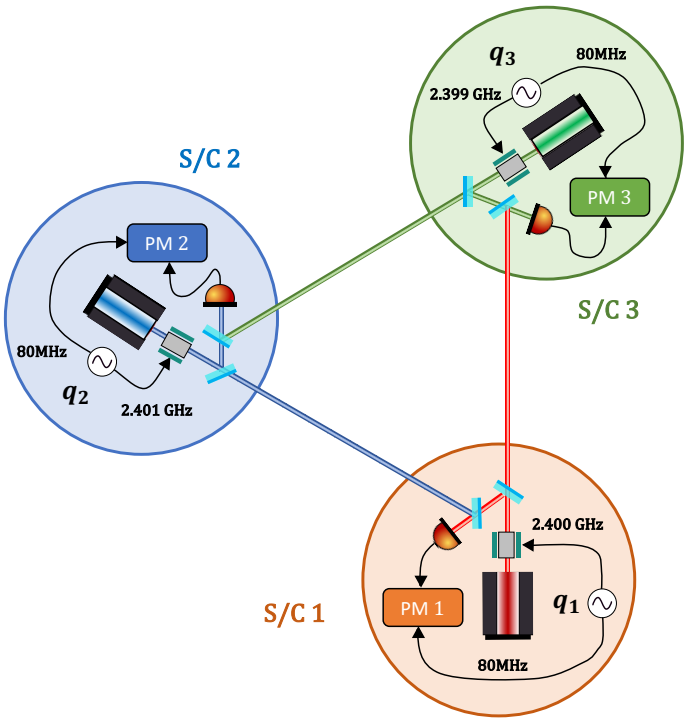

FIGURE 3.2: Simplified topology of LISA simulated by the Hexagon. PR signals on SC 1, 2, and 3 correspond to Eqs. (3.8b) and (3.18b), Eqs. (3.9b) and (3.19b), and Eqs. (3.10b) and (3.20b), respectively.

the same heterodyne frequency, while the three beatnotes in "3S" all have different heterodyne frequencies. As long as such rules are met, any setups with different cabling are understood as the same topology.

Figure 3.3 depicts such topologies. Three topologies with a single PM are shown on the top. The 1PM2S topology corresponds to the so-called π measurement because of the π phase shift between the two redundant outputs of a BS. This is often used as a useful and simple quantity for evaluating readout or ghost beam couplings for diagnostic [38, 42]. The 1PM3S topology is a minimum necessity to configure an optical three-signal. This is the simplest topology to optically evaluate the phase extraction, including its nonlinear effect, as discussed in Section 3.1. The 1PM3S-max topology connects all six PRs on the Hexagon interferometers to a single PM. Hence, it enables a three-signal test in the balanced-detection mode (see Appendix C), potentially giving more clues to limiting noise sources.

In the middle of Figure 3.3, the only meaningful topology with two PMs is illustrated. One of the BS outputs is connected to one PM, while the other complementary port is connected to the other PM. This would be the most straightforward setup with multiple PMs. Notably, most technology investigations in this thesis are doable already with this setup, like clock synchronization or absolute ranging. However, the most complete way to test the technologies is to configure three-signal tests.

Therefore, the most complex topologies in the Hexagon interferometer are shown on the bottom in Figure 3.3: the 3PM3S topologies. The 3PM3S topology on the left is the simplest, where three optical beatnotes are connected to three different PMs. Figure 3.2 corresponds to this category. In the 3PM3S-balanced and 3PM3S-bidirectional topologies, all six PRs are active but connected to PMs based on different criteria. The 3PM3S-balanced topology connects a specific pair of redundant optical beatnotes to a single PM. This enables us to first balance the beatnote signals in a single PMs before clock-synchronizing the balanced signals among three PMs. The 3PM3S-bidirectional topology

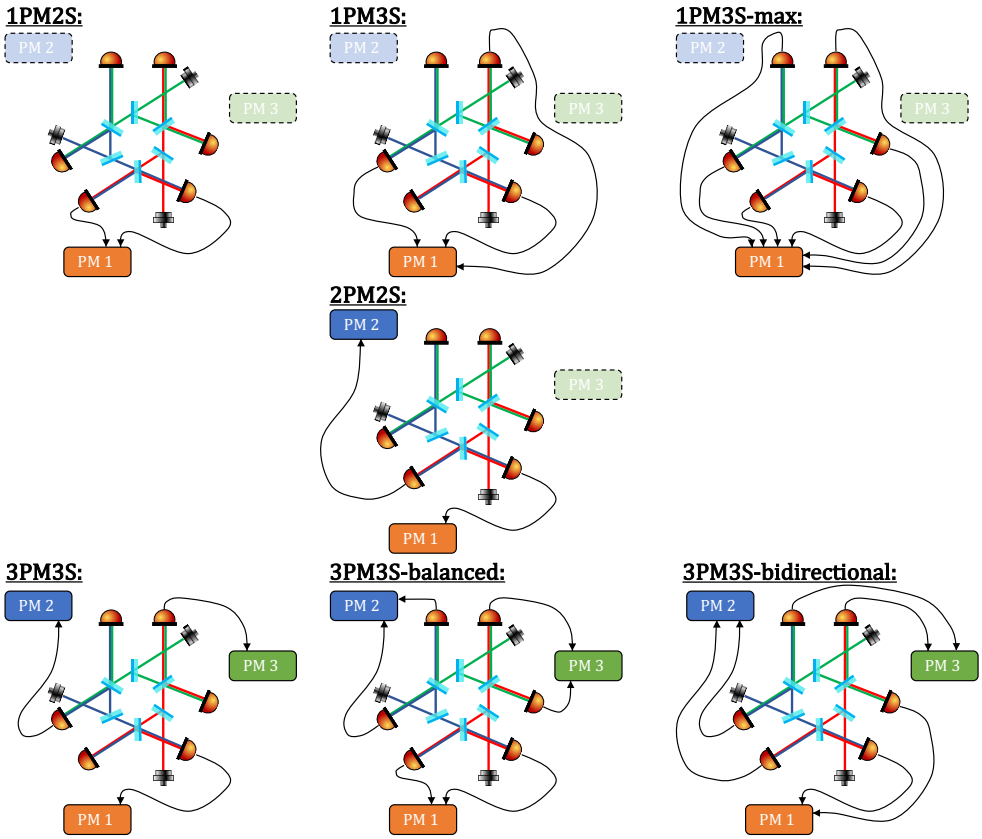

FIGURE 3.3: The Hexagon topologies. **Top:** three topologies with a single PM. **Middle:** one topology with two PMs. **Bottom:** three topologies with three PMs.

configures a bidirectional link between a specific pair of two PMs by connecting the redundant optical beatnotes to the different PMs. The Hexagon derived by the reduction of LISA in Section 3.3 corresponds to this topology. The optimal topology depends on the technology under test.

The Hexagon topologies used in each chapter in this thesis are summarized in Table 3.1.

Chapter	Topologies
Chapter 4	1PM3S, 2PM2S, 3PM3S
Chapter 6	2PM2S
Chapter 7	2PM2S (, 3PM3S-bidirectional)

TABLE 3.1: Hexagon topologies used in experiments in the thesis. Same demonstrations presented in Chapter 7 with the 3PM3S-bidirectional topology are ongoing.

3.5 SIGNIFICANCE FOR THE MISSION

The Hexagon is a unique on-ground test facility for various LISA technologies. Integrating clocks, electronics, optics, PRs, FDS, and PMs, the Hexagon can evaluate the devices from different perspectives and produce LISA-like signal sets, as discussed in Section 3.3. The Hexagon's role in the LISA mission is summarized to wrap up this chapter.

Phase extraction: Evaluation of the phase extraction via PRs and PMs is, as highlighted so far, a primary goal of the Hexagon. For proper investigations, three-signal tests must be performed; hence, the 1PM3S topology is the simplest solution to this, as deeply discussed in [38]. However, some

noise couplings in phase extraction (e.g., anti-aliasing filter effects) cannot be probed by a single PM; see Appendix E. Therefore, the complete test of phase extraction chains would require the 3PM3S topology.

Frequency distribution: As summarized in Section 2.6, a LISA SC generates different frequency signals, all synchronized to its USO, and the chain of the frequency down-conversion from a GHz-clock signal to a PT signal is performance-critical. A part characterization is typically performed by a simple split test, as described in Appendix D.3. However, such a test has a limitation, e.g., a PT distribution chain on a PM cannot be probed. In addition, the definition of the critical chain is based on the assumption that a local timing transformation via PT correction, formulated in Section 2.6.2, works as expected. Those points cannot be tested with a stand-alone operation of FDS. 2PM2S or 3PM3S is the most comprehensive way to test frequency distribution.

A backend electronics (BEE) of a LISA PM nominally has eight channels, plus one PT channel. With signal amplification, the single PT signal is distributed to the eight science channels.

Data processing: The Hexagon experimental data would be valuable inputs to LISA on-ground data analysis pipelines to evaluate it with actual (not synthetic) data. The diagram of the possible pipeline architectures is shown in Figure 3.4. As "L0.5 Data" in the diagram, the Hexagon can produce only telemetry data, especially PRN ranges and "interspacecraft" interferometric signals. Nevertheless, this would be enough to test some parts of "Ranging Sensor Fusion"; ambiguity resolution, bias estimation, and potentially ranging noise reduction (the first two will be the scope of Chapter 7). Clock synchronization can also be performed via carrier measurements, sideband measurements, TDIR, and/or PRNR (see Chapter 4 for the TDIR version and Chapter 7 for the introduction of PRNR). "TTL Subtraction" could not be simulated because beam angles cannot be actively controlled in the Hexagon. And actual TDI, described by a grey block including "Reduce Laser Frequency Noise", reduces to a simple three-signal combination (see Section 3.3). The descriptions above are in a big picture, so many subsets, which the Hexagon data can demonstrate, are omitted: interpolation for re-sampling, detrending, filtering, etc. In addition, a quick-look tool like glitch detection would also be a part to be evaluated with the Hexagon data, which is not shown in the diagram.

The AEI has developed a separate optical testbed called tilt-dynamics optical bench simulator (TDOBS) for this purpose.

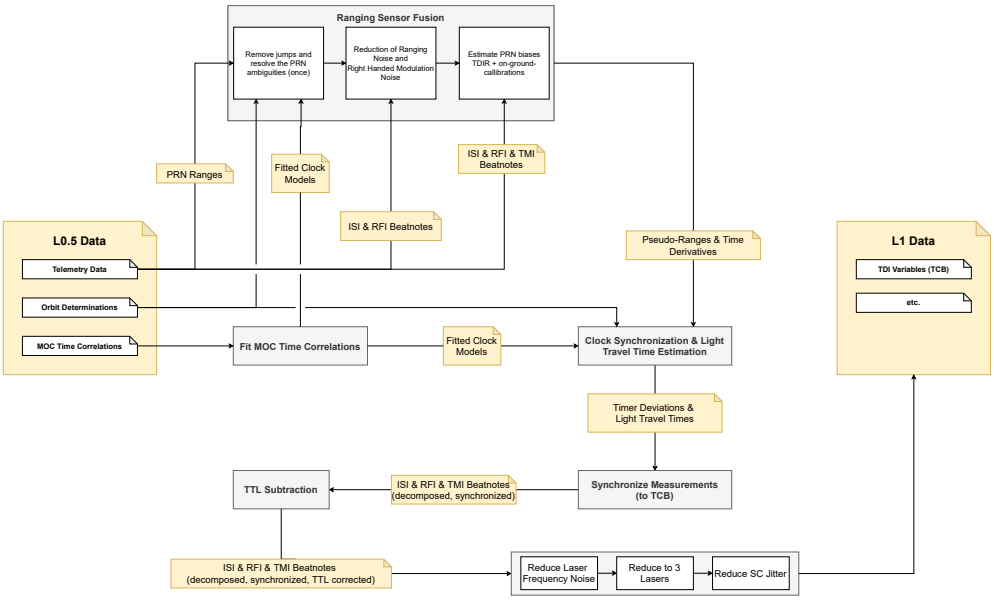

FIGURE 3.4: Diagram of one of the LISA on-ground processing pipelines, provided by Jan Niklas Reinhardt.

Part II

INTERSATELLITE CLOCK SYNCHRONIZATION

4

CLOCK SYNCHRONIZATION IN THE HEXAGON

Evolving from the 1PM3S topology by the previous research [38, 43], the first three-signal test with multiple PMs in the Hexagon to evaluate clock synchronization will be presented in this chapter. In this iteration, a PRN modulation for PRNR was not implemented yet in the Hexagon PMs; hence, clock synchronization was performed by the combination of TDIR-like processing and sideband measurements. One of the three PMs is a so-called elegant bread board (EBB) PM, developed by Oliver Gerberding [30], while the other two are based on FPGA mezzanine card (FMC), developed by Christoph Bode. The latter is referred to as "FMC PM" or "Hexagon PM" in this thesis. The main result in this chapter was published in [44].

4.1 SETUP

The experimental setup applying the clock synchronization in a hexagonal optical testbed was first proposed in [37] and is illustrated in Figure 4.1: the 3PM3S topology from Section 3.4. Conceptually, the three colored PM-clock assemblies together with the optical devices like lasers and EOM can be interpreted as the three LISA SC; also see Figure 3.2.

Three optical heterodyne beatnotes are generated pairwise from the three lasers. Two lasers act as secondaries locked to the remaining primary with LISA-like MHz offsets. This laser-lock system also features active noise injections, as described in Appendix F. The MHz offsets are time-invariant for any measurements in this section. The beatnotes are consecutively detected by complementary PRs pairs and fed to PMs. By design, the phases of the three beatnotes should cancel out in a three-signal combination [39, 43], also as mentioned in Section 3.1. Residual noise measures the PM and metrology chain performance.

The setup features five independent clocks with frequencies around 2.4 GHz. They are categorized into two groups: unprimed clocks for directly driving PMs and primed clocks for driving EOMs. The latter creates GHz sidebands via phase modulations.

Each of the unprimed clocks, running at 2.400 GHz, drives a PM module called frequency distribution module (FDM) [35]. Each FDM in turn consists of two frequency-divider chains: one to derive the 75 MHz PT, and the other to generate 80 MHz sampling clocks driving the ADC and digital clocks of the PMs. The PT calibrates the ADC sampling jitter and removes noise occurring in the 80 MHz clock generation. Hence, its application requires high phase fidelity in the PT chain.

The primed clocks are connected to an EOM each. Note that the virtual clock $1'$, identical to 1, is introduced to ease the modeling in Section 4.2. To achieve a 1 MHz offset between the carrier-carrier beatnote and sideband-sideband beatnotes, the clocks $1'$, $2'$ and $3'$ run at 2.400 GHz, 2.401 GHz and 2.399 GHz, respectively.

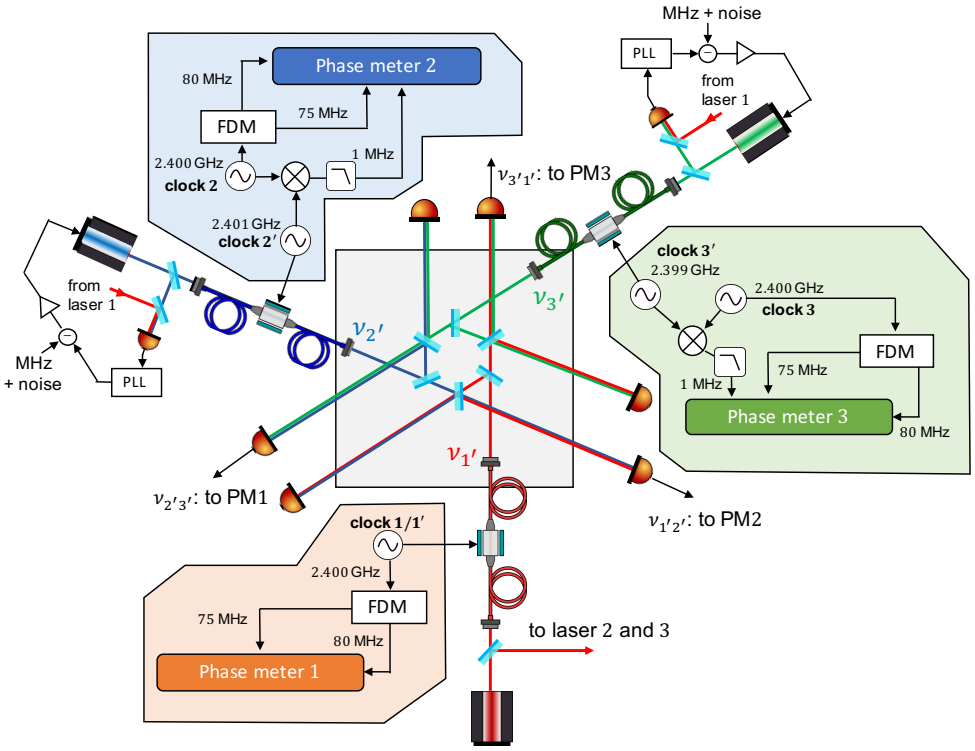

FIGURE 4.1: Schematic of the experimental setup to demonstrate clock synchronization. The three lasers are locked to each other with MHz offsets and noise injections, interfere pairwise, and generate three optical beatnotes. Their combination should cancel out by design and allow the metrology chain characterization, e.g., including the three PMs. Five clocks together with three optical and two electrical beatnotes are used to achieve synchronization between PMs.

To derive the differential clock signal between unprimed clocks driving the PMs, they must be related to the optical sideband-sideband beatnotes mentioned. This is done by tracking electrical beatnotes between pairs of the local primed and unprimed clocks, i.e., 2′-2 and 3′-3. The complete clock tone transfer is conceptually summarized in Figure 4.2. Throughout the rest of this article, clock 1 is chosen as a primary clock, while clocks 2 and 3 are secondary.

In LISA, the setup will be slightly different and more symmetric. Each SC will be equipped with two EOMs, one per arm, driven by 2.400 GHz and 2.401 GHz. This ensures the aforementioned 1 MHz offset. Furthermore, the different GHz signals will ultimately be derived from a single onboard 10 MHz USOs. However, the three USOs on the three SCs will not be actively synchronized to each other but individually free-running.

As mentioned, the PMs operate at a sampling frequency of 80 MHz generated by the FDMs. In LISA, the data streams must be low-pass-filtered to avoid aliasing and decimated via several stages to a lower data rate before being downlinked to earth. The current PM implementation in this experiment utilizes a FPGA-based CIC filter as a first stage to decimate the phase readout towards an intermediate data rate around 610 Hz. At these rates, more sophisticated FIR filters are applied in software to decimate further to 3.4 Hz as the final readout rate. Note that the LISA baseline for the final data rate was increased to 4 Hz. As described in Appendix E, the data analysis is sensitive to insufficient low-pass filtering. The same effects will impact the data processing for LISA, which, in turn, will require careful design of the onboard processing.

While the hexagonal optical bench and PRs are hosted in a vacuum chamber with a moderate vacuum level around 1 mbar, the three PMs are mounted in housings with active temperature stabilization. The other components in Figure 4.1 are placed in the air.

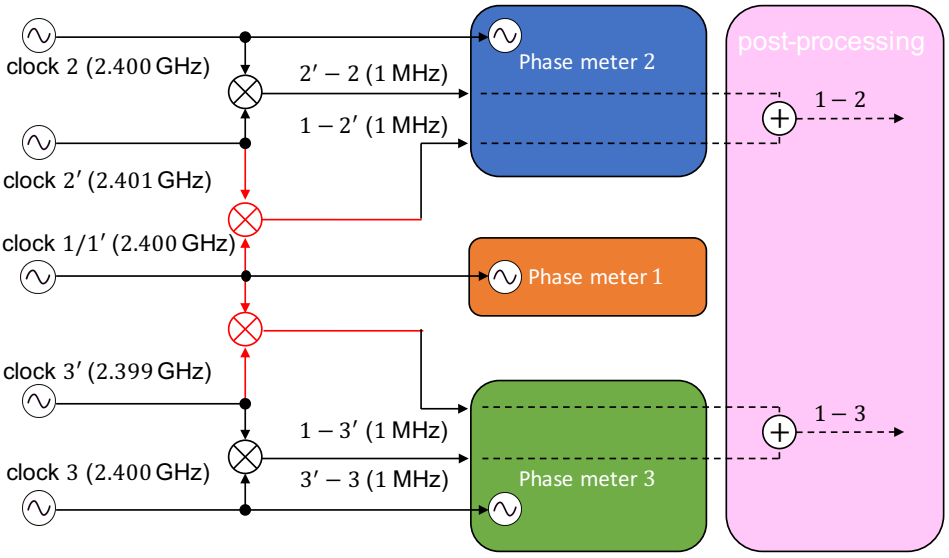

FIGURE 4.2: Conceptual diagram of the clock tone transfer. The solid-black lines, the solid-red lines, and the dashed-black lines denote electrical signals, optical signals, and digital data, respectively.

4.2 MODEL

The mathematical model of the clock synchronization in this experiment can be derived by reducing the model for LISA presented in [23]. The LISA PM will be capable of providing data in either phase or frequency. While the final data format is not yet decided, this work assumes that the data is downlinked in frequency units, which avoids the need to handle frequent phase wrapping due to the MHz beatnotes. Consequently, our experimental data is also modeled and processed using frequency units similar to [45], which is only integrated to compute the phase spectral density at the end. Frequency measurements in this section are assumed to be already corrected by a PT signal to suppress ADC jitter, as described in [31, 39] and Section 2.6.2. As mentioned in Section 2.4, the formulation in this section is based on the PM outputs at a few Hz, assuming the unity transfer function of any down-sampling process in the observation band. Note that imperfections in the down-sampling process can impact the final results of our analysis, which will be studied in detail in Appendix E. However, in this section, the in-band properties of the interferometric signals are described, and thus any impact of the filters and decimation stages is neglected.

While the notation conventions used in [23] are loosely followed, a notable difference is that this lab experiment does not need to refer to external time frames like the SC proper times. Instead, the clock $1/1'$ is chosen as a reference or primary clock, and all variables are written in that clock time frame, which will always be labeled with the index m ($= m'$).

4.2.1 *Measurements*

The measurements available from the experiment are first described, focusing on how the different clocks impact them. This chapter considers only the usb beatnote signal.

The signals in this experiment can be categorized into three types: optical carrier-carrier beatnotes, optical sideband-sideband beatnotes, and the differential clock signal between the primed and unprimed clocks generated

by an electrical frequency mixer. These three signals can be expressed in the primary clock time frame,

$$\nu^{\tau_m}_{c,i'j'}(\tau) = \nu^{\tau_m}_{j'}(\tau) - \nu^{\tau_m}_{i'}(\tau), \tag{4.1}$$

$$\nu^{\tau_m}_{\mathrm{sb},i'j'}(\tau) = \nu^{\tau_m}_{c,i'j'}(\tau) + f_{j'}(1+\dot{q}_{j'}(\tau)) - f_{i'}(1+\dot{q}_{i'}(\tau)), \tag{4.2}$$

$$\nu^{\tau_m}_{\mathrm{mix},i}(\tau) = f_{i'}(1+\dot{q}_{i'}(\tau)) - f_i(1+\dot{q}_i(\tau)), \tag{4.3}$$

where f_i is the nominal frequency of the clock i in the GHz regime [1]. Note that all unprimed clocks have the same nominal frequency $f_i = 2.400\,\mathrm{GHz}$. Our goal is to construct a noise-free signal combination, which in the primary clock frame would be trivially given as

This corresponds to the 1PM3S topology from Section 3.4.

$$\Delta^{\tau_m}_{1\mathrm{PM}}(\tau) = \nu^{\tau_m}_{c,2'3'}(\tau) + \nu^{\tau_m}_{c,1'2'}(\tau) + \nu^{\tau_m}_{c,3'1'}(\tau) \equiv 0. \tag{4.4}$$

However, since the signals presented in Eq. (4.1) are recorded according to the independent clocks i and thus have their expressions modified according to Eq. (2.11), all measurements need to be synchronized before $\Delta^{\tau_m}_{1\mathrm{PM}}(\tau)$ can be computed.

4.2.2 *Clock synchronization*

Any signals sampled by the secondary clocks need to be interpolated to adjust their time stamps and rescaled to compensate for the multiplicative factor in Eq. (2.11). For the former, it is first shown that a time shift by $\delta\tau_i(\tau)$ perfectly compensates the time-stamping errors in Eq. (2.10),

$$\begin{aligned}\phi^{\tau_i}(\tau + \delta\tau_i(\tau)) &= \phi^{\tau_m}(\tau^{\tau_i}_m(\tau + \delta\tau_i(\tau))) \\ &= \phi^{\tau_m}(\tau),\end{aligned} \tag{4.5}$$

since

$$\begin{aligned}\tau^{\tau_i}_m(\tau + \delta\tau_i(\tau)) &= \tau + \delta\tau_i(\tau) - \delta\tau_i(\tau^{\tau_i}_m(\overbrace{\tau + \delta\tau_i(\tau)}^{\tau^{\tau_m}_i(\tau)})) \\ &= \tau.\end{aligned} \tag{4.6}$$

Here, the following relation was used: $\tau^{\tau_i}_m(\tau^{\tau_m}_i(\tau)) = \tau$.

The first step to getting $\delta\tau_i(\tau)$ from our measurements is to combine Eqs. (4.1) to (4.3) to get a differential measurement between the primary clock m and the secondary clock i,

The latest design with the PA feed-forwarding scheme (see Section 2.2.2) simplifies differential clock measurements: $\dot{r}^{\tau_m}_{im'} = \nu^{\tau_m}_{\mathrm{sb},i'm}/f_i$.

$$\begin{aligned}\dot{r}^{\tau_m}_{im'}(\tau) = \dot{r}^{\tau_m}_{im}(\tau) &= \frac{1}{f_i}\left[\left(\nu^{\tau_m}_{\mathrm{sb},i'm}(\tau) - \nu^{\tau_m}_{c,i'm}(\tau)\right) + \nu^{\tau_m}_{\mathrm{mix},i}(\tau)\right] \\ &= \dot{q}_m(\tau) - \dot{q}_i(\tau) \\ &= -\dot{q}_i(\tau).\end{aligned} \tag{4.7}$$

1 In this iteration, the PA feed-forward, described in Section 2.2.2, was not implemented; hence, the sideband signal also includes the redundant information, like the carrier beatnote dynamics and the 1 MHz offset.

The actual measurements in this combination are recorded according to the clock i, as shown in Figure 4.2. They can be expressed by applying Eq. (2.11) to $\dot{r}_{im}^{\tau_m}(\tau)$,

$$\begin{aligned}\dot{r}_{im}^{\tau_i}(\tau) &= \frac{\dot{r}_{im}^{\tau_m}(\tau_m^{\tau_i}(\tau))}{1+\dot{q}_i(\tau_m^{\tau_i}(\tau))} \\ &= \frac{-\dot{q}_i(\tau_m^{\tau_i}(\tau))}{1+\dot{q}_i(\tau_m^{\tau_i}(\tau))}.\end{aligned} \tag{4.8}$$

$\dot{r}_{im}^{\tau_i}(\tau_i)$ can be integrated over the measurement time, which gives, using Eqs. (2.10) and (2.11),

$$\begin{aligned}r_{im}^{\tau_i}(\tau) &= \int_0^{\tau} \dot{r}_{im}^{\tau_i}(\tau')d\tau' \\ &= -q_i(\tau_m^{\tau_i}(\tau)).\end{aligned} \tag{4.9}$$

Here, our measured $r_{im}^{\tau_i}(\tau)$ is missing the initial $\delta\tau_{i,0}$. Hence, a free parameter $\delta\hat{\tau}_{i,0}$ is added to Eq. (4.9),

$$\begin{aligned}r_{im,0}^{\tau_i}(\tau) &= r_{im}^{\tau_i}(\tau) - \delta\hat{\tau}_{i,0} \\ &= -q_i(\tau_m^{\tau_i}(\tau)) - \delta\hat{\tau}_{i,0} \\ &\approx -\delta\tau_i(\tau_m^{\tau_i}(\tau)),\end{aligned} \tag{4.10}$$

where the last approximation is only realized after fitting the correct value for $\delta\hat{\tau}_{i,0}$, i.e., the residual timing error $\delta\hat{\tau}_{i,0\mathrm{e}}$ is small enough,

$$|\delta\hat{\tau}_{i,0\mathrm{e}}| = |\delta\hat{\tau}_{i,0} - \delta\tau_{i,0}|\,. \tag{4.11}$$

This gives us $\delta\tau_i$, but still evaluated at $\tau_m^{\tau_i}(\tau)$. The timestamp can be adjusted by numerically solving the following nested equation,

$$\begin{aligned}\delta\tau_i(\tau) &= \delta\tau_i(\tau_m^{\tau_i}(\tau+\delta\tau_i(\tau))) \\ &= -r_{im,0}^{\tau_i}(\tau+\delta\tau_i(\tau)).\end{aligned} \tag{4.12}$$

Note that the final results in this experiment do not significantly change when using $r_{im,0}^{\tau_i}(\tau)$ instead of $\delta\tau_i(\tau)$ for the interpolation. The reason is that the sub-ppm frequency offsets between the clocks result in a negligible timing error over the typical measurement times in the lab. Nevertheless, the more exact expression given in Eq. (4.12) will be used to time-shift the measurements to the primary clock frame. In addition, it is necessary to undo the frequency scaling in Eq. (2.11) by applying a multiplicative factor. In total, the following is computed,

$$\begin{aligned}\tilde{\nu}_{c,i'j'}^{\tau_i}(\tau) &= \frac{\nu_{c,i'j'}^{\tau_i}(\tau+\delta\tau_i(\tau))}{1+\dot{r}_{im}^{\tau_i}(\tau+\delta\tau_i(\tau))} \\ &\approx \nu_{c,i'j'}^{\tau_m}(\tau).\end{aligned} \tag{4.13}$$

The final signal combination in frequency can now be formed,

$$\begin{aligned}\Delta_{3\mathrm{PM}}(\tau;\delta\hat{\tau}_{i,0}) &= \nu_{c,2'3'}^{\tau_1}(\tau) + \tilde{\nu}_{c,1'2'}^{\tau_2}(\tau) + \tilde{\nu}_{c,3'1'}^{\tau_3}(\tau) \\ &\approx \Delta_{1\mathrm{PM}}^{\tau_m}(\tau),\end{aligned} \tag{4.14}$$

which reduces to the noise-free Eq. (4.4) after $\delta\hat{\tau}_{i,0}$ is fitted to the correct value of $\delta\tau_{i,0}$. Therefore, the 3PM3S performance $\Delta_{\mathrm{3PM}}(\tau;\delta\hat{\tau}_{i,0})$ will be compared with the 1PM3S performance $\Delta^{\tau_m}_{\mathrm{1PM}}(\tau)$ to evaluate clock synchronization.

Eq. (4.10) introduced the estimate of a missing initial timer offset $\delta\hat{\tau}_{i,0}$ as a fitting parameter. This experiment optimizes the estimate using the TDIR-like algorithm [46]. This algorithm fits $\delta\hat{\tau}_{i,0}$ by minimizing the residual noise power in the final signal combination $\Delta_{\mathrm{3PM}}(\tau;\delta\hat{\tau}_{i,0})$. If the residual timing error $\delta\hat{\tau}_{i,0\mathrm{e}}$ is considered without the approximation in the last line of Eq. (4.10), Eq. (4.13) can be re-formulated in phase via Eq. (4.5),

$$\begin{aligned}\tilde{\phi}^{\tau_i}_{c,i'j'}(\tau) &= \phi^{\tau_i}_{c,i'j'}(\tau+\delta\tau_i(\tau)+\delta\hat{\tau}_{i,0\mathrm{e}})\\ &= \phi^{\tau_m}_{c,i'j'}\left(\tau^{\tau_i}_m(\tau+\delta\tau_i(\tau)+\delta\hat{\tau}_{i,0\mathrm{e}})\right)\\ &\approx \phi^{\tau_m}_{c,i'j'}(\tau+\delta\hat{\tau}_{i,0\mathrm{e}}).\end{aligned} \tag{4.15}$$

The approximation in the last line is for $\delta\tau_i(\tau)\approx\delta\tau_i(\tau+\delta\hat{\tau}_{i,0\mathrm{e}})$. This gives the final signal combination in phase, including the residual timing error due to the TDIR algorithm,

$$\begin{aligned}\int d\tau\cdot\Delta_{\mathrm{3PM}}(\tau;\delta\hat{\tau}_{i,0}) &= \phi^{\tau_1}_{c,2'3'}(\tau)+\tilde{\phi}^{\tau_2}_{c,1'2'}(\tau)+\tilde{\phi}^{\tau_3}_{c,3'1'}(\tau)\\ &\approx \left(\phi^{\tau_1}_{c,1'2'}(\tau+\delta\hat{\tau}_{2,0\mathrm{e}})-\phi^{\tau_1}_{c,1'2'}(\tau)\right)\\ &\quad+\left(\phi^{\tau_1}_{c,3'1'}(\tau+\delta\hat{\tau}_{3,0\mathrm{e}})-\phi^{\tau_1}_{c,3'1'}(\tau)\right),\end{aligned} \tag{4.16}$$

where $\phi^{\tau_1}_{c,2'3'}$ was broken into the virtual phase signals $\phi^{\tau_1}_{c,1'2'}$ and $\phi^{\tau_1}_{c,3'1'}$ from the first to the second line,

$$\begin{aligned}\phi^{\tau_1}_{c,2'3'}(\tau) &= \phi^{\tau_1}_{c,3'}(\tau)-\phi^{\tau_1}_{c,2'}(\tau)\\ &= -\left(\phi^{\tau_1}_{c,1'}(\tau)-\phi^{\tau_1}_{c,3'}(\tau)\right)-\left(\phi^{\tau_1}_{c,2'}(\tau)-\phi^{\tau_1}_{c,1'}(\tau)\right)\\ &= -\phi^{\tau_1}_{c,3'1'}(\tau)-\phi^{\tau_1}_{c,1'2'}(\tau).\end{aligned} \tag{4.17}$$

The residual phase noise level per secondary clock in the frequency domain is, hence, written by,

$$\begin{aligned}\delta\tilde{\phi}^{\tau_i}_{c,i'j'}(f) &= \tilde{\phi}^{\tau_i}_{c,i'j'}(f)\cdot\Delta L\left(f;\delta\hat{\tau}_{i,0\mathrm{e}}\right)\\ &\approx \tilde{\phi}^{\tau_i}_{c,i'j'}(f)\cdot 2\pi f\delta\hat{\tau}_{i,0\mathrm{e}},\end{aligned} \tag{4.18}$$

$$\Delta L\left(f;\delta\hat{\tau}_{i,0\mathrm{e}}\right) = \left|1-\mathrm{e}^{-j2\pi f\delta\hat{\tau}_{i,0\mathrm{e}}}\right|. \tag{4.19}$$

In Eq. (4.19), the delay factor from Eq. (1.20) is introduced with some adaptions of notation for later. The input beatnote phase noise $\tilde{\phi}^{\tau_i}_{c,i'j'}(f)$ is under control via noise injection implemented on the laser-lock system, as shown in Figure 4.1. The requirement-driven beatnote noise level in LISA is, neglecting the spectrum shape, $60\,\mathrm{Hz}/\sqrt{\mathrm{Hz}}$ from Figure 1.6. All considered, to reach the $1\,\mathrm{pm}/\sqrt{\mathrm{Hz}}$ allocation to clock synchronization per secondary clock, the TDIR accuracy needs to achieve $\delta\hat{\tau}_{i,0\mathrm{e}}\approx$16.7 ns since

$$\begin{aligned}2\pi\,\mu\mathrm{rad}/\sqrt{\mathrm{Hz}} &= \delta\tilde{\phi}^{\tau_i}_{c,i'j'}(f)\\ &\approx \frac{60\,\mathrm{Hz}/\sqrt{\mathrm{Hz}}}{f}\cdot 2\pi f\delta\hat{\tau}_{i,0\mathrm{e}}.\end{aligned} \tag{4.20}$$

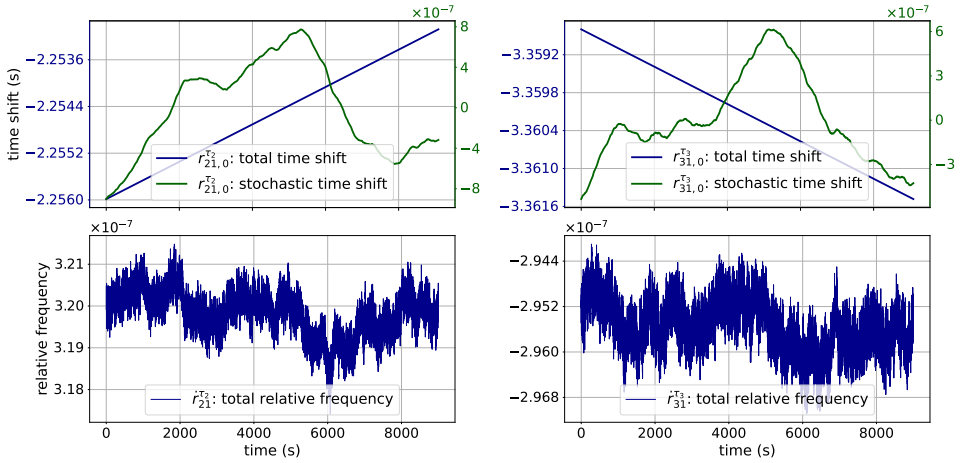

FIGURE 4.3: Two differential clock signals in time. **Left:** clocks 1-2. **Right:** clocks 1-3. **Bottom:** the total relative frequency offsets. The mean values were estimated at 0.320 ppm and 0.296 ppm. **Top:** the clock time shifts. The total time shifts are in blue, and the stochastic components are in green.

4.3 RESULT

Using the setup in Section 4.1, the clock synchronization based on the model provided in Section 4.2 was experimentally demonstrated.

As shown in Figure 4.1, the two secondary lasers were locked to the primary laser with fixed MHz offsets. On top, LISA-like frequency noises were added at the lock error point; see Appendix F. The MHz beatnote frequencies of $\nu_{c,1'2'}$, $\nu_{c,2'3'}$ and $\nu_{c,3'1'}$ were chosen as follows: 23.3, 6.6 and 16.7 MHz. The white frequency noise of the beatnotes was set to $60\,\mathrm{Hz}/\sqrt{\mathrm{Hz}}$, mimicking current noise allocations for LISA. All complimentary PR signals were fed to PM 1 to configure the 1PM3S topology. The associated three-signal combination is, hence, measured with a single clock and serves as a measurement of the testbed sensitivity for the clock synchronization, i.e., $\Delta^{\tau_m}_{1\mathrm{PM}}(\tau)$ in Eq. (4.4).

The filter order of the Lagrange interpolation, to realize the time shifting described in Eq. (4.13), was 121. At both ends, 150 samples of interpolated data were truncated. Regarding the TDIR-like optimization of the initial offsets $\delta\hat{\tau}_{i,0}$, the noise contribution in the final signal combination $\Delta_{3\mathrm{PM}}(\tau;\delta\hat{\tau}_{i,0})$ above 0.8 Hz was filtered out before the computation of its noise power. This was done to avoid the disturbance by the dominant interpolation error close to the Nyquist frequency.

Figure 4.3 shows the two differential clock measurements from Figure 4.2 in both relative frequency offsets and time shifts based on the signals described by Eqs. (4.7) to (4.10). The mean values of the relative frequency offsets were 0.320 ppm and 0.296 ppm between clocks 1-2 and 1-3, respectively. Additionally, the initial offsets $\delta\tau_{i,0}$ were derived based on TDIR-like processing: $\delta\hat{\tau}_{2,0} \approx 2.26\,\mathrm{s}$ and $\delta\hat{\tau}_{3,0} \approx 3.36\,\mathrm{s}$.

The three-signal test with three independent PMs was conducted under these conditions. The results will be split into two parts presented in the following sections.

A LISA software tool called PyTDI [47] was used for interpolation.

4.3.1 *Performance*

The first result is purely about the clock synchronization performance, summarized in Figure 4.4. Pink is one of the beatnote phase noises, which shows $1/f$ behavior due to the injected white frequency noise. Yellow indicates the

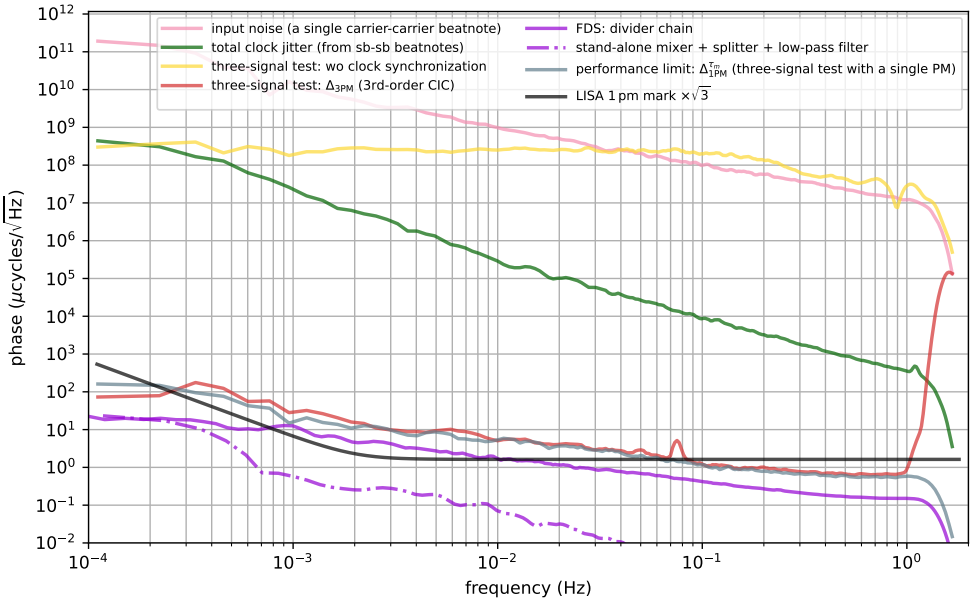

FIGURE 4.4: Performance of a three-signal test using clock synchronization. Pink shows one of the input beatnote noises. The three-signal measurement with three independent PMs (yellow) can be suppressed by applying clock synchronization (red) down to the testbed sensitivity (grey). Noise projections of the FDM and additionally used components are shown in violet and violet-dot-dashed, respectively.

raw three-signal test with non-synchronized PMs. It is dominated by effects due to the clock's initial offsets. After the secondary clocks were synchronized to the primary clock, see Eq. (4.14), the three-signal performance (red) was suppressed from the separately measured differential clock jitters (green) by three orders of magnitude at 1 Hz up to 6 orders of magnitude at 0.1 mHz. At this state, the measurement is limited by the testbed noise monitored with a single PM (grey). It deteriorated slightly, compared with earlier measurements [43], due to changes in the setup and is the focus of further ongoing noise hunting to bridge the remaining gap to the standard LISA $1\,\text{pm}/\sqrt{\text{Hz}}$ mark for three channels of a PM (black) in the observation band.

This does not necessarily mean the requirement on the red curve, where other devices like FDS are also integrated.

Anticipating future limitations and analyzing the remaining noise margin against the current testbed sensitivity, noise projections of electrical devices in the sensitive clock path were performed. More precisely, the FDM noise was measured separately and scaled to the heterodyne frequencies of this particular measurement (violet). This device's PT chain consists of five by-2 dividers, an amplifier, a filter, and a power splitter. Their in-air thermal stability notably affects the FDM performance. Besides, the total noise projection of other electrical components, namely stand-alone mixers, etc., shown in Figure 4.1, were again separately measured (violet-dot-dashed).

The pink and red curves, together with Eq. (4.18), allow us to characterize the achieved noise suppression in terms of an equivalent residual clock desynchronization, which in TDIR is ultimately limited by the noise floor of the testbed. Assuming the same TDIR accuracy and the uncorrelated beatnote noises with the same level for two secondary terms in Eq. (4.14), the total residual phase noise can be derived just by multiplying Eq. (4.18) by $\sqrt{2}$. By comparing the total residual with the performance curve (red), this residual is estimated at a level of approximately 6.15 ns, which corresponds to 1.84 m in the units of light travel time or range; see Figure 4.5. This accuracy is expected to improve further alongside the overall testbed sensitivity or by lifting an input beatnote noise (see Section 4.4). For comparison, the expected PRN ranging precision is around 40 cm rms at the data rate of 3 Hz [33], with the caveat that the PRN measurements might have an undetermined bias of

This is guaranteed because the beatnote noise injection presented in Appendix F uses different random seeds for different laser locks.

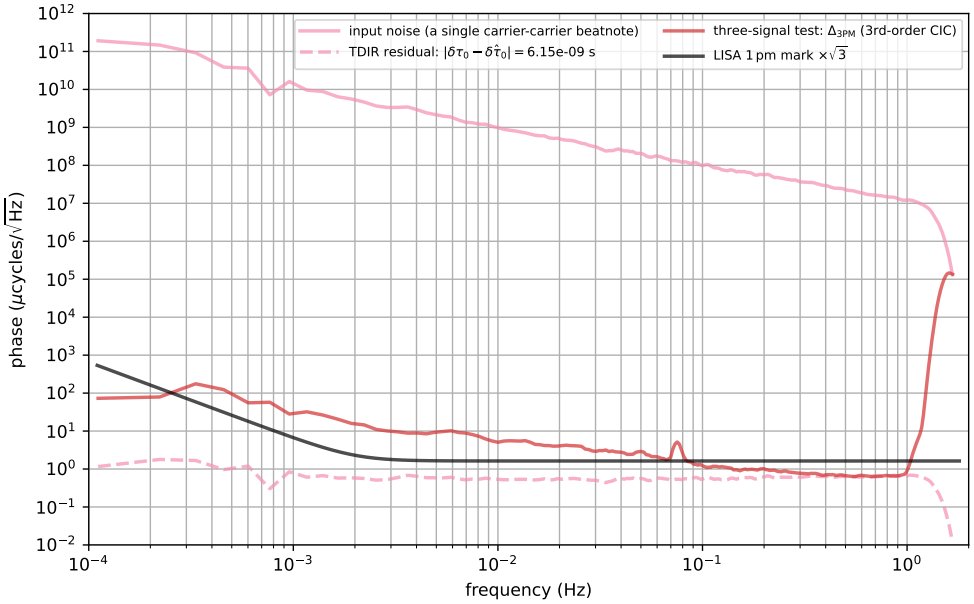

FIGURE 4.5: TDIR precision in a three-signal test. Dashed-pink is the total phase noise due to the residual clock desynchronization after TDIR. All other curves are identical to Figure 4.4.

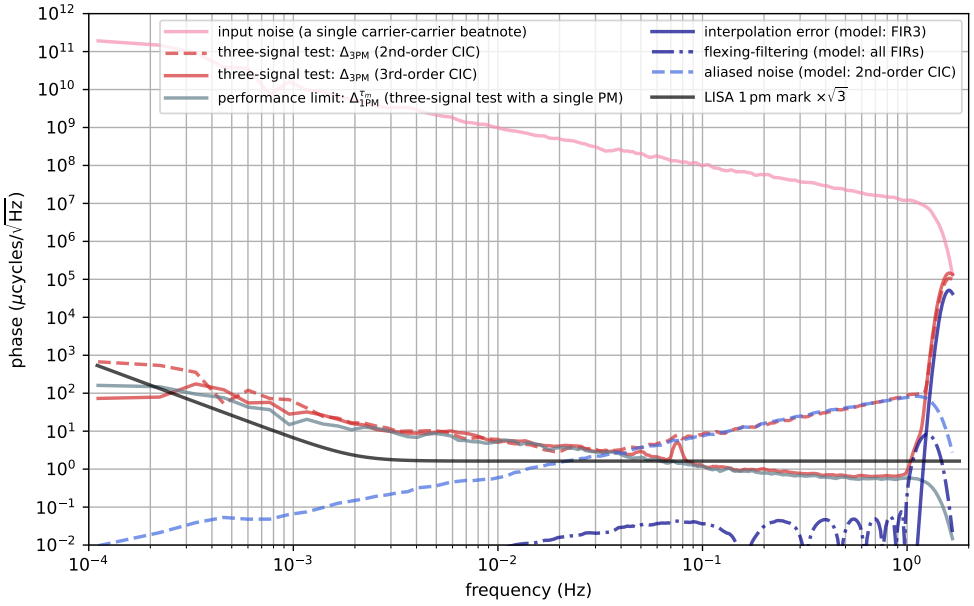

FIGURE 4.6: Noise couplings to a three-signal test with clock synchronization. Pink, solid-red, grey, and black are identical to the ones in Figure 4.4. Limitations due to an insufficient 2nd order CIC filter match the model of the aliased noise (red-dashed, blue-dashed, respectively). Further limitations are due to interpolation errors (navy) and the flexing-filtering coupling (navy-dot-dashed).

several meters due to cables and processing delays, which could be calibrated with TDIR.

4.3.2 *Noise couplings: quick look*

Figure 4.6 shows the second part of the result, namely the verification of noise couplings stemming from LISA data processing: aliased noise, flexing-filtering coupling, and interpolation error. Before this research, these noise sources have been studied analytically and numerically, but not experimentally. This is the first verification with experimental data. Their analytical models are summarized in Appendix E.

Two noise couplings were verified for the regime above 1 Hz. The mentioned final FIR decimation stage is significant for both models. Firstly, the bump close to the Nyquist frequency can be explained well by the analytical model of Lagrange interpolation errors (navy) described in Appendix E.2. The

interpolation error sharply drops down to numerical noise levels towards lower frequencies. Secondly, the flexing-filtering coupling (navy-dot-dashed) described in Appendix E.3 limited the performance around 1 Hz. To gain more margin around 1 Hz, the FIR filters could be tuned more carefully, or an inverse filter could be applied in post-processing, as will be investigated in Section 4.3.3.

As mentioned in Appendix E.1, the filter design of the CIC decimation stage has a significant impact due to aliasing effects. This effect was estimated based on the averaged model in Eq. (E.6). Using a 2nd-order CIC, the injected frequency noise $60\,\mathrm{Hz}/\sqrt{\mathrm{Hz}}$ around the slow sampling rate of the CIC was aliased to the observation band. It dominates the associated three-signal measurements (red-dashed) at the upper Hz regime according to its model (blue-dashed). In contrast, a 3rd-order CIC showed sufficient suppression and was used instead.

Figure 4.3 shows the measured time shifts (top blue) varied by around 2 ms over a measurement time of 9000 s. This is longer than the period of the sinusoidal coupling of the aliasing in Eq. (E.5): $1/f_s$ with f_s of around 610 Hz for the CIC decimation stage.

4.3.3 *Noise couplings: further investigations*

Some noise investigations will be further deepened in this section, analyzing the same experimental data from different aspects: the aliasing effect in the time domain, the suppression of the flexing-filtering coupling with an inverse filter, and the transformation of a local timing reference from the 80 MHz system clock to the PT signal.

Aliasing effect: The aliased noise has a sinusoidal coupling factor $2\,|\sin(\pi n[k] f_s \delta\tau_i)|$, originating from a commutator between time-shifting and sampling processes; see Eq. (E.5). The timer deviation ramps over the measurement time, and the phase noise residual converges on the averaged noise floor, as discussed in Section 4.3.2. The time-domain analysis will be provided below to verify this coupling dynamics properly. For this purpose, the measurement with the 2nd-order CIC filter will be used below to make it dominant.

Using the beatnotes between the laser $1'$ and $2'$ at the PM 1 and PM 2 [2], the 2PM2S topology was analyzed for the sake of simplicity, focusing on only one of the secondary PMs,

$$\Delta_{\mathrm{2PM}}(\tau; \delta\hat{\tau}_{2,0}) = \nu_{c,1'2'}^{\tau_1}(\tau) - \tilde{\nu}_{c,1'2'}^{\tau_2}(\tau). \tag{4.21}$$

This allows us to focus on the timer deviation $\delta\tau_2$ instead of the combined effect of the two timer deviations in the case of the three-signal test.

Figure 4.7 shows the phase noise residual Δ_{2PM} with clock synchronization in the top panel, while the bottom plots the measured $\delta\tau_2$ and the corresponding coupling factor $2\,|\sin(\pi n[k] f_s \delta\tau_2)|$ with $k = 1$ and $f_s \approx 610\,\mathrm{Hz}$. The residual phase noise is modulated by the scanning timer deviation as predicted by the model. This non-linear coupling mechanism is unavoidable in TDI and clock synchronization in LISA. The 2nd-order CIC filter with the $60\,\mathrm{Hz}/\sqrt{\mathrm{Hz}}$ beatnote noise allocation resulted in the noise level two-order above the $1\,\mathrm{pm}/\sqrt{\mathrm{Hz}}$ mark around 1 Hz, as shown in Figure 4.6. Hence, it is not realistic to suppress the aliased noise via laser noise allocation. This brings us to the conclusion that the 3rd-order CIC filter is necessary for LISA.

2 The one at the PM 1 $\nu_{c,1'2'}^{\tau_1}$ was used for the 1PM3S topology, while the one at the PM 2 $\nu_{c,1'2'}^{\tau_2}$ was used for the 3PM3S topology in the previous sections.

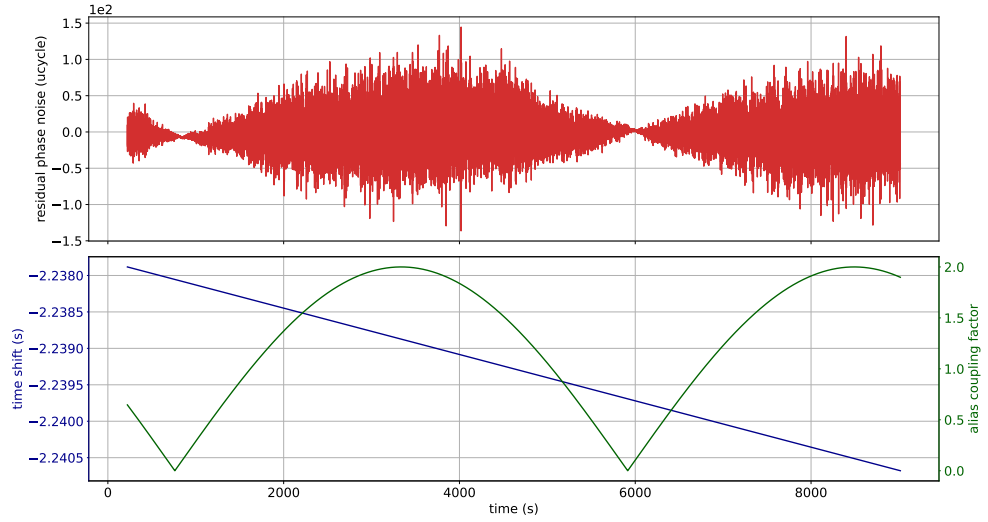

FIGURE 4.7: Aliased noise in the time domain. **Top:** the residual phase noise between two PMs with clock synchronization (interpolation error filtered out). **Bottom:** the timer deviation between the PMs measured via sideband beatnotes (blue) and the corresponding alias coupling factor (green).

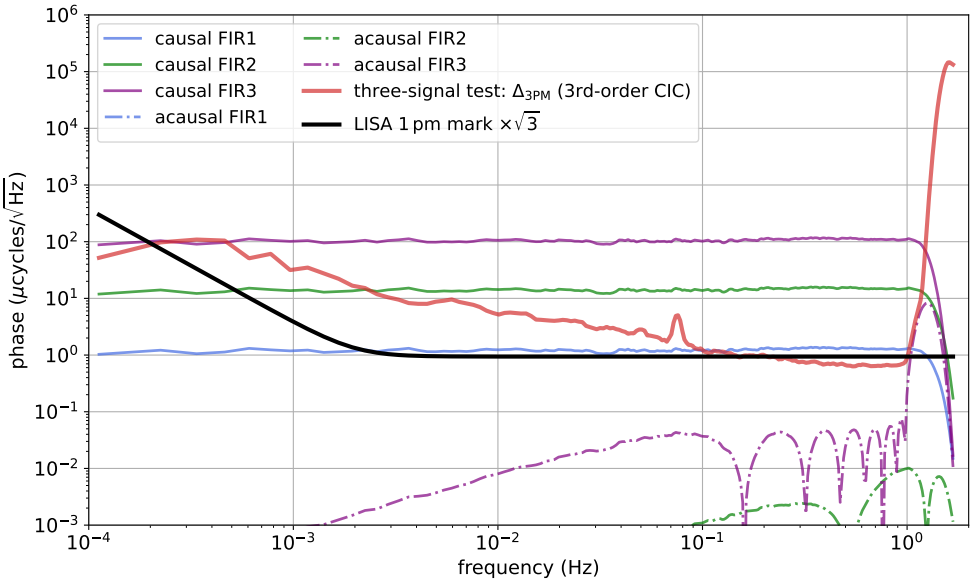

FIGURE 4.8: Flexing-filtering couplings in a three-signal test.

Flexing-filtering coupling: The flexing-filtering coupling is proportional to the frequency derivative of a filter transfer function; see Eq. (E.18). The anti-aliasing (AA) filters for real-time processing onboard are causal, and group delays typically dominate their frequency derivatives, as shown in the bottom panel in Figure 2.11. However, those dominant contributions are automatically canceled because the identical filters were applied to any signals in Section 4.2.1. As a result, only the contributions of the frequency derivatives of filters' magnitudes remained and appeared around 1 Hz in Figure 4.6.

Figure 4.8 shows the cancellations more explicitly with the flexing-filtering coupling of each filter with both causal (solid) and acausal (dot-dashed) versions. The three-signal performance in red overcame all noise floors with causal filters and was limited by the acausal version of the third and last FIR filter.

The same filter as the actual causal version, but with a group delay zeroed; also see Section 2.4.

LISA would impose a moderate requirement [3] on filter flatness from the perspective of the flexing-filtering coupling. Nevertheless, a post-processing

3 The latest study shows that the angular-frequency derivatives of AA filters must be below 0.27 for any frequency below 1.1 Hz (Olaf Hartwig, personal communication, 2023). This requirement is already met with the current FIR filters in this experiment.

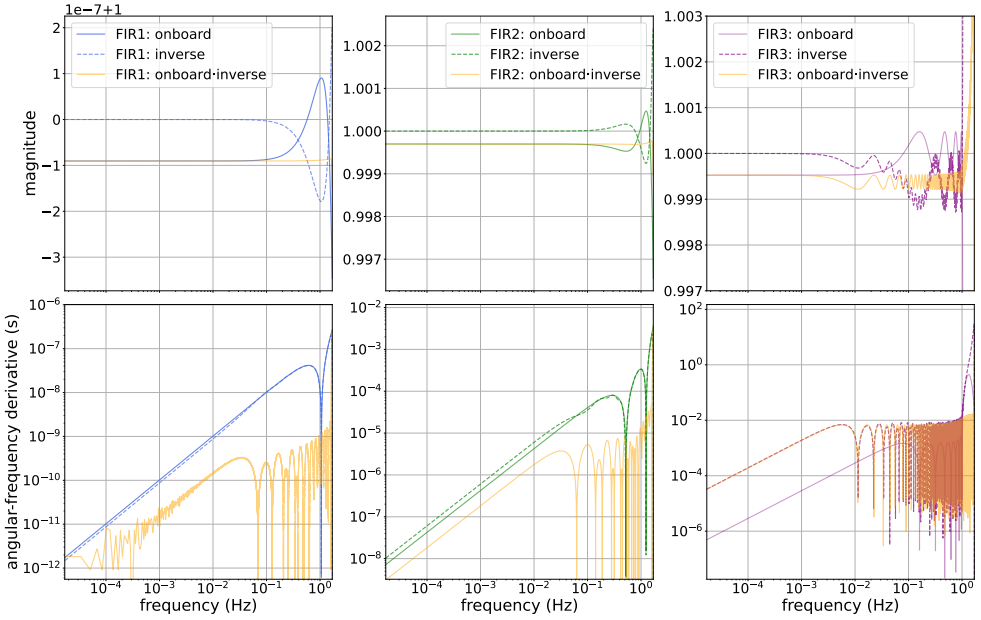

FIGURE 4.9: Compensation for distortions of onboard FIR filters with inverse filters in the LISA observation band. Solid curves are the filters implemented onboard, identical to the ones in Figure 2.11, and dashed curves are inverse filters (the numbers of taps are 51, 51, and 301 for FIR 1, FIR 2, and FIR 3, respectively). Orange is the total response.

method to suppress the noise was investigated further. The idea is to apply inverse filters of the onboard FIR filters to compensate for distortions of signal magnitudes induced by the filters. Theoretically, a complete inverse filter of a FIR filter is a IIR filter. However, such a IIR filter is not guaranteed stability. Hence, the quasi-inverse FIR filter was derived. Figure 4.9 shows the onboard filters (solid), the derived inverse filters (dashed), and the response after the compensation (solid-orange). The numbers of taps are 51, 51, and 301 for FIR 1, FIR 2, and FIR 3, respectively.[4] Notice that the bump in the FIR 3 above 1 Hz (bottom right) that limited the three-signal performance was suppressed by one order of magnitude. Also, the flat direct current (DC) levels of the inverse filters were restricted to the unity; otherwise, signal magnitudes were influenced. This has a significant impact on clock synchronization because differential clock measurements in Eq. (4.8) do scale with the filter level, but time stamps of carrier measurements do not,

The onboard FIR filters also affect signal magnitudes due to non-unity DC levels as shown in Figure 4.9. However, such level shifts are compensated for on an onboard computer.

$$\begin{aligned}(1+\delta_{\mathrm{fir}})\phi^{\tau_i}(\tau+(1+\delta_{\mathrm{fir}})\delta\tau_i(\tau)) &\neq (1+\delta_{\mathrm{fir}})\phi^{\tau_i}(\tau+\delta\tau_i(\tau)) \\ &= (1+\delta_{\mathrm{fir}})\phi^{\tau_m}(\tau) \quad \because \text{Eq. (4.5)}, \quad (4.22)\end{aligned}$$

where δ_{fir} is a deviation of the DC level of the (quasi-inverse) FIR filter from the unity. The error in the estimation of time stamps grows with a measurement time as $\delta_{\mathrm{fir}}\dot{q}_i^o\tau$ where $\dot{q}_i^o$ is the sub-ppm clock frequency offset, and the TDIR accuracy is limited by around this value. The subtraction of in-band stochastic clock jitters is also limited by $O(\nu^o q_i^\epsilon \delta_{\mathrm{fir}})$ due to the scaling.

Finally, the inverse filter of the FIR 3 with the unity DC level was applied to the same measurement of the three-signal test. The resulting performance is shown in solid blue in Figure 4.10. It goes below the flexing-filtering coupling with the onboard FIR 3, suppressing the significant bump above 1 Hz below the performance limit (orange-dot-dashed). Notice that the performance with

4 In order not to cause additional delays due to the inverse filtering, the filters were applied twice to a signal, once forward and once backward, in the following analysis. Hence, the effective number of taps is doubled, and the filter magnitude is squared. Figure 4.9 plots the squared responses.

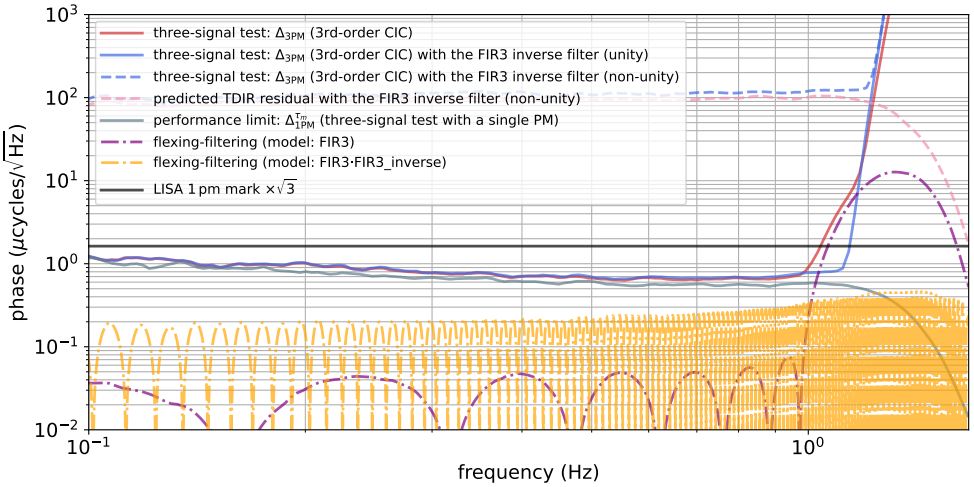

FIGURE 4.10: Improvement of the three-signal performance with the inverse filter.

the inverse filter with the non-unity DC level (dashed-blue) deteriorated significantly, from 6.15 ns to 807 ns in TDIR precision.

Although the suppression of the flexing-filtering coupling of the onboard filter was successfully demonstrated above, this operation actually would not be necessary (or optimal) for LISA: a requirement on filter flatness would be moderate and met even by the current filter designs (see footnote 3). Applying the same filters to GW templates would also be possible to avoid distortions of the SNR.

Local timing reference: Any PM signals in the analytical model in Section 4.2 are, as mentioned, assumed to be already corrected by PT signals. Also, any experimental results in this chapter up until now are based on the correction. The PT correction was introduced initially to remove the ADC jitter from the scientific signals; however, more importantly, in the latest frequency distribution scheme (see Section 2.6), this correction transforms the local timing reference from the 80 MHz system clock to the PT signal, which is designed to feature more stable phase fidelity with the GHz-clock sideband.

Figure 4.11 shows the performance without PT corrections in orange, i.e., according to the 80 MHz system clock as the timing reference. This is limited by the PT phase readout in dashed-green, which is a good estimate of the relative noise between the 80 MHz system clock and the GHz-clock sideband.[5] Hence, red, orange, and dashed green verify that our frequency distribution scheme has the expected impact on clock synchronization.

The phase fidelity between the PT and clock outputs of the FDS was separately measured by the PM implemented on Red Pitaya (dashed violet) [6]. This converges on the dashed green below 4 mHz, while the white noise floor at 10 μcycle/$\sqrt{\text{Hz}}$ and the peak around 70 mHz seem to be attributable to the PM onboard clock signal chain, which comprises a comparator, a low voltage differential signaling (LVDS) driver, and a clock buffer.

The removal of the noise of non-critical paths on the FDS via PT corrections seems not to be good enough because the 70 mHz peak residual can be recognized in red. This point remains to be investigated, and the relatively

5 This means that $\dot{q}^{\epsilon}_{\text{CLK}}$ is dominant in Eq. (2.21).

6 Red Pitaya has a sampling rate of 125 MHz; hence, it can measure the 80 MHz clock as an aliased 45 MHz signal. According to another measurement, dashed violet in Figure 4.11 seems to be limited by the test setup above 30 mHz.

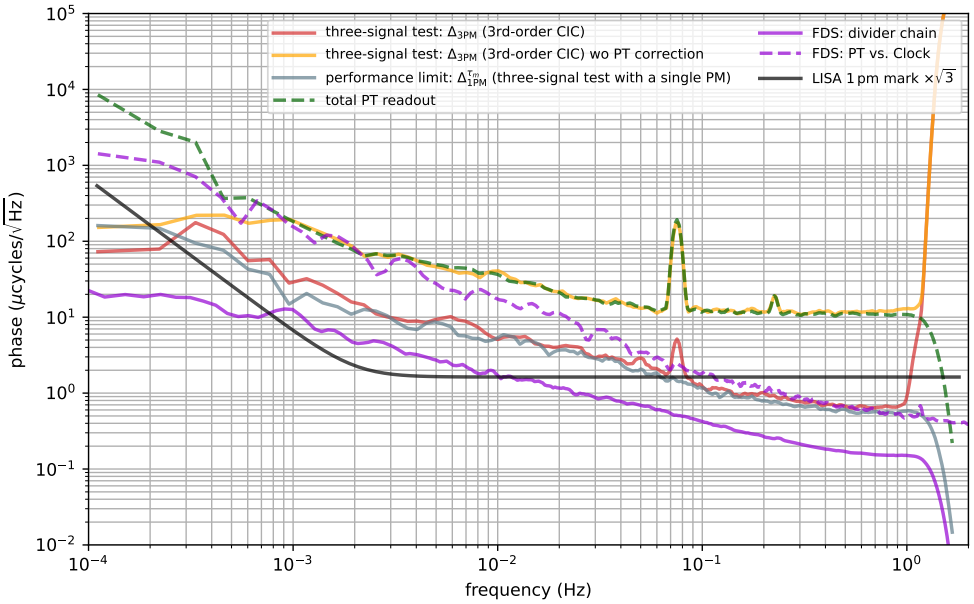

FIGURE 4.11: Transformation of the local timing reference in a three-signal test. The three-signal measurement with clock synchronization without PT corrections (orange) is expectedly limited by the noise of the clock chain, estimated via PT phase readout itself (dashed-green).

moderate requirement could be assigned to the phase fidelity between the 80 MHz clock and the GHz-clock sideband in the future.

4.4 TONE-ASSISTED TDIR

Secondary noises limit the accuracy of the TDIR, as was the case in Section 4.3. In LISA, the limiting source would be an astrophysical background due to unresolved binaries, TM acceleration noises, or shot noise floor, depending on the frequency region to be probed for the ranging. In the Hexagon, as described in Figure 4.5, the accuracy is limited by the testbed sensitivity at the high frequency, which would be an electronic additive noise.

A method called *tone-assisted TDIR* improves the ranging accuracy [48, 49], by intentionally injecting a sinusoidal tone in the high-frequency region of the PM measurement band,

A clear distinction between the PM measurement band and the observation band.

$$\nu_T(\tau) = |\nu_T| \sin(2\pi f_T \tau), \tag{4.23}$$

e.g., $f_T = 1$ Hz. The tone will be applied to some of the laser-lock loops. This is then distributed via laser locks throughout the system. This is to enhance SNR of TDIR, and only noises at the particular tone frequencies are analyzed in post-processing. One critical constraint is that the tones must be injected so that all TDIR targets couple with at least one of the tones.

In TDIR, "signal" is a laser frequency noise. In contrast, "noise" means any other contributions, even GWs

The method is a handy tool for manipulating the TDIR accuracy by controlling the tone amplitude and frequency in Eq. (4.23). From the perspective of a technology testbed like the Hexagon, this would reduce the necessary efforts of noise hunting to improve the sensitivity aiming for better accuracy.

4.4.1 *Theory*

A baseline in LISA is to inject a tone to an error point of a Pound-Drever-Hall (PDH) lock for frequency stabilization of a primary laser. However, the Hexagon is currently not equipped with any frequency stabilization. Hence, instead of a primary laser, tones can be injected to reference frequencies of

offset frequency locks for secondary lasers (i.e., 2′ and/or 3′). In this case, three beam frequencies are expressed in an arbitrary time frame,

$$\nu_{c,1'}(\tau) = \nu_0 + \delta\nu_{1'}(\tau), \tag{4.24}$$
$$\nu_{c,2'}(\tau) = \nu_{c,1'}(\tau) + O_{1'2'} + \delta\nu_{1'2'}(\tau) + \nu_{T2'}(\tau), \tag{4.25}$$
$$\nu_{c,3'}(\tau) = \nu_{c,1'}(\tau) + O_{1'3'} + \delta\nu_{1'3'}(\tau) + \nu_{T3'}(\tau), \tag{4.26}$$

where $O_{i'j'}$ is a MHz offset frequency, $\delta\nu_{i'j'}(\tau)$ is a residual frequency noise, and $\nu_{Tj'}(\tau)$ is an injected frequency tone. These single laser frequencies are mixed via the Hexagon interferometer and result in three beatnotes,

$$\nu_{c,1'2'}(\tau) = O_{1'2'} + \delta\nu_{1'2'}(\tau) + \nu_{T2'}(\tau), \tag{4.27}$$
$$\nu_{c,2'3'}(\tau) = O_{1'3'} + \delta\nu_{1'3'}(\tau) + \nu_{T3'}(\tau) - \left(O_{1'2'} + \delta\nu_{1'2'}(\tau) + \nu_{T2'}(\tau)\right), \tag{4.28}$$
$$\nu_{c,3'1'}(\tau) = -O_{1'3'} - \delta\nu_{1'3'}(\tau) - \nu_{T3'}(\tau). \tag{4.29}$$

With a small error of timing estimation $\delta\hat{\tau}_{i,\mathrm{e}}$, the three-signal combination, in the same 3PM3S topology as Section 4.2, leaves the residual frequency noises after the synchronization to clock 1,

$$\Delta_{3\mathrm{PM}}(\tau) = \nu^{\tau_1}_{c,1'2'}(\tau) + \nu^{\tau_1}_{c,2'3'}(\tau + \delta\hat{\tau}_{2,\mathrm{e}}) + \nu^{\tau_1}_{c,3'1'}(\tau + \delta\hat{\tau}_{3,\mathrm{e}}) \tag{4.30}$$
$$= (\delta\hat{\tau}_{2,\mathrm{e}} - \delta\hat{\tau}_{3,\mathrm{e}})\left(\delta\dot{\nu}_{1'3'}(\tau) + \dot{\nu}_{T3'}(\tau)\right) - \delta\hat{\tau}_{2,\mathrm{e}}\left(\delta\dot{\nu}_{1'2'}(\tau) + \dot{\nu}_{T2'}(\tau)\right), \tag{4.31}$$

Eq. (4.31) meets the requirement of tone-assisted TDIR: the coupling of the timing errors $\delta\hat{\tau}_{i,\mathrm{e}}$ into the signal combination $\Delta_{3\mathrm{PM}}$ is lifted by injected frequency tones ν_T.

The accuracy of tone-assisted TDIR is ultimately limited by a stochastic secondary-noise floor [49],

$$\delta\hat{\tau}_{i,\mathrm{e,n}} = \frac{2\widetilde{\phi}_n(f_T)}{|\nu_T|\sqrt{T_m f_s}}, \tag{4.32}$$

where $\widetilde{\phi}$ is the ASD of secondary phase noises, T_m is a measurement time, and f_s is a data rate. The additional subscript n represents the particular performance-limiting mechanism.

On the other hand, some secondary noises could be lifted by the tone in the same way as the laser noise. SNR cannot be improved anymore once the tone in such secondary noises dominates the original stochastic noise floor $\widetilde{\phi}_n$; hence, it could limit the ranging accuracy, if not treated. Two relevant noises will be discussed below: the flexing-filtering coupling and the DPLL error.

The tone in the secondary noise is also deterministic. Thus, it could be subtracted in post-processing, though no effort for this subtraction was made in this thesis.

The flexing-filtering coupling scales with an input frequency noise according to Eq. (E.18). At the limit, the residual frequency tone becomes equal to the corresponding flexing-filtering coupling,

$$\widetilde{\nu}_T \cdot \Delta L(f_T; \delta\hat{\tau}_{i,\mathrm{e,ff}}) = |FF(2\pi f_T; \nu_T, \mathbf{T}_i, \mathbf{F})|. \tag{4.33}$$

The limit of the timing accuracy per secondary clock can be derived by solving Eq. (4.33) for the residual timing error $\delta\hat{\tau}_{i,\mathrm{e,ff}}$,

$$\delta\hat{\tau}_{i,\mathrm{e,ff}} \approx \dot{q}_i \cdot \left|\frac{d\tilde{\mathbf{F}}(\omega_T)}{d\omega}\right|, \tag{4.34}$$

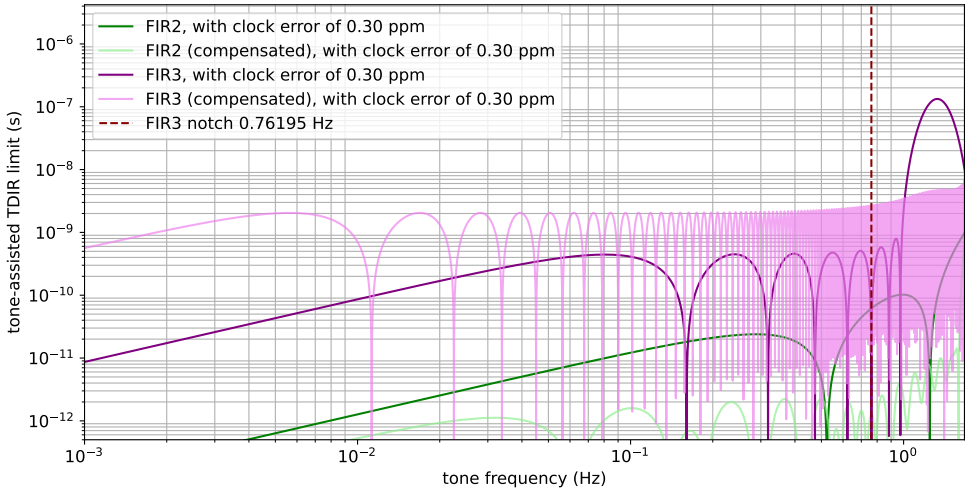

FIGURE 4.12: Limit of the timing accuracy with tone-assisted TDIR per secondary clock due to the flexing-filtering coupling, as a function of a tone frequency f_T. The compensated cases are from orange curves in Figure 4.9.

which is determined only by the fractional frequency error of the clock i and the angular-frequency derivative of the filter at the tone frequency f_T.[7]

Figure 4.12 shows the limit in terms of FIR 2 and FIR 3. Due to FIR 3 (dark purple), the accuracy limit rapidly deteriorates above 1 Hz toward higher frequencies. If the tone needs to be placed in this region, the compensation filter, introduced in Section 4.3.3, helps improve the performance further (light purple). In case the tone allows to be below 1 Hz, it can be placed at one of the notches of FIR 3, e.g., 0.761 95 Hz. FIR 2 becomes the limiting factor (dark green), and applying the compensation to this filter would be a good option (light green). Therefore, depending on the tone frequency f_T, the filter to be compensated for could be properly selected.

This particular compensation filter with 301 taps adversely lifts the flexing-filtering coupling below 1 Hz. At the same time, it significantly attenuates the high-frequency bump. Much more taps would be needed to gain attenuation throughout the frequency band.

The DPLL error is determined by the transfer function of DPLL. Hence, the residual frequency tone is equated to such a DPLL error, from Eq. (2.5),

$$\widetilde{\nu}_T \cdot \Delta L(f_T; \delta\hat{\tau}_{i,\mathrm{e,pll}}) = \widetilde{\nu}_T \cdot |E_{\mathrm{PLL}}(z_T)|. \tag{4.35}$$

Solving Eq. (4.35) for $\delta\hat{\tau}_{i,\mathrm{e,pll}}$ gives

$$\delta\hat{\tau}_{i,\mathrm{e,pll}} \approx \frac{2}{A_{\mathrm{het}}\pi} \cdot 2^{C_p} \cdot \frac{2\pi f_T}{k_i} \cdot \frac{1}{f_s^2}, \tag{4.36}$$

where some approximations were applied: a low-frequency limit (see Eq. (F.1)), a large open-loop gain $G_{\mathrm{PLL}}(z_T) \gg 1$, and a dominant f^{-2} shape (see Eq. (2.1)). Notice that such a tone in error should also appear in sideband PLLs. But this was ignored because it must be coherent and share the same sign between the upper and lower sideband beatnotes; hence, it can be canceled by combining them to extract differential clock signals.

The actual limit of the accuracy of tone-assisted TDIR would be given by the noisiest contribution out of the three above [8],

$$\delta\hat{\tau}_{i,\mathrm{e}} = \max\left(\delta\hat{\tau}_{i,\mathrm{e,n}}, \delta\hat{\tau}_{i,\mathrm{e,ff}}, \delta\hat{\tau}_{i,\mathrm{e,pll}}\right). \tag{4.37}$$

7 Same as Appendix E.3, $\dot{q}_i$ is assumed to be a constant slope of a linear timer deviation here.

8 The way to combine the three contributions is not super clear because the flexing-filtering coupling and the DPLL error are the deterministic residual tone, while the secondary-noise limitation is stochastic.

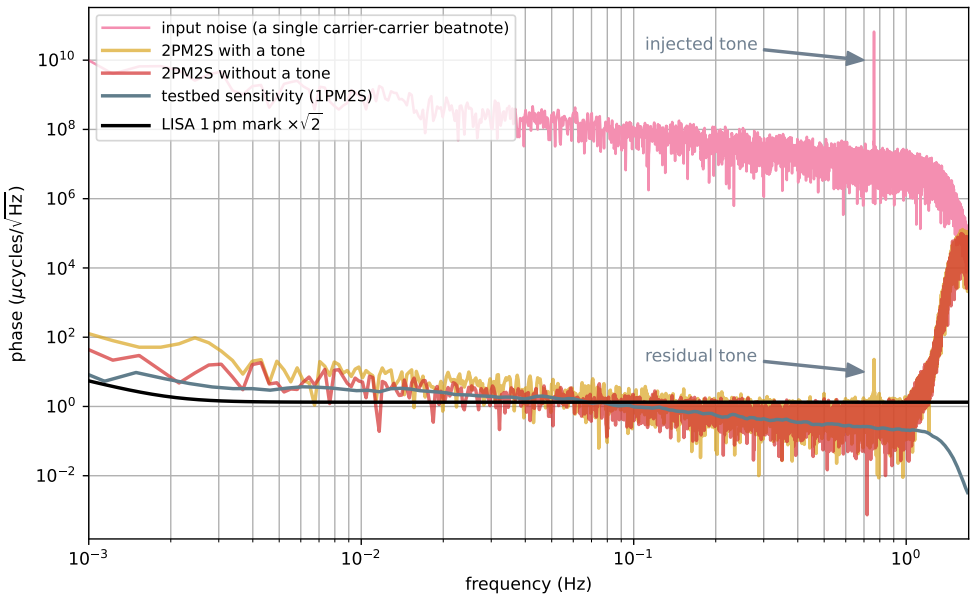

FIGURE 4.13: Clock synchronization with tone-assisted TDIR. The testbed sensitivity (grey) has logarithmic-spaced frequency bins, while the others have linear-spaced bins to show the tone properly.

4.4.2 *Demonstration*

Tone-assisted TDIR was demonstrated in the 2PM2S topology, i.e., clock synchronization between two independent PMs. Unfortunately, the tone in the DPLL error will be canceled after the synchronization in this topology because both PMs look at the same beatnote with the same amplitude, which results in the same DPLL error in terms of the deterministic residual tone; hence, $\delta\hat{\tau}_{i,e,\mathrm{pll}}$ in Eq. (4.36) cannot be probed by this topology. The tone was injected by modulating a beatnote reference frequency in a laser lock system. See Appendix F.2.2.

Figure 4.13 shows the overview of the results. The tone had a depth of 10 kHz and a frequency of 0.762 Hz (pink), which is nearly at the notch of the flexing-filtering coupling of FIR 3 in Figure 4.12. After clock synchronization, the performance (yellow) almost reached the testbed sensitivity (grey), measured by a single PM, except for the residual tone. The clock synchronization performance without the tone injection is also plotted in red as a reference. Notice that some of them have linearly-spaced frequency bins instead of the logarithmic ones used up to here to prevent the tone from being washed out by the resolutions.

Figure 4.14 zooms in on the frequencies around the tone, adding more curves. First, as expected, the residual tone in yellow was caused by the flexing-filtering coupling of FIR 2 (green). The one of FIR 3 (purple) is notched at the tone frequency as intended. This case already reaches the accuracy of 7.17×10^{-11} s, which corresponds to 2.15×10^{-2} m in displacement. Nevertheless, to improve the ranging accuracy further, the FIR 2 compensation filter was applied in post-processing. This suppressed the residual tone (light green) and improved performance (blue). The resulting accuracy is 8.37×10^{-12} s, which corresponds to 2.51×10^{-3} m in displacement. A bump around the tone frequency (in blue and yellow) impedes it from reaching the accuracy of 1.99×10^{-12} s, computed by the testbed sensitivity in grey and the measurement time of 3500 s based on Eq. (4.32). The cause of the bump remains to be understood. Finally, notice that this experimental topology is, as mentioned,

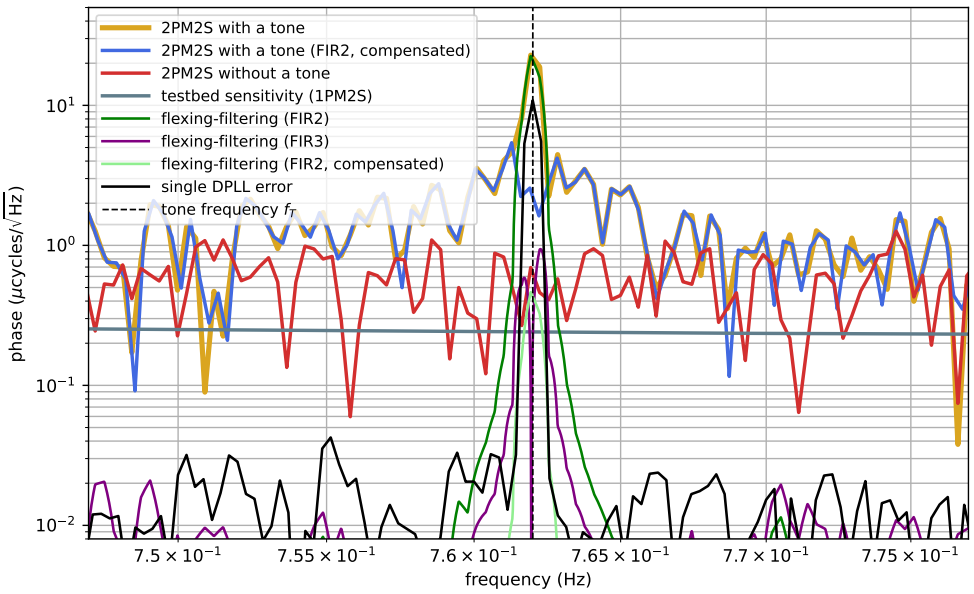

FIGURE 4.14: Clock synchronization with tone-assisted TDIR, zooming in on the tone. The performance (yellow) is limited by the flexing-filtering coupling by FIR 2 (green). This can be further suppressed by compensating for FIR 2 (blue).

insensitive to the tone in the DPLL error, plotted in black. Hence, the performance with the FIR 2 compensation is actually supposed to be limited by the DPLL error in this particular example [9]; 3.46×10^{-11} s or 1.04×10^{-2} m.

4.5 SUMMARY AND OUTLOOK

This chapter presented the first demonstration of clock synchronization with multiple PMs in the Hexagon experiment. It can be considered a big leap concerning the previous single-PM case in three regards: model, setup, and data analysis. The analytical model has been built by mapping the LISA counterparts to the Hexagon. Departing from a simple linear combination for the three-signal test in the single-PM case, the model links the experiment and LISA. The setup requires not only multiple PMs but also FDSs to perform clock synchronization at LISA performance levels. Such a setup is an integrated platform to test key devices for LISA. According to the model, data analysis requires more numerical treatments, planned for LISA: extracting differential clock signals, time-shifting signals via interpolation, the TDIR-like algorithm, etc.

The 3PM3S topology successfully verified several LISA technologies. The clock-synchronization performance in Figure 4.4 showed sub-picometer performance above 60 mHz and below 10 pm/$\sqrt{\text{Hz}}$ LISA single-link performance level over the entire observation band. The result was achieved with the 1.84 m-accuracy TDIR and the 6-order suppression of in-band stochastic clock jitters around the mHz regime. Furthermore, the measurement also proved noise couplings stemming from clock synchronization (and also TDI in LISA) firstly with real data: the aliasing effect, the flexing-filtering coupling, and the interpolation error. The flexing-filtering coupling could be further suppressed with the post-processing compensation for the AA filters implemented on PM software for data decimations.

9 It could be possible to subtract the residual tone in the DPLL error and/or the flexing-filtering coupling in post-processing because of its deterministic nature.

A different TDIR operation, tone-assisted TDIR, was also demonstrated using the 2PM2S topology. This study pointed out that the tone suppression would be limited by the PLL error or the flexing-filtering coupling before it becomes stochastic-noise limited. Suppressing the flexing-filtering coupling with a compensation filter, the accuracy reached 8.37×10^{-12} s, i.e., 2.51×10^{-3} m in range.

Some non-trivial future tasks remain to be completed. First, clock synchronization ideally needs to be verified to the level of $1\,\mathrm{pm}/\sqrt{\mathrm{Hz}}$. As shown in Figure 4.4, the current performance is most likely limited by the optical setup's sensitivity (e.g., ghost beams and/or residual polarization errors). In addition, FDSs are operated in the air currently in the Hexagon, which also impedes the achievement of the $1\,\mathrm{pm}/\sqrt{\mathrm{Hz}}$ mark; also see Appendix D.3 for the improvement under vacuum conditions. Second, the potential residual of the relative noise between the 80 MHz system clock and the PT signal, observed in Figure 4.11, could be critical. The LISA clock synchronization scheme relies on the high suppression of this noise via PT corrections, with an insignificant contribution to the overall noise budget. Third, a complete representation of the LISA interspacecraft interferometers needs to be achieved, in particular by implementing the weak-light condition around $\mathcal{O}(100\,\mathrm{pW})$. All measurements so far were taken under the nominal state, i.e., $\sim \mathcal{O}(100\,\mu\mathrm{W})$. Fourth, LISA on-ground processing pipelines, shown in Figure 3.4, can be mapped to the Hexagon to be tested with real data. All the data analyses have been performed by the author's software so far.

Part III

INTERSATELLITE ABSOLUTE RANGING

5

PSEUDORANDOM NOISE RANGING AND DATA COMMUNICATION

LISA interferometric arms will be unequal and time-varying due to orbital motions, coupling laser frequency noise in the mHz observation band. TDI will synthesize a virtual equal-arm interferometer in post-processing to suppress this overwhelming noise contribution. This algorithm relies on PRNR estimations in-flight with an accuracy of 1 m rms over an on-ground data rate by applying a low-depth binary phase modulation technique on each laser link, so-called binary phase-shift keying (BPSK). This technique also enables optical data communication between SCs.

This chapter focuses on general descriptions and a summary of the latest development of the technologies to provide preliminary information for the later chapters in Part III. Iouri Bykov initiated the development, which was then further continued and ported to Hexagon PMs by the author.

5.1 DESIGN OVERVIEW

The overview of the PM FPGA architecture from this perspective comprises *transmitter* and *receiver*, as illustrated in Figure 5.1.

The *transmitter* side generates a transmitted PRN code with a dedicated PRN LUT. The local/transmitted data Data_{tx} is encoded on the PRN code via exclusive-or (XOR) operation. "Data" here will include not only PM science data but also check symbols for coding. After the modulation signal is scaled in amplitude for a target modulation depth, the analog signal after a digital-to-analog converter (DAC) is applied to an EOM. On real hardware, the GHz-clock sideband signal must be added to the PRN modulation signal before the EOM, as shown in Figure 2.1; however, the part is omitted in Figure 5.1.

The *receiver* side aims to extract two primary pieces of information: an intersatellite pseudo-range, a combination of the intersatellite light-travel time

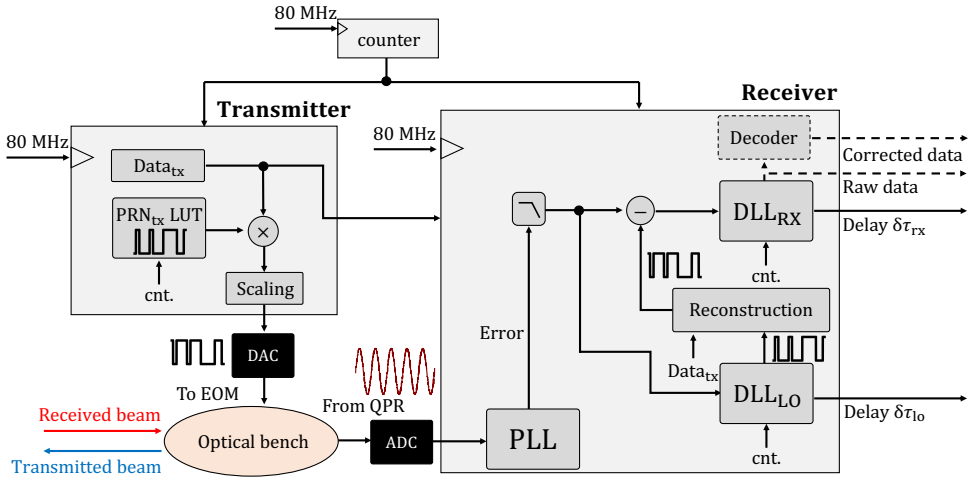

FIGURE 5.1: Overview of the FPGA architecture from the perspective of PRNR and data communication. Data decoding might happen in the OBC. Therefore, the decoder is bounded by dashed lines.

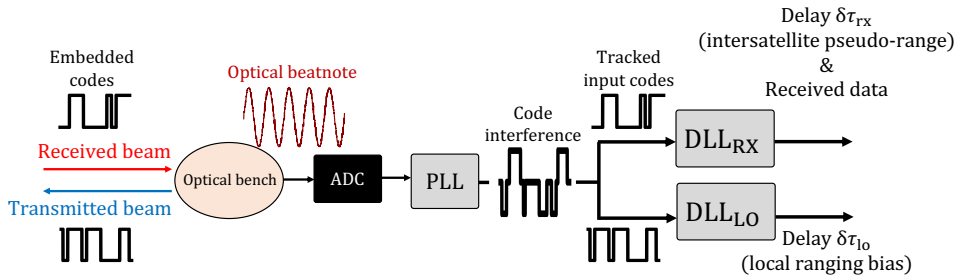

FIGURE 5.2: Simplified diagram of two DLL instances. The polarity change of one of the PRN codes due to the beam interference is not visually considered.

and clock offsets, and data from a distant SC. The core module is DLL, which uses the PLL error signal as an input, as mentioned in Section 2.3. Two PRN signals, from a distant SC and the local *transmitter* side, are both present in the input signal. Two dedicated DLL instances, called DLL_{RX} and DLL_{LO} in this thesis, are implemented to track each of the nearly-orthogonal PRN signals; also see Figure 5.2 for the simplified diagram. DLL_{RX} is the primary measurement that contains the intersatellite pseudo-range and data from the distant SC, while DLL_{LO} is to enhance the performance of DLL_{RX} and estimate ranging biases. The former is achieved by subtracting the local PRN code from the input of DLL_{RX}, so-called interfering code cancellation (ICC): hence, the code interference can be highly suppressed [50]. The encoded data must be feed-forwarded from the transmitter to the receiver to compensate for the polarity change, which has also been implemented. The latter (i.e., the ranging bias) is critical for absolute ranging and is one of the main topics in Chapter 7.

5.2 PRN CODE

The PRN codes are, on top of the PM system clock rate f_s (i.e. 80 MHz), parameterized by three key values: a PRN ambiguity L_{code}, a data-bit rate f_{bit}, and a PRN chip rate f_{chip}:

- **PRN ambiguity L_{code}:** the finite code length results in a PRNR ambiguity. This ambiguity must be more than twice as long as a ranging uncertainty via ground observations, which would be around 50 km due to an orbit determination and a mission operation center (MOC) time correlation.
- **Data-bit rate f_{bit}:** The target data-bit rate in LISA is 60 kbps. If any coding, e.g., Reed Solomon (RS) coding, is implemented, an effective data rate $f_{\text{bit}}^{\text{eff}}$, to which the requirement must be applied, differs from a raw data rate $f_{\text{bit}}^{\text{raw}}$.
- **PRN chip rate f_{chip}:** the chipping rate is determined by the number of the system clock cycles n_{chip} over the duration, i.e., $f_{\text{chip}} = f_s / n_{\text{chip}}^{\text{cycle}}$. This influences couplings of ranging noises and biases and the required bandwidth of QPR and BEE as well as necessary margins in the frequency plan.

In this thesis, n_B^A means the number of A per B as applied to Table 5.1

The current nominal parameters for LISA and their notation are summarized in Table 5.1, and also visualized in Figure 5.3. The parameters are also selected in line with our PM timing architecture. However, the PRN parameter set is still under discussion [1]. Our classical parameter set is shown in square

1 The parameter set can be easily switched with no hardware modifications.

parenthesis in the table. Such a parameter set is referred to as the "2^n parameter set" in this thesis and used for all experiments (and many simulations) in Chapters 6 and 7. Note that RS coding is assumed in the rest of this thesis; however, the optimal coding technique is under discussion.

Each PMS is equipped with one PRN code; hence, LISA requires six PRN codes in total. The orthogonal set of six PRN codes for experiments in this thesis was designed by Gerhard Heinzel.

Parameter	Value	Comment
Primary		
System clock rate f_s	80 MHz	
Number of PRN codes N_{prn}	6	one per laser
System clock cycles per PRN chip $n_{\text{chip}}^{\text{cycle}}$	50 [64]	
PRN chips per data-bit window $n_{\text{bit}}^{\text{chip}}$	20 [16]	$n_{\text{bit}}^{\text{cycle}} = n_{\text{chip}}^{\text{cycle}} \cdot n_{\text{bit}}^{\text{chip}}$
Data bits per PRN code $n_{\text{code}}^{\text{bit}}$	125 [64]	$n_{\text{code}}^{\text{cycle}} = n_{\text{bit}}^{\text{cycle}} \cdot n_{\text{code}}^{\text{bit}}$
RS symbol parameters $(n_{\text{rs}}, k_{\text{rs}})$	(255, 205)	
Number of bits per symbol m_{rs}	8	one byte per symbol
Code type		see Chapter 6
Secondary		
PRN chip rate f_{chip}	1.6 MHz [1.25 MHz]	$f_{\text{chip}} = f_s / n_{\text{chip}}^{\text{cycle}}$
Raw data rate $f_{\text{bit}}^{\text{raw}}$	80 kbps [78 125 bps]	$f_{\text{bit}}^{\text{raw}} = f_{\text{chip}} / n_{\text{bit}}^{\text{chip}}$
Effective data rate $f_{\text{bit}}^{\text{eff}}$	64.3 kbps [62.8 kbps]	$f_{\text{bit}}^{\text{eff}} = (k_{\text{rs}}/n_{\text{rs}}) \cdot f_{\text{bit}}^{\text{raw}}$
Code repetition rate f_{code}	640 Hz [1221 Hz]	$f_{\text{code}} = f_{\text{bit}}^{\text{raw}} / n_{\text{code}}^{\text{bit}}$
PRNR ambiguity L_{code}	468 km [246 km]	$L_{\text{code}} = c / f_{\text{code}}$

TABLE 5.1: Current nominal parameters of PRN codes for LISA. The primary parameters are to be implemented on hardware, while the secondary parameters are the resulting values in the scientific view. Values for the implementation in this thesis are, if different, shown in square parenthesis. This parameter set is named "2^n parameter set". c is the speed of light.

5.3 TECHNOLOGY DESCRIPTION

The basic working principles of PRNR and data communication are briefly described in this section, together with analytical forms of their performances under ideal cases.

5.3.1 *Ranging*

Noise types and their couplings to the delay estimate are discussed in this section, similarly to [51] but adapted to our case. The PRN signal chain, described in Section 2.3.1, is first formulated. After that, the noise couplings are discussed based on the linear model of a DLL.

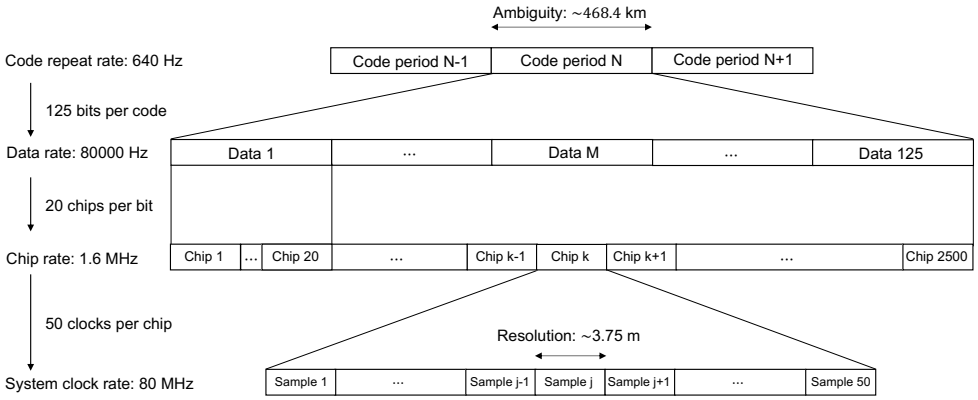

FIGURE 5.3: Diagram of the current nominal PRN code parameters for LISA. Notice that the values are different from the implementation in this thesis. See Table 5.1 for the ones for this thesis.

A carrier-carrier beatnote with PRN modulations was formulated in Eq. (1.11). The following expresses the same signal but with some adaptations for this section,

$$V_c(\tau) = A_c \cdot \sin\Big(\omega_{\text{het}}\tau + \delta\phi(\tau) + m_{\text{prn}}\left(c_{\text{rx}}(\tau - \delta t_{\text{rx}}(\tau) - \delta\tau_{\text{rx}}(\tau)) - c_{\text{tx}}(\tau - \delta t_{\text{tx}}(\tau))\right)\Big) + \delta V_{\text{add}}(\tau), \tag{5.1}$$

where $\delta\tau_{\text{rx}}$ is a target delay of ranging, so-called *pseudo-range*; $\delta\phi$ is any input phase noise; δt is a timing noise of a PRN code, including ranging biases, except for the pseudo-range; δV_{add} is any additive noise contribution; super- and sub-scripts “rx" and “tx" represent received and transmitted codes. Hence, c_{rx} and c_{tx} are the codes to be tracked by DLL_{RX} and DLL_{LO}, respectively. Notice that the encoded data were, for simplicity, absorbed into the codes by,

$$\text{DATA}_i \otimes c_i \longrightarrow c_i \quad (i = \text{rx}, \text{tx}). \tag{5.2}$$

As described in Section 2.3.1, the input signal Eq. (5.1) is filtered by the PLL error function e_{PLL} [2] and the pre-DLL low-pass filter ℓ_{DLF}. They form a band-pass filter around PRN chip rate f_{chip}. The impulse response of this compound filter is represented by $h = e_{\text{PLL}} * \ell_{\text{DLF}}$ via convolution ($*$). The frequency response of the filters was shown in Figure 2.7.

The input to DLL $u_e(\tau)$ can be modeled via the mixing with a local copy $\sin(\omega_{\text{het}}\tau)$ and the convolution with the impulse response of the compound filter,

$$u_e(\tau) = h * \Big(\delta\phi(\tau) + m_{\text{prn}}\left(c_{\text{rx}}(\tau - \delta t_{\text{rx}}(\tau) - \delta\tau_{\text{rx}}(\tau)) - c_{\text{tx}}(\tau - \delta t_{\text{tx}}(\tau))\right) + \sqrt{2}\cdot\frac{\delta V_{\text{add}}^{f_{\text{het}}}(\tau)}{A_c}\Big), \tag{5.3}$$

where $\delta V_{\text{add}}^{f_{\text{het}}}(\tau)$ expresses only down-converted components of $\delta V_{\text{add}}(\tau)$ with a factor of $\sqrt{2}$ in the PLL mixing process [40].

2 e_{PLL} corresponds to $F_{\text{PD}} \cdot E_{\text{PLL}}$ in the frequency domain, where F_{PD} is a phase detector transfer function (see Eq. (2.3)) and E_{PLL} is a PLL error transfer function (see Eq. (2.5)).

The band-pass filter h can be approximated to a flat response at F_{PD} ($= A_c/4$; see Eq. (2.3)) around f_{chip} in magnitude, while it induces group delays $\Delta t_k^h(\tau)$, which form additional contributions into $\delta t_{\mathrm{rx}}(\tau)$ as ranging biases,

This approximation neglects the distortion of perfect square codes due to the band-pass filter.

$$u_e(\tau) \approx \frac{A_{\mathrm{prn}}}{4} \cdot \Big(c_{\mathrm{rx}}(\tau - \delta t_{\mathrm{rx}}^h(\tau) - \delta\tau_{\mathrm{rx}}(\tau - \Delta t_{\mathrm{rx}}^h(\tau))) - c_{\mathrm{tx}}(\tau - \delta t_{\mathrm{tx}}^h(\tau)) \Big) + h * \left(\delta\phi(\tau) + \sqrt{2} \cdot \frac{\delta V_{\mathrm{add}}^{f_{\mathrm{het}}}(\tau)}{A_c} \right), \tag{5.4}$$

$$A_{\mathrm{prn}} = m_{\mathrm{prn}} \cdot A_c, \tag{5.5}$$

$$\begin{aligned} \delta t_k^h(\tau) &= \delta t_k(\tau - \Delta t_k^h(\tau)) + \Delta t_k^h(\tau) \\ &\approx \delta t_k(\tau) + \Delta t_k^h(\tau) \qquad (k = \mathrm{tx}, \mathrm{rx}), \end{aligned} \tag{5.6}$$

where code amplitudes turned into $A_{\mathrm{prn}}/4$ due to F_{PD}. Notice that a group delay Δt_k^h is formulated as a time-variant term. The potential time dependency is attributable to a modulation of the PLL error function (blue in Figure 2.7) due to fluctuations of an input beatnote amplitude A_c.

DLL computes a correlation between $u_e(\tau)$ and the dedicated code: c_{rx} for $\mathrm{DLL_{RX}}$ and c_{tx} for $\mathrm{DLL_{LO}}$. This results in the code interference between c_{rx} and c_{tx}, which is another additive noise in DLL. After all, the input signals and total additive noise in the linear model of DLL can be expressed by,

$$\tau_{\mathrm{rx}}(\tau) = \tau - \delta t_{\mathrm{rx}}^h(\tau) - \delta\tau_{\mathrm{rx}}(\tau - \Delta t_{\mathrm{rx}}^h(\tau)), \text{ for } \mathrm{DLL_{RX}} \tag{5.7}$$

$$\tau_{\mathrm{tx}}(\tau) = \tau - \delta t_{\mathrm{tx}}^h(\tau), \text{ for } \mathrm{DLL_{LO}} \tag{5.8}$$

$$\delta u_{\mathrm{add,dll}}(\tau) = \frac{\sqrt{2}}{4} \cdot \left(A_{\mathrm{prn}} \cdot \delta u_{\mathrm{INT}}(\tau) + A_c \cdot \delta\phi^{f_{\mathrm{chip}}}(\tau) + \sqrt{2} \cdot \delta V_{\mathrm{add}}^{f_{\mathrm{het}}+f_{\mathrm{chip}}}(\tau) \right), \tag{5.9}$$

where the group delay Δt_k^h for $\delta\phi$ and δV_{add} are scientifically trivial; hence, omitted for simplicity. $\delta u_{\mathrm{INT}}(\tau)$ is the normalized interference between c_{rx} and c_{tx}, determined by the PRN codes' orthogonality and the correlation integration window $n_{\mathrm{bit}}^{\mathrm{chip}}$ [51]. Another overall $\sqrt{2}$ factor in Eq. (5.9) is due to the mixing process in DLL. Potential sources in different noise terms are discussed below, except for the code interference δu_{INT},

- **Input timing noise $\delta t_k^h(\tau)$:** ranging biases are categorized into the term $\Delta t_k^h(\tau)$, i.e, QPR, cables, PLL, pre-DLL filters, etc. There would also be in-band contributions, like the change of transfer functions of electronics induced by temperature fluctuations. EOM would contribute as well.

- **Heterodyne phase noise $\delta\phi^{f_{\mathrm{chip}}}(\tau)$:** components around f_{chip} contributes as an additive noise. Temperature fluctuations, optical bench path length fluctuations, or laser noises are all expected to be extremely small and negligible. EOM might have some contributions to this term.

- **PLL additive noise $\delta V_{\mathrm{add}}^{f_{\mathrm{het}}+f_{\mathrm{chip}}}(\tau)$:** well-known additive noises are listed here; shot noise, electronic noise, RIN, etc. The residual PT signal or heterodyne second harmonics can be listed here; also see Appendix D.2.

The delay estimate $\hat{\tau}_k$ of DLL_k can be derived via a linear model in the frequency domain,

$$\widetilde{\hat{\tau}}_k = \frac{G_{\mathrm{DLL}}}{1+G_{\mathrm{DLL}}} \cdot \widetilde{\tau}_k + \frac{1}{f_s}\frac{G_{\mathrm{DLL}}/F_{\mathrm{err}}}{1+G_{\mathrm{DLL}}} \cdot \widetilde{\delta u}_{\mathrm{add,dll}} \tag{5.10}$$

$$\approx \widetilde{\tau}_k + \frac{\widetilde{\delta u}_{\mathrm{add,dll}}}{f_s \cdot F_{\mathrm{err}}}, \tag{5.11}$$

$$F_{\mathrm{err}} = \frac{(A_{\mathrm{prn}}/4)}{(n_{\mathrm{chip}}^{\mathrm{cycle}}/2)} = \frac{A_{\mathrm{prn}}}{2n_{\mathrm{chip}}^{\mathrm{cycle}}}, \tag{5.12}$$

where G_{DLL} is an open-loop transfer function of DLL and F_{err} is an error gain. The second line assumes $|G_{\mathrm{DLL}}| \gg 1$, which is the case in our observation band. The f_s^{-1} factor applied to the additive noise converts the integer samples to time.

Shot noise will be taken as an example in the following because it is expected to dominate in PLL additive noises $\delta V_{\mathrm{add}}^{f_{\mathrm{het}}+f_{\mathrm{chip}}}$. Its contribution to the delay estimate $\delta\tau_{\mathrm{shot}}$ is given by plugging Eq. (5.12) and the third term in Eq. (5.9) into the second term of Eq. (5.11),

$$\begin{aligned}\widetilde{\delta\tau}_{\mathrm{shot}} &= \frac{\sqrt{2}}{2m_{\mathrm{prn}}f_{\mathrm{chip}}} \cdot \frac{\sqrt{2}\widetilde{\delta V}_{\mathrm{shot}}}{A_c} \\ &= \frac{\sqrt{2}}{2m_{\mathrm{prn}}f_{\mathrm{chip}}} \cdot \widetilde{\delta\phi}_{\mathrm{shot}},\end{aligned} \tag{5.13}$$

where $\widetilde{\delta\phi}_{\mathrm{shot}}$ is the shot noise contribution to the phase extraction of a heterodyne beatnote. Assuming one QPR is invested for the PRNR, $10\,\mathrm{pm}/\sqrt{\mathrm{Hz}}$ is transformed to a phase noise of $59\,\mu\mathrm{rad}/\sqrt{\mathrm{Hz}}$ via the beam wavelength. Finally, based on $m_{\mathrm{prn}} = 0.10\,\mathrm{rad}$ and $f_{\mathrm{chip}} = 1.6\,\mathrm{MHz}$, $\widetilde{\delta\tau}_{\mathrm{shot}}$ is estimated at $0.26\,\mathrm{ns}/\sqrt{\mathrm{Hz}}$, which corresponds to the range of $7.8 \times 10^{-2}\,\mathrm{m}/\sqrt{\mathrm{Hz}}$.

5.3.2 *Data communication*

Apart from PRNR, this section focuses on data communication. As depicted in Figure 5.1, the transmitter side of a PM encodes binary data (i.e., PM science data + coding check symbols) via XOR operation. This encoding is visualized in Figure 5.4. The receiver side correlates the received PRN code with data encoded (dashed yellow) with a local copy of it without data (blue). After coherently integrating the correlation over a data-bit window, the sign of the integrated correlation tells us the encoded data.

RS coding has been implemented in our design, and the following analysis relies on RS coding, though the coding technique is not decided yet. This section assumes the ideal additive white Gaussian noise (AWGN) case for analytical and numerical investigations unless there is a remark.

Using the error function, bit error rate (BER) of BPSK without RS coding is formulated in a simple form,

$$P_{\mathrm{b}}^{\mathrm{raw}} = \frac{1}{2}\mathrm{erfc}\left(\sqrt{\frac{E_b}{N_0}}\right), \tag{5.14}$$

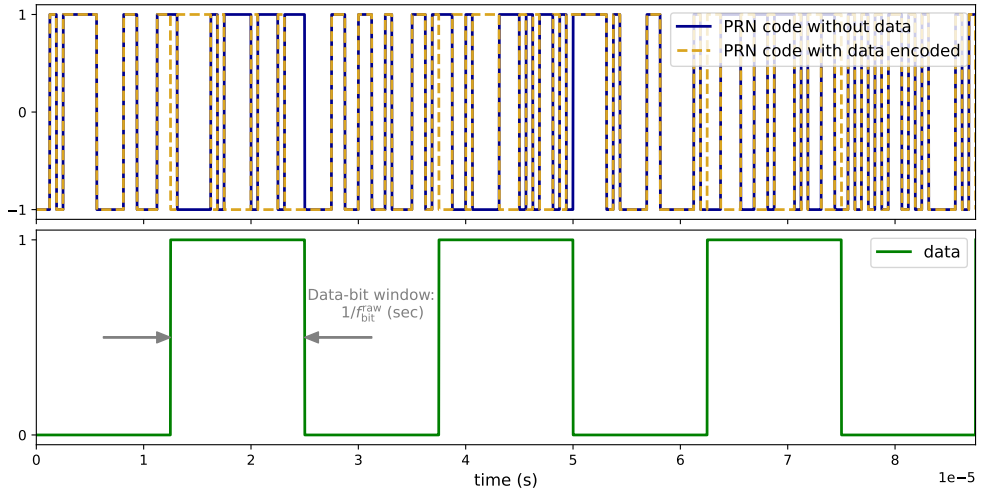

FIGURE 5.4: Data encoding on PRN code. The current nominal parameter set from Table 5.1.

where energy-per-bit-to-noise-density ratio (E_b/N_0) is in units of a linear magnitude, which is related to the normal E_b/N_0 unit of dB as dB $= 10\log_{10}$(linear mag.).

RS coding represents data stream with elements called *symbols* that are m_{rs}-bit values. Based on symbols, two values, as described in Table 5.1, parameterizes RS coding and determine its performance: the number of symbols per codeword n_{rs} and the number of symbols per data k_{rs}. Hence, one codeword invests $(n_{\text{rs}} - k_{\text{rs}})$ symbols for error correction codes. As a result, the number of symbol errors RS coding can correct within one codeword is,

$$t_{\text{rs}} = \frac{1}{2}(n_{\text{rs}} - k_{\text{rs}}). \tag{5.15}$$

BER improved with such corrections via RS coding can be expressed as a function of a raw symbol error rate P_s^{raw},

$$P_b^{\text{RS}}(n_{\text{rs}}, k_{\text{rs}}) \approx \frac{1}{m_{\text{rs}}}\frac{1}{n_{\text{rs}}}\sum_{l=t_{\text{rs}}+1}^{n_{\text{rs}}} l\binom{n_{\text{rs}}}{l}s^l(1-s)^{n_{\text{rs}}-l}, \tag{5.16}$$

$$s = 1 - (1 - P_s^{\text{raw}})^h, \tag{5.17}$$

$$h = m_{\text{rs}}/\log_2 M, \tag{5.18}$$

where M is the modulation order. Under BPSK, $M = 2$ and $P_s^{\text{raw}} = P_{\text{b}}^{\text{raw}}$.

Eq. (5.16) tells us the improvement of BER via RS(n_{rs},k_{rs}), plotted in Figure 5.5 with parameters in Table 5.1. The theoretical prediction (orange) is confirmed by a numerical experiment (blue circle) [3,4]. This shows that, with this parameter set under the ideal AWGN case, the raw BER without RS coding must be below around 5.6×10^{-3} to achieve 10^{-6} after the decoding.

3 Numerical experiment's algorithm: **1.** Generate an RS codeword in bits from data in symbols, from which a codeword stream with whatever length is also generated; **2.** Based on a given BER without RS coding, bit errors are injected into positions randomly chosen with uniform distribution; **3.** Pick up one codeword from the whole stream, convert it to symbols, and compute the number of symbol errors within the codeword; **4.** If the number of symbol errors exceeds t_{rs}, the number of bit errors in the codeword is added to the total number of bit errors; **5.** Repeat 3 and 4 for all codewords; **6.** Compute a final BER from the total number of bits and bit errors.

4 Note that step 4 assumes that the RS decoder returns the raw codeword without changes when it fails to decode data, which is not strictly true. In addition, a possible conversion from the original codeword into another codeword due to errors is neglected.

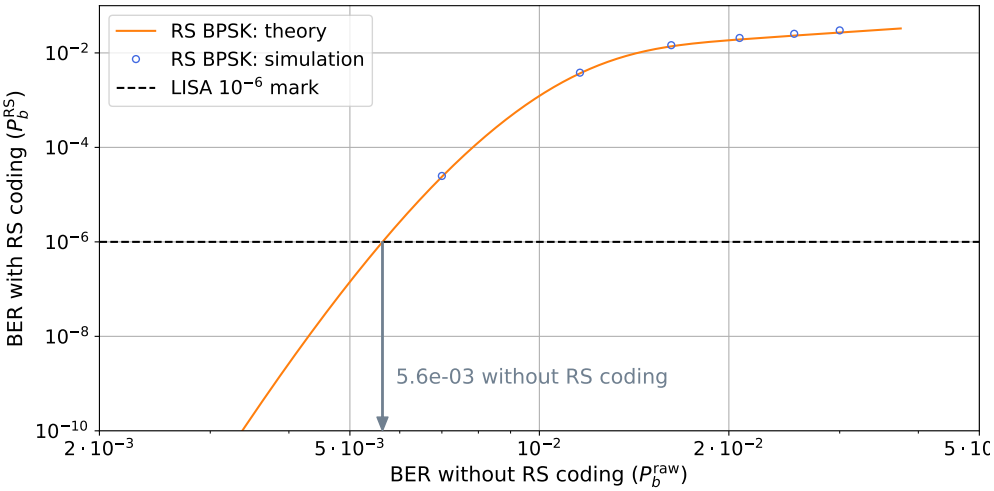

FIGURE 5.5: Comparison of BER with and without RS coding. $n_{\mathrm{rs}} = 255$, $k_{\mathrm{rs}} = 205$, and $m_{\mathrm{rs}} = 8$. The theoretical prediction by Eq. (5.16) (orange) is compared with the numerical experiment (blue circle).

To place the analytical form in the context of LISA, E_b/N_0 in dB can be related to carrier-to-noise-density ratio (C/N_0) of a carrier beatnote in dB Hz and/or a phase noise floor in rad/$\sqrt{\mathrm{Hz}}$,

$$\begin{aligned} E_b/N_0 &= \frac{1}{f_{\mathrm{bit}}^{\mathrm{raw}}} \frac{C_{\mathrm{prn}}}{N_0} \\ &\approx \frac{m_{\mathrm{prn}}^2}{f_{\mathrm{bit}}^{\mathrm{raw}}} \frac{C_{\mathrm{het}}}{N_0}, \\ &= \frac{m_{\mathrm{prn}}^2}{f_{\mathrm{bit}}^{\mathrm{raw}}} \cdot 20 \log_{10} \left(1/\widetilde{\phi}\right). \end{aligned} \tag{5.19}$$

BER with and without RS coding can be computed as a function of C/N_0 of the carrier-carrier beatnote or a phase noise floor $\tilde{\phi}$ from Eq. (5.14), Eq. (5.16), and Eq. (5.19); see Figure 5.6. A shot noise floor for a single QPR in a long-arm interferometer [52] is also plotted as a reference [5]. This figure suggests that RS coding is not necessary in the science mode in the ideal AWGN case. However, the real noise feature would be far from pure Gaussianity. Considering the dramatic change of BER with noise floor and property, experimental investigations are necessary to estimate actual BER, keeping the AWGN analysis provided in this section as a reference.

5 According to the performance model [52], a shot noise level for a long-arm interferometer, composed of four QPR, is 5 pm/$\sqrt{\mathrm{Hz}}$. Hence, 10 pm/$\sqrt{\mathrm{Hz}}$ is assumed for a single QPR.

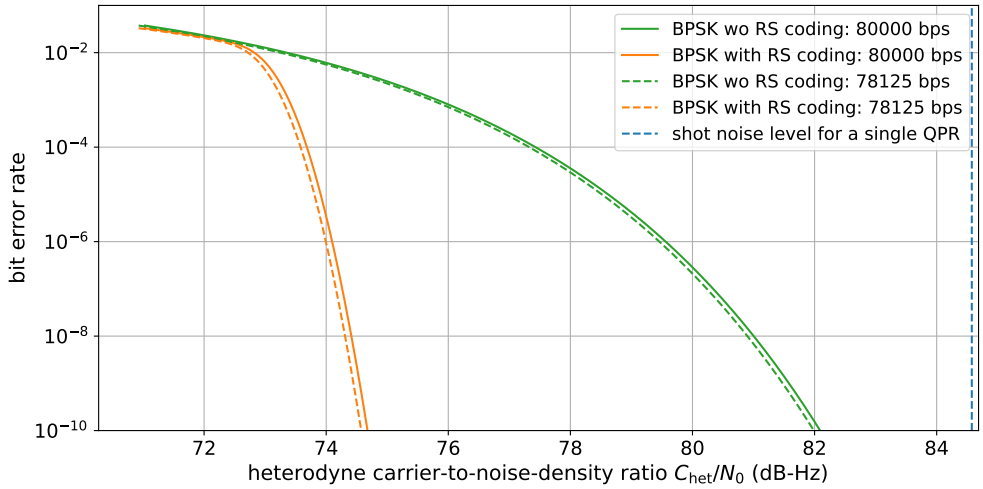

FIGURE 5.6: BER with and without RS coding as a function of C/N_0. A PRN modulation depth m_{prn} is 0.1 rad.

6 IMPACT ON PHASE TRACKING

Evolving from the iteration of the Hexagon experiment presented in Part II, PRN modulations and DLL were implemented on the setup to test inter-satellite absolute ranging and data communication. Before describing the primary tests with such new features, which will be presented in Chapter 7, one question can be raised at this stage: *Is any non-negligible impact of PRN modulations on phase tracking expected?* This chapter will discuss the point, reveal the significant impact of our conventional codes (that limits the carrier phase estimation to $O(100\,\mathrm{pm}/\sqrt{\mathrm{Hz}})$ accuracy), and discuss/implement/test alternative PRN codes to suppress the impact way below the $1\,\mathrm{pm}/\sqrt{\mathrm{Hz}}$ mark. Notation follows Table 5.1.

6.1 BPSK IN THE VIEW OF PHASE TRACKING

An impact of random BPSK is formulated in this section. PRN modulations are additive noise sources from the perspective of phase tracking, yielding a noise floor around a heterodyne beatnote as shown in Figures 1.4 and 1.5. This couples to a phase estimation via the ratio of the PRN amplitude spectral density $\widetilde{A}_{\mathrm{prn}}(f)$ to a root-mean-square (RMS) power of a heterodyne beatnote signal $A_{\mathrm{het,rms}}$ around the signal frequency f_{het},

$$\delta\widetilde{\phi}(f) = 2\sqrt{2}\cdot\widetilde{A}_{\mathrm{prn}}(f+f_{\mathrm{het}})/A_{\mathrm{het,rms}}, \tag{6.1}$$

where f is Fourier frequency; 2 is attributable to the mixing process in a phase-locked loop (PLL) and the fact that the PRN modulation is coherent with itself around f_{het}; and $\sqrt{2}$ is due to the two orthogonal PRN codes, c_{rx} and c_{tx} from Chapter 5.

The optical signal Eq. (1.2) contains multiple optical beatnotes. Hence, focusing on one of the beatnotes, there are two types of additive noise coupling mechanisms:

- *PRN mainlobe additive noise*: additive noise induced by the PRN modulation connected to the beatnote itself; e.g., a carrier beatnote to a carrier beatnote,
- *PRN sidelobe additive noise*: additive noise due to the PRN modulation leaked from another beatnote to the beatnote frequency; e.g., a carrier beatnote to a sideband beatnote.

6.1.1 *BPSK mainlobe additive noise*

The mainlobe additive noise is the well-recognized issue with BPSK and motivates the coding technique like Manchester encoding, introduced in the next section. A random BPSK double-sided power spectral density gives

$$\tilde{A}^2_{\mathrm{BPSK}}(f; A_{\mathrm{het,rms}}, f_{\mathrm{het}}) = \frac{(A_{\mathrm{het,rms}}\cdot m_{\mathrm{prn}})^2}{2f_{\mathrm{chip}}}\cdot \mathrm{sinc}^2\left(\frac{|f-f_{\mathrm{het}}|}{f_{\mathrm{chip}}}\right), \tag{6.2}$$

where the sinc function is defined by,

$$\mathrm{sinc}(x) = \begin{cases} 1, & \text{at } x = 0, \\ \sin(\pi x)/(\pi x), & \text{at } x \neq 0. \end{cases} \tag{6.3}$$

Substituting $\widetilde{A}_{\mathrm{BPSK}}$ to $\widetilde{A}_{\mathrm{prn}}$ in Eq. (6.1), the BPSK mainlobe coupling to phase tracking is derived,

$$\begin{aligned} \delta\widetilde{\phi}_{\mathrm{BPSK,main}}(f) &= 2\sqrt{2} \cdot \widetilde{A}_{\mathrm{BPSK}}(f + f_{\mathrm{het}}; A_{\mathrm{het,rms}}, f_{\mathrm{het}}) / A_{\mathrm{het,rms}} \\ &= 2\frac{m_{\mathrm{prn}}}{\sqrt{f_{\mathrm{chip}}}} \cdot \mathrm{sinc}\left(\frac{f}{f_{\mathrm{chip}}}\right), \end{aligned} \tag{6.4}$$

which depends only on m_{prn} and f_{chip}; therefore, common for all heterodyne beatnotes. LISA-like parameters, m_{prn} of 0.1 rad and f_{chip} of 1.6 MHz, results in 158 µrad/$\sqrt{\mathrm{Hz}}$. The LISA normal requirement mark on carrier phase tracking (i.e., 1 pm/$\sqrt{\mathrm{Hz}}$) is transformed to about 5.9 µrad/$\sqrt{\mathrm{Hz}}$ via a beam wavelength 1.064 µm, which is two-order below the random BPSK mainlobe additive noise. Therefore, introducing the PRN modulation causes, if not treated, unacceptable deterioration of carrier phase tracking. Concerning the sideband beatnotes, its tracking error couples to performance via clock synchronization. This coupling scales with $\omega_{\mathrm{het}}/\omega_{\mathrm{sb},i}$, $\sim O(10^{-2})$ in LISA; hence, there is still some margin.

6.1.2 *BPSK sidelobe additive noise*

The sidelobe additive noise is characteristic of the LISA-like optical signal with multiple beatnotes in Eq. (1.2). The leak of the PRN modulation on a heterodyne signal 0 to the heterodyne signal 1 is given by

$$\begin{aligned} \delta\widetilde{\phi}_{\mathrm{BPSK,side,01}}(f) &= 2\sqrt{2} \cdot \widetilde{A}_{\mathrm{BPSK}}(f + f_{\mathrm{het,0}} + f_{\mathrm{het,1}}; A_{\mathrm{het,rms,0}}, f_{\mathrm{het,0}}) / A_{\mathrm{het,rms,1}} \\ &= 2\frac{A_{\mathrm{het,rms,0}}}{A_{\mathrm{het,rms,1}}} \frac{m_{\mathrm{prn}}}{\sqrt{f_{\mathrm{chip}}}} \cdot \mathrm{sinc}\left(\frac{f + f_{\mathrm{het,1}}}{f_{\mathrm{chip}}}\right). \end{aligned} \tag{6.5}$$

Contrary to the mainlobe additive noise, the sideband beatnotes would become the focus of this coupling because the carrier beatnote would normally have much higher power than the sideband beatnotes. Following the optical signal Eq. (1.2), this particular case can be formulated,

$$\delta\widetilde{\phi}_{\mathrm{BPSK,side,c2sb}}(f) = 2\frac{J_0^2(m_{\mathrm{sb}})}{J_1^2(m_{\mathrm{sb}})} \frac{m_{\mathrm{prn}}}{\sqrt{f_{\mathrm{chip}}}} \cdot \mathrm{sinc}\left(\frac{f + \Delta f_{\mathrm{sb}}}{f_{\mathrm{chip}}}\right) \tag{6.6}$$

$$\approx 0 \quad \text{if } f \ll \Delta f_{\mathrm{sb}} \text{ and } f_{\mathrm{chip}} = \Delta f_{\mathrm{sb}}, \tag{6.7}$$

where $\Delta f_{\mathrm{sb}} = \Delta\omega_{\mathrm{sb}}/2\pi$. The first condition in the second line (i.e., $f \ll \Delta f_{\mathrm{sb}}$) is always met because f here is the in-band Fourier frequency, which is less than a few Hz, while Δf_{sb} is the order of MHz. This additive noise depends on parameters of both PRN and clock-sideband modulations. $\mathrm{sinc}\left(\frac{f+\Delta f_{\mathrm{sb}}}{f_{\mathrm{chip}}}\right)$ implies that the relative frequency between f_{chip} and Δf_{sb} is particularly important as computed in Eq. (6.7). Depending on other mission conditions, the optimal parameters of those modulations must be carefully designed.

6.2 ADAPTING PRN CODES

Section 6.1 raised the significant drawback with random BPSK from the perspective of phase tracking. Starting with normal BPSK, this section adapts a PRN code to the optical signal in Eq. (1.2), particularly in the LISA case. Assuming that the PRN modulation is an auxiliary function in a mission, the adaption here will be performed so that phase-tracking parameters, which are already optimized from other points of view in a mission, are intact [1].

The main criteria are listed below,

1. Low PRN power at DC: motivated by the mainlobe additive noise in Section 6.1.1,
2. $f_{\text{chip}} \approx \Delta f_{\text{sb}}$: motivated by the sidelobe additive noise in Section 6.1.2,
3. Data transfer: binary data is encoded on a PRN sequence to be transferred from one satellite to another.

Criterion 1 suggests that a PRN code needs to be somehow *balanced*, which means the code has a zero average by being composed of the same number of binaries (-1 and 1).

Criterion 2 implies that the PRN chip rate f_{chip} must be set as close to Δf_{sb} as possible. This means the clock cycles per PRN chip $n_{\text{chip}}^{\text{cycle}}$ must be deduced from the system clock rate f_s for digital signal processing,

$$n_{\text{chip}}^{\text{cycle}} = f_s / f_{\text{chip}} = [f_s / \Delta f_{\text{sb}}], \tag{6.8}$$

where the ceiling or floor will be selected so that the resulting chip rate becomes closer to Δf_{sb}.

Criterion 3 is expected to give a requirement on the data bit rate $f_{\text{bit}}^{\text{raw}}$ for intersatellite communication. This conditions the PRN chips per data bit,

$$n_{\text{bit}}^{\text{chip}} = f_{\text{chip}} / f_{\text{bit}}^{\text{raw}}. \tag{6.9}$$

When adapting the PRN codes with the criteria, a fundamental question would be, *over which length must the code be balanced?*. This length will be called "balancing length" for the rest of this section and be denoted by N_{balance}.

The most naive treatment would be to balance the full PRN code length, i.e., $N_{\text{blance}} = n_{\text{code}}^{\text{chip}}$. This cannot be accomplished based on usual shift registers because it has the odd length of $2n - 1$ with a non-zero average, like Gold codes for global positioning system (GPS). PRN codes with $2n$ length have been developed by Gerhard Heinzel to overcome this issue by numerical optimization. This type of PRN code will be called *a full-balanced (PRN) code* and has been used at the AEI for years [33, 53, 54], until this thesis.

However, this feature is spoiled once data is encoded because a data bit sequence is expected to be nearly random. This requires the balancing length to be shorter or equal to the data bit window $n_{\text{bit}}^{\text{chip}}$. Such a balancing length solves the code unbalance due to random data, and the maximum possible

1 In LISA, all beatnotes, including sideband-sideband beatnotes, should be within the heterodyne bandwidth of 5 MHz to 25 MHz. This frequency planning prefers the smaller sideband offset Δf_{sb} as long as sideband-sideband beatnotes are well apart from carrier-carrier beatnotes. All considered, the current nominal sideband offset is 1 MHz.

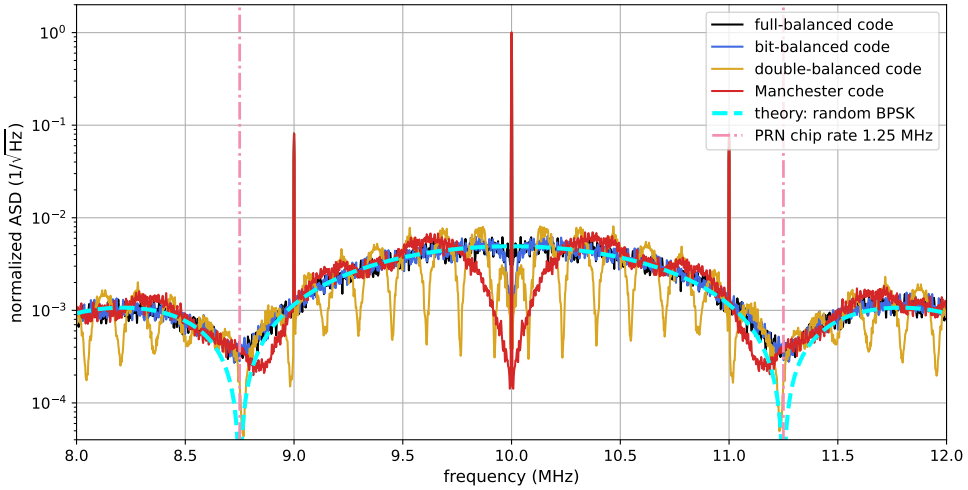

FIGURE 6.1: Normalized ASDs of heterodyne beatnotes with different PRN codes and random data encoded. $\Delta f_{\mathrm{sb}} = 1\,\mathrm{MHz}$. The theory is from Eq. (6.2). The 2^n parameter set from Table 5.1.

length $n_{\mathrm{bit}}^{\mathrm{chip}}$ keeps the largest number of possible chips, which eases orthogonalizing multiple PRN codes in a mission (i.e., six for LISA). This code will be referred to as *a bit-balanced (PRN) code*.

Alternatively, *Manchester code* would be a solution candidate where one chip is split into two (-1 and 1). This corresponds to the balancing length of two PRN chips. In this case, the original PRN chip rate must be halved to fit the fixed sideband offset following Eq. (6.8). Then, the derived original chips are split into two, resulting in the same code length. Note that Manchester coding, in turn, could cause the potentially significant degradation of code orthogonality because of the much smaller number of possible chip combinations.

Finally, an unexpected peak at f_{chip} was numerically observed in the spectrum of a beatnote signal with low-pass filtered PRN codes. This remains to be investigated, but criterion 2 above is not optimal if such a peak is actual. *A double-balanced (PRN) code*, proposed by Pascal Grafe, could be used for this purpose. In this code, the first half of the data-bit window is balanced, which is repeated in the second half. As a result, this results in notches at some integer multiples of the data-bit rate $f_{\mathrm{bit}}^{\mathrm{raw}}$ away from the beatnote frequency; hence, the sideband beatnotes would be placed at one of the notches.

The four PRN codes are summarized in Table 6.1, and Figure 6.1 shows normalized ASDs of the LISA-like signals with the PRN codes, the sideband beatnotes, and random data encoded. The noise term δI in Eq. (1.7), including shot noise, RIN, and PR noise, is not considered.

TABLE 6.1: Different PRN code types. Notice that the number of possible chip combinations for the full-balanced code $2^{**}n_{\mathrm{bit}}^{\mathrm{chip}}$ is not strictly true; however, the condition on this code type is applied to the full code, while one data bit is the scope here. Thereby, focusing on an arbitrary bit, the "possible" combination (i.e., no condition) is applied in this context.

Code	Balancing length $\mathrm{N_{blance}}$	Balanced (with data)	Possible chip combinations per bit	Comment
full-balanced	$n_{\mathrm{code}}^{\mathrm{chip}}$	False	$2^{**}n_{\mathrm{bit}}^{\mathrm{chip}}$	Used in [33, 53, 54]
bit-balanced	$n_{\mathrm{bit}}^{\mathrm{chip}}$	True	${}_{n_{\mathrm{bit}}^{\mathrm{chip}}}\mathrm{C}_{n_{\mathrm{bit}}^{\mathrm{chip}}/2}$	
double-balanced	$n_{\mathrm{bit}}^{\mathrm{chip}}/2$	True	${}_{n_{\mathrm{bit}}^{\mathrm{chip}}/2}\mathrm{C}_{n_{\mathrm{bit}}^{\mathrm{chip}}/4}$	
Manchester	2	True	$2^{**}\left(n_{\mathrm{bit}}^{\mathrm{chip}}/2\right)$	

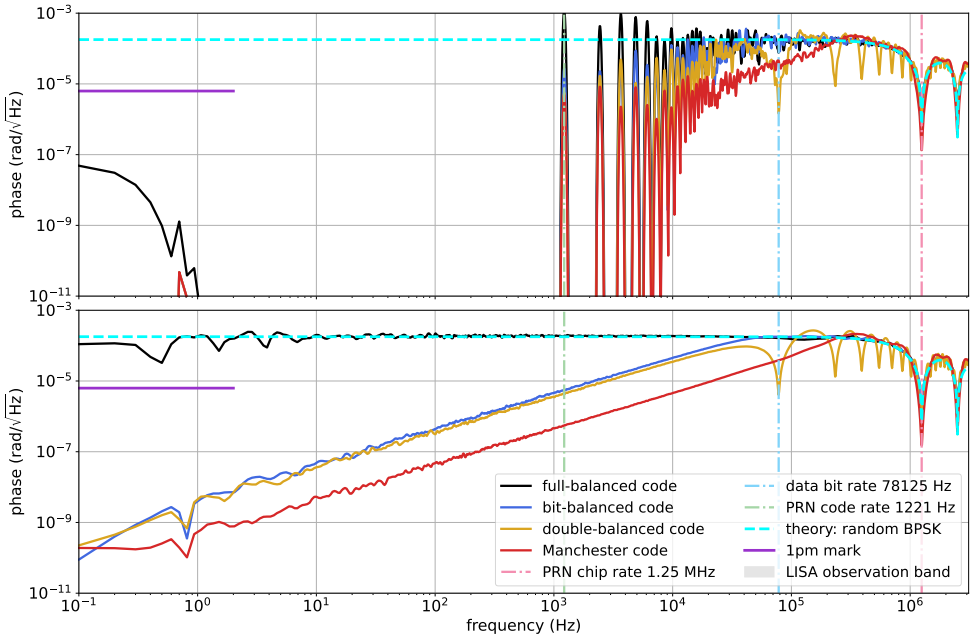

FIGURE 6.2: Simulated PRN mainlobe additive noise. **Top:** noises without random data encoded. **Bottom:** noises with random data encoded. The bump below 1 Hz in the top is artifacts of ASD computation. The 2^n parameter set from Table 5.1.

Figure 6.2 shows the simulation of the mainlobe additive noise coupling of different PRN codes, corresponding to Eq. (6.4). All codes have zero power below the full code rate; however, the data encoding recovers the noise floor of the random BPSK with the full-balanced code (black and dashed-cyan). The other three codes (blue, yellow, and red) attenuate noise powers toward low frequencies even with random data encoded because the balancing length is shorter than the data-bit length (i.e., $N_{\mathrm{balance}} \leq n_{\mathrm{bit}}^{\mathrm{chip}}$). All of the three meet the LISA mark of $1\,\mathrm{pm}/\sqrt{\mathrm{Hz}}$ (magenta) with enough margin in the LISA band (a grey area).

Figure 6.3 shows the impact of the different numbers of possible chips on auto-correlations as a function of lags in PRN chip. The correlations integrated over the full PRN-code length (i.e., coherent sum over the data-bit window + incoherent integration over the full length) are plotted here. The flat correlation background is observed in the full- and bit-balanced codes because they include no internal periodicity. On the other hand, oscillations/bumps are observed in double-balanced and Manchester codes, every $n_{\mathrm{bit}}^{\mathrm{chip}}$ and 2, respectively. In particular, the double-balanced code shows strong peaks of around 0.5 at the lags half-data-bit away from the alignment. This could cause the wrong acquisition delay of DLL. Nevertheless, none would be excluded from candidates for a final code design only based on the simulated correlation property without experimental investigations.

Figure 6.4 shows PRN sidelobe additive noises as functions of a clock-sideband modulation depth m_{sb} (left) and a clock-sideband offest frequency Δf_{sb}. This is common for the two PRN code types. The noise in sideband PLLs can be further suppressed by combining usb-usb and lsb-lsb beatnotes in Eq. (1.2). Blue is the case only with the single sideband (SSB), while yellow is the worst-case performance with the double sideband (DSB) where the improvement is limited by a factor of $\sqrt{2}$. The left panel shows that the SSB case needs the modulation depth of 0.7 rad, corresponding to 25 % for sidebands. This is a great reduction of laser power invested for the carrier signal. Hence, the most efficient way to reduce this noise is to manipulate

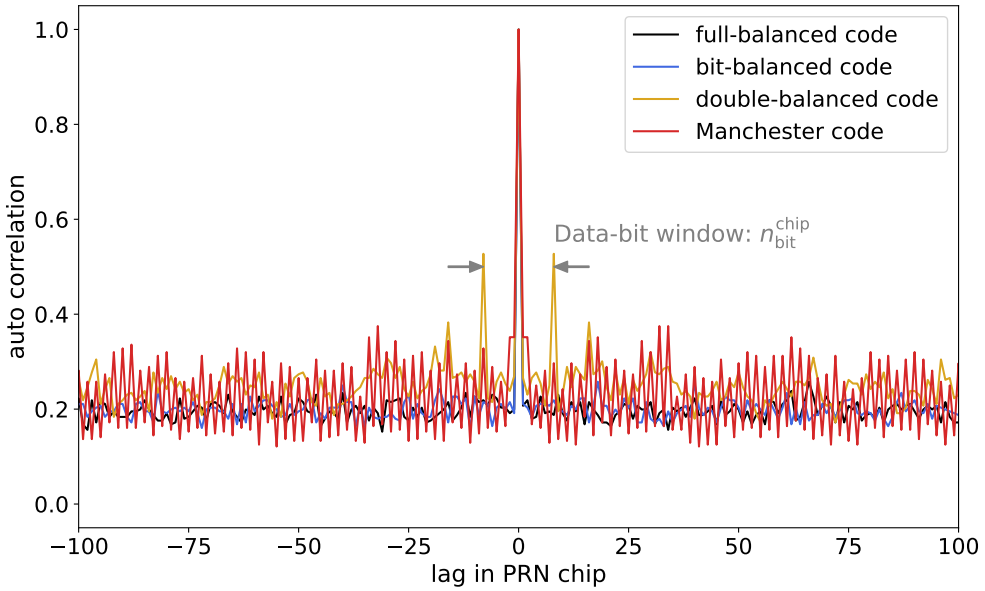

FIGURE 6.3: Auto correlations of different PRN codes. To focus on an inherent code property, pure codes are analyzed without filtering by a band-pass filter in Figure 2.7. The 2^n parameter set from Table 5.1.

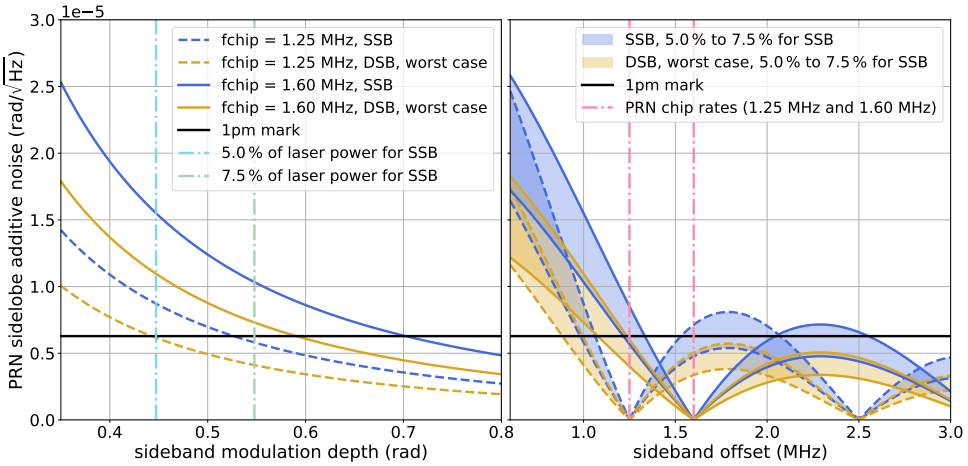

FIGURE 6.4: PRN sidelobe additive noise as a function of the clock-sideband modulation depth (left) or the clock-sideband offset frequency (right). The bit-balanced code is assumed.

the relationship between the PRN chip rate f_{chip} and the sideband frequency offset Δf_{sb}, as shown on the right. The offset between the two frequencies is preferred to be less than 300 kHz assuming the SSB case with 5 % beam power for SSB as the worst scenario [2].

6.3 EXPERIMENTAL DEMONSTRATION

The PRN mainlobe and sidelobe additive noises were experimentally demonstrated in separate setups. The full-balanced and bit-balanced PRN codes, numerically developed by Gerhard Heinzel, were implemented on our PMs. Only the 2^n parameter set from Table 5.1 has been implemented on the PMs for this thesis. The PMs were equipped with the DAC boards to generate PRN sequences according to the PM clocks. All measurements in this section share the PRN modulation depth m_{prn} of 0.1 rad, corresponding to 1 % of laser power. To be clear, the PRN chip rate and data bit rate were 1.25 MHz and 78 125 Hz because of the 2^n parameter set. A description of the encoded data can be found in Section 7.4.

2 As already mentioned to motivate the double-balanced code, a spurious peak was numerically observed at f_{chip}, once the PRN code is low-pass filtered. Depending on the conclusion, the description here would change.

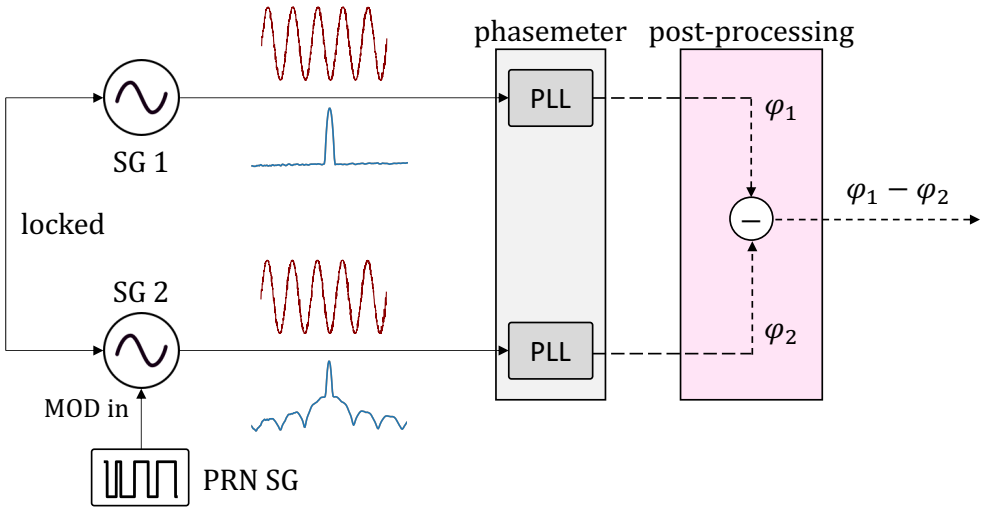

FIGURE 6.5: Electrical setup to probe the PRN mainlobe additive noise. Red and blue visualize signals in time and frequency domains, respectively.

6.3.1 *Mainlobe additive noise*

A dedicated electrical setup was configured to probe the mainlobe additive noise; see Figure 6.5. Two commercial signal generators were locked to each other, and both generated radio-frequency (RF) sinusoidal signals, as mimics of carrier beatnotes, connected to different channels of a phasemeter. One of the signal generators was phase-modulated by a PRN code sequence. The impact of this PRN phase modulation on phase tracking can be revealed by taking a difference between the two phases in post-processing. The sensitivity of this setup is limited by the quality of the lock between the two signal generators. To minimize the coupling of this noise source, a relatively low RF frequency, i.e., 6.5 MHz, was used. Notice that the PRN mainlobe additive noise does not depend on this frequency, according to Eq. (6.4).

Figure 6.6 shows the results of residual phase spectral densities in the LISA observation band. Grey is the area below the sensitivity of this setup. No impact was, as expected, recognized from the full-balanced PRN code without data encoded (dashed-black). However, as numerically demonstrated in Figure 6.2, this balancing was spoiled with random data encoded, and the white noise floor predicted by the random BPSK appeared around 129 µrad/$\sqrt{\text{Hz}}$ (solid-black and dashed-cyan). Finally, the bit-balanced PRN code overcame this white noise floor even with random data and returned to the testbed sensitivity (blue). The ASD of the bit-balanced code with data is proportional to Fourier frequency (see Figure 6.2); hence, achieving sub-pm performance around 1 Hz would guarantee that the 1 pm/$\sqrt{\text{Hz}}$ mark is accomplished over the LISA band.

6.3.2 *Sidelobe additive noise*

The PRN sidelobe additive noise was demonstrated using the 2PM2S topology, same as Eq. (4.21). The measurements were taken with different sideband frequency offset Δf_{sb} to demonstrate the dependency of this noise coupling on the relation between Δf_{sb} and the PRN chip rate f_{chip}. The clock-sideband modulation depth was relatively moderate, i.e., 0.4 rad, corresponding to 4 % of a beam power for each sideband.

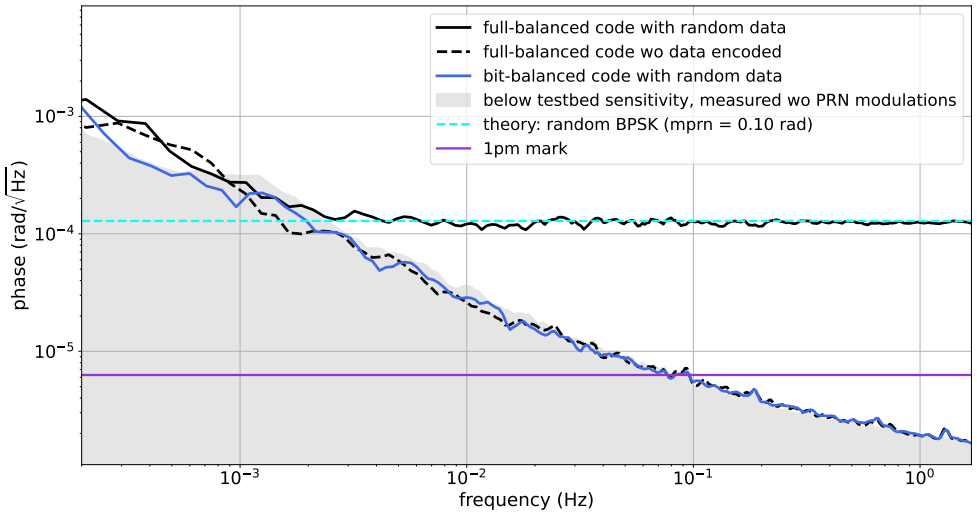

FIGURE 6.6: Measured PRN mainlobe additive noise with different codes.

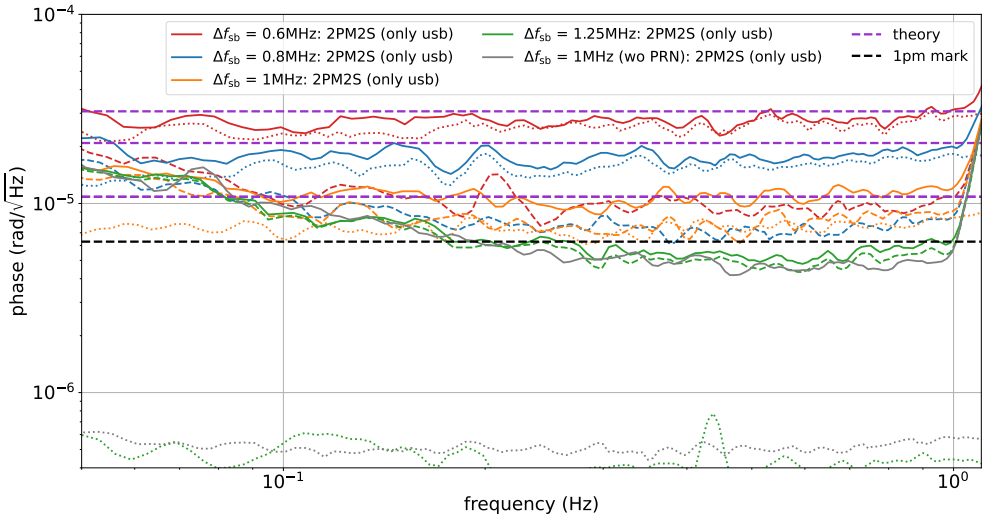

FIGURE 6.7: Measured PRN sidelobe additive noise with different sideband offset frequencies. The bit-balanced code was used. For each measurement (red, blue, orange, green, and grey), solid and dashed curves show the performance using SSB and DSB, respectively. Dotted curves are null combinations between opposite sideband beatnotes, i.e., (usb+lsb)/2.

Figure 6.7 shows the results of clock synchronization between the two independent PMs via differential clock signals extracted from the sideband beatnotes. Solid and dashed curves differ between the phases at the two phasemeters after clock synchronization in the SSB and DSB modes, respectively. The SSB mode is limited by the corresponding sidelobe noise floors in theory (dashed-magenta). This can also be measured by a null combination between the usb-usb and lsb-lsb beatnotes (dotted curves). The performance improvements, at least, by a factor of $\sqrt{2}$ were observed in the DSB mode. The smaller sideband offsets resulted in better suppression ratios, which might be because the coherence of PRN codes at opposite sideband beatnote frequencies was better maintained with lower dispersions through the system.

6.4 SUMMARY

This chapter presented the impact of PRN modulations on phase tracking as an intermediate step from clock synchronization with TDIR in Chapter 4 to absolute ranging with PRNR in Chapter 7. This included the model of such an PRN impact, the proposal of the new PRN codes, and experimental demonstrations of different noise couplings and their suppressions. The PRN-induced additive noise was formulated in the frame of LISA interferometric

signals with carrier-carrier beatnotes and sideband-sideband beatnotes. The degradation of the sideband phase-tracking couples to the detector performance via clock synchronization. This study revealed that the former PRN codes at the AEI (i.e., the full-balanced code) spoiled the carrier phase-tracking performance to $129\,\mu\mathrm{rad}/\sqrt{\mathrm{Hz}}$ with the modulation depth of 0.1 rad once random data is encoded on PRN codes. This unacceptable noise coupling, concerning the $6\,\mu\mathrm{rad}/\sqrt{\mathrm{Hz}}$ requirement, can be highly suppressed by balancing codes over the data-bit length (i.e., the bit-balanced code) or even shorter, as shown in Figure 6.6. The noise coupling via sidebands was also demonstrated using the 2PM2S topology; see Figure 6.7. It turned out that the conventional 1 MHz offset of the sideband beatnotes from the carrier could impede the $1\,\mathrm{pm}/\sqrt{\mathrm{Hz}}$ mark, at least in the SSB mode. In the author's view, it would be beneficial to design the entire system so that requirements can be met in the SSB mode because the DSB operation could be prohibited for some interferometers during some mission periods; see Appendix D.1. To make sideband readout shot-noise-limited, the frequency offset needs to be well selected, together with the PRN code type.

7

ABSOLUTE RANGING IN THE HEXAGON

Laser frequency noise in LISA needs to be significantly suppressed using TDI, which relies on the information of intersatellite light travel times and timer deviations. Such a proper input to TDI is called pseudo-range $R_{ij}^{\tau_m}$: the difference between the local clock time of the receiving SC at the event of reception of a beam, and the local clock time of the transmitting SC at the event of emission of the beam [29],

$$R_{ij}^{\tau_m}(\tau) = \tau_j^{\tau_m}(\tau - d_{ij}(\tau)) - \tau_i^{\tau_m}(\tau), \tag{7.1}$$

d_{ij} is the intersatellite light travel time from SC j to SC i.

PRNR is a baseline method to provide TDI with the absolute range, while TDIR, demonstrated in Chapter 4, acts as an independent ranging monitor using science data. The latter is affected by secondary noises in phase readout and GW signals and requires a long averaging time to produce a single estimate with sub-meter accuracy. In this sense, PRNR is expected to be a robust and continuous absolute-ranging monitor. Therefore, in the LISA data analysis pipeline, PRNR will run in the mainstream, while TDIR will be located in the cross-checking stream.

The requirement on PRNR noise power over an on-ground data rate is 1 m rms, as introduced in Chapter 5. There was a series of studies on the PRNR precision at the AEI and the Australian National University (ANU) around ten years ago. They showed sub-meter precisions under LISA-like beam powers [54, 53, 33] or code interferences with independent clocks [55, 51, 50].

However, the previous research focused on in-band stochastic fluctuations of PRNR, while PRNR needs to function as *absolute* ranging that requires the study on absolute values, in addition to fluctuations on top of them. The main scope of this chapter is the demonstration of extracting the information of such an absolute range from PRNR in the Hexagon, but also in a way as applicable to LISA as possible.

Two fundamental obstacles impede the absolute ranging with PRN modulations: PRNR ambiguity and PRNR bias. The former is $O(100\,\mathrm{km})$, determined by the finite code repetition rate, as mentioned in Chapter 5. The latter is $O(100\,\mathrm{m})$, which can be defined as any contribution to PRNR observables except for the pseudo-ranges.

Section 7.1 configures a simple setup with two PMs (i.e., the 2PM2S topology from Figure 3.3). This covers most of the concepts of absolute ranging in the Hexagon. The extension of the experiment to the 3PM3S topology is the future work. Section 7.2 provides analytical models of the experiment, which their experimental demonstrations will follow in Section 7.3. Apart from PRNR, the preliminary investigation of data communication will also be discussed in Section 7.4.

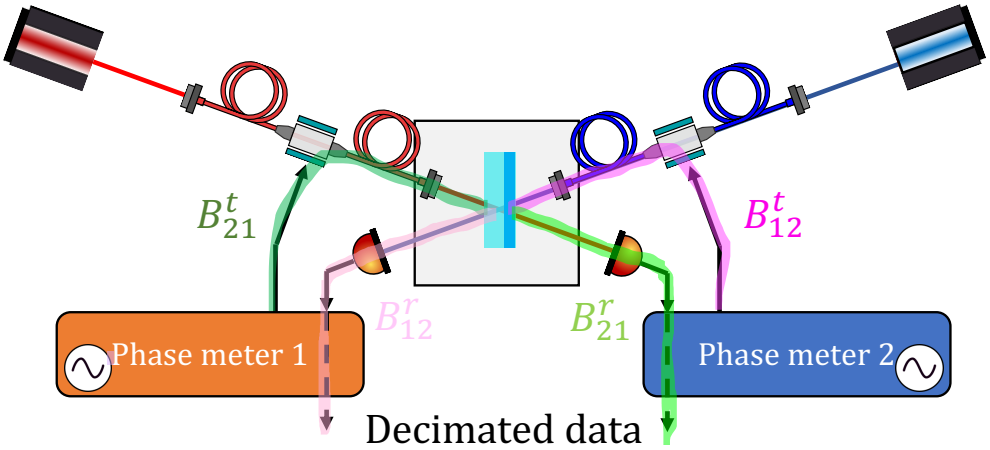

FIGURE 7.1: Schematic of the bidirectional ranging in the Hexagon. Ranging biases are categorized into two: *receiver bias* and *transmitter bias* with superscripts of r and t, respectively.

7.1 SETUP

The goal of this section is to demonstrate the entire on-ground processing for PRNR: resolving the PRNR ambiguity, estimating the ranging bias in the received-PRNR estimate with the local, and applying PRNR to the timestamp adjustment in clock synchronization, instead of TDIR discussed in Chapter 4.

Just a re-naming of the 2PM2S topology, from Figure 3.2, in the view of PRNR.

For this purpose, a bidirectional-ranging setup was configured; see Figure 7.1. This corresponds to a LISA intersatellite link without an intersatellite distance: the combining BS on the two SCs converges on a single BS. Therefore, an ideal PRNR estimate in the Hexagon is an intact differential clock signal: the pseudo-range with $d_{ij} = 0$ in Eq. (7.1). Any physical (i.e., optical, electrical, or digital) delays in PRNR observables are categorized into an extra delay sensed by PRN signals, i.e., *ranging bias*. In Figure 7.1, one-way bias is split into two parts, having a combining BS as a boundary: the transmitter side and the receiver side. The bias on each side will be referred to as *transmitter bias* and *receiver bias*, respectively. They are expected to have different characteristics, as will be discussed later.

The OB must be able to be constructed from the design with negligible errors from the PRNR perspective.

Notice that the bias estimation in this section (or in the Hexagon in general) is not 100 % translatable to LISA, where a transmitted beam does not share the same optical path on the OB with a local beam to interfere with a received beam. However, it is only a difference in picometer-stable optical path lengths, which is "constant" for the sub-meter scale PRNR investigates. Thereby, the information of optical path lengths from an OB design can be taken into account in post-processing as a correction value. This simple process would be the only calibration the Hexagon cannot demonstrate.

7.2 MODEL

PRNR observables will be modeled in analytical forms below. Raw PRNR estimates have an ambiguity L_{code}, as mentioned in Section 5.2, due to the finite code length. Hence, the PRNR estimates need to be combined with other monitors in any case to resolve the ambiguity; TDIR or ground observations, which comprise orbit determinations and MOC time correlations. In the Hexagon, TDIR is the only independent monitor from PRNR. Therefore, the

missing ambiguity offset a_{prn} must be derived from the initial timer offset estimate by TDIR (see Section 4.2),

$$a_{\text{prn}} = \text{round}\left[\delta\hat{\tau}_{i,0}/(L_{\text{code}}/c)\right] \cdot (L_{\text{code}}/c) \tag{7.2}$$

In the following formulation, PRNR ambiguity will be assumed to be already resolved.

7.2.1 *Measurements*

As described above, the Hexagon does not simulate an intersatellite light travel time, and an ideal PRNR estimate is a pure differential timer; hence, any physical light (or signal more in general) travel time is absorbed into a ranging bias B_{ij}. The PRN estimate $R_{ij}^{\text{prn},\tau_m}(\tau)$ is given by,

$$R_{ij}^{\text{prn},\tau_m}(\tau) = \tau_j^{\tau_m}(\tau - B_{ij}(\tau)) - \tau_i^{\tau_m}(\tau), \tag{7.3}$$

which corresponds to the replacement of d_{ij} in Eq. (7.1) with B_{ij}. The superscript "prn" is to clearly distinguish the PRN estimate from a TDIR counterpart below. Notice that the ranging bias B_{ij} was assumed time-variant.

Figure 7.1 decomposed the ranging bias into the transmitter and receiver sides,

$$B_{ij}(\tau) = B_{ij}^t + B_{ij}^r(\tau), \tag{7.4}$$

where the superscripts t and r represent the transmitter and receiver biases, respectively. Notice that the time dependency is only applied to the receiver bias. The transmitter side contains digital signal processing, electronics, cables, and stable optics (fibers, EOMs, optical paths on OB, etc.). Hence, it wouldn't drift by the scale that PRNR probes. Compared with the transmitter bias, some receiver biases are caused by more complex mechanisms mainly because PRN signals go through PLLs [1], as discussed in Section 2.3.1 or shown in Figure 5.1. Hence, the codes are also distorted and delayed by a PLL transfer function. This could yield the non-negligible time dependency of the receiver bias because the PLL transfer function scales with a heterodyne beatnote amplitude (see Eq. (2.1)), which would slowly drift over time.

This is an effective amplitude at the input of PLL; therefore, a beam power is not the only factor of the amplitude drift meant here. For example, the change of a heterodyne beatnote frequency, according to the LISA frequency plan [22], is another factor because of non-flat frequency responses of devices on the receiver side, like QPR.

Applying the timer model in Eq. (2.6) to Eq. (7.4), the four DLL observables (one received and local code tracking per PM) can be formulated as follows,

$$\begin{aligned} R_{ij}^{\text{prn},\tau_i}(\tau) &= \tau_j^{\tau_i}(\tau - B_{ij}(\tau)) - \tau_i^{\tau_i}(\tau) \\ &= \delta\tau_j^{\tau_i}(\tau - B_{ij}(\tau)) - B_{ij}(\tau) \quad \text{for DLL}_{\text{RX}}, \end{aligned} \tag{7.5}$$

$$\begin{aligned} R_{ii,j}^{\text{prn},\tau_i}(\tau) &= \tau_i^{\tau_i}(\tau - B_{ii,j}(\tau)) - \tau_i^{\tau_i}(\tau) \\ &= -B_{ii,j}(\tau) \quad \text{for DLL}_{\text{LO}}, \end{aligned} \tag{7.6}$$

where the local ranging bias is defined by,

$$B_{ii,j}(\tau) = B_{ji}^t + B_{ij}^r(\tau). \tag{7.7}$$

1 In addition to the PLL-based time dependency, featured in the later sections, transfer functions of other devices on the receiver side would have frequency-dependent group delays; QPRs or electronics on the PM analog BEE. Thereby, they would induce a time-dependent bias in conjunction with the heterodyne frequency change.

The index notation was slightly extended for the local-PRNR observable: the local code i is compared to itself after following its transmission path B^t_{ji} and the reception path of the received code j B^r_{ij}. Notice that the superscript τ_i representing the reference time frame is also added to the timer deviation in Eq. (7.5), in contrary to Section 2.5 and Chapter 4, to clarify the reference frame in the following formulation. In addition, it must be remarked that (especially receiver) biases depend on specific code sequences [56]; thereby, the receiver biases between the local and received codes are not identical. However, the analytical forms in this section neglect the effect, and this point will be revisited in Section 7.3.3 both numerically and experimentally.

Finally, the ranging estimate by TDIR and sideband measurements, discussed in Eqs. (4.10) and (4.12), is redefined by,

$$\begin{aligned} R^{\mathrm{tdir+sb},\tau_i}_{ij}(\tau) &= q_j(\tau - B_{ij}(\tau)) + \delta\hat{\tau}_{j,0} \\ &\approx \delta\tau^{\tau_i}_j(\tau - B_{ij}(\tau)) \end{aligned} \tag{7.8}$$

Notice that the same delay is assumed between the PRN code and GHz-clock sidebands in Eq. (7.8). This is an oversimplification, and a more decent model must be built in the future. Nevertheless, the simplification would be expected not to influence results significantly because it couples as a cross term with $\dot{q}_j \sim \mathcal{O}(10^{-7})$.

where the delay due to the trip of a clock signal from PM j to PM i B_{ij} is considered, which was omitted in the model in Chapter 4. Notice that TDIR also senses a non-common delay between the carrier signals at the two PMs, yielded after the combining BS. Hence, the interpretation of the initial timer offset $\delta\tau_{i,0}$ must be elaborated in this ranging context, being decomposed into two parts,

$$\delta\tau_{i,0} = \delta\tau_{i,0,\mathrm{PM}} + \Delta B^r_c, \tag{7.9}$$

where ΔB^r_c is such a non-common delay between the carrier phases on the different receiver sides and $\delta\tau_{i,0,\mathrm{PM}}$ denotes a pure time lag of the starting time of PM i from PM j. In the 2PM2S topology in the Hexagons, ΔB^r_c would be expected to be smaller than PRNR noise variances: First, a delay due to the system function of DPLL (see Eq. (2.4)) would be negligible, likely smaller than pico-second, in contrast to a group delay of its error function (see Eq. (2.5)); Second, the two carrier beatnotes share the same heterodyne frequency [2]; Third, all cables on the receiver sides were confirmed to share the same lengths between PMs.

7.2.2 *Round trip*

A round-trip measurement can be performed in this setup by combining PRN estimates at the two PMs. This acts as a functional test: the cancellation of differential clock signals in the two received-PRNR estimates and the estimation of the round-trip ranging biases by the two local-PRNR estimates. The success in this demonstration verifies the consistency of PRNR between the two PMs, which is a good intermediate step to the next experiment, "TDIR and PRNR".

To combine the received-PRNR estimates on two independent PMs, the estimate at the secondary PM $R^{\mathrm{prn},\tau_2}_{21}$ needs to be evaluated in the primary time frame τ_1. The first step is to express the received-PRNR estimate at the

2 In LISA, the carrier beatnotes at two SC facing each other have different heterodyne frequencies; hence, a non-flat response of a QPR would contribute to this term by the order of 1 m.

secondary PM $R_{21}^{\mathrm{prn},\tau_2}$ with the timer deviation of its driving clock against the primary,

$$\begin{aligned} R_{21}^{\mathrm{prn},\tau_2}(\tau) &= \delta\tau_1^{\tau_2}(\tau - B_{21}(\tau)) - B_{21}(\tau) \\ &= -\delta\tau_2^{\tau_1}\left(\tau_1^{\tau_2}(\tau - B_{21}(\tau))\right) - B_{21}(\tau), \end{aligned} \tag{7.10}$$

since

$$\delta\tau_i^{\tau_j}(\tau) = -\delta\tau_j^{\tau_i}\left(\tau_i^{\tau_j}(\tau)\right), \tag{7.11}$$

in general from Eqs. (2.6) and (2.8).

The second step is to transform the time frame with the TDIR-derived timer deviation $R_{21}^{\mathrm{tdir+sb},\tau_1}(\tau)$, same as done for clock synchronization in Chapter 4,

$$\begin{aligned} R_{21}^{\mathrm{prn},\tau_1}(\tau) &= R_{21}^{\mathrm{prn},\tau_2}\left(\tau + R_{12}^{\mathrm{tdir+sb},\tau_1}(\tau)\right) \\ &\approx -\delta\tau_2^{\tau_1}\left(\tau_1^{\tau_2}(\tau - B_{21}(\tau) + \delta\tau_2^{\tau_1}(\tau - B_{12}(\tau)))\right) - B_{21}(\tau) \\ &\approx -\delta\tau_2^{\tau_1}\left(\tau_1^{\tau_2}(\tau_2^{\tau_1}(\tau - B_{21}(\tau)))\right) - B_{21}(\tau) \\ &= -\delta\tau_2^{\tau_1}(\tau - B_{21}(\tau)) - B_{21}(\tau). \end{aligned} \tag{7.12}$$

The second line neglects the time-stamping by the TDIR-derived timer for ranging bias $B_{21}(\tau)$, assuming that the biases drift very slowly over time concerning the scale of a few seconds. In the third line, the cross term between $\dot{q}_2(\sim\mathcal{O}\left(10^{-7}\right))$ and $B_{12} - B_{21}(\sim\mathcal{O}\left(10\,\mathrm{ns}\right))$ was neglected.

Finally, the round-trip measurement can be formed by combining $R_{12}^{\mathrm{prn},\tau_1}(\tau)$ and $R_{21}^{\mathrm{prn},\tau_1}(\tau)$,

$$\begin{aligned} R_{121}^{\mathrm{prn},\tau_1}(\tau) &= R_{12}^{\mathrm{prn},\tau_1}(\tau) + R_{21}^{\mathrm{prn},\tau_1}(\tau) \\ &\approx \delta\tau_2^{\tau_1}(\tau - B_{12}(\tau)) - \delta\tau_2^{\tau_1}(\tau - B_{21}(\tau)) - (B_{12}(\tau) + B_{21}(\tau)) \\ &\approx 0 + \left(R_{11,2}^{\mathrm{prn},\tau_1}(\tau) + R_{22,1}^{\mathrm{prn},\tau_2}(\tau)\right). \end{aligned} \tag{7.13}$$

This shows that the timer deviations, including initial timer offsets, appear in anti-symmetric forms at the two PMs and cancel out in the round-trip combination. It leaves only a round-trip ranging bias $B_{12} + B_{21}$, which can be estimated via the sum of the local estimates $R_{11,2}^{\mathrm{prn},\tau_1}(\tau) + R_{22,1}^{\mathrm{prn},\tau_2}(\tau)$ in principle.

7.2.3 *TDIR vs. PRNR*

The round-trip measurement above works as a functional test of PRNR observables; however, it is still somewhat relative-ranging and does not fully function as a test of the absolute-ranging feature because the timer deviations cancel between the received-PRNR estimates. Furthermore, this test is complete even without ambiguity resolution. In addition, also concerning the bias estimation, the measurement tests the agreement between the received- and local-PRNR estimates in terms of the round-trip. However, a one-way bias needs to be derived ideally.

As modeled in Eq. (7.5), PRNR can estimate all contributions to a timer deviation $\delta\tau_j^{\tau_i}(\tau)$, including its initial timer offset. PRNR is expected to function as *absolute* ranging because of the feature. This is a significant difference from frequency measurements of sideband beatnotes, which required the assist by TDIR to get an initial constant; see Section 4.2.2.

An efficient way to verify the absolute-ranging feature of PRNR in the Hexagon would be to compare it with TDIR (+ sideband measurements), which was demonstrated at the LISA performance level in Chapter 4. The received-PRNR estimate at the primary PM, i.e., PM 1, can be compared with the TDIR estimate above,

The one at the secondary PM can also be compared, if needed, after the time-frame transformation in Eq. (7.10).

$$\begin{aligned} R_{12}^{\mathrm{prn},\tau_1}(\tau) &= \delta\tau_2^{\tau_1}(\tau - B_{12}(\tau)) - B_{12}(\tau) \\ &\approx R_{12}^{\mathrm{tdir+sb},\tau_1}(\tau) - B_{12}(\tau). \end{aligned} \tag{7.14}$$

Pseudo-range (in the Hexagon) can be defined by $R_{12}^{\mathrm{tdir+sb},\tau_1}$ because TDIR is bias-free. Hence, if the two ranging observables are compared, they differ by the ranging bias of B_{12}. The PRNR bias can be mostly removed by combining the received-PRNR estimate with the local,

In order not to inject the local-PRNR noise, the local-PRNR estimate must be somehow smoothened in advance for the actual application: polynomial fitting, low-pass filtering, etc.

$$\begin{aligned} R_{12,\mathrm{corr}}^{\mathrm{prn},\tau_1}(\tau) &= R_{12}^{\mathrm{prn},\tau_1}(\tau) - R_{11,2}^{\mathrm{prn},\tau_1}(\tau) \\ &\approx R_{12}^{\mathrm{tdir+sb},\tau_1}(\tau) - \Delta B_{12}^t. \end{aligned} \tag{7.15}$$

$$\Delta B_{ij}^t = B_{ij}^t - B_{ji}^t \tag{7.16}$$

The residual bias is the difference between the two transmitter biases ΔB_{12}^t, which will be referred to as a transmitter bias mismatch. Remarkable is the rejection of the time dependency of the biases by canceling the receiver biases between the received and local-PRNR estimates [3]. Concerning the transmitter biases, in an ideal case, the difference is negligible by design because all SC must be constructed based on the same design. Nevertheless, the on-ground calibration should be performed, and the measured difference must be noted as a correction value for post-processing. The Hexagon is currently not very strict with the same cable lengths, fiber lengths, etc, on the transmitter sides. The mismatch would amount to 10 ns or around 10 m in range as a ballpark. Hence, analogous to the on-ground calibration for LISA, the Hexagon requires calibration once before a test campaign.

Finally, the application of PRNR to clock synchronization is discussed. The descriptions above suggest that there are three PRNR-derived timer deviations: the ambiguity-resolved case $R_{12}^{\mathrm{prn},\tau_1}$ in Eq. (7.14), the bias-corrected case via the local estimate $R_{12,\mathrm{corr}}^{\mathrm{prn},\tau_1}$ in Eq. (7.15), and the further calibrated case via prior calibration, written by $R_{12,\mathrm{cal}}^{\mathrm{prn},\tau_1} (= R_{12,\mathrm{corr}}^{\mathrm{prn},\tau_1} + \Delta B_{12}^t)$. To think of the time-stamping with such PRNR estimations in a general manner, an arbitrary form $R_{ij,x}^{\mathrm{prn},\tau_i}$, including a PRNR noise term, is provided by,

$$R_{ij,x}^{\mathrm{prn},\tau_i}(\tau) = \delta\tau_j^{\tau_i}(\tau - B_{ij}(\tau)) + \Delta B_{ij}(\tau) + N_{ij}^{\mathrm{prn}}(\tau), \tag{7.17}$$

where ΔB_{ij} is the residual bias and N_{ij}^{prn} is the in-band stochastic noise of the received-PRNR with the order of magnitude of $\mathcal{O}\left(1\,\mathrm{ns}/\sqrt{\mathrm{Hz}}\right)$. Listed below are different ways to apply PRNR to the time-stamping, according to Eq. (4.13), to be demonstrated in later sections. "Formulation" expresses the estimated timer deviation $\delta\hat{\tau}_j^{\tau_i}$ as an input to time-stamping in each case:

The local-PRNR noise is expected to be averaged out with fitting or filtering, as mentioned in the previous sidenote.

- **Case 1 Simple application:** use the pure PRNR estimate $R_{ij,x}^{\mathrm{prn},\tau_i}(\tau)$. Apart from the discussion on ranging biases, this case is expected to

3 Remember that the dependency of ranging biases on actual codes is neglected in this formulation, as discussed below Eq. (7.7). The residual due to this effect will be discussed in Section 7.3.3.

limit the performance of clock synchronization above the $1\,\mathrm{pm}/\sqrt{\mathrm{Hz}}$ mark due to the in-band PRNR noise N_{ij}^{prn}. According to Eq. (4.13), the coupling of the ranging noise to the synchronized beatnote frequency is, to the first-order approximation, the product of the time derivative of the carrier beatnote and the ranging noise $\dot{\nu}_{c,i'j'}^{\tau_m}(\tau) \cdot N_{ij}^{\mathrm{prn}}(\tau)$. Formulation:

$$\delta\hat{\tau}_j^{\tau_i}(\tau) = R_{ij,x}^{\mathrm{prn},\tau_i}(\tau). \tag{7.18}$$

- **Case 2 Initial estimate:** use only the initial estimate $R_{ij,x}^{\mathrm{prn},\tau_i}(0)$ and combine it with sideband measurements, representing the time evolution of the timer deviation. This case eliminates the coupling of the in-band ranging fluctuations mentioned in Case 1. In the statistical view, the standard deviation of the ranging noise term over the full data rate $\mathrm{std}[N_{ij}^{\mathrm{prn}}]$ couples to the initial-offset estimate as-is. Formulation:

$$\delta\hat{\tau}_j^{\tau_i}(\tau) = q_j(\tau - B_{ij}(\tau)) + R_{ij,x}^{\mathrm{prn},\tau_i}(0). \tag{7.19}$$

- **Case 3 Averaged estimate:** use the averaged difference between the PRNR estimate and the integration of the sideband measurement for the initial-offset estimate [41]. This further suppresses the impact of the noise variance on the accuracy of the initial estimate by the number of averaged samples N_s, i.e., $\mathrm{std}[N_{ij}^{\mathrm{prn}}]/\sqrt{N_s}$. Assuming this is negligible against ΔB_{ij}, the PRNR performance in terms of clock synchronization would be expected to be limited by the ranging bias estimation. Formulation:

$$\delta\hat{\tau}_j^{\tau_i}(\tau) = q_j(\tau - B_{ij}(\tau)) + \mathrm{avg}[R_{ij,x}^{\mathrm{prn},\tau_i}(\tau) - q_j(\tau - B_{ij}(\tau))]. \tag{7.20}$$

In the description (also for Case 2), N_{ij}^{prn} is assumed to have a zero mean. If not, an additional offset will remain a (potentially non-negligible) contribution from the noise term.

- **Case 4 Kalman filter:** apply a Kalman filter to combine PRNR and sideband measurements to reduce the ranging noise. This enables the incorporation of proper noise models into the data processing. Contrary to the Hexagon, pseudo-ranges in LISA comprise not only the timer deviations but also the intersatellite light travel times. A Kalman filter can also be used to disentangle the two components via pseudo-ranges and ground observations [57, 58]; however, this is out of the scope of this thesis.

7.3 DEMONSTRATION

The modeled experiments were demonstrated in the 2PM2S topology in the Hexagon. Nominal test conditions, used commonly for measurements (if not specifically remarked), are listed in Table 7.1.

7.3.1 *Round trip*

As mentioned in Section 7.2.2, the round-trip measurement acts as an intermediate functional test toward applying PRNR to clock synchronization.

Figure 7.2 shows the result. The top panel plots the received-PRNR estimates at the two independent PMs. As expected from Eq. (7.10), the differential timer appears with opposite signs at the two PMs. The initial values are

TABLE 7.1: Nominal parameters for bidirectional ranging experiments in Section 7.3.

Parameter	Value / Condition
beam power level	$\mathcal{O}\,(100\,\mu W)$ for all beams
sideband offset frequency	1.25 MHz
sideband modulation depth	0.4 rad
sideband operation	SSB mode for clock sync.
PT frequency	37.5 MHz
PRN parameters	2^n parameter set from Table 5.1
PRN modulation depth	0.1 rad
PRN code type	bit-balanced code from Table 6.1
Data communication	random data encoded
TDIR operation	tone-assisted
TDIR tone amplitude	10 kHz
TDIR tone frequency	0.762 Hz (also see Section 4.4)

confined within the PRN ambiguity. The wrapping at the borders is already corrected by the method described in Appendix G; hence, the time series surpasses the ambiguity borders later.

The local-PRNR estimates can be found in the second panel. They are free from clock deviations and reveal the local ranging biases, according to Eq. (7.6). The ranging biases amount to around 400 m in this case, and most of them must be attributable to digital signal processing on FPGA. For example, the pre-DLL low-pass filter has a group delay of around 50 m in itself. Also, a relative delay between the driving counters for the $\mathrm{PRN}_{\mathrm{tx}}$ LUT and a LUT in $\mathrm{DLL}_{\mathrm{LO}}$ in Figure 5.1 could be significant: one clock cycle corresponds to 3.75 m because of the 80 MHz clock rate. The detailed bias budget remains to be created.

The third and bottom panels show the round-trip measurement by combining PRNR observables at the two PMs to verify Eq. (7.13). Note that the received-PRNR estimates (black) are less noisy because of ICC than the local (purple). As mentioned above, filtering is necessary for the local estimates because a slow component is only needed to remove the significant bias from the received-PRNR estimates. In this example, a FIR low-pass filter with the naively-selected corner of 10 mHz was applied (pink). As shown in the bottom panel, the round-trip bias could be estimated with the remaining offset of 66.8 cm. The residual offset was attributed to ICC; see Section 7.3.3.

This experiment successfully confirmed the fundamental functions and the consistency between the two PMs: the sum of the two received-PRNR estimates properly canceled timer deviations and left the round-trip bias, which could be mostly removed via the local-PRNR estimates.

7.3.2 *TDIR vs. PRNR*

The round-trip measurement is, as mentioned, somewhat relative-ranging because the timer deviation, including the initial offset, is canceled between the two PMs. Also, it senses all biases in the setup; thereby, correcting the biases from individual received-PRNR estimates cannot be evaluated. This

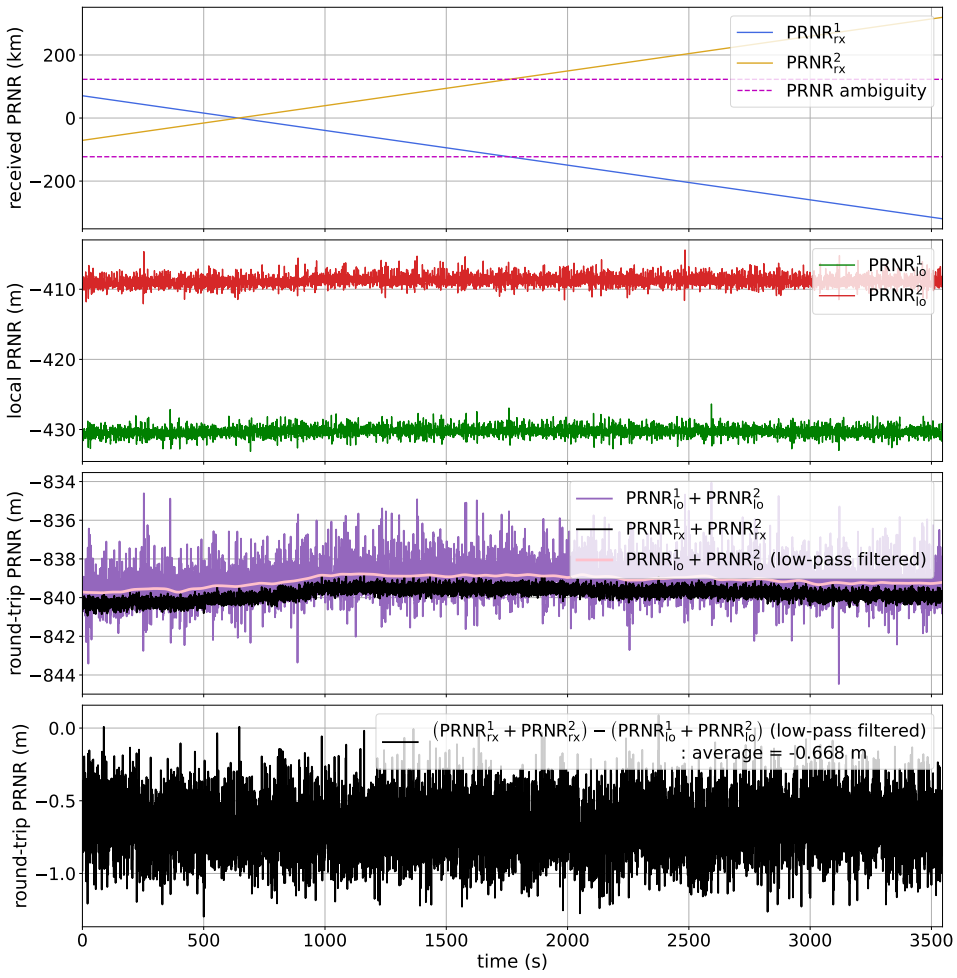

FIGURE 7.2: Round-trip ranging, combining PRNR observables at two PMs. **Top:** received-PRNR estimates, influenced by differential clock signals. **Second:** local-PRNR estimates. **Third:** round-trip estimates for the received and local ranging. **Bottom:** the residual in the difference in the round-trip estimate between the received and local ranging: i.e., black−pink in the third panel.

section assesses the absolute-ranging feature of PRNR utilizing TDIR as a reference.

The entire demonstration can be split into prior calibration and science mode. The main target of prior calibration is to derive the transmitter bias mismatch ΔB^t_{12} in Eq. (7.16). Then, the science mode aims to demonstrate the in-flight ranging, intentionally applying a drift of a heterodyne frequency and considering the calibration value from the prior calibration. Both modes require the PRNR ambiguity resolution and bias correction. It is noteworthy that standard TDIR is enough to resolve the ambiguity of $\mathcal{O}(100\,\mathrm{km})$. Nevertheless, to use TDIR as a good reference (i.e., a proper pseudo-range), the TDIR accuracy was maximized with the tone injection; see Section 4.4 for tone-assisted TDIR and Table 7.1 for parameters. The FIR 2 compensation was applied.

Prior calibration: The results of prior calibration are summarized in Figure 7.3, using the same PM 1 measurement as Figure 7.2. The raw received-PRNR estimate, confined in the ambiguity range at the beginning, is shown in the top panel. This can be ambiguity-resolved using the TDIR-derived timer (black), which results in a dashed-light-blue curve in the second panel. The curves show good consistency over time, including the time evolution due to a timer deviation between two clocks. A difference between the two, $R^{\mathrm{prn},\tau_1}_{12} - R^{\mathrm{tdir+sb},\tau_1}_{12}$ from Eq. (7.14), is shown in the third panel in light blue. This reveals a ranging bias in the received-PRNR estimate, around 424 m. Its estimate by the local ranging and a low-pass-filtered curve are shown in green and light green. Finally, the bias-corrected received-PRNR estimate, $R^{\mathrm{prn},\tau_1}_{12,\mathrm{corr}}$ from Eq. (7.15), is plotted in the bottom panel. This shows fluctuations with 15.3 cm rms, due to the residual code interference after ICC, on top of a nearly constant residual ranging bias of 6.07 m. According to Eq. (7.15), the residual bias corresponds to the transmitter bias mismatch ΔB^t_{12}, neglecting the dependency of the ranging bias on specific codes and the impact of ICC, which are revisited in Section 7.3.3. This can be used as a calibration value for the science mode.

The tone-assisted TDIR accuracy in this particular measurement was 2.26 mm.

Before moving on to the science-mode demonstration, another functional test was conducted to be confident of the system further: extra cables were inserted into different points in the setup. This way, some points, which are not entirely guaranteed only with Figure 7.3, can be confirmed:

They are all 2 m cables with the velocity factor of 0.85: an effective length is 2.35 m.

- The residual offset, shown in the bottom panel in Figure 7.3, really senses the transmitter bias mismatch ΔB^t_{12},
- TDIR senses the non-common delay between the carrier phases ΔB^r_c as reformulated in Eq. (7.9),
- The extra-cable-induced bias on the receiver side can be corrected via the local-PRNR estimate.

Figure 7.4 shows the difference of the bias-corrected received-PRNR estimates against TDIR, copying the default-setup curve from the bottom of Figure 7.3 (light blue). Yellow added the cable to the PM 1 transmitter side, which increases B^t_{21} and eventually increases the transmitter bias mismatch ΔB^t_{12} by 2.35 m (Point 1). After that, the extra cable was inserted only into the PM 1 receiver side (pink): increasing B^t_{12}. This effect must be removed from the

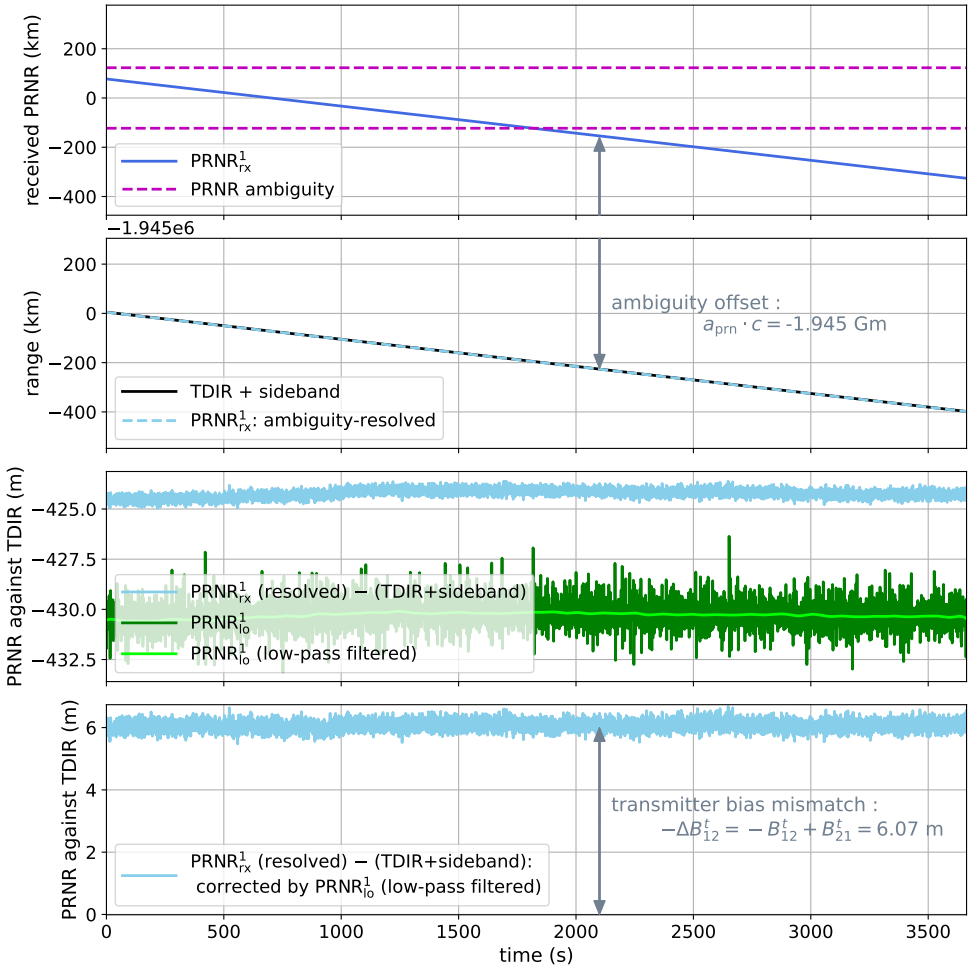

FIGURE 7.3: PRNR prior calibration. **Top:** a raw received-PRNR estimate, with the initial value restricted to the ambiguity range. **Second:** TDIR-derived timer and the ambiguity-resolved received-PRNR estimate. **Third:** the difference between the two in the second and the polynomial fit of a local-PRNR estimate. **Bottom:** the PRNR-to-TDIR mismatch with the bias correction via the local-PRNR estimate.

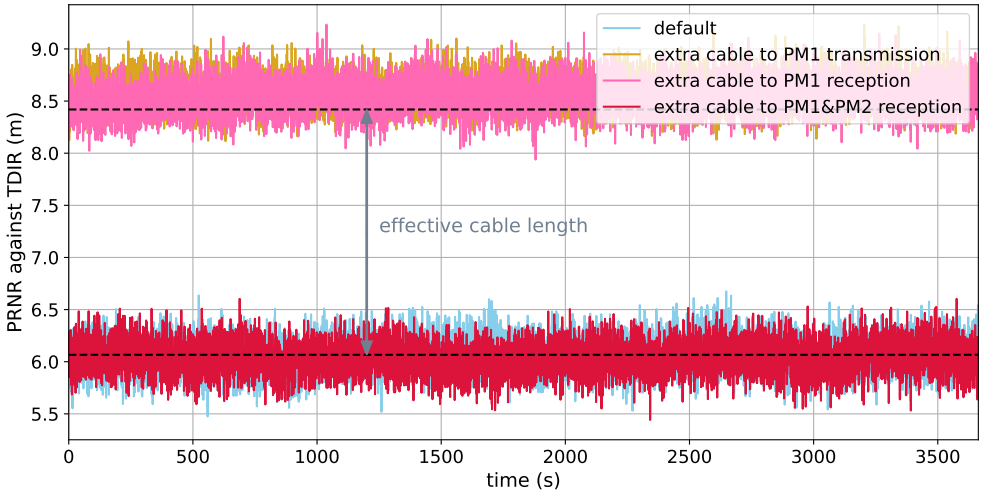

FIGURE 7.4: Bias-corrected received-PRNR estimate against TDIR with extra cable insertions.

received PRNR via the local. However, the cable-driven bias is observed in pink. This offset originates from the TDIR estimate (i.e., the reference in this test), which senses the non-common delay between the carrier phases on the receiver sides ΔB_c^r (Point 2) [4]. Finally, red inserted the extra cables into both reception sides. In this case, the TDIR estimate returns to the value in the default setup, while all the PRNR observables sense the extra bias. This being back to the default light-blue curves proves that such an extra bias due to the cable was properly corrected between the received and local-PRNR estimates (Point 3). The entire process can be formulated based on Eq. (7.16),

$$\begin{aligned} R_{12,\mathrm{corr}}^{\mathrm{prn},\tau_1}(\tau) - R_{12}^{\mathrm{tdir+sb},\tau_1}(\tau) &\approx -\left(B_{12}^t - B_{21}^t\right) && \text{for cyan (default)} \\ &\to -\left(B_{12}^t - \left(B_{21}^t + B_{\mathrm{cable}}\right)\right) && \text{for yellow} \\ &\approx R_{12,\mathrm{corr}}^{\mathrm{prn},\tau_1}(\tau) - \left(R_{12}^{\mathrm{tdir+sb},\tau_1}(\tau) + B_{\mathrm{cable}}\right) && \text{for pink} \\ &\to R_{12,\mathrm{corr}}^{\mathrm{prn},\tau_1}(\tau) - R_{12}^{\mathrm{tdir+sb},\tau_1}(\tau) && \text{for red,} \end{aligned} \quad (7.21)$$

where the right arrows represent additional cable insertions.

Science mode: The goal of this demonstration is to evaluate the absolute-ranging performance of PRNR under its nearly stand-alone operation; TDIR is used only to resolve PRNR ambiguity. PRNR will be combined with the transmitter bias mismatch calibrated in the prior calibration mode. To represent some features of the LISA constellation, a heterodyne frequency is sinusoidally modulated over the almost entire heterodyne band: 6 MHz to 24 MHz. This turns into the modulation of the effective signal amplitude at DPLL due to the non-flat magnitude responses of PRs and circuit elements on the PM analog BEE. This signal amplitude modulation, in turn, causes a time dependency of the receiver bias via the DPLL transfer function, as discussed below Eq. (7.4). Also, non-flat group delays of the components on the signal chain cause a direct coupling from the heterodyne frequency to the receiver bias.

This coupling process and mitigation by the local-PRNR estimate are shown in Figure 7.5. The top panel is the sinusoidal modulation applied to a carrier-carrier beatnote frequency from 6 MHz to 24 MHz with the frequency of

4 Hence, to the accuracy where receiver biases are guaranteed to be well corrected between the received and local-PRNR estimates, this type of investigations would act as a characterization of TDIR.

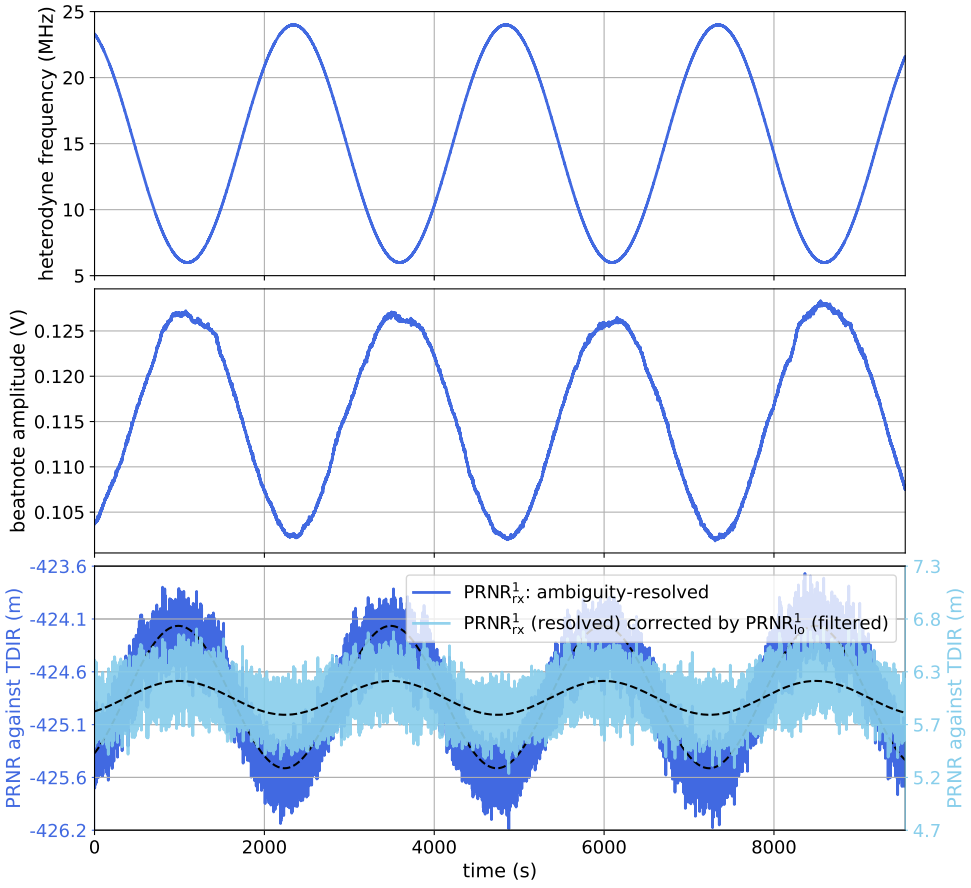

FIGURE 7.5: Sinusoidal modulation of a heterodyne beatnote frequency and its impact on PRNR. **Top:** a modulated carrier-carrier beatnote frequency. **Middle:** a carrier-carrier beatnote amplitude at the FPGA input. **Bottom:** PRNR against TDIR. Dashed-black curves are sinusoidal fits for two cases. To visually compare the two cases, the widths of the y-axis are adjusted.

0.4 mHz (see Appendix F for the injection of dynamics to a heterodyne frequency). As plotted in the middle, the frequency modulation couples to a signal amplitude via the phase-extraction chain. In this particular setup, the signal amplitude changed by around 20 % over the LISA heterodyne band. Finally, the bottom compares the received-PRNR estimate (blue) with its corrected version by the local (light-blue). The 1.40 m-peak-to-peak bias oscillation in blue was suppressed to the 0.33 m-peak-to-peak by the local correction in light blue. The values were estimated by sinusoidal fits (dashed-black). The residual after the correction is due to the dependency of the PLL-induced group delay on specific PRN codes; see Section 7.3.3 for discussions. This result suggests that the PRNR bias could be removed with accuracy better than 1 m, with the aids from the local-PRNR estimate.

Finally, PRNR is applied to time-stamping for clock synchronization instead of TDIR. The injected tone will be investigated to evaluate the synchronization performance, as done in Section 4.4. The averaged estimate, i.e., Case 3 from Section 7.2, was adopted as a nominal application. Figure 7.6 shows the performance of clock synchronization between the two PMs with different inputs for time-stamping: tone-assisted TDIR in black, PRNR only with the ambiguity resolution in blue, PRNR with the bias correction by the local PRNR in light blue, and PRNR with the bias correction via the local PRNR and the transmitter bias mismatch calibrated in the prior calibration mode in gold. The ambiguity-resolved PRNR estimate (blue) still shows the residual laser noise floor in addition to the tone, while the other two PRNR cases (light blue and gold) suppressed the noise floor down to the testbed noise, leaving the different tone residuals. The residual ranging errors, calibrated

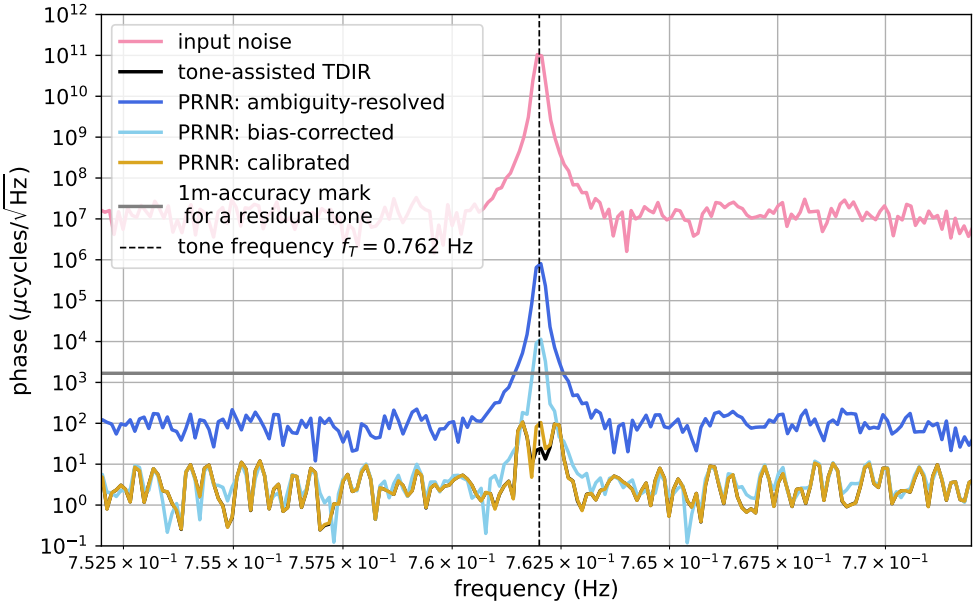

FIGURE 7.6: Clock synchronization with PRNR, under different bias treatments. Case 3 (averaged estimate), from Section 7.2, was applied to derive a timer deviation for time-stamping using PRNR. The ranging accuracies, computed by the residual tones, are 1.40 cm (black), 462.3 m (blue), 6.55 m (light blue), and 6.01 cm (gold).

from the residual tones, are 1.40 cm (black), 462.3 m (blue), 6.55 m (light blue), and 6.01 cm (gold), respectively. The transmitter bias mismatch limits the performance with the correction only via the local PRNR. This can be overcome with the information from the prior calibration, which successfully results in the accuracy below the 1 m mark.

7.3.3 *Further investigations*

The previous sections put the models into reality by providing the first demonstrations with the experiments. Studies, especially on bias correction, will be elaborated here with further research.

In-band ranging noise coupling: At the end of Section 7.2, the different cases of the PRNR application for clock synchronization were listed. The clock synchronization performances shown in Figure 7.6 were based on Case 3 with the averaged estimates. Here, different cases will be compared to clarify each feature, particularly Case 1 against Cases 2 and 3, to verify the coupling of the in-band PRNR noise to clock synchronization via time-stamping.

Figure 7.7 shows the comparison over a bit broader frequency band to visualize the noise coupling. Case 1 (purple) shows a unique noise floor, where the PRNR estimate is directly plugged to clock synchronization for time-stamping. This can be explained well by the theoretical prediction of the first-order term of the noise coupling (red): $\int \dot{\nu}^{\tau_m}_{c,i'j'}(\tau) \cdot N^{\text{prn}}_{ij}(\tau) d\tau$ for a phase in the unit of cycle, as mentioned in Section 7.2. $N^{\text{prn}}_{ij}(\tau)$ was computed by subtracting the sideband-derived timer, i.e., q_j, from the received-PRNR estimate. This noise floor expectedly disappeared in Cases 2 (green) and 3 (gold), where the PRNR estimate is used only for the derivation of the initial timer offset and then combined with the sideband measurements to derive the timer deviation. The two cases suppressed the stochastic noise to the TDIR case (black), leaving the residual tones at different levels. The ranging accuracy of Case 2 is estimated at 0.53 m, which can be further improved to 6.01 cm by the averaging in Case 3. 0.53 m in Case 2 is above the worst case

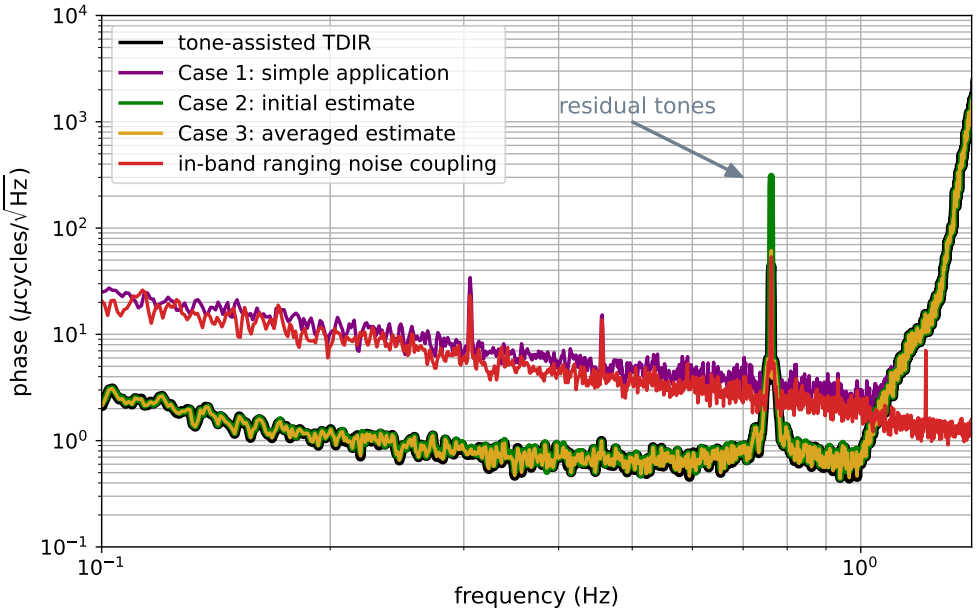

FIGURE 7.7: Coupling of the in-band PRNR noise to clock synchronization via time-stamping. Different cases are compared with the calibrated PRNR estimates. Case 3 (gold) and TDIR (black) are identical to the ones in Figure 7.6, except for changes in ASD resolutions for a cosmetic purpose.

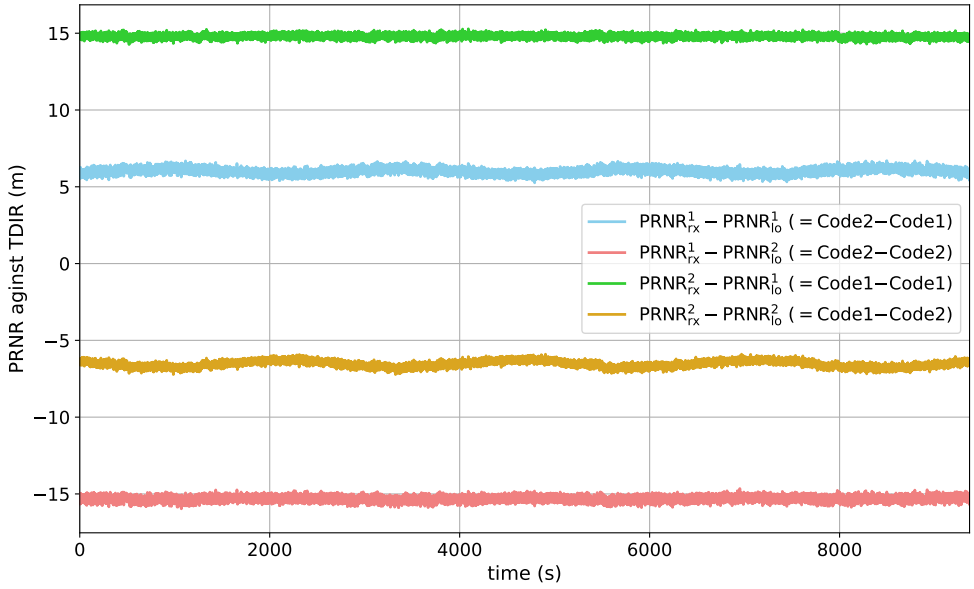

FIGURE 7.8: Different combinations of PRNR observables at two PMs against TDIR. Cyan is identical to the one in the bottom in Figure 7.5. Legends show what PRNR observables track which code from the bit-balanced code set: Code 1 and Code 2 from PM 1 and PM 2, respectively.

of the bias-estimation accuracy, i.e., 0.33 m, derived from Figure 7.5. Thus, this demonstrated the impact of the in-band PRNR noise variance and the suppression of it by the averaging in Case 3.

Bias dependency on specific code sequences: Even after the correction by the local-PRNR estimate, the 0.33 m-peak-to-peak residual modulation in the ranging bias was observed in cyan in the bottom plot in Figure 7.5. This was attributed to the dependency of ranging biases on specific codes; see Figure 7.8. The figure shows four combinations from the four PRNR observables, including the nominal one used for clock synchronization (cyan). All observables are according to the primary clock, with time-stamping if needed. While the combinations of the observables tracking different codes (cyan and gold) show such a residual modulation, almost flat time series were measured in the difference between the observables tracking the same codes at different PMs (pink and green).

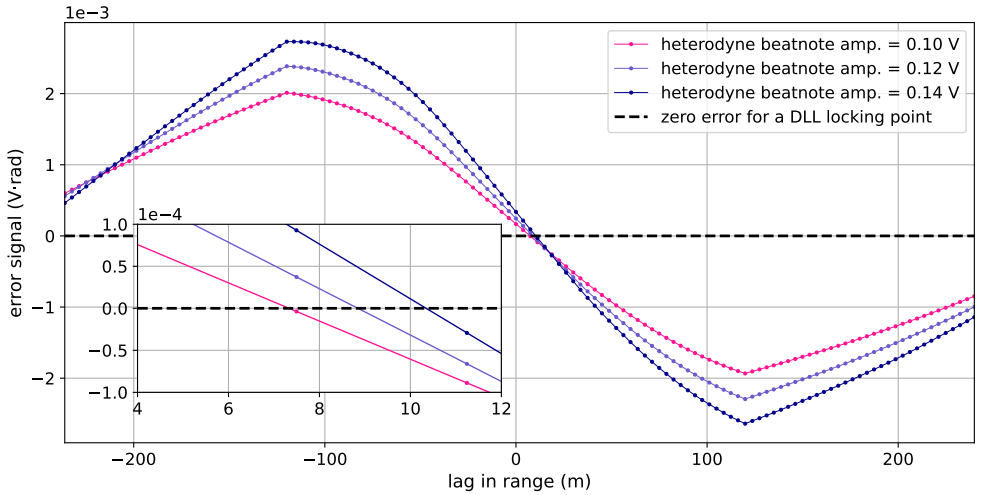

FIGURE 7.9: Simulated DLL error signals with different beatnote signal amplitudes. The bit-balanced Code 0 is used with random data encoded. The mini panel zooms in around locking points.

The bias dependency on specific code sequences leaves residuals even after the correction via local PRNR in this way. Such a residual bias eventually limits the absolute-ranging accuracy with PRNR; hence, this point is critical for PRNR. Therefore, to deepen knowledge here, numerical simulations were performed. In the following, six codes in a particular code set are labeled by Code 0 to Code 5. In addition to the bit-balanced code used for any measurements in this chapter up until now, the different code type, namely Manchester code, will also be analyzed and demonstrated for comparison. All simulations encode synthetic random data on received PRN codes.

Propagating from the PLL input to its error point, PRN codes are distorted and delayed due to the PLL transfer function (see Section 2.3). As a result, a DLL locking point is shifted from a nominal position, and the shift appears as a ranging bias in PRNR observables. Figure 7.9 shows simulated DLL error signals based on the bit-balanced Code 0 delayed by PLL transfer functions with different heterodyne amplitudes [5]. The amplitudes were selected to cover the modulated amplitude range, shown in Figure 7.5. The other PLL parameters are identical to the ones used in the experiment [6]. The locking points with the different heterodyne amplitudes deviate from the nominal position at the zero lag due to the PLL effect. In addition, they also differ from each other by a few meters, the source of the bias time dependency.

Figure 7.10 plots such ranging biases as functions of the heterodyne amplitude for all six codes in the bit-balanced code set (top) and the Manchester code set (bottom). Concerning the bit-balanced codes, the biases are clear linear functions of beatnote amplitudes, and their slopes give coupling factors from the heterodyne amplitudes to the PLL-induced biases. All measurements in Sections 7.3.1 and 7.3.2 implemented Code 1 and Code 0 on the PM 1 and PM 2, respectively. Therefore, Code 0 (blue) corresponds to the ambiguity-resolved received-PRNR estimate in Figure 7.5. The simulation predicts a

5 Numerical simulation algorithm: **1.** Generate a PRN code sequence with the 80 MHz resolution and a certain duration (0.1 s for this particular example); **2.** Encode synthetic random data on the PRN sequence; **3.** Define a PLL with a given beatnote amplitude; **4.** Propagate the data-encoded sequence through the PLL transfer function (Python Control Systems Library was used for the time-domain analysis); **5.** Compute early and late correlations, and eventually an error signal, between the received code sequence and the original intact code; **6.** Repeat 2 to 5 with different beatnote amplitudes; **7.** Repeat 2 to 6 with different random data sequences to check its effect (three times repeated for this particular example).

6 Except for the number of registers in the loop D

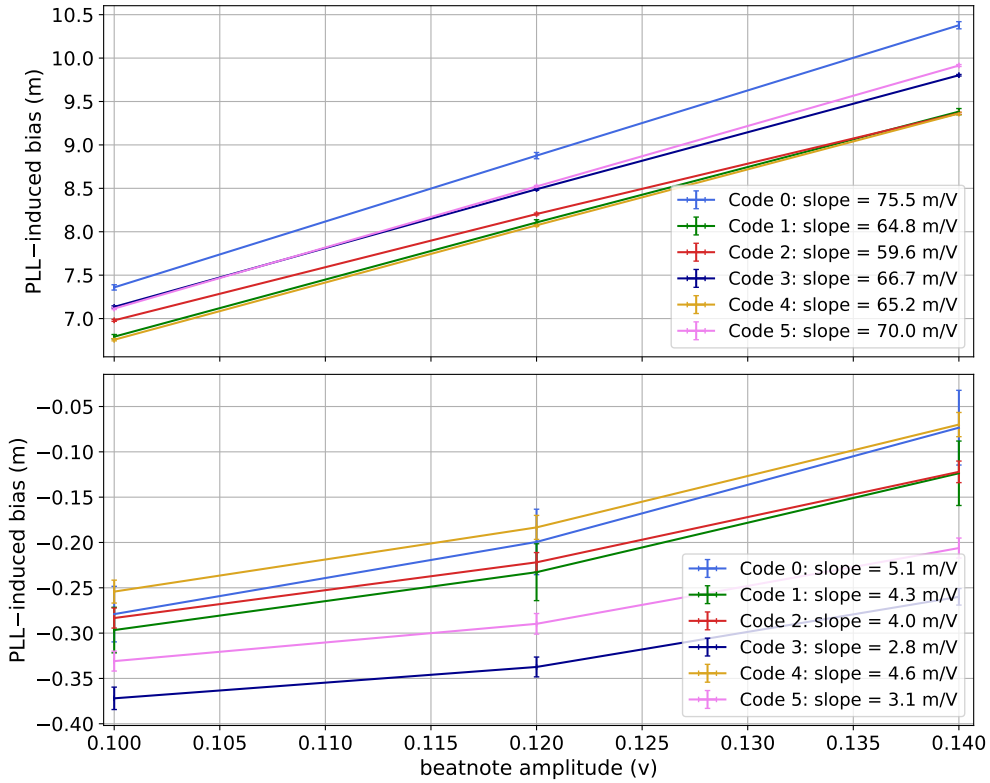

FIGURE 7.10: Simulated coupling from a heterodyne amplitude to a PRNR bias via PLL. An error bar was estimated by repeating the same simulation with different synthetic random data (see footnote 5 for simulation algorithm). **Top:** the bit-balanced code set. **Bottom:** the Manchester code set.

coupling factor of 75.5 m/V for Code 0, which results in a 1.85 m-peak-to-peak bias modulation. This is in the right order, compared with the measured 1.40 m-peak-to-peak modulation. The simulation was executed on a single code and neglected many realistic features, like code interferences, the code relative drifts due to timer deviations, or ICC. In addition, the simulation focuses only on the coupling via amplitude modulation, while there also exists a direct coupling from the heterodyne frequency to the receiver bias via non-flat group delays of the components like PRs as mentioned. Hence, there is some more space in the numerical studies to refine. In Figure 7.5, the bias in the received Code 0 was corrected via the local Code 1, which left the residual modulation with the 0.33 m peak-to-peak amplitude. Combining the simulated coupling factors of the two codes and the measured amplitude modulation, the simulation estimates the residual modulation peak-to-peak after the correction at 0.26 m. This is also almost consistent with the measurement. This analysis suggests a way to further mitigate the residual time-variant bias after the correction via the local PRNR, namely using (or designing) codes with the same coupling factor.

Once apart from the bit-balanced codes, the bottom panel of Figure 7.10 reflects a well-known advantage of Manchester codes [51, 56]. As discussed in Chapter 6, Manchester coding significantly attenuates the power of PRN codes towards low frequencies, pushing the noise power to higher frequencies. Hence, most of its noise power exists around the frequency region where the PLL error function is flat (see Figure 2.7 for an example of the PLL error function). As a result, Manchester codes are expected to be less susceptible to PLL, which is proved by one-order smaller biases than the bit-balanced codes in Figure 7.10. The response of biases to the beatnote amplitudes seems rather quadratic in the scoped region. Nevertheless, the coupling factors

were derived with a linear approximation and written in legends. Those are correspondingly one order smaller than the bit-balanced codes.

The discussions above raised two potential improvements, evolving from the first result in the previous section: the use of codes with similar coupling factors and Manchester code to suppress coupling factors themselves. To demonstrate the first point with the existing codes from Figure 7.10, Code 0 on the PM 2 was replaced with Code 4 having the coupling factor of 65.2 m/V, closest to 64.8 m/V for Code 1 on the PM 1. For the second point, The Manchester Code 0 and Code 1 were implemented on the PM 1 and PM 2, respectively.

Under the conditions, the same measurements with the frequency modulation were repeated; see Figure 7.11. Blue curves are the copies from Figure 7.5 with the bit-balanced 0-1 pair as references. Golden shows the bit-balanced 4-1 pair, while red corresponds to the Manchester 0-1 pair. Remarkable with the bit-balanced 4-1 pair is the better suppression of the residual bias modulation, as predicted by the simulation. The modulation peak-to-peak amplitude was attenuated from 1.14 m to 3.89 cm via the bias correction with the local-PRNR estimate (i.e., Code 1), almost one-order better than 0.33 m for the bit-balanced 0-1 pair in blue. This makes the bias correction, and eventually PRNR, way more robust. The application of this case to clock synchronization achieved the accuracy of 2.44 cm with the averaging in Case 3; see Figure 7.12.

The Manchester 0-1 pair (i.e., red in Figure 7.11) suppressed the coupling of the heterodyne amplitude to the biases: the ambiguity-resolved estimate, without the bias correction, already showed the sub-meter bias modulation amplitude, i.e., 0.47 m in peak-to-peak. A qualitative mismatch against the simulation in Figure 7.10 is the negative response of the ambiguity-resolved bias (darker-red) to the heterodyne amplitude. The simulation showed positive slopes also for the Manchester code set. This remains to be investigated. The 0.47 m modulation was suppressed to 0.11 m via the bias correction.

To wrap up this part, the values from the simulation and the measurements are summarized in Table 7.2. Qualitatively, the measurements have good agreement with the simulations. For better consistency, the numerical investigation would need to be more elaborated, as mentioned above. Although clock synchronization performances with the averaging are also listed as references, the leading figure of merit is the bias modulation amplitude after the correction, which determines the worst case in clock synchronization. Hence, the bit-balanced 4–1 pair performed the best. In conclusion, concerning PRNR, it would be critical to design a code set so that all codes share as much of the same coupling factor as possible.

Impact of ICC: At the end of the series of bias investigations, the impact of code interferences and ICC will be briefly mentioned in the following. For this purpose, the round-trip measurement summarized in Figure 7.2 will be revisited. The entire round-trip bias could be corrected by the sum of the local-PRNR estimates, leaving the 66.8 cm residual offset. The bias dependency on specific code sequences, verified above, cannot explain this offset: the dependence must be canceled between the received sum and the local sum in principle. However, in the latest implementation of DLLs, the local and received codes are not tracked equally: ICC minimizes the code interference only for the received-PRNR estimates. This asymmetry potentially

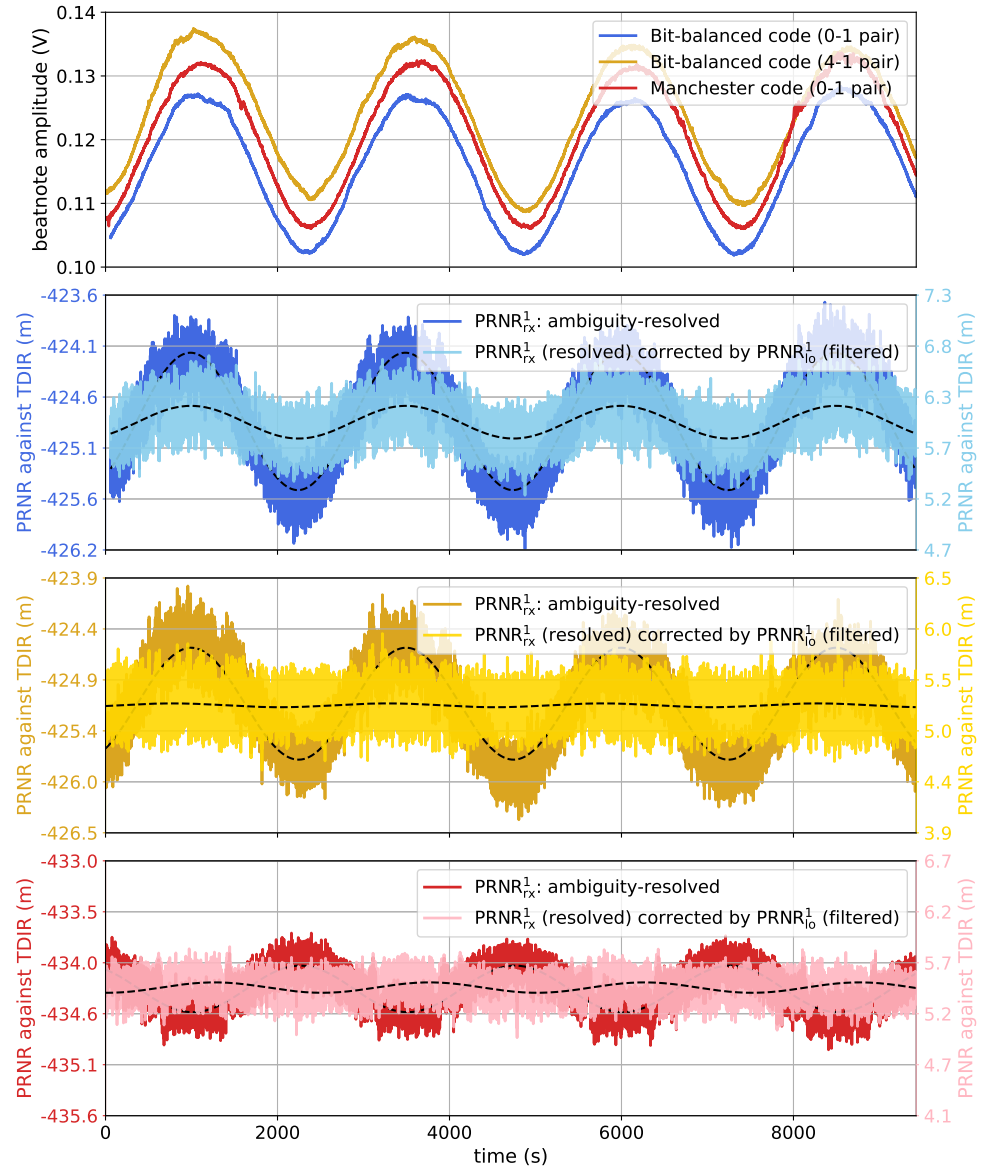

FIGURE 7.11: Comparison of the amplitude coupling to PRNR biases between different code pairs. **Top:** amplitude modulations, induced by the heterodyne frequency modulations. **Second:** PRNR against TDIR with the bit-balanced 0-1 pair (copy from the bottom of Figure 7.11). **Third:** PRNR against TDIR with the bit-balanced 4-1 pair. **Bottom:** PRNR against TDIR with the Manchester 0-1 pair. Dashed-black curves are sinusoidal fits for two cases. To visually compare the two cases, the widths of the y-axis are adjusted. Offsets between amplitudes with different pairs are due to actual beam power drifts between each measurement.

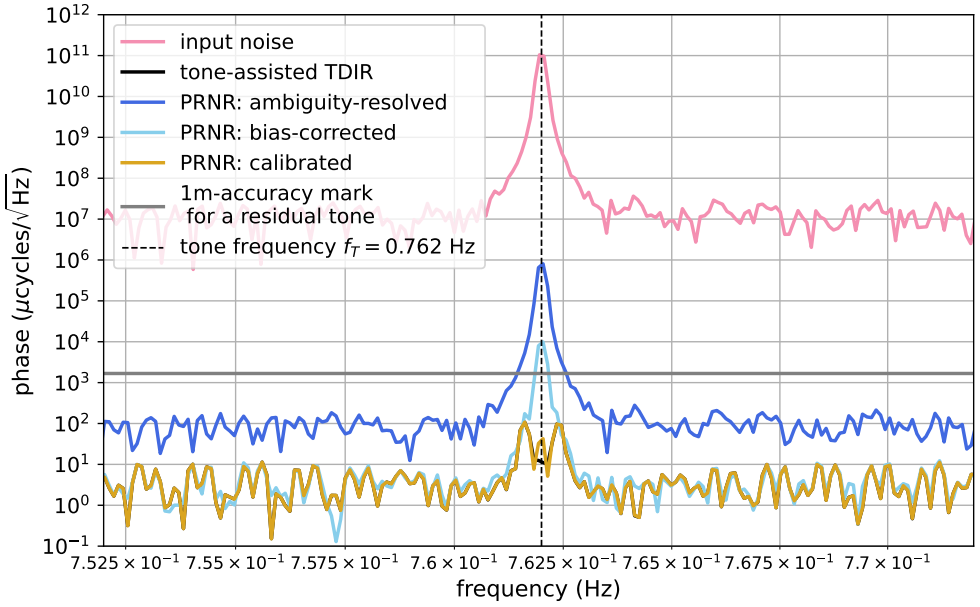

FIGURE 7.12: Clock synchronization with the bit-balanced 4-1 pair, under different bias treatments. Case 3 (averaged estimate), from Section 7.2, was applied to derive a timer deviation for time-stamping using PRNR. The ranging accuracies, computed by the residual tones, are 6.36 mm (black), 462.7 m (blue), 5.68 m (light blue), and 2.44 cm (gold).

Quantity	**Bit-balanced:** 0-1	**Bit-balanced:** 4-1	**Manchester:** 0-1
		Simulation	
Bias pp (b.c.)	1.85 m	1.64 m	1.32×10^{-1} m
Bias pp (a.c.)	2.62×10^{-1} m	8.82×10^{-3} cm	2.10×10^{-2} cm
		Measurement	
Bias pp (b.c.)	1.40 m	1.14 m	4.75×10^{-1} m
Bias pp (a.c.)	3.34×10^{-1} m	3.89×10^{-2} m	1.06×10^{-1} m
Clock sync.	6.01×10^{-2} m	2.44×10^{-2} m	2.34×10^{-2} m

TABLE 7.2: Summary of PRNR bias modulations and clock synchronization performances. The code numbers indicating a pair follow "RX-LO" from the PM 1 perspective. Clock synchronization is based on the averaged PRNR estimates. pp: peak-to-peak. b.c.: before correction. a.c: after correction.

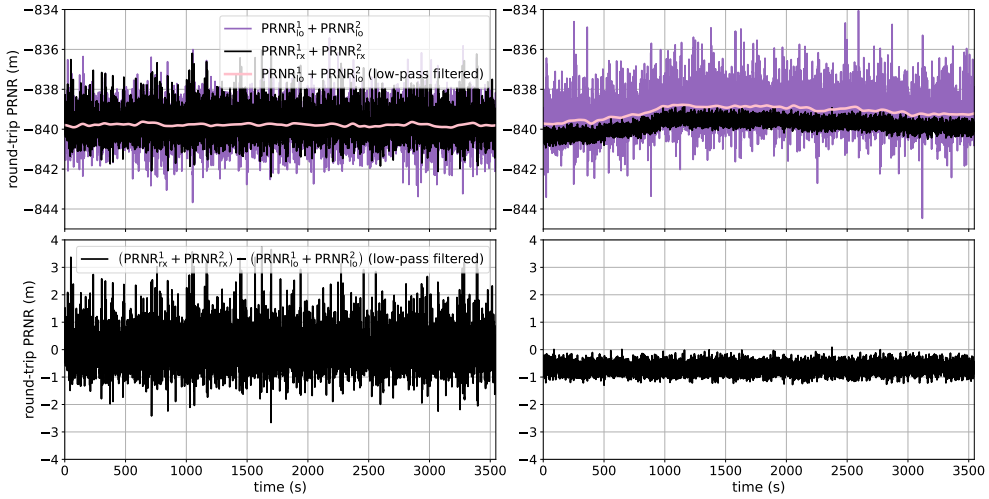

FIGURE 7.13: Measured impact of ICC on PRNR bias estimations in round-trip measurements. **Left:** without ICC. **Right:** with ICC (copy from Figure 7.2).

differentiates biases in the local and the received, even though they share the same code sequence. This was identified as the cause of the additional offset observed in the round-trip measurement.

To be compared to the nominal case with ICC in Figure 7.2, the round-trip measurement was repeated without ICC; see Figure 7.13. In the particular examples, ICC suppressed the in-band noise amplitude from 66.1 cm rms to 15.3 cm rms per a received-PRNR observable, over a full data rate, i.e., $\approx$ 3.39 Hz. However, ICC also affected ranging biases. As shown in the left column, the code interference is almost symmetrical between the local- and received-PRNR estimates without ICC, and the bias correction via the local left only the residual offset of 2.01 mm. This is way smaller than the one in the nominal case with ICC, i.e., 66.8 cm.

The impact of ICC on bias estimation via the local PRNR was verified here. However, it must be remarked that this effect is already considered in the bias-corrected estimates in the prior calibration mode, i.e., absorbed into the calibrated constant 6.07 m in Figure 7.3. Thereby, as long as the prior calibration is performed for all interspacecraft interferometers once, this ICC effect would not necessarily need to be considered later in science mode. This implies the powerfulness of such a prior calibration protocol: it can absorb many technical details, which might be tricky to accurately consider with theory, simulation, or part characterization, into a single calibrated constant.

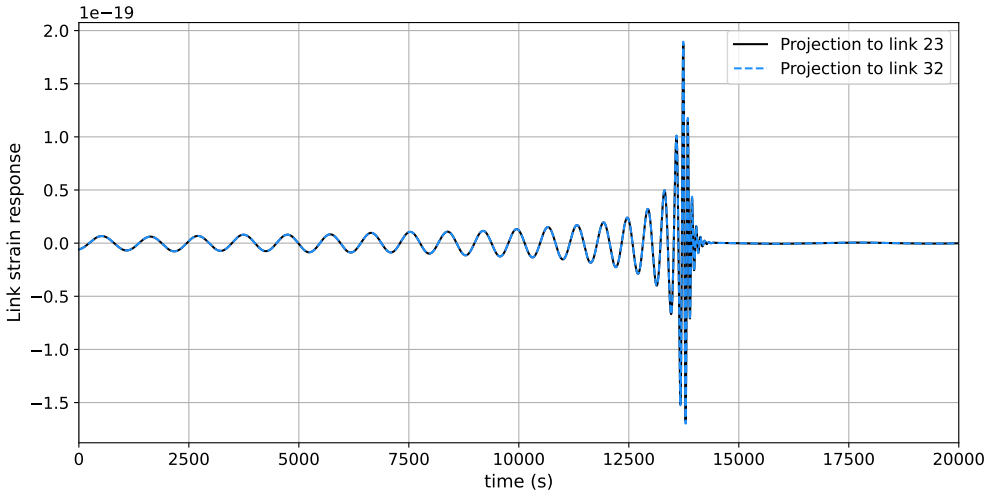

FIGURE 7.14: Injected GW signal from MBHB. Some source parameters are listed below:

Parameter	Value
Mass 1	9.2×10^5 $M_\odot$
Mass 2	7.0×10^5 $M_\odot$
Distance	7.7×10^3 Mpc
Redshift	1.1

Science case with a GW signal: Up to this point, it has been studied how well PRNR can perform as *absolute* ranging in the nearly stand-alone operation: only with aids by calibrated constants and any monitor with sub-millisecond accuracy for ambiguity resolution. PRNR is expected to perform with sub-meter accuracy, removing the time (or also SC) dependencies of ranging biases via the combination of the local and received-PRNR observables.

This primarily means a transmitter bias mismatch in Eq. (7.16). In LISA, the difference in optical pathlengths between the local and received beams must be additionally taken into account, which is purely constant in the sub-meter scale.

To wrap up this section, the study on PRNR is put into a science case with a GW signal in LISA. Due to the injection of some synthetic data in post-processing, this deviates from experimental demonstrations of technologies. In addition, the experimental setup and signals are quite inconsistent with injected GW signal and noise floors, which are representative for LISA; nevertheless, this would be one way to formulate the significance of the studied PRNR operation. The investigation below is rather qualitative or sketchy than quantitative due to the inconsistency between synthetic signals and setups.

Shot noises, shaped by the averaged LISA antenna pattern, and low-frequency-approximated TM acceleration noises were injected incoherently into frequency data of the two PMs in post-processing. See Eqs. (1.22) and (1.23). In addition, the projections of a GW signal from MBHB to a pair of bidirectional links in LISA were injected differentially into frequency data of the two PMs in post-processing as well so that the 2PM2S topology can sense it. The MBHB signal was taken from LISA Data Challenge *Sangria* [7], which is based on IMRPhenomD [59]. The projection of the GW signal to the particular links is plotted in Figure 7.14. A measurement duration was 20 000 s. Concerning TDIR, although tone-assisted TDIR was used as a reference for the evaluation of PRNR in previous sections, normal TDIR without tones would be still a baseline TDIR operation in LISA. Therefore, such normal TDIR was applied here.

The performances of clock synchronization with the synthetic signals are shown in Figure 7.15. Based on the injected shot noises (solid black), TM acceleration noises (dashed black), and the actual Hexagon testbed limit (dotted black), the synthetic sensitivity is shown in grey. The injected MBHB spectrum is drawn by the blue area.

PRNR is not affected by GWs in its target scale in general. Hence, it is expected to continuously generate pseudo-ranges with sub-meter accuracy,

7 Data credit: Maude Le Jeune and Stanislav Babak. LISA Data Challenge Sangria (LDC2a), October 2022. 10.5281/zenodo.7132178

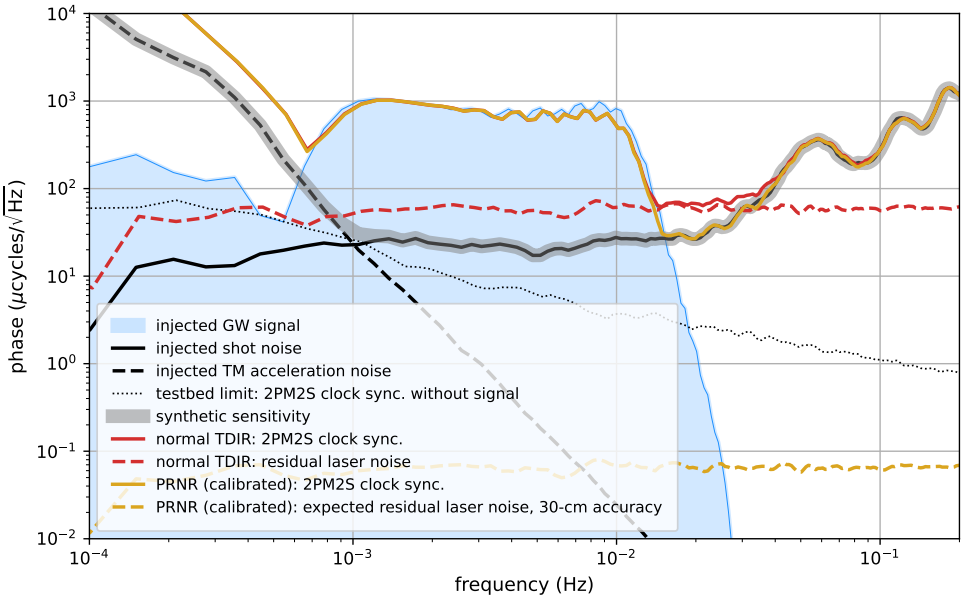

FIGURE 7.15: Ranging with the existence of a GW signal from MBHB.

limited by the bias correction accuracy. This feature was demonstrated via residual laser noises in the calibrated-PRNR case (dashed gold), estimated to be less than 30 cm. As a result, the "detector" output (solid gold) properly achieves the sensitivity (grey) and detects the MBHB signal (blue) [8].

On the other hand, the performance degradation was observed in the TDIR case (solid red): the residual laser noise (dashed red) above the synthetic sensitivity (grey). Such a potential degradation highly depends on data segments to be analyzed, a test frequency band for the TDIR algorithm, GW parameters, etc. In this sense, TDIR would not be stable utilizing primary science data (i.e., interferometric phases). Notice that using TDIR as a baseline PRNR bias estimator in science mode could, in turn, lose the robustness of PRNR.

In summary, the PRNR robustness can be highly enhanced by introducing the local PRNR as a real-time monitor of PRNR biases. Therefore, PRNR is a robust and continuous absolute ranging method for LISA.

7.4 DATA COMMUNICATION

All ranging measurements in this thesis also feature data communication. They are all under the "normal-light" condition with all beam powers of $O(100\,\mu W)$ for the time being. However, the code interference is present, which could be potentially a limiting noise source, if not treated by its mitigation technique (i.e., ICC); also see [51, 50]. The preliminary result of data communication under such a condition will be summarized below. Notice that the 2^n parameter set from Table 5.1 was used; hence, the raw data-bit rate was 78 125 bps.

Even if treated, the residual interference could limit the ranging performance, depending on the distortion of codes, which highly depends on the code types.

The encoded data structure is shown in Figure 7.16, in hexadecimal numbers. As listed in Table 5.1, the length of the RS codeword n_{rs} is selected at 255 bytes, and 205 bytes out of the codeword are scientific data, or called *message*. Accordingly, the remaining 50 bytes are RS check symbols, which determines the error-correction performance; see Eq. (5.15). The 205-byte message comprises a 15-byte start marker and 190-byte data. In principle,

8 The degradation from TM acceleration noise, shown in both PRNR and TDIR, is unknown.

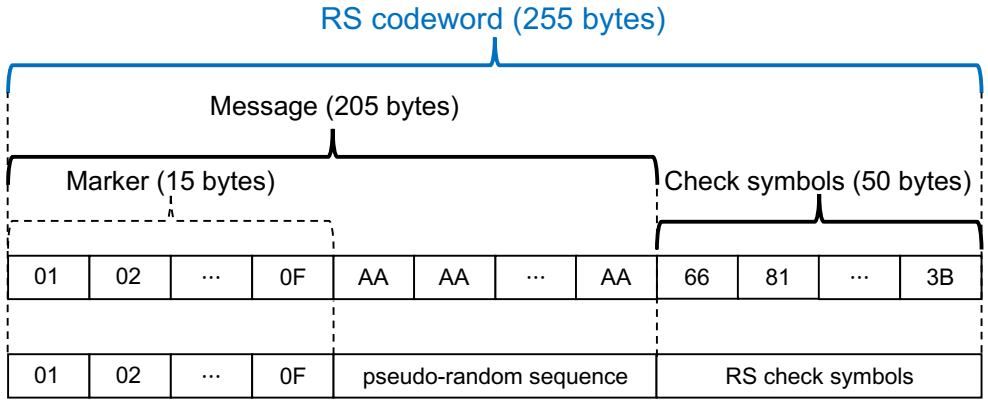

FIGURE 7.16: Structure of encoded data sequence in hexadecimal numbers. 1 byte corresponds to 1 symbol: see Table 5.1. **Top:** a periodic sequence used for performance investigations of data communication. **Bottom:** a pseudo-random sequence representing real data in LISA.

the start marker is needed only for the first communicated codeword to let the decoder know the start of the codeword. However, the current PM prints the start marker in every codeword for ease of implementation. Two data types were implemented, as shown on the top and the bottom in Figure 7.16: the *AA* periodic data and the pseudo-random data. Any ranging measurements without investigations of data communication feature the independent pseudo-random data for each PM, representing the LISA case. Such a pseudo-random sequence is generated by a triangular dither generator developed by Oliver Gerberding [30].

The data communication test was conducted, considering one of PMs in Figure 7.1 as a receiver and the other as a transmitter. The pseudo-random data was encoded on the local PRN code, while the periodic data was encoded on the received PRN code and compared with the intact data in post-processing. The results with the different PRN code types from Chapter 6 under different operations (with/without RS coding and/or ICC) are summarized in Table 7.3.

Code	Interference	BER: wo RS	BER: with RS
Bit-balanced	without ICC	6.52×10^{-3}	2.68×10^{-4}
	with ICC	4.21×10^{-3}	2.71×10^{-7}
Double-balanced	without ICC	4.11×10^{-3}	4.25×10^{-4}
	with ICC	6.42×10^{-4}	$< 1.0 \times 10^{-9}$
Manchester	without ICC	1.17×10^{-3}	1.35×10^{-4}
	with ICC	1.81×10^{-6}	$< 1.0 \times 10^{-9}$

TABLE 7.3: Data communication results under the normal-light condition with code interference.

First, let's focus on the case without RS coding, where measurement durations were all 2000 s: All codes show improvements with ICC, and the code, less distorted by the PLL error function, results in better improvement, as expected. The distortion by PLL is determined by the code power within the PLL bandwidth. See Figures 6.1 and 6.2 for the code spectrums. Figure 7.17 shows the results in the time domain. The middle panel shows instant BER every RS codeword: with ICC in the large panel and without ICC in the small panel over a shorter period. The received and interfering local codes drift against each other due to independent clocks. The drift frequency over one PRN chip is called the "chip slip rate", e.g., 0.375 Hz with the PRN chip rate

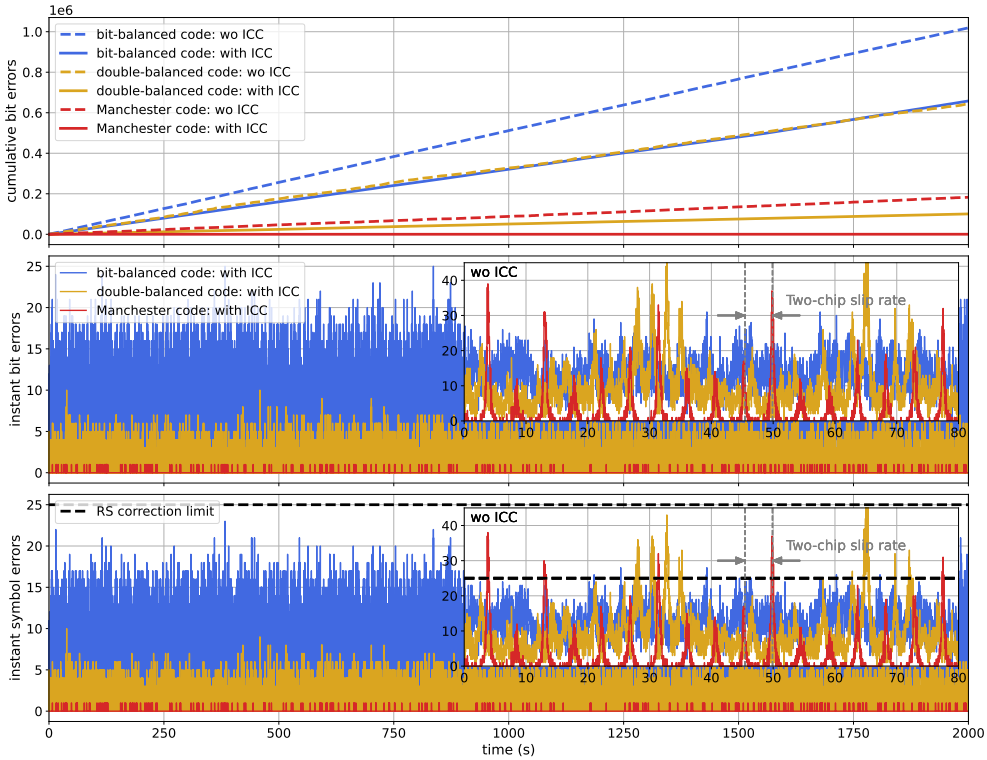

FIGURE 7.17: Measured raw data errors without RS coding. **Top:** cumulative bit errors over a measurement time. Middle: instant bit errors in each codeword. **Bottom:** instant symbol errors in each codeword. In the middle and bottom, the large panels show the errors with ICC, while the small panels show the ones without ICC over a shorter time segment.

of 1.25 MHz and the clock frequency difference of 0.3 ppm [9]. In addition, the code interference is maximized when chip transitions between two codes are aligned (confirmed by simulation; also see [51]). They imply that the code interference exhibits a periodicity at the chip slip rate. For example, Manchester code showed periodic peaks at the two-chip slip rate due to the code interference because of its coding nature, which was removed by ICC as shown in Figure 7.17.

Second, RS coding corrects the errors up to 25 bytes per codeword. All measurements in Table 7.3 in this case shared the duration of 12 800 s, corresponding to the number of bits of 10^9. The double-balanced and Manchester codes yield no error with ICC over the duration, while the bit-balanced code still showed some errors.

Figure 7.18 projects the measurements, with and without RS coding, to the theoretical line from Figure 5.5. In analogy to Welch's method, the error bars were computed by splitting the entire duration into 50 %-overlapping segments. The double-balanced and Manchester codes without ICC are especially far from the theory, which comes from the highly limited improvements by RS coding compared with the cases with ICC: see Table 7.3. This seems to be because the two cases showed remarkable periodicities due to chip slips (see Figure 7.17), which deviated the system more from the ideal AWGN case, assumed for the theoretical curve.

7.5 SUMMARY AND OUTLOOK

This chapter studied the absolute-ranging feature of PRNR rather than its in-band stochastic noises that were investigated by previous research. A

9 0.3 ppm is the typical clock offset of the Hexagon USO; see Figure 4.3.

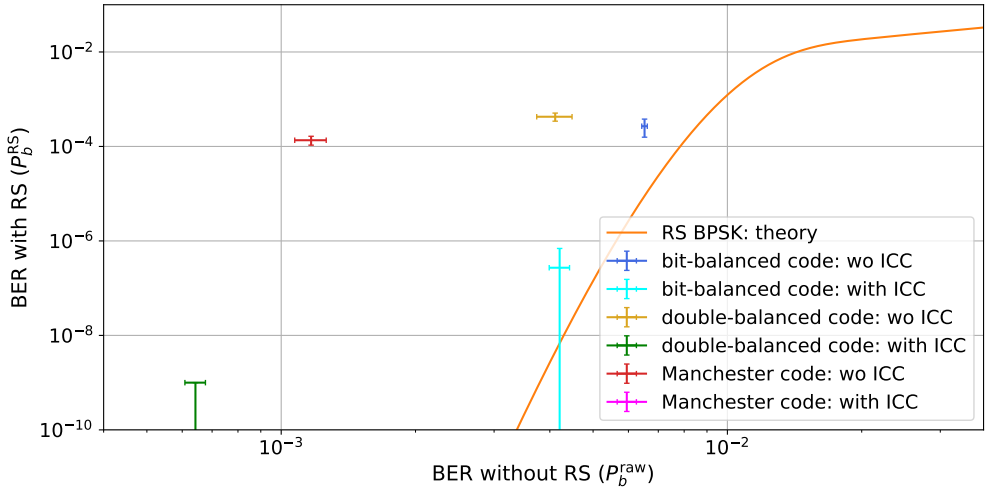

FIGURE 7.18: Projection of measured data errors to a theory. "Manchester code: with ICC" is out of the x-axis range because of a small BER without RS coding (see Table 7.3) but included in legends for completeness.

proper investigation of absolute ranging needs a reference to resolve PRNR ambiguity and distinguish ranging biases from pseudo-ranges. TDIR, which have been demonstrated in Chapter 4, was used as such a reference in this chapter. This algorithm, in turn, required multiple PMs to be synchronized; therefore, the 2PM2S topology with bidirectional ranging was adopted as the simplest possible setup.

The first investigation utilized round-trip measurements to check consistency between two PMs. As expected, the timer deviations were measured in opposite polarities at different PMs and canceled out between them well, including the stochastic clock jitters. In addition, the investigation confirmed that ranging biases in the received-PRNR estimates were appropriately monitored by the estimates of the newly introduced local PRNR.

The second and core investigation demonstrated the entire process from raw PRNR outputs of PMs to their application to clock synchronization. In this investigation, TDIR was used to resolve PRNR ambiguity and also as the reference absolute ranging estimate. The model predicted that some constant biases could not be corrected via the local PRNR (called transmitter bias mismatch in the text), which required one iteration of prior calibration. In LISA, the same could be performed on ground before the launch and/or even in flight before switching to science mode. After such prior calibration, a heterodyne frequency was intentionally modulated over the almost full heterodyne band (i.e., 6 MHz to 24 MHz) to simulate LISA science mode, in which heterodyne frequencies drift over time according to SC relative motions. This frequency modulation turned into the modulation of effective signal amplitude at PLLs due to non-flat magnitude responses of signal chains (e.g., PRs), which eventually caused the modulation of biases in PRNR. In addition to the primary coupling, the frequency modulation can directly couple to the PRNR biases via non-flat group delays of signal chains. The time-variant ranging biases could be corrected via the local-PRNR, with an accuracy better than 0.33 m. Numerical simulations also confirmed this coupling process and the bias correction. Furthermore, the numerical simulation suggested that another code pair was expected to mitigate the residual time dependency of ranging bias, sharing as much of the same coupling factor as possible. Being back to measurements, such mitigation was demonstrated, and the residual time dependency was further suppressed to 3.89 cm. Finally, the application of the calibrated PRNR to the time-stamping of PM outputs performed clock

synchronization with the accuracy of 8.14×10^{-10} s, or 2.44 cm in range after the averaging of the PRNR estimates. This study put some fundamental aspects of PRNR, which have been claimed to function, into reality, like ambiguity resolution. In addition, it also proposed some new features and adjustments to enhance the robustness of this technology: prior calibration protocol, bias correction via the newly implemented local PRNR, and the further elimination of the bias time dependency based on a new criterion for the PRN code design (i.e., similar coupling factors). They could advance confidence that PRNR can continuously provide sub-meter absolute ranging information robustly.

Apart from absolute ranging, the preliminary results of data communication were also provided with different PRN code types, introduced in Chapter 6. This showed BERs below the LISA 10^{-6} mark with the combination of ICC and RS coding for all code types.

Some main future tasks are listed: First, the experiment should be extended to the 3PM3S-bidirectional topology from Figure 3.3. Although the 2PM2S topology, presented in this chapter, covered the most absolute-ranging concepts, the 3PM3S-bidirectional topology can produce a more representative signal set for LISA. In addition, it provides a neater test feature for phase extraction, namely the probe of nonlinearity. Second, as mentioned in Section 4.5, the technology must be investigated under weak-light conditions to represent interspacecraft interferometers in LISA. Third, identifying bias origins in the signal chain from the transmitter to the receiver would be helpful. It works as a cross-check of the local-PRNR estimates and the calibrated constant. Fourth, the investigation in Section 7.3 did not correct time-dependent carrier phase biases due to non-flat group delays of signal chains. It would be trivial in the test setup because the two PRs monitor the same beatnote in principle; hence, such biases are expected to be common for both chains, and TDIR, i.e., the reference in this experiment, does not sense it. However, this would become important in the 3PM3S-bidirectional topology. Nevertheless, unlike PRN signals, estimating such biases in carrier phases would be straightforward because an optical beatnote is a simple sinusoidal signal. Fifth, automatic gain control of the digitized heterodyne beatnote eliminates the primary source of the time dependency of ranging biases; therefore, it is pretty worthwhile implementing in the author's view. Sixth, beatnote phases also provide integration constants of their frequency signals with much shorter ambiguity than PRNR, i.e., $\mathcal{O}(10\,\text{cm})$ for the sidebands and 1064 nm for the carrier. Therefore, it would even be possible to resolve sideband ambiguity [57] via cm-accurate PRNR, demonstrated in this chapter. The current nominal plan completes the phase information with occasional anchor points. However, it would also be an option to provide continuous phases as nominal outputs instead of combining continuous frequencies and occasional phase anchors. The original motivation to use frequencies was to ease the onboard processing: drastic ramps due to MHz frequencies must be treated with particular care to avoid artifacts at the decimation stages. However, such treatment is in any case essential to DLL outputs (see Appendix G for the preliminary solution in this thesis) that contain a monotonic ramp contribution (i.e., the timer deviation). Therefore, applying such a solution to PLL seems feasible. Incorporating beatnote phases into the "ranging ladder" must be exciting.

Part IV

APPENDIX

A

NOVEL OPTICAL HEAD DESIGN FOR DEEP FREQUENCY MODULATION INTERFEROMETRY

Tracking moving masses in several degrees of freedom with high precision and a large dynamic range is central in many current and future gravitational physics experiments.

The deep frequency modulation interferometry (DFMI) and deep phase modulation interferometry (DPMI) techniques [60, 61] enable this goal in a compact optical setup. Past investigations of DFMI [62, 42] before the optical head (OH) proposed in [63] employed a separate Mach-Zehnder interferometer (MZI) as a frequency reference to stabilize the laser. This additional interferometer increases the complexity of the setup, mitigating one of the main advantages of the technique. To overcome this issue, the next generation of this technology incorporates both the inertial sensor and the reference interferometer in the same optic.

This chapter describes the design work undertaken to develop the custom pentaprism shown in [63]: the mechanical design, the manufacturing feasibility, and performance as a frequency reference and inertial sensor. Departing from an original concept proposed by Yichao Yang, the author joined the project as one of the main contributors to conceptualization, methodology, and numerical simulation, together with Yichao Yang and Miguel Dovale Álvarez.

A.1 DEEP FREQUENCY MODULATION INTERFEROMETRY

The critical feature of DFMI is applying frequency modulation to a laser source, which is deep enough to detect the accumulated phase difference between two arms. The signal $P_{\mathrm{PD}}(t)$ at a photo detector (PD) takes the form

$$P_{\mathrm{PD}}(t) \propto 1 + C\cos(\phi + \gamma\cos(\omega_m t + \psi)), \tag{A.1}$$

where ϕ is the target interferometric phase, $\gamma = 2\pi\Delta f\Delta\tau$ is the effective modulation depth, which is composed of the frequency modulation depth Δf and the light travel time shift $\Delta\tau = \Delta L/c$ between the two arms of the interferometer (c is the speed of light and ΔL is the optical pathlength difference), $\omega_m = 2\pi f_m$ is the modulation frequency, and ψ is the modulation phase, and C is the interferometric constant.

There exist a variety of ways to analyze this signal. The classical method is to demodulate the signal with several harmonics and fit parameters (ϕ, γ, ψ, and signal amplitude) using a Levenberg-Marquardt routine. Alternatively, the PD signal itself Eq. (A.1) can be an input to algorithms, e.g., a Kalman filter (KF) or a particle filter (PF).

To provide high-sensitivity displacement measurements, two interferometers are combined: a TM interferometer to interrogate the position of a TM and a reference interferometer to provide a reference signal with which to remove laser frequency noise that would otherwise spoil the TM interferome-

Parameter	Value
TM IFO intra-prism pathlength (mm)	212.53
Reference IFO intra-prism pathlength (mm)	156.55
TM IFO arm-length difference (mm)	500.55
Reference IFO arm-length difference (mm)	143.98
S_2 to TM surface distance (mm)	180.88
AOI to the TM (deg)	9.71

TABLE A.1: Geometrical parameters relevant to the structural analysis and noise investigations. IFO: interferometer.

ter measurement. Such frequency noise δf_0 can be subtracted from the TM interferometer by

$$\phi_{\text{tm}} = 2\delta\phi + 2\pi\delta f_0 \Delta\tau_{\text{tm}} + \sigma_{\text{tm}}, \tag{A.2}$$

$$\phi_{\text{ref}} = 2\pi\delta f_0 \Delta\tau_{\text{ref}} + \sigma_{\text{ref}}, \tag{A.3}$$

$$\phi_{\text{tm}} - \frac{\Delta\tau_{\text{tm}}}{\Delta\tau_{\text{ref}}}\phi_{\text{ref}} = 2\delta\phi_{\text{tm}} + \sigma_{\text{tm}} + \frac{\Delta\tau_{\text{tm}}}{\Delta\tau_{\text{ref}}}\sigma_{\text{ref}}, \tag{A.4}$$

where $\delta\phi$ is the phase shift due to the perceived TM longitudinal motion, scaled by a factor of approximately two due to the reflection at the TM (the exact factor depends on angle of incidence (AOI)), and σ terms represent other secondary noise sources. As mentioned above, the analysis of Eq. (A.1) estimates the effective modulation depth γ, giving us $\Delta\tau$ in turn. Eq. (A.4) suggests that the accuracy of this estimation limits the cancellation of the frequency noise. A typical relative readout accuracy is $\delta\gamma/\gamma \approx 4.5 \times 10^{-6}$.

A.2 OPTICAL HEAD DESIGN

The proposed custom-design prism [63] is shown in Figure A.1. The prism is a seamless piece of fused silica glass obtained via the optical contacting of two parts and comprises three main optical surfaces ($S_{1,2,3}$) and two side surfaces. Surfaces S_1 and S_3 are used for laser beam splitting and recombination of the two hosted interferometers. Surface S_2 features two different coatings and serves a double purpose: an inner portion of the surface is highly-reflective (HR)-coated to act as a mirror for the reference interferometer, and the remainder of the surface is anti-reflective (AR)-coated to serve as a transparent window for the TM interferometer. The two side surfaces are AR-coated to transmit unwanted beams out, with their relative angle optimized for this purpose.

Using optical fibers and fiber injector optical subassembly (FIOS), a single frequency-modulated laser signal is split and delivered to one or several of these OHs, enabling us to sense the motion of a system in multiple degrees of freedom and eliminating the need for a separate frequency reference. Hence, a single-element dual-interferometer (SEDI) inertial sensor is realized.

The nominal parameters of the setup are summarized in Tables A.1 and A.2. These parameters are also used in the optical simulations presented in the later sections.

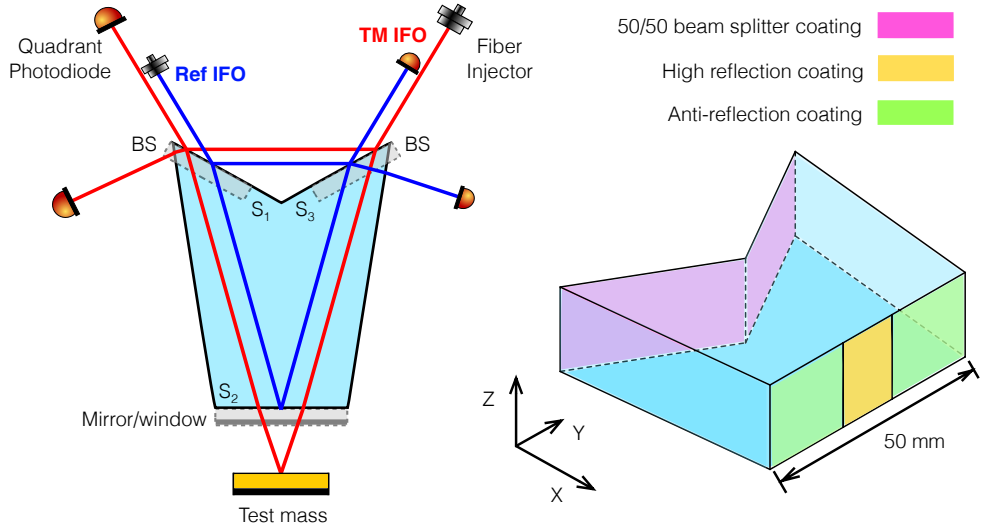

FIGURE A.1: SEDI optical head layout. **Left:** a frequency-modulated laser beam is split and delivered via two optical fibers to the heptagonal prism. The prism has three main optical surfaces: S_1 and S_3 as BSs, and S_2 as a mirror and a window for the reference and TM interferometers. **Right:** the required optical coatings on the prism.

TABLE A.2: Parameters of the SEDI simulation setup.

Optical head	
(width, height, depth) [mm]	(80.0, 30.0, 50.0)
(α, γ, side angle) [deg]	(120.0, 90, 6.5)
Quadrant photodiodes	
(width, height, depth) [mm]	(25.0, 25.0, 40.0)
active radius [mm]	0.25
slit width [mm]	0.25×0.05
optical distance from the prism [mm]	TM:100.0, Ref: 120.0
Beams	
waist radius [mm]	0.3
waist offset from the FIOS [mm]	100.0
distance from the FIOS to the prism [mm]	TM:37.0, Ref:50.0
AOI to the input surface [deg]	60.0
AOI to the TM [deg]	9.71

A.3 STRUCTURAL ANALYSIS: GHOST BEAMS

For reaching pm/$\sqrt{\text{Hz}}$ displacement sensitivities or lower, it is essential to keep stray light noise in check. Such unwanted stray lights (or "ghost beams") could interfere with one of the main beams and/or another ghost beam and impinge on a detector. The former case is the most critical because the strong power of the main beam maximizes the resulting phase noise. In this case, the relative power of a ghost beam to one of the nominal beams needs to be less than 3.5×10^{-11} to reach pm/$\sqrt{\text{Hz}}$ precision [64].

Our custom OH is carefully designed to deal with ghost beams accordingly to keep them from affecting the measurement. By sweeping the parameter space of possible prism geometries, it is possible to choose a geometry that guarantees suppression of ghost beams to a very large degree, see Figure A.2.

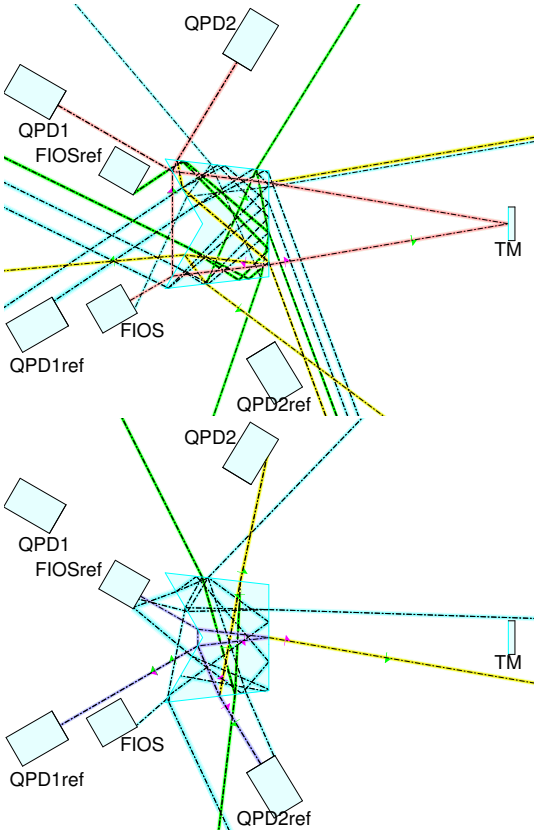

FIGURE A.2: Ghost beams in the SEDI setup. **Top:** the TM interferometer. **Bottom:** the reference interferometer. Absolute errors of 10^{-2} are introduced in the power transmission coefficient of each surface. Ghost beams down to a power threshold of 10^{-12} relative to the nominal beam power are considered. The nominal beams in the TM and reference interferometers are in red and blue. Ghost beams with different relative power thresholds are colored differently: down to $[10^{-3}, 1]$ in yellow, $[10^{-7}, 10^{-3}]$ in green, and $[10^{-12}, 10^{-7}]$ in cyan.

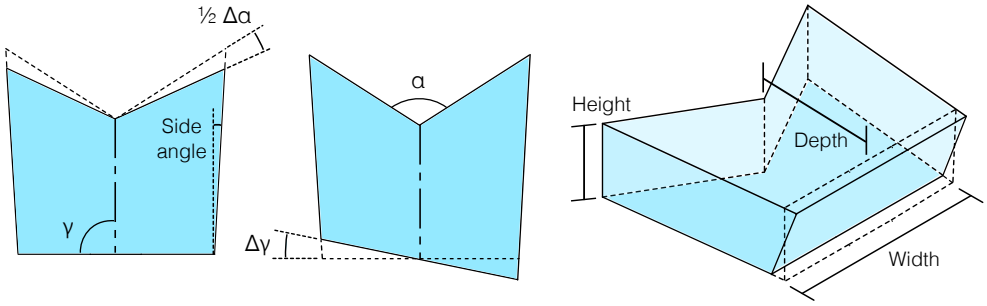

FIGURE A.3: Critical manufacturing tolerances are divided into two categories. Tolerances affecting the relative alignment between optical surfaces, parameterized by α and γ (left and middle), lead to in-plane beam misalignments that can be compensated for in both interferometers by tuning the direction of the incident beams; tolerances affecting the perpendicularity of the optical surfaces with respect to the prism base (right) cause off-plane beam misalignments and result in an unavoidable loss of interferometric contrast.

A.4 STRUCTURAL ANALYSIS: MANUFACTURING TOLERANCE

A disadvantage of any experiment using complex optical elements is dealing with manufacturing tolerances and imperfections. For example, relative alignment errors between the three optical surfaces of the OH can cause a bad overlap between the interferometer arms and poor interferometric contrast. Similarly, the perpendicularity of the optical surfaces with respect to the prism base is essential to maintain both interferometers in-plane, as small deviations from such perpendicularity can cause the beams to veer off-plane significantly. This section evaluates the susceptibility of our OH to such manufacturing tolerances, illustrated in Figure A.3.

The first type of manufacturing imperfection is xy-plane geometry, parameterized by two angles: α sets the relative angle between the beam splitting and recombination surfaces S_1 and S_3, while γ is the one between the mirror/window surface S_2 and the prism symmetry axis in this cut plane. Deviations are introduced to these angles in the IFOCAD model, and the resulting degradation of the interferometric contrast is computed. Figure A.4 shows such

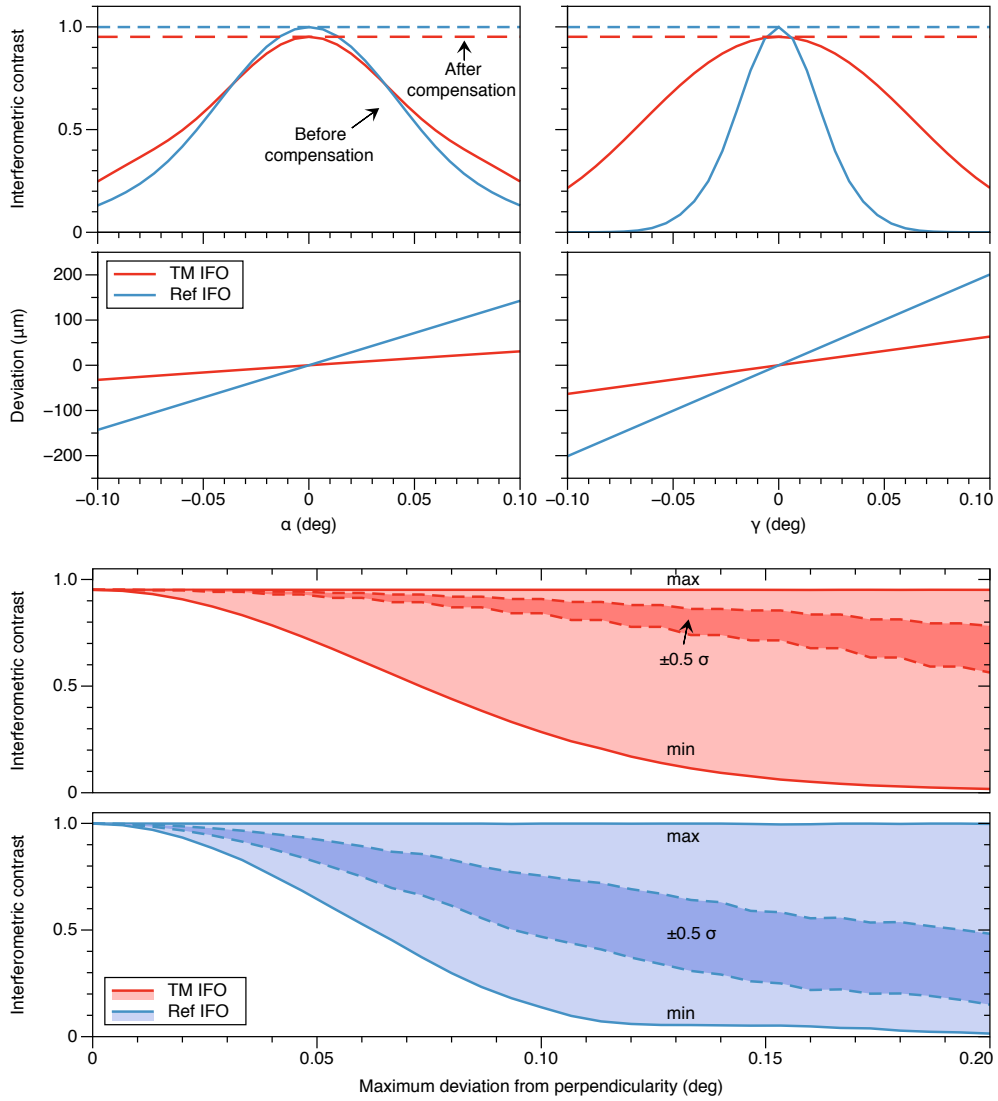

FIGURE A.4: Prism sensitivity to manufacturing imperfections in the xy plane, as parameterized by α (left) and γ (right). **Top:** the degradation of the interferometric contrast with and without compensation by altering the alignment of the input beam direction. **Bottom:** the deviation from the nominal optical path length difference between arms due to the required compensation.

FIGURE A.5: Prism sensitivity to perpendicularity imperfections. The plots show the degradation of the interferometric contrast as a function of the amplitude of the uniform distribution of deviations from perpendicularity injected into all three optical surfaces. The number of Monte Carlo samples at each point is 1000. The dark-shaded area bordered by dashed lines corresponds to $\pm 0.5\,\sigma$, while the light-shaded region is bordered by continuous lines representing the maximum and minimum of the distribution.

degradation can be completely compensated for by fine-tuning the direction of the incident beams in the range of 1 mm translation and 0.5° rotation. Hence, the detector is insensitive to this type of manufacturing imperfections.

The second type of imperfection is for the perpendicularity of the optical surfaces with respect to the prism base. This manufacturing error is far more difficult to compensate for after the construction. Hence, the tolerance specification needs to be set based on the results of simulations. A Monte Carlo simulation is performed where errors are injected into all three critical surfaces following a uniform distribution. The resulting distributions of the interferometric contrast are shown in Figure A.5. This simulation shows that deviations of up to 0.1° are allowable while maintaining the interference contrast greater than 14 % in the reference interferometer and greater than 28 % in the TM interferometer[1].

1 Based on discussions with the precision glass machining companies, this perpendicularity requirement is feasible.

noise source	magnitude	TM IFO	Reference IFO
frequency noise	100 MHz	1.78×10^{5}	5.11×10^{4}
refractive index fluctuation	1×10^{-5} K	1.41×10	1.04×10
thermal deformation	1×10^{-5} K	5.21×10^{-1}	7.92×10^{-1}
FIOS jitter: pitch	1.0 µrad	4.00×10^{-2}	6.76×10^{-3}
FIOS jitter: yaw	1.0 µrad	1.57×10^{-1}	3.30×10^{-2}
FIOS jitter: displacement	10 nm	1.14×10^{-4}	5.68×10^{-5}
TM TTL coupling	20 nrad	1.14×10^{-3}	-
PM noise [64]	0.4 µrad	6.77×10^{-2}	6.77×10^{-2}

TABLE A.3: Amplitude of the displacement noise of two interferometers, in the unit of $\mathrm{pm}/\sqrt{\mathrm{Hz}}$, in a single OH due to the main noise sources. The coefficient of thermal expansion and the dn/dT term of fused silica are taken to be $0.55 \cdot 10^{-6}\,\mathrm{K}^{-1}$, and $9.6 \cdot 10^{-6}\,\mathrm{K}^{-1}$, respectively. IFO: interferometer.

A.5 NOISE BUDGET

The previous sections support the feasibility of the geometry of this novel OH design. This section presents the performance of the SEDI inertial sensor.

The laser frequency noise mentioned above is overwhelming if not dealt with. Using the reference interferometer, this noise source can be subtracted from the primary sensing signal as described in Eq. (A.4).

Thermal noise could also be severe. Refractive index variations are expected to be especially relevant due to the interferometers' long arms having significant intra-prism optical pathlength, as listed in Table A.1.

Other noise sources considered are the angular and translational jitter of the FIOS and the TM tilt-to-length (TTL) coupling. The latter takes the value of $0.06\,\mathrm{pm}\,\mu\mathrm{rad}^{-1}$ at 20 nrad [2] assuming a perfectly manufactured prism.

The estimated levels of these noises are listed in Table A.3. A laser is assumed to be free-running in the observation band. The temperature noise floor aligns with the requirements achieved at the optical components level in space-based experiments such as LISA Pathfinder [65].

The spectral density based on the noise budget is shown on the left panel in Figure A.6. All noises but the laser frequency and thermal fluctuations are shaped with a LISA noise shape function [14] as an example.

A.6 PERFORMANCE ENHANCEMENT

We aim to apply DFMI for sensing multiple degrees of freedom of a TM, i.e., to introduce more OH's and be able to gather more TM interferometer signals. For the rest of this section, we explore the existence of signal combinations among two TM interferometers to ideally suppress laser frequency noise and the next limiting noise source at low frequencies: thermal noise.

2 This stability is assumed to be achieved by a feedback loop to the TM position.

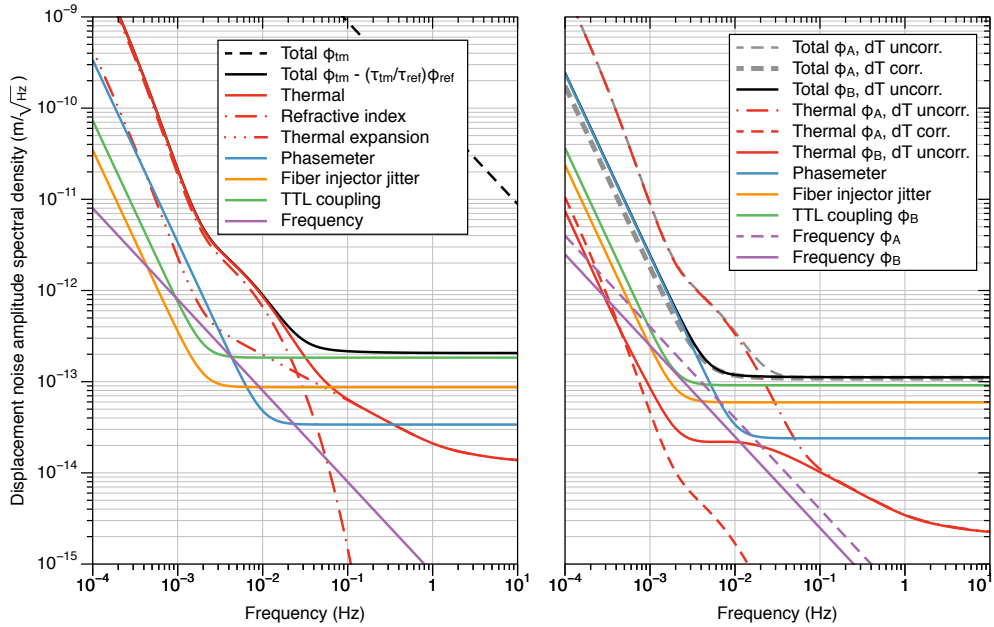

FIGURE A.6: Performance of the SEDI inertial sensor using a single OH (left), and two OHs probing one TM from opposite sides (right). These figures include characteristic imperfections of the manufactured prisms and an absolute ranging error of 1 µm affecting the calibration factor. The right panel shows two cases in which the interferometer temperature fluctuations are correlated or uncorrelated between the two OHs used (*dT* corr. and *dT* uncorr. respectively).

The simplest configuration would probe a TM from opposite sides with two DFMI setups [3]. The conceptual schematic is shown at the top of Figure A.7. First, phase signals in a multiple-SEDI setup are formulated:

$$\phi^L_{\rm tm} = 2\delta\phi + 2\pi\delta f_0 \Delta\tau^L_{\rm tm} + \frac{2\pi}{\lambda_0}\Theta^L_{\rm tm}\delta T^L + \zeta_{\rm tm}, \tag{A.5}$$

$$\phi^R_{\rm tm} = -2\delta\phi + 2\pi\delta f_0 \Delta\tau^R_{\rm tm} + \frac{2\pi}{\lambda_0}\Theta^R_{\rm tm}\delta T^R + \zeta_{\rm tm} + 2\epsilon_{\rm tm}, \tag{A.6}$$

$$\phi^L_{\rm ref} = 2\pi\delta f_0 \Delta\tau^L_{\rm ref} + \frac{2\pi}{\lambda_0}\Theta^L_{\rm ref}\delta T^L + \zeta_{\rm ref}, \tag{A.7}$$

$$\phi^R_{\rm ref} = 2\pi\delta f_0 \Delta\tau^R_{\rm ref} + \frac{2\pi}{\lambda_0}\Theta^R_{\rm ref}\delta T^R + \zeta_{\rm ref} + 2\epsilon_{\rm ref}, \tag{A.8}$$

where

$$\Theta^i_j = \Theta_j + \Delta\Theta^i_j = a^i_j(\Delta l) + b^i_j(\Delta n) \tag{A.9}$$

is the coupling coefficient of temperature fluctuations δT^i to the pathlength signal of the interferometer labeled by $j = \{\text{tm,ref}\}$ and $i = \{\text{L,R}\}$ is used to label the left (L) and right (R) OH. This coupling coefficient consists of the two contributions $a^i_j(\Delta l)$ and $b^i_j(\Delta n)$, respectively, due to the optics' thermal expansion and refractive index change. Θ_j is the nominal coefficient determined by design, and $\Delta\Theta^i_j$ is a correction term, which is attributable, e.g., to compensations of the manufacturing imperfections discussed in the previous section. The ζ_j terms represent common-mode noises between the left and right interferometers, and the ϵ_j terms represent uncorrelated noise sources.

Notice that the common δT^i is used for two interferometers on the side i. This is the remarkable feature of SEDI, which accommodates two interferometers in a single prism. We now investigate the aforementioned two points: a signal combination among TM interferometers and thermal noise subtraction with the reference interferometers.

3 Same as the setup employed by [42]

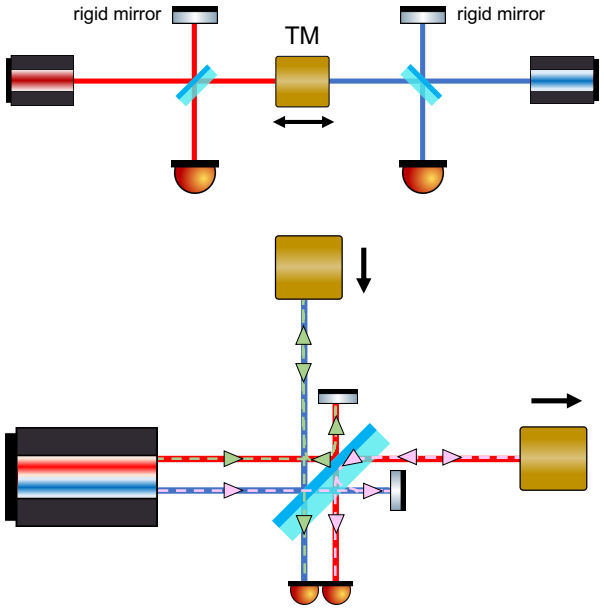

FIGURE A.7: Conceptual schematic of the two-side configuration of optical heads. Illustrated are only TM interferometers. Top: the actual two-sided setup. Bottom: the equal-arm topology, configurable in post-processing.

A.7 COMBINATION OF TM INTERFEROMETERS

First, we investigate the signal combination of the two TM interferometers. Because the TM motion signal $\delta\phi$ has differential couplings to the right and left interferometers, the signal can be extracted as

$$\begin{aligned}\phi^A_{\mathrm{tm}} &= \left(\phi^L_{\mathrm{tm}} - C_{f,\mathrm{tm}}\phi^R_{\mathrm{tm}}\right)/2\left(1+C_{f,\mathrm{tm}}\right)\\ &\simeq \delta\phi + \frac{\pi\delta f_0}{2}\left(\Delta\tau^L_{\mathrm{tm}} - C_{f,\mathrm{tm}}\Delta\tau^R_{\mathrm{tm}}\right) + \delta\theta^A_{\mathrm{tm}}(\delta T) + \frac{\epsilon_{\mathrm{tm}}}{2},\end{aligned} \tag{A.10}$$

where

$$C_{f,tm} = \frac{\Delta\tau^L_{\mathrm{tm}}}{\Delta\tau^R_{\mathrm{tm}}} = 1 + \Delta C_{f,\mathrm{tm}} + \delta C_{f,\mathrm{tm}} \tag{A.11}$$

is the calibration factor to reduce residual laser frequency noise to the limit of the measurement accuracy of 1 µm of arm-length difference[4]. $\Delta C_{f,\mathrm{tm}}$ accounts for the deviation due to the compensation of manufacturing imperfections in the xy plane, estimated to be $O(10^{-3})$ from Figure A.4. $\delta C_{f,\mathrm{tm}}$ accounts for the error in the estimation of the arm-length difference, which is $O(10^{-5})$[5]. The introduction of this calibration factor represents the fine-tuning of arm lengths of two interferometers to synthesize an equal-arm interferometer insensitive to laser frequency noise. This is conceptually illustrated in the bottom of Figure A.7.

A.8 THERMAL NOISE REDUCTION WITH REFERENCE INTERFEROMETERS

Finally, we investigate the ability to reduce thermal noise using the reference interferometer signals. The similarity between the temperature fluctuations in the left and right OHs is, in principle, unknown, making thermal noise a

4 This factor is unity in an ideal case assuming the identical parameters are adopted for the left and right setups.

5 This would set the performance limit of suppression of laser frequency noise.

potentially limiting noise source. Expanding the thermal noise coupling term from Eq. (A.10) yields

In the worst case, thermal noises on the two OHs are incoherent, and the thermal noise curve in the left of Figure A.6 exists as-is.

$$\frac{2\lambda_0}{\pi}\delta\theta^A_{\rm tm}(\delta T) = \Theta_{\rm tm}\left(\delta T^L - C_{f,\rm tm}\delta T^R\right) + \Delta\Theta^L_{\rm tm}\delta T^L - C_{f,\rm tm}\Delta\Theta^R_{\rm tm}\delta T^R. \tag{A.12}$$

The reference interferometers can be finally invoked to suppress the thermal noise term further;

$$\begin{aligned}\phi^B_{\rm tm} &= \phi^A_{\rm tm} - C_T\left(\phi^L_{\rm ref} - C_{f,\rm ref}\phi^R_{\rm ref}\right)/2\left(1 + C_{f,\rm tm}\right)\\ &\simeq \delta\phi + \delta\theta^B_{\rm tm}(\delta T) + \frac{\epsilon_{\rm tm}}{2} + \frac{C_T\epsilon_{\rm ref}}{2},\end{aligned} \tag{A.13}$$

where

$$C_T = \frac{\Theta_{\rm tm}}{\Theta_{\rm ref}} = \frac{a_{\rm tm}(\Delta l) + b_{\rm tm}(\Delta n)}{a_{\rm ref}(\Delta l) + b_{\rm ref}(\Delta n)} \tag{A.14}$$

is a calibration factor determined by design [6]. The residual thermal noise $\theta^B_{\rm tm}(\delta T)$ reads

$$\begin{aligned}\frac{2\lambda_0}{\pi}\delta\theta^B_{\rm tm}(\delta T) &\simeq \left(\Theta^L_{\rm tm} - C_T\Theta^L_{\rm ref}\right)\delta T^L - \left(C_{f,\rm tm}\Theta^R_{\rm tm} - C_T C_{f,\rm ref}\Theta^R_{\rm ref}\right)\delta T^R\\ &\simeq \left[\Delta\Theta^L_{\rm tm} - C_T\Delta\Theta^L_{\rm ref}\right]\delta T^L\\ &\quad - \left[\Delta\Theta^R_{\rm tm} + \Delta C_{f,\rm tm}\Theta_{\rm tm} - C_T\left(\Delta\Theta^R_{\rm ref} + \Delta C_{f,\rm ref}\Theta_{\rm ref}\right)\right]\delta T^R.\end{aligned} \tag{A.15}$$

Only the cross terms of δT with $\delta\Theta$ and $\Delta C_{f,j}\Theta$ remain; hence, the major thermal noise contribution can be eliminated regardless of its correlation between the two OHs. Performances of these combinations Eqs. (A.10) and (A.13) are plotted on the right of Figure A.6.

This thermal noise reduction scheme assumes that the TM and reference interferometers in the same OH are affected coherently by the thermo-optical fluctuations in the optic. This assumption seems to be valid based on COMSOL simulations performed by Miguel Dovale. Nevertheless, the influence of an arbitrary correlation between the two interferometers accommodated in a single prism is analyzed and plotted in Figure A.8.

6 This factor relates the thermally induced optical pathlength variations in the TM interferometer to those in the reference interferometer and is determined purely geometrically.

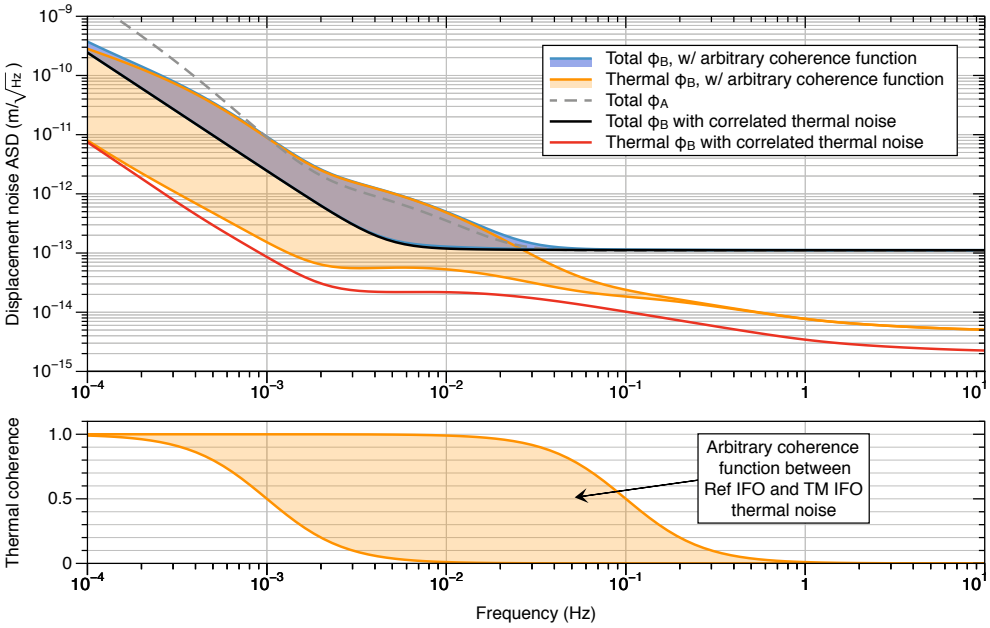

FIGURE A.8: Influence of an arbitrary correlation in temperature noise between two interferometers in a single OH on the performance of the dual-OH setup. The coherence function is assumed to take the form $1/\sqrt{1+(f/f_c)^2}$, where f is the Fourier frequency and f_c is the cut-off frequency, yielding perfect correlation at frequencies $f \ll f_c$, and total uncorrelation at frequencies $f \gg f_c$. In this example, we show the resulting displacement noise for an arbitrarily distributed coherence function with $f_c \in (10^{-3}, 10^{-1})$ Hz.

B

NEW TOPOLOGY OF ON-AXIS LASER RAGING INTERFEROMETRY

The Gravity Recovery and Climate Experiment (GRACE) mission [66], in orbit since March 2002 to the end of its science mission in October 2017, was a joint mission of the National Aeronautics and Space Administration (NASA) and the German Aerospace Center (DLR). Twin satellites, in a trailing formation flying $\sim 500\,\mathrm{km}$ above the Earth with a nominal separation of 200 km on a near-polar orbit, mapped the spatial and temporal variations of the Earth's gravity field.

The Gravity Recovery and Climate Experiment Follow-On (GRACE-FO) mission [66] was launched in May 2018, again as a US-German collaboration. This follow-up mission employs the laser ranging interferometry (LRI) as a technology demonstrator, and the OB was of the so-called "off-axis" type [67], in which the receiving (RX) light and the transmitting (TX) light propagate into and out of the OB through different apertures.

On the other hand, the "on-axis" topology [68, 69] shares the same optical path for the two beams with a single baffle and telescope at the cost of a more complex OB setup, including polarizing optics.[1] Such a single telescope is, if a telescope is implemented, advantageous to practical constraints of space missions on mass, space, cost, etc. This chapter proposes the new "on-axis" topology as a part of preparatory studies for a next generation gravity mission (NGGM). The detailed description can be found in [70]. Based on conceptualization by Yichao Yang and Vitali Müller, the author contributed to methodology and numerical simulation, together with Miguel Dovale Álvarez.

B.1 OPTICAL BENCH DESIGN

Some general design requirements are applied to the OB regardless of its topology. Here, two critical requirements are featured: a beam alignment system and a stable virtual reference point (RP).

The first point influences various aspects of LRI. For example, the carrier-to-noise ratio (CNR) of the heterodyne beatnote needs to be high enough to maintain stable transponder mode and to suppress shot noise which could be dominant with a long baseline at high frequencies instead of laser frequency noise. The alignment can be automatically achieved by combining a fast steering mirror (FSM) and an imaging system. On top, this solution ensures that the TTL couplings on both the local and distant OBs are significantly suppressed.

The second point is to guarantee the invariance of measured ranges under small rotations on an arbitrary axis of the SC around its center of mass, where an accelerometer is located. The virtual RP needs to be physically accessible and co-located with the SC center of mass. A reasonable value for the in-flight

1 This type of topology is also adopted in LISA.

TTL coupling is of the order of $100\,\mu m\,rad^{-1}$, which has been demonstrated by the GRACE-FO LRI [71], and, to some extent, can be reduced further by in-flight calibrations.

B.2 LAYOUT

The proposed OB design is depicted in Figure B.1. The RX beam enters the OB via mirror M1, which images the virtual RP (i.e., the SC c.m.) into the RX/TX reference point aperture located in the OB. The local oscillator (LO) and TX beams originate from a single beam injected into the OB via a fiber injector. After passing a suitably aligned polarizer, this initial beam contains 8 % p-polarized and 92 % s-polarized light. Through interacting with the polarizing beamsplitter PBS2, the beam is split into the TX beam (p-pol), which is transmitted out of the SC via the same path as the RX beam, and the LO beam (s-pol), which propagates to PBS1 where it interferes with the RX beam. The RX-LO beatnote is then captured by both QPDs QPD1 and QPD2 in a balanced detection scheme. A total of three retarder waveplates (WP1, WP2, and WP3) are placed north, west, and east of PBS2 to keep all beams in orthogonal polarization states before the RX-LO interference at PBS1. The main purpose of introducing WP2 with its slow axis at 22.5° is to allow both the local and the remote SC optical benches to share identical optical layouts, as they both receive and transmit beams with $-45°$ and 45° linear polarizations, respectively.

The acquisition system comprises an imaging system and a focal plane detector to image the RX light. Such a scheme is commonly used in space laser communication terminals [72].

A total of five two-lens imaging systems are implemented with four lenses: two of the so-called RX imaging systems, which share lens L3 (L3-L1 and L3-L2); two of the so-called LO imaging systems, which share lens L4 (L4-L1 and L4-L2); and the so-called TX imaging system (L4-L3). They also serve as Keplerian telescopes: compressing or enlarging the beams to what is desired [2].

The layout enables range measurements to be insensitive to some particular path-length fluctuations on the bench. In this layout, the north and south of PBS2 are insensitive. The former is common for the RX and LO beams; hence, its fluctuation does not change an interference pattern. The latter is common for the TX and LO beams, meaning the transponder scheme compensates for its fluctuation.

B.3 CHARACTERISTICS

The unique characteristics of the layout introduced in Appendix B.2 are highlighted here.

First, in the RX and LO imaging systems, the first lens acts on only one of the two interfering beams, while the second acts on both. This allows magnifications of all imaging systems to be tuned to flexibly adjust the size of the beams to match the RX/TX aperture, as well as the active area of the PRs.

2 For example, to adapt the size of the interfering beams to the active area of the PDs, or to enlarge the size of the transmit beam to decrease its divergence.

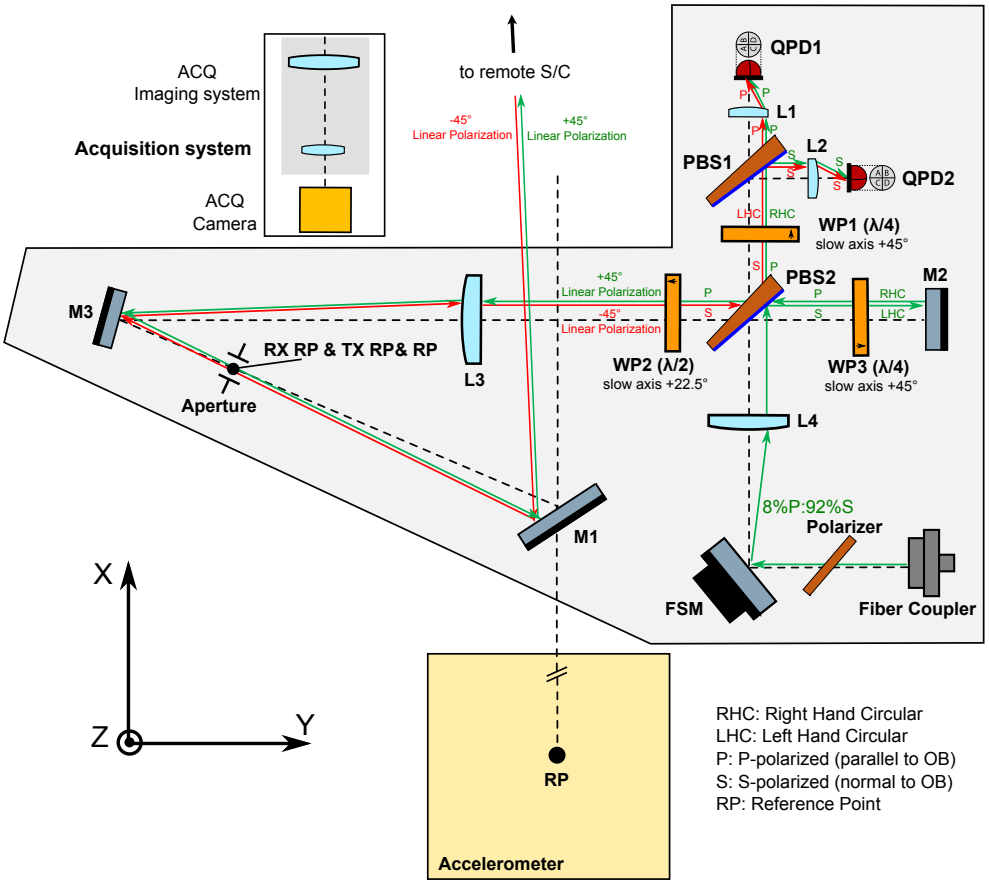

FIGURE B.1: LRI optical bench layout. The green arrows depict the path and direction of the LO and TX beams, originating from a single beam injected into the bench via a fiber injector. The red arrows depict those of the RX beam, which couples into the bench via mirror M1. The polarization state of each beam is indicated (RHC: right-hand circular; LHC: left-hand circular). The RX and TX RPs coincide in the left focal plane of lens L3, along the optical axis between mirrors M3 and M1. The RX/TX RP is imaged into the SC center of mass, where an accelerometer is located. The range measurement is invariant under rotations of the SC around this point. The RX and LO beams interfere at polarizing beamsplitter PBS1 and are captured by the pair of quadrant photodiodes QPD1 and QPD2 in a balanced detection configuration.

The resulting configuration is unique, compared with other interferometers employing imaging systems with all lenses placed after the interferometer's beam combiner [69, 68, 67, 73]. Therefore, the impact of non-common effects between the two first lenses is scrutinized as analyzed in Appendix B.7.2.

Second, this layout does not introduce any complex structure for a retro-reflective function. GRACE-FO LRI adopted the triple-mirror assembly as a retroreflector, further studied [74]. The recent study [69] proposed a corner cube retroreflector. On the other hand, the layout shown in Figure B.1 achieves the retro-reflective function with a single mirror M2 in between the TX imaging system. This simple "retroreflector" would be beneficial to ease the construction and/or to make itself less susceptible to in-flight environmental perturbations.

Last but not least, all polarizing components are placed inside imaging systems. This implies that any tilted beam incident on imaging systems passes through polarizing components with constant tilt only with a beam walk. That could be beneficial for polarization interferometers.

B.4 COMPARISON WITH FORMER DESIGNS

The proposed layout is compared in Table B.1 against the original and modified GRACE-FO LRI OBs [3]. Two configurations of the new LRI OB ("A" and "B") differ in the radius of the injected local beam.

3 The modified GRACE-FO LRI OBs are for a fair comparison with the new LRI OB "A" using the same aperture design.

Table B.1: Comparison of optical parameters between two configurations of the proposed LRI OB design, the GRACE-FO LRI OB, and two modified versions of the GRACE-FO LRI OB. For CNR, considered is a 50 µrad misalignment of the local SC with respect to the line-of-sight to the remote SC [67, 68].

	New LRI OB "A"	*New LRI OB "B"*	*GRACE-FO*	*GRACE-FO Mod 1*	*GRACE-FO Mod 2*
aperture size	8.0 mm	8.0 mm	4.0 mm	8 mm	8.0 mm
LO waist radius	2.5 mm	1.0 mm	2.5 mm	2.5 mm	6.6 mm
RX magnification	0.064	0.064	0.125	0.064	0.064
LO magnification	0.168	0.168	0.125	0.064	0.064
TX magnification	2.646	2.646	n/a	n/a	n/a
het. efficiency	0.85	0.23	0.67	0.2	0.85
TX divergence angle	65 µrad	131 µrad	149 µrad	138 µrad	65 µrad
CNR (ideal)	94.2 dB	82.9 dB	81.2 dB	82.5 dB	94.9 dB
CNR (misaligned)	88.8 dB	81.4 dB	80.0 dB	81.2 dB	89.5 dB

Since the magnification of each beam cannot be adjusted independently in GRACE-FO unlike the new LRI OB (see Appendix B.3), the "Modified 1" design results in a great degradation of heterodyne efficiency. As illustrated in the "Modified 2" design, enlarging the waist radius of the LO beam leads to similar CNR performance as the new LRI OB "A" design. However, this requires the increased optical complexity of achieving such a large waist size.

This comparison shows the excellence of the new layout in scalability as highlighted in Appendix B.3.

B.5 OPTICAL SIMULATION

This is chosen due to the smaller size of the beam injected into the OB, which is straightforward to realize using commercially available fiber injectors.

The IFOCAD model of the new LRI OB "B"design from Table B.1 is built to quantitatively assess the OB from several aspects under the RX beam rotation: TTL noise, beam alignments and their robustness under environmental perturbations. The model is illustrated using OPTOCAD [75] in Figure B.2.

The simulation presented in the later sections has some interesting features in the context of IFOCAD modeling:

- TTL coupling over 200 km SC separation
- FSM control loop using differential wavefront sensing (DWS) signals
- Flat-top beam due to the clipping at the aperture

The first point makes this simulation unique because none of the former IFOCAD models simulates such a long baseline. Simulation is based on a double-precision floating-point format with a dynamic range of 10^{16}. Hence, the model can simulate length changes with the precision of the order of 0.1 nm out of 200 km.

The second point requires a fast optimization to derive a proper FSM rotation angle matching an injected RX rotation. These two rotation angles are related via a constant factor in theory, depending on magnifications.

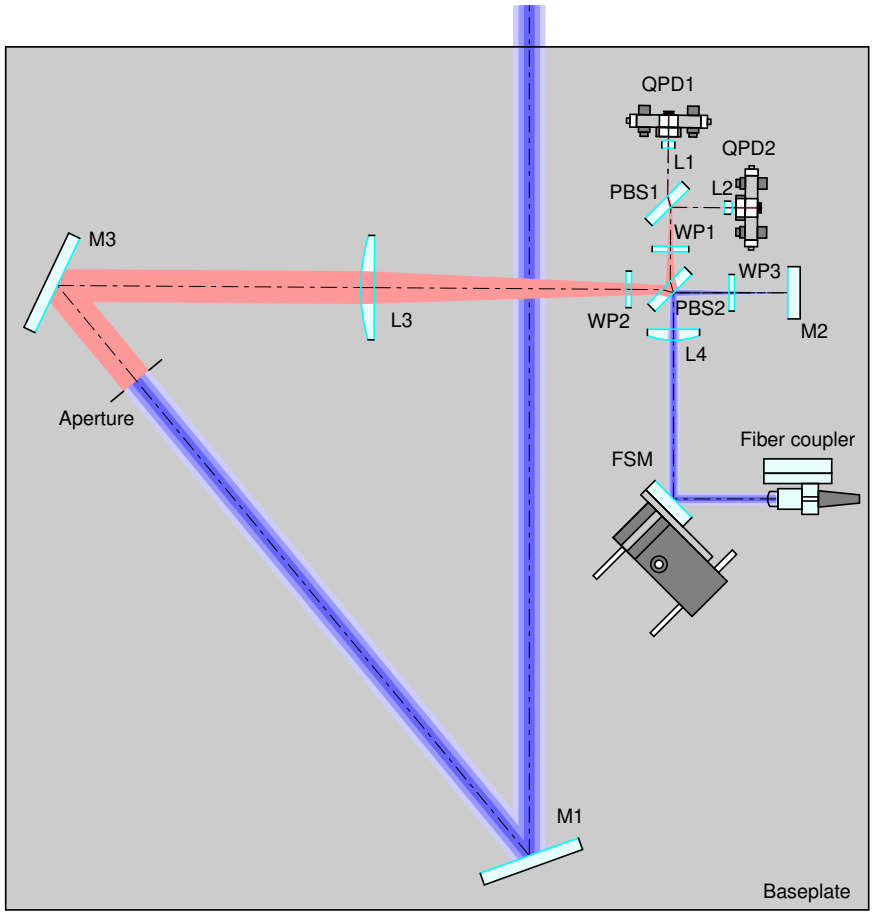

FIGURE B.2: LRI OB as modelled in IFO-CAD and drawn in OPTOCAD. The RX beams start at the receive aperture (red). The TX and LO beams stem from the beam injected into the OB by the fiber injector (blue). The baseplate assumed in the thermal analysis is drawn as a rectangle enclosing all the components on the OB.

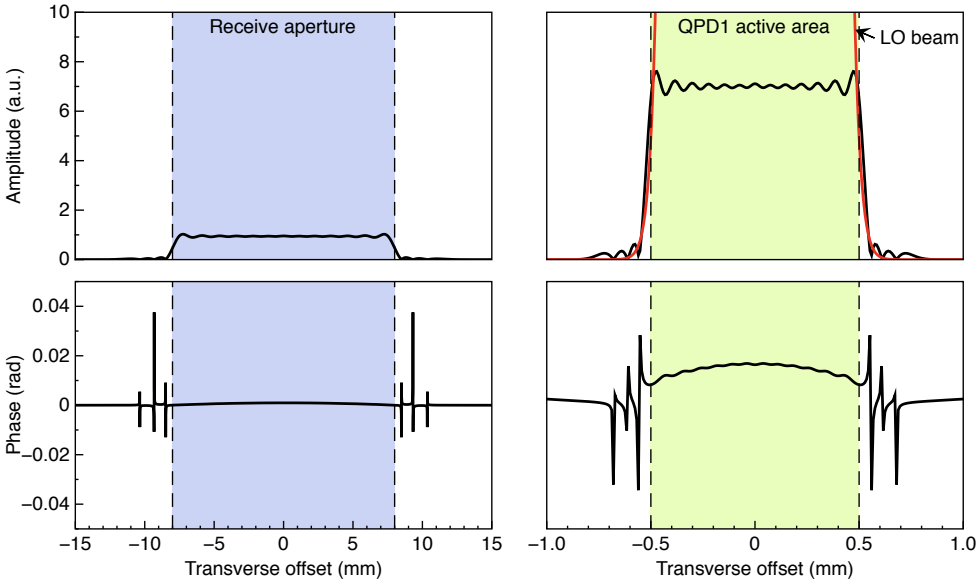

FIGURE B.3: Amplitude and phase of the "flat-top" RX beam at the receive aperture and at the surface of QPD1, in the horizontal direction. The dashed lines indicate the boundaries of the aperture and the active area of the photodiode, respectively. The RX beam is modeled in IFOCAD using the mode-expansion method. The amplitude of the local oscillator beam at QPD1 is shown in red, showing good spatial overlap with the RX beam, despite the much larger peak amplitude.

Simulation first optimizes a FSM angle at a certain RX angle and deduces this factor from their ratio. The derived linear function with the factor lets us start with a good initial estimate. This largely reduces the workload of the rest of the optimizations.

To realize the third point, the mode expansion method (MEM) [76] is adopted. In the MEM, the electrical field of the incoming Gaussian beam $E(x,y)$ is decomposed into Hermite-Gaussian modes $u_{mn}(x,y;q)$,

$$E_{MEM}(x,y) = \sum_{m=0}^{N_{max}} \sum_{n=0}^{N_{max}-m} a_{mn} u_{mn}(x,y;q) \exp(-iks), \tag{B.1}$$

where a_{mn} is the mode amplitude, k is the wavenumber, s is a propagation distance, and N_{max} is the maximum expansion order, which limits the decomposition performance. Figure B.3 shows the amplitude and phase of the RX beam at the receive aperture and at the surface of QPD1, as obtained via the MEM simulation with N_{max} of 30.

Polarization and stray light effects are neglected in the following simulation. These will be the subject of future investigations.

B.6 SIMULATION PROTOCOL

The whole simulation comprises the setup configuration and the scientific simulation. Their protocols are summarized as follows:

Setup configuration:

(i) initialize OB components with the rough positioning,

(ii) optimize imaging systems by fine-tuning the position of,

  (a) the QPDs along the nominal optical axis to minimize the beam walk of the LO beam on the detector planes

  (b) L3 to minimize the separation between the front focal point of L1 and the effective focal point of the system composed of L3, WP2, PBS2, WP1 and PBS1,

(c) the receiving aperture to minimize the interferometer's TTL coupling, as sensed by both QPDs, under pitch and yaw rotations of the SC with an active FSM[4],

(d) M2 such that the effective focal point of the TX imaging system is located at the RX/TX RP, and thus near-perfect TX beam pointing to the remote SC is achieved.

Scientific simulation:

(i) the local SC analysis,

(a) the RX Gaussian beam is propagated from the remote to the local SC, tilted at the aperture and clipped by the MEM,

(b) the flat-top RX beam is propagated through the setup,

(c) the RX beam is interfered with the LO beam whilst the FSM is being actively controlled using DWS loops,

(d) the longitudinal pathlength signal (LPS) variations are measured, and the local TTL coupling is evaluated,

(ii) the remote SC analysis,

(a) the position of a distant single-element photo detector (SEPD) representing the remote OB is derived by intersecting the RX beam direction with a sphere of 200 km radius centered around the unfolded RX RP,

(b) a large Gaussian beam acting as a remote LO beam is generated at the distant SEPD,

The radius of this LO beam is set large enough such that this distant system acts as a perfect transponder, measuring a range unaffected by the wavefront of the interfering beams.

(c) the TX beam is propagated to this SEPD and interfered with the remote LO beam,

(d) the LPS measured by the distant SEPD is obtained and the TX beam TTL coupling is evaluated.

B.7 RESULTS

Following the protocol in Appendix B.6, the scientific simulation is conducted with and without environmental perturbations. This simulation shows the variation of relevant quantities as a function of the RX beam angle in both the pitch and yaw degrees of freedom for the interferometer with closed-loop control of the FSM.

B.7.1 *Ideal performance*

The results in an ideal situation are depicted in Figure B.4. The figure shows (in order from top to bottom) the position acquired by the FSM under a given misalignment; the measured in-loop (QPD1) and out-of-loop (QPD2) horizontal and vertical DWS signals; the deviation of the TX beam from the inter-satellite line of sight; the RX and LO beam walk at the QPDs; the

4 Using the DWS signals at QPD1 to actuate on the steering mirror's pitch and yaw degrees of freedom to yield optimally overlapped phasefronts between the RX and LO beams at the detectors

TTL coupling experienced at the local SC; and the TX beam TTL coupling measured at the distant SC in perfect-transponder mode.

The required FSM tilt angle is not the same as the RX beam angle due to magnifications and the OB's geometry. A beam tilt angle before an imaging system is translated to the angle after it via magnification. The RX and LO beams must be aligned, i.e., share the same angle at QPD; hence, their tilt angles before each imaging system θ_{RX} and θ_{LO} are related by

$$\theta_{RX}/\alpha_{RX} = \theta_{LO}/\alpha_{LO}, \tag{B.2}$$

where α_{RX} and α_{LO} are magnifications of the imaging systems. In addition, the FSM tilt angle θ_{FSM} is translated to the LO beam angle via a scaling factor β,

$$\theta_{LO} = \beta \cdot \theta_{FSM}. \tag{B.3}$$

The factor β depends on the degree of freedom: $\beta = 2$ and $\sqrt{2}$ for the yaw and pitch motions, respectively. Eqs. (B.2) and (B.3) give us the FSM tilt angle to compensate for the RX beam tilt,

$$\theta_{FSM} = \frac{1}{\beta}\frac{\alpha_{LO}}{\alpha_{RX}}\theta_{RX}. \tag{B.4}$$

Hence, the RX beam angle θ_{RX} of 2000 µrad in yaw and pitch can be compensated for by the FSM angles of 2625 µrad and 3712 µrad (see Table B.1 for magnifications). The top panels for yaw (left) and pitch (right) show the consistent FSM angles.

The out-of-loop DWS signals are small but orders of magnitude greater than the in-loop signals due to the asymmetry between the reflection and transmission ports of PBS1. The numerical error of double precision is visible in the TX beam TTL coupling as mentioned at the beginning of Appendix B.5.

As mentioned in Appendix B.3, the installation error of M2 directly affects the OB's retro-reflective function by changing the position of the TX RP, thereby introducing extra TTL coupling to the range measurement. This effect is modeled and characterized, and it is determined that with positional tolerances of 0.05 mm and angular tolerances of 50 µrad, the extra TTL coupling in all three rotation axes is $\sim$10 µm rad^{-1}. This performance impact is similar to that of the triple-mirror-assembly of the GRACE-FO LRI, where the misalignment of the three mirrors introduced a TTL coupling of less than 20 µm rad^{-1} in all three rotation axes [77].

B.7.2 *Thermal drift*

Finally, a thermal analysis is carried out as a representative environmental perturbation to ensure that the proposed OB layout is robust against thermoelastic deformation and refractive index variations due to temperature drifts. This analysis is critical since the RX and LO imaging systems, as highlighted in Appendix B.3, feature different sets of components on their respective sensitive paths. This means that, e.g., any thermal effects introduced by lenses L3 and L4 are not common-mode between the interfering beams.

The expected thermal drift on the optical bench is $\pm$3 K/orbit [66]. Hence, the temperature is swept within this range, and the thermoelastic expansion

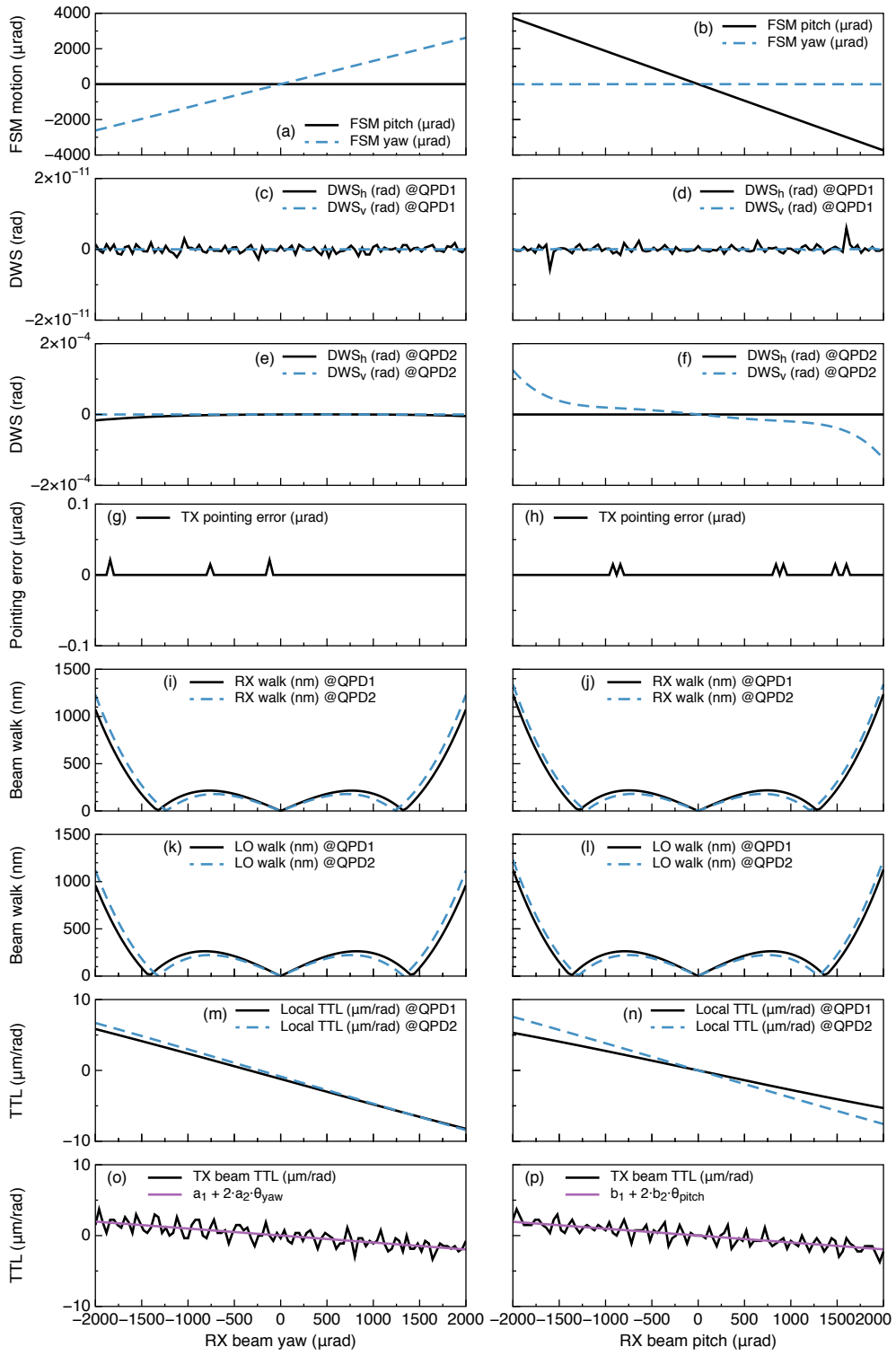

FIGURE B.4: LRI ideal simulation: Angular motion of the local SC causes the received beam's incidence angle at the receive aperture to change (the abscissas). A steering mirror is actuated (a, b) via two independent DWS control loops that zero the DWS_h and DWS_v signals in QPD1 (c, d), keeping the RX and LO phase fronts nearly parallel at both detectors. QPD2 is out of loop and measures nearly zero DWS_h and DWS_v (e, f). The TX imaging system ensures that the TX beam is antiparallel to the RX beam in the inter-SC path (g, h). The RX and LO imaging systems ensure that the RX and LO beams experience minimal beam walk at the detectors (i-l), as well as minimal TTL coupling, measured both locally (m, n) and at the distant SC (o, p).

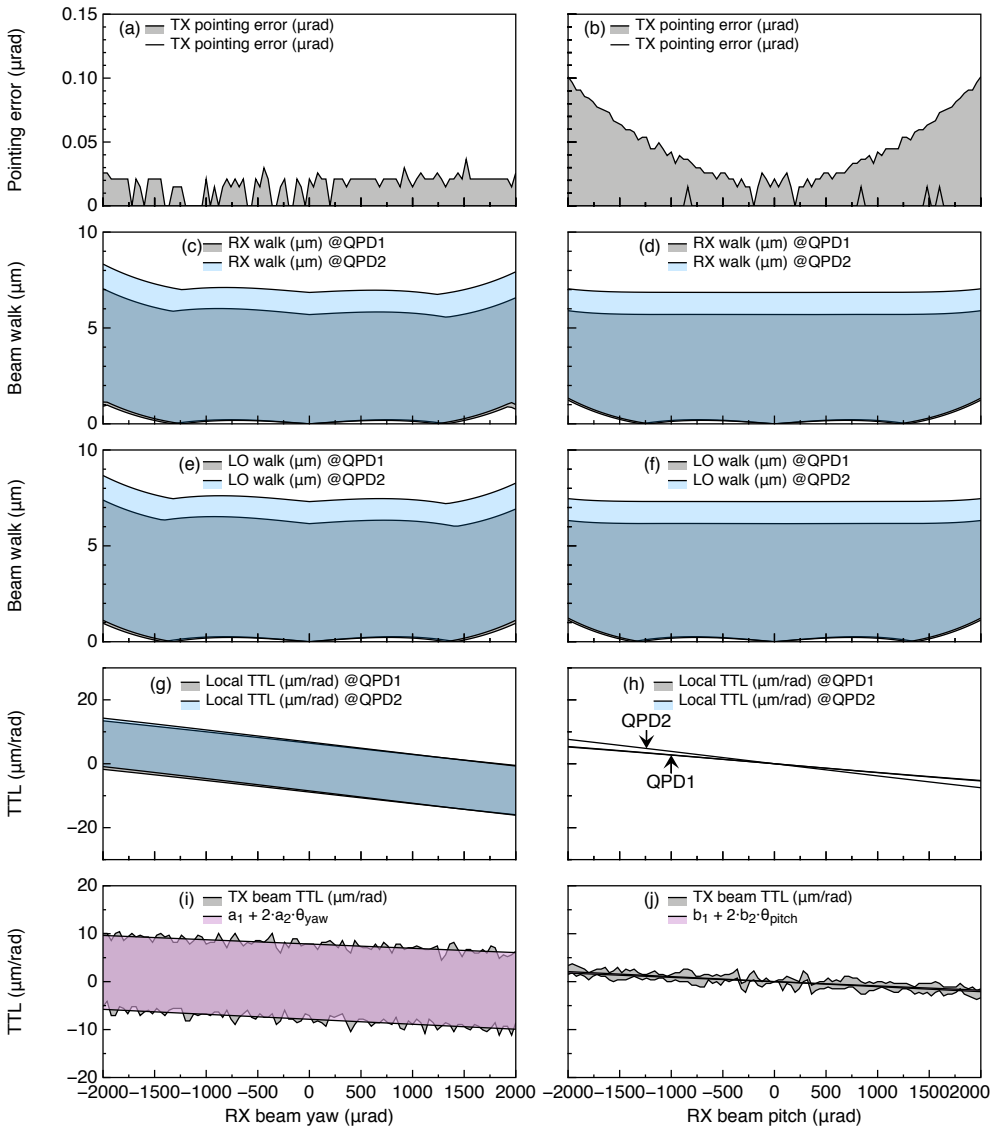

FIGURE B.5: LRI thermal analysis. The temperature is swept in the ±3 K range in seven steps, and the TTL coupling simulation is carried out for each step of temperature and RX beam tilt in the pitch and yaw degrees of freedom. The shaded regions shown in the plots are bounded by the maximum and minimum results for TX pointing error (a, b), RX beam walk (c, d), LO beam walk (e, f), local TTL coupling (g, h), and TX beam TTL coupling (i, j) throughout the temperature range.

and the refractive index change are uniformly applied to all optical components. The components are assumed to be attached to a baseplate that expands uniformly, changing the components' positions w.r.t. the baseplate's center of mass [5]. The results are shown in Figure B.5. This shows the maximum magnitude of the total TTL coupling of 18.1 μm rad^{-1} and 1.16 μm rad^{-1} over 300 μrad in yaw and pitch, respectively. These are both below the GRACE-FO requirement of 80 μm rad^{-1} [67], and thus verify the feasibility of the design in terms of the orbital thermal drift.

5 For the optical components, the thermal coefficients of fused silica are used, $\alpha = 5.5 \times 10^{-7}$ 1/K, and $\beta = 9.6 \times 10^{-6}$ 1/K, where α measures the fractional length change ($\Delta L/L$ per Kelvin) and β measures the fractional refractive index change ($\Delta n/n$ per Kelvin). On the other hand, the baseplate is assumed to be made of Titanium with $\alpha = 8.6 \times 10^{-6}$ 1/K

C

OPTICAL NOISE IN HETERODYNE INTERFEROMETRY

Optical noises in heterodyne interferometry will be arbitrarily categorized in this chapter. This will reveal that the particular type of noise coupling can be mitigated via balanced detection, for example, laser RIN [78].

C.1 PHASE NOISE CATEGORIZATION

In this section, coupling mechanisms of phase noise in heterodyne interferometry are arbitrarily categorized into several types. The electromagnetic fields used in this section are listed below,

$$E_a(t) = |E_a| e^{i\omega_a t}, \tag{C.1}$$

$$E_b^A(t) = |E_b| e^{i\left((\omega_a+\omega_{\text{het}})t+\phi_s(t)+\phi_n^A(t)\right)}, \tag{C.2}$$

$$E_b^B(t) = |E_b| e^{i((\omega_a+\omega_{\text{het}})t+\phi_s(t))} + |E_n| e^{i\left(\omega_a t+\phi_n^B(t)\right)}, \tag{C.3}$$

$$E_b^C(t) = |E_b| e^{i((\omega_a+\omega_{\text{het}})t+\phi_s(t))} + |E_n| e^{i\left((\omega_a+\omega_{\text{het}})t+\phi_n^C(t)\right)}, \tag{C.4}$$

where $E_a(t)$ is a reference beam, $E_b(t)$ is a measurement beam, $\phi_s(t)$ is a target phase signal, $\phi_n(t)$ is any phase noise encoded in the particular way and $|E_n|$ is an amplitude of the noise term.

For the sake of simplicity, a combining BS is assumed to be a perfect 50:50 BS in the rest of this section. On top, only AC contributions in the power of superimposed fields are of interest, hence, discussed.

C.1.1 *Phase noise: Type A*

This type of phase noise is directly embedded in a phase of an electromagnetic field. A signal measured by a PR is a power of the superposition of the two fields. After a combining BS, the AC term of the power on each complementary port has the following expressions,

$$\begin{aligned}\delta P^A(t) &= 2\,\text{Re}(E_a E_b^{A^*}) \\ &= 2|E_a||E_b|\cos\left(\omega_{\text{het}}t+\phi_s(t)+\phi_n^A(t)\right),\end{aligned} \tag{C.5}$$

$$\begin{aligned}\delta P_\pi^A(t) &= -2\,\text{Re}(E_a E_b^{A^*}) \\ &= 2|E_a||E_b|\cos\left(\omega_{\text{het}}t+\phi_s(t)+\phi_n^A(t)+\pi\right).\end{aligned} \tag{C.6}$$

By demodulating either of the signals, the phases can be extracted.

$$\delta\phi^A(t) = \phi_s(t)+\phi_n^A(t), \tag{C.7}$$

$$\delta\phi_\pi^A(t) = -\phi_s(t)-\phi_n^A(t). \tag{C.8}$$

Type A represents any displacement/misalignment noises caused by a variety of mechanisms, e.g., SC motions, TM motions, TTL couplings, original laser noises, OB mechanical fluctuations, etc.

C.1.2 *Phase noise: Type B*

This type of phase noise appears in one of two electromagnetic fields as an additional term oscillating at the other beam frequency. The AC term of the power on each complementary port has the following expressions,

$$\begin{aligned}\delta P^B(t) &= 2\,\mathrm{Re}(E_a E_{b,1}^{B^*}) + 2\,\mathrm{Re}(E_{b,1}^{B} E_{b,2}^{B^*}) \\ &= 2|E_a||E_b|\cos\left(\omega_{\mathrm{het}}t + \phi_s(t)\right) \\ &\quad + 2|E_b||E_n|\cos\left(\omega_{\mathrm{het}}t + \phi_s(t) + \phi_n^B(t)\right), \end{aligned} \tag{C.9}$$

$$\begin{aligned}\delta P_\pi^B(t) &= -2\,\mathrm{Re}(E_a E_{b,1}^{B^*}) + 2\,\mathrm{Re}(E_{b,1}^{B} E_{b,2}^{B^*}) \\ &= 2|E_a||E_b|\cos\left(\omega_{\mathrm{het}}t + \phi_s(t) + \pi\right) \\ &\quad + 2|E_b||E_n|\cos\left(\omega_{\mathrm{het}}t + \phi_s(t) + \phi_n^B(t)\right), \end{aligned} \tag{C.10}$$

where $E_{b,1}^B$ and $E_{b,2}^B$ are the first and second terms of E_b^B in Eq. (C.3) and $\phi_n^B(t)$ is assumed to be DC. We can derive the phase signals by demodulation as follows,

$$\begin{aligned}\delta\phi^B(t) &= \phi_s(t) + \arctan\left(\frac{|E_n|\sin\phi_n^B(t)}{|E_a| + |E_n|\cos\phi_n^B(t)}\right) \\ &\approx \phi_s(t) + \frac{|E_n|}{|E_a|}\sin\phi_n^B(t), \end{aligned} \tag{C.11}$$

$$\begin{aligned}\delta\phi_\pi^B(t) &= \phi_s(t) + \arctan\left(\frac{|E_n|\sin\phi_n^B(t)}{-|E_a| + |E_n|\cos\phi_n^B(t)}\right) \\ &\approx \phi_s(t) - \frac{|E_n|}{|E_a|}\sin\phi_n^B(t), \end{aligned} \tag{C.12}$$

Increasing the power of the "reference beam" $|E_a|$ can improve SNR as long as the noise amplitude $|E_n|$ is not proportional to it.

Type B has a unique feature: this can be suppressed by balanced detection using both ports of a combining BS, see Appendix C.2.

C.1.3 *Phase noise: Type C*

This type of phase noise appears in one of two electromagnetic fields as an additional term oscillating at the same frequency.

$$\begin{aligned}\delta P^C(t) &= 2\,\mathrm{Re}(E_a E_b^{C^*}) \\ &= 2|E_a|\left[|E_b|\cos\left(\omega_{\mathrm{het}}t + \phi_s(t)\right) + |E_n|\cos\left(\omega_{\mathrm{het}}t + \phi_s(t) + \phi_n^C(t)\right)\right], \end{aligned} \tag{C.13}$$

$$\begin{aligned}\delta P_\pi^C(t) &= -2\,\mathrm{Re}(E_a E_b^{C^*}) \\ &= -2|E_a|\left[|E_b|\cos\left(\omega_{\mathrm{het}}t + \phi_s(t)\right) + |E_n|\cos\left(\omega_{\mathrm{het}}t + \phi_s(t) + \phi_n^C(t)\right)\right], \end{aligned} \tag{C.14}$$

The phase signals are,

$$\begin{aligned}\delta\phi^C(t) &= \phi_s(t) + \arctan\left(\frac{|E_n|\sin\phi_n^C(t)}{|E_b| + |E_n|\cos\phi_n^C(t)}\right)\\ &\approx \phi_s(t) + \frac{|E_n|}{|E_b|}\sin\phi_n^C(t), \qquad \text{(C.15)}\\ \delta\phi_\pi^C(t) &= -\phi_s(t) - \arctan\left(\frac{|E_n|\sin\phi_n^C(t)}{|E_b| + |E_n|\cos\phi_n^C(t)}\right)\\ &\approx -\phi_s(t) - \frac{|E_n|}{|E_b|}\sin\phi_n^C(t), \qquad \text{(C.16)}\end{aligned}$$

The noise characteristic of Type C is, in a sense, between Type A and Type B. Phase noise is shifted by π together with a signal phase on a secondary port, as with Type A. On the other hand, analogous to Type B, increasing the nominal beam power $|E_b|$ could improve the performance, depending on the feature of the noise amplitude $|E_n|$. For example, one typical noise source in Type C, i.e., an on-axis ghost beam, would have $|E_n|$ proportional to $|E_b|$. This cannot be suppressed only by changing power in such a case.

C.2 BALANCED DETECTION

This section shows that homodyning the heterodyne beatnotes at both output ports of a combining BS mitigates Type-B noises: so-called balanced detection. This scheme coherently adds complementary signals via the combination written by

$$\delta\phi_{\mathrm{BD}} = \frac{1}{2}\left(\delta\phi(t) - \delta\phi_\pi(t)\right). \qquad \text{(C.17)}$$

Remember that a perfect 50:50 BS is assumed throughout this chapter. In a real case, the balancing must be performed with the information of BS transmission and reflection coefficients provided by calibrations; hence, the balancing performance is limited by the accuracy of the calibration, which can be modeled by a balancing efficiency [78].

Type-B noises can be canceled out by balanced detection: plugging Eq. (C.11) and (C.12) into Eq. (C.17) ends up with,

$$\begin{aligned}\delta\phi_{\mathrm{BD}}^B &= \frac{1}{2}\left(\delta\phi^B(t) - \delta\phi_\pi^B(t)\right)\\ &= \frac{1}{2}\left[\left(\phi_s(t) + \frac{r|E_b|}{|E_a|}\left(\phi_s(t) + \phi_n^B(t)\right)\right) - \left(-\phi_s(t) + \frac{r|E_b|}{|E_a|}\left(\phi_s(t) + \phi_n^B(t)\right)\right)\right]\\ &= \phi_s(t). \qquad \text{(C.18)}\end{aligned}$$

D

PILOT TONE FREQUENCY

A PT frequency in LISA has been nominally 75 MHz [30, 36, 38]. The higher frequency better monitors the ADC jitter, lifting its coupling against other secondary noises. However, the frequency must be selected carefully, considering its impact on other scientific channels: carrier and sideband PLLs, and DLL. This chapter studies such impacts and proposes a new frequency, i.e., 37.5 MHz, which was, for example, nominally used in Chapter 7.

D.1 IMPACT ON PLL

Due to the aliasing effect, a PT signal is aliased to a frequency below Nyquist frequency at ADC. For the nominal 80 MHz sampling rate, this can be written,

$$\nu_{\mathrm{PT}}(\tau) \xrightarrow{\text{sampling}} \begin{cases} \nu_{\mathrm{PT}}(\tau), & \text{if } \nu_{\mathrm{PT}}(\tau) < 40\,\mathrm{MHz}, \\ 80\,\mathrm{MHz} - \nu_{\mathrm{PT}}(\tau), & \text{if } \nu_{\mathrm{PT}}(\tau) > 40\,\mathrm{MHz}. \end{cases} \tag{D.1}$$

The 75 MHz PT signal, hence, is aliased to 5 MHz. This means that 5 MHz (and frequencies close to it) is a "prohibited" frequency from the perspective of carrier and sideband PLLs. In addition, in case the higher harmonics of 75 MHz exist, e.g., due to a low-noise amplifier on the analog frontend, the integer multiples of 5 MHz are potentially risky frequencies as well. A LISA constellation consists of nine carrier-carrier beatnote frequencies (i.e., six interspacecraft and three reference interferometers) and eighteen sideband-sideband beatnote frequencies attached to them. Hence, it would not be possible to select all of them away from any of the integer multiples of 5 MHz over the mission.

Naively speaking, PLL bandwidth, i.e., 10 kHz to 100 kHz.

Shifting the PT frequency from 75 MHz to a frequency below Nyquist frequency of 40 MHz would partially solve this problem; e.g. 37.5 MHz. This is because such a frequency can push the aliased frequencies in the heterodyne band to way higher harmonics, i.e., a second harmonics for 5 MHz, a fourth harmonics for 10 MHz, etc.

The preliminary demonstration of this effect was done in a simple electrical split test by Thomas S. Schwarze. The result is shown in Figure D.1. Blue has main and PT frequencies of 10 MHz and 76.2 MHz, respectively. From this reference, only a PT signal is changed into 75 MHz (solid-red), then a significant impact above the $1\,\mathrm{pm}/\sqrt{\mathrm{Hz}}$ mark, due to the second harmonics of 75 MHz, was observed. After that, maintaining 75 MHz for the PT signal, the main frequency was changed into 20 MHz (dashed-red), which recovered the reference performance. This suggests that the impact becomes negligible with the fourth harmonics. The same measurements were repeated with a 37.5 MHz (yellow). The 10 MHz main frequency still shows the influence above 0.4 Hz; however, it is highly suppressed from the 75 MHz PT signal as expected.

This issue also applies to the sideband phase tracking: when the carrier beatnote has the same frequency as the sum or difference between the aliased

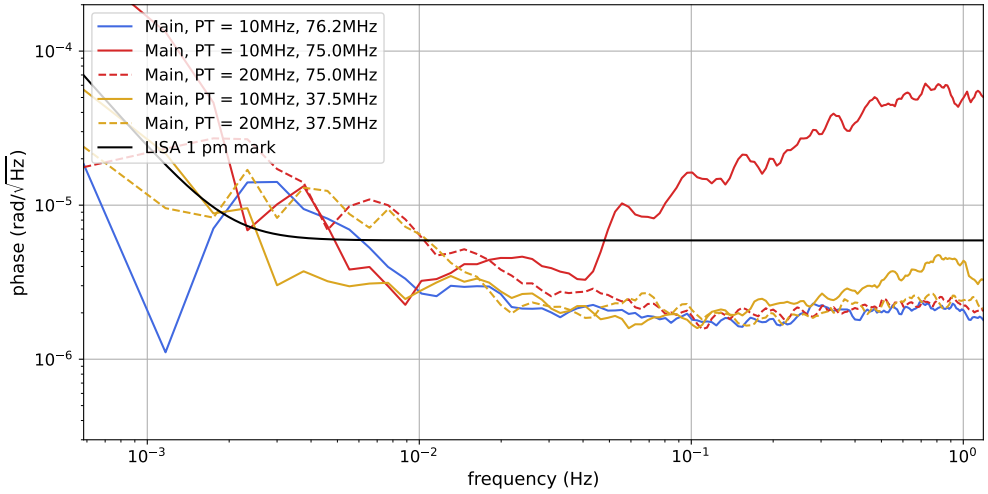

FIGURE D.1: Dependency of the PT impact on carrier PLL on their frequencies. Measurements were taken by Thomas S. Schwarze.

PT frequency and the sideband frequency offset from the carrier Δf_{sb}. This effect was observed when sinusoidally scanning the carrier-carrier beatnote frequency over the almost full heterodyne band (i.e., 6 MHz to 24 MHz) for the ranging study in Section 7.3.2. Figure D.2 shows the frequencies of carrier and sideband beatnotes. This measurement chose the 37.5 MHz PT signal and the sideband offset Δf_{sb} of 1.25 MHz; therefore, the lsb beatnote is expected to be disturbed most in case it is around 5 MHz to which the second harmonic of the PT signal is aliased. This was confirmed, as shown in the middle panel of the figure. The lsb-lsb beatnote would not be available at all for clock synchronization over the time window when the carrier beatnote is roughly within the frequencies of 5 MHz $+ \Delta f_{\mathrm{sb}} \pm 25$ kHz. In LISA, an interferometer within this band could not operate in the DSB mode. Although the disturbance was not observed for the carrier frequency within 10 MHz $\pm \Delta f_{\mathrm{sb}} \pm 25$ kHz, in either of the usb or lsb beatnotes, this region is expected to be also forbidden with the 75 MHz PT signal. This further narrows down the mission period over which all interferometers can operate in the DSB mode.

Sideband PLL is based on phase feed-forward introduced in Section 2.2.2. Hence, its output is restricted to a target differential clock signal.

In conclusion, selecting the PT frequency seems to be quite important so that its higher harmonics aliased to the heterodyne band are pushed to way higher orders. Halving the nominal frequency is the easiest solution, accomplished just by adding one more by-2 frequency divider on CFDS, i.e., 75 MHz to 37.5 MHz.

D.2 IMPACT ON DLL

The frequency of a PT signal would also be influential on DLL because the PT signal, mixed with a local copy of a carrier-carrier beatnote, does exist at the PLL error point, from which the PRN signal is extracted for DLL. As shown in Figure 2.7, the pre-DLL low-pass filter must reject the heterodyne second harmonics. Such "mixed" PT signals also are expected to be suppressed simultaneously; however, this becomes challenging, or even impossible, depending on the PT frequency.

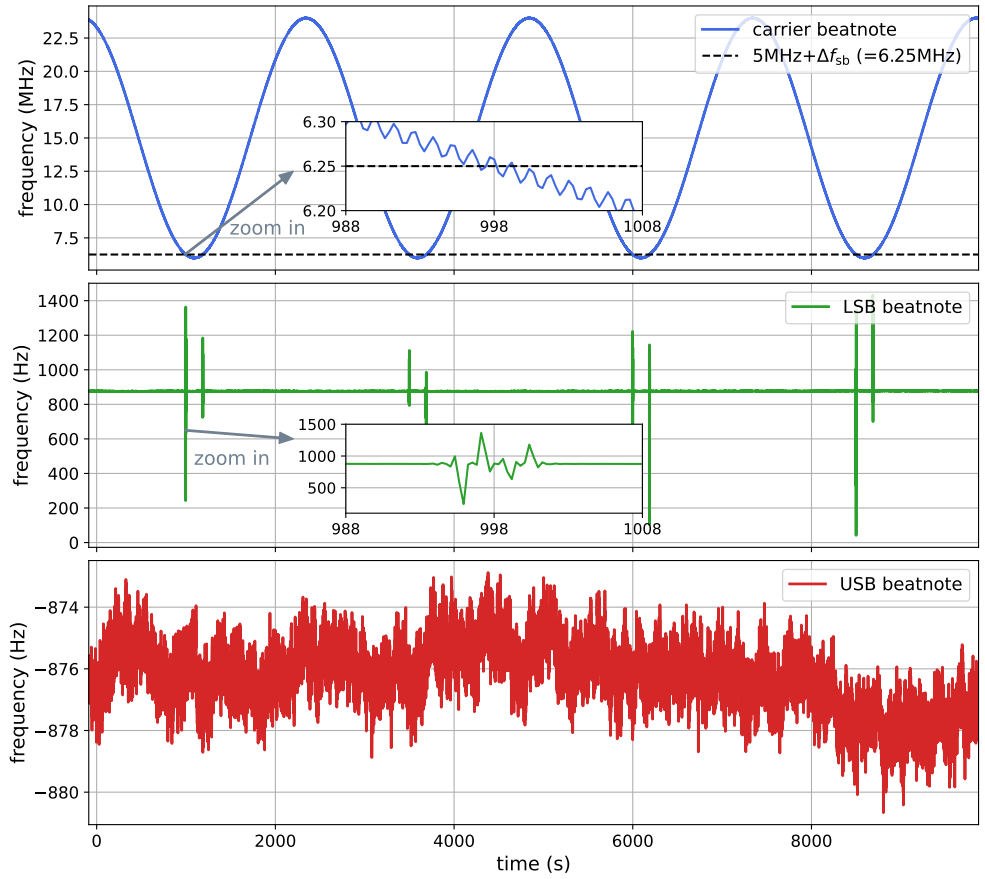

FIGURE D.2: Disturbance of a lsb-lsb beatnote due to the aliased PT signal. **Top:** a carrier-carrier beatnote, identical to blue in the top panel in Figure 7.5. **Middle:** a lsb-lsb beatnote. **Bottom:** an usb-usb beatnote. The input PT signal and the sideband frequency offset from the carrier were 37.5 MHz and 1.25 MHz, respectively. The mini panels zoom in to the period of the first glitch. The smaller oscillations in the mini panel on the top are due to the active tone injection at 0.762 Hz for tone-assisted TDIR for ranging characterization; see Chapter 7.

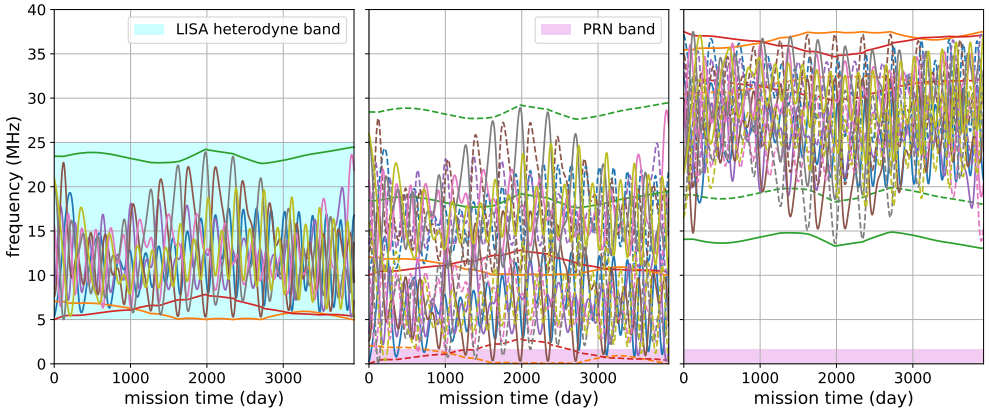

FIGURE D.3: PT frequencies at a PLL error point (orbit: ESA-leading, N1a_L1). **Left:** beatnote frequencies in different interferometers. **Middle:** PT frequencies at a PLL error with the PT frequency of 75 MHz. **Right:** same as the middle, but with the PT frequency of 37.5 MHz. For the middle and right, solid and dashed curves show two frequencies into which the input PT signal is split due to the mixing process.

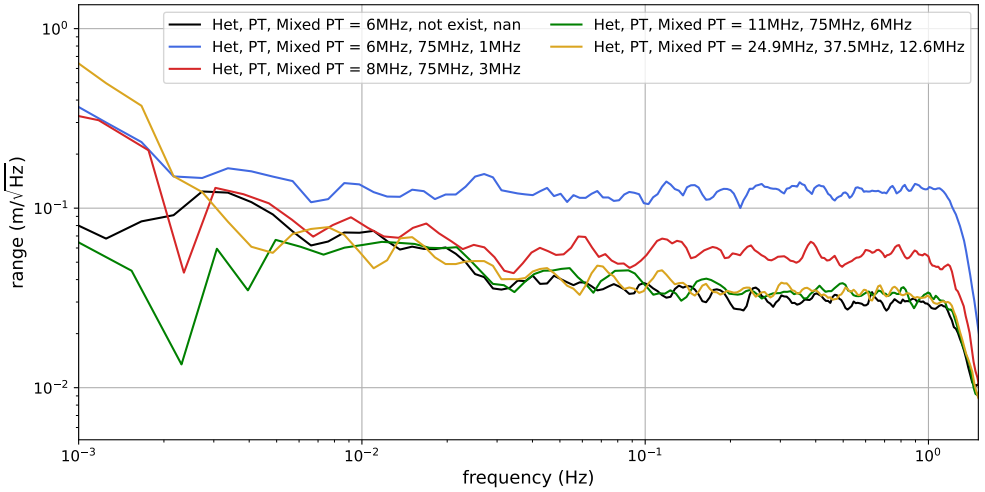

FIGURE D.4: Demonstration of the impact of a PT signal on PRNR. Legends show frequencies of heterodyne beatnotes, PT signals, and slower mixed PT signals.

The mixed PT frequency changes with heterodyne frequencies and, correspondingly, with frequency plans [22] (or LISA orbits more fundamentally) and interferometers. The PLL mixing process yields two PT frequencies,

$$\nu_{\mathrm{PT}}(\tau) \xrightarrow{\text{mixing}} \nu_{\mathrm{PT}}(\tau) \pm \nu_{\mathrm{het}}(\tau). \tag{D.2}$$

Figure D.3 shows the mixed PT frequencies in different LISA interferometers with the PT frequencies of 75 MHz (middle) and 37.5 MHz (right). "N1a_L1" in the ESA-leading orbit is taken as an example. With the 75 MHz PT signal, many interferometers result in very low frequencies below 10 MHz, and some of them even invade into the PRN band, which makes it impossible to distinguish the mixed PT signals from the PRN signal using the pre-DLL low-pass filter. On the other hand, the 37.5 MHz PT signals successfully push its mixed versions to higher frequencies (the possible lowest is 12.5 MHz in theory). This eases extracting the target PRN signal via the low-pass filter.

This was experimentally demonstrated using the 2PM2S topology same as Section 7.1, with the local PRN code off; see Figure D.4. Clocks are independent between two PMs, and the timer deviation is already removed, using sideband measurements, in the figure. The combination of the 6 MHz heterodyne frequency and the 75 MHz (blue) results in a slower mixed PT frequency of 1 MHz, and showed the degradation of the performance, compared with the one without the PT signal (black). The performance converged on black with the mixed PT frequency increased via the heterodyne frequency (red, green). The worst case with the 37.5 MHz PT signal is shown in yellow. No impact was observed on this precision. It must be remarked that the green and yellow cases did not depend on the existence of the pre-DLL low-pass filer. It would be because the mixed PT signal is much faster than the data-bit window, over which the DLL input is accumulated to compute an error signal, and the deterministic sinusoidal signal is averaged out. This point remains to be investigated.

D.3 TIMING FIDELITY

Appendices D.1 and D.2 reveal that a PT signal have non-negligible influences on PLL and DLL, depending on its frequency. Changing it from 75 MHz to 37.5 MHz would minimize such impacts. Or more in general, a PT frequency,

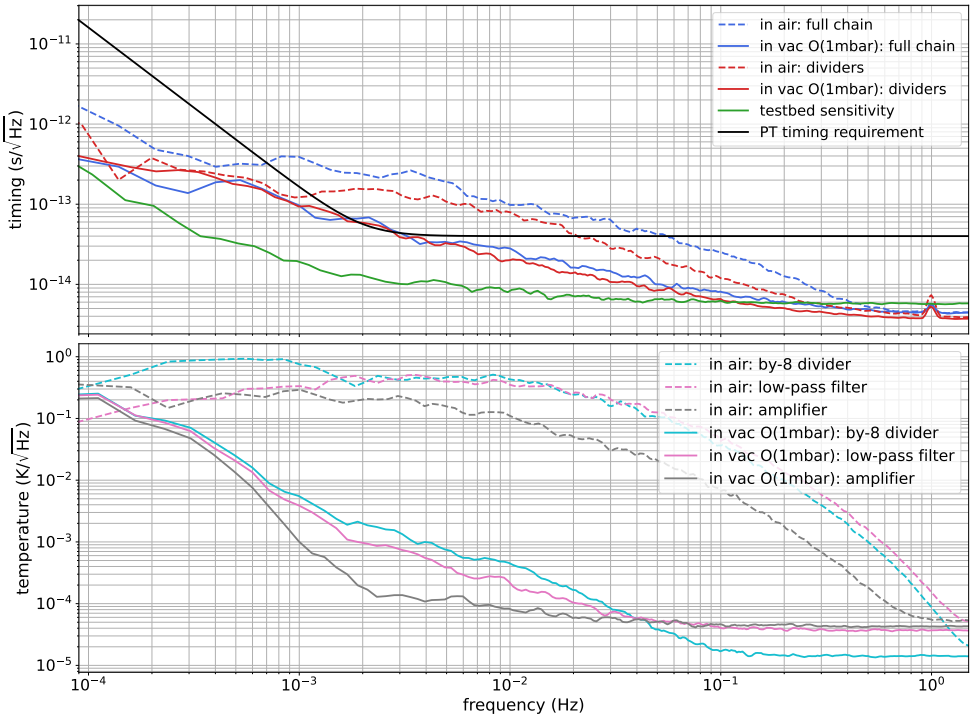

FIGURE D.5: CFDS performance-critical-chain timing fidelity with a 37.5 MHz PT signal. **Top:** timing fidelity in the air (dashed) and in vacuum (solid). **Bottom:** temperature stability on each component on the performance-critical PT generation chain

directly aliased to the LISA heterodyne band (i.e. 5 MHz to 25 MHz), would not be a good option.

However, the higher frequency better monitors the ADC jitter, lifting its coupling against other secondary noises. From the perspective of CFDS shown in Figure 2.12, the PT signal must be generated by down-converting a GHz-clock sideband signal. Therefore, generating a lower frequency is expected to introduce more timing jitter. Hence, lowering a PT frequency makes it more difficult to meet the $40\,\mathrm{fs}/\sqrt{\mathrm{Hz}}$ requirement (see Eq. (2.15)) on a performance-critical chain of CFDS.

Figure D.5 shows the timing fidelity of the performance-critical chain of TRL 5 CFDS with 37.5 MHz PT signals. A common 2.400 GHz signal was applied to the inputs to the frequency-divider chains of two independent CFDS instances. Then, the phases of their 37.5 MHz PT signals were extracted by a PM, and the difference was computed in post-processing. The full performance in vacuum (solid-blue) is compliant with the timing requirement, except for a small bump around 2 mHz. The frequency dividers (solid-red) are the dominant noise sources (the performance-critical chain also includes a low-noise amplifier, a low-pass filter, and a power splitter). See [25] for the detailed description.

E

NOISE COUPLINGS IN CLOCK SYNCHRONIZATION

E.1 ALIASING EFFECT

Laser frequency noises at high Fourier frequencies are folded into the observation band due to aliasing in the decimation stages. Hence, clock synchronization must consider this frequency regime, out of the observation band, using carefully designed anti-aliasing filters. As time-stamping and sampling operations do not commute (see below), the residuals of aliased frequency noise will otherwise spoil the measurements. A brief summary of this will be given in the following, while a detailed model will be presented in [79].

A decimation stage is a combination of an anti-aliasing filter and down-sampling. This process is expressed introducing a sampling operator **S** and a filter operator **F**,

$$\nu_S(\tau) = \mathbf{SF}\nu(\tau'), \tag{E.1}$$

where $\nu_S(\tau)$ is a measured frequency after filtering and down-sampling. The one-sided power spectrum of ν_S is made up of the in-band contribution and any folded/aliased power that results from down-sampling,

$$S_{\nu_S}(f) = \sum_{k=0}^{\infty} \tilde{\mathbf{F}}(f) S_\nu^{(k)}(f). \tag{E.2}$$

where $\tilde{\mathbf{F}}(f)$ is the modulus squared of the filter's transfer function. $S_\nu^{(k)}(f)$ denotes the k^{th} alias which is given by

$$S_\nu^{(k)}(f) = \begin{cases} S_\nu(n[k]f_s + f), & n[k] = \frac{k}{2} \quad \text{if } k \text{ is even} \\ S_\nu(n[k]f_s - f), & n[k] = \frac{k+1}{2} \quad \text{if } k \text{ is odd} \end{cases} \tag{E.3}$$

Using the introduced formalism, a split measurement, i.e., the difference between the same signals measured by independent two PMs, is written with the adjustment of one of the timestamps in post-processing,

$$\begin{aligned} y(\tau) &= \mathbf{SF}\nu(\tau') - \mathbf{T}_i^{-1}\mathbf{SFT}_i\nu(\tau') \\ &= \mathbf{T}_i^{-1}\left([\mathbf{T}_i, \mathbf{S}]\mathbf{F} + \mathbf{S}[\mathbf{T}_i, \mathbf{F}]\right)\nu(\tau'), \end{aligned} \tag{E.4}$$

where the time-stamping operator $\mathbf{T}_i$ and its inverse operator $\mathbf{T}_i^{-1}$ are introduced. They represent the time shifts due to the timer deviation between the primary and secondary clocks and the compensation for it by time-shifting, respectively. Notice that a timer deviation was assumed to be constant here; hence, $\dot{q}_i(\tau')$, which generally appears in a denominator like Eq. (2.11), was neglected. The first term shows the commutator between time-stamping and sampling, which is the focus of the rest of this section. The second term is the one between time-stamping and filtering, which is called flexing-filtering coupling [80] and described in Appendix E.3.

The k-th contribution to the total ASD is derived by taking a square root of the ensemble average of the squared modulus of the Fourier transform $\mathcal{F}$,

$$\begin{aligned}\tilde{Y}^{(k)}(f) &= \sqrt{\left\langle \left| \mathcal{F}\left[\mathbf{T}_i^{-1}[\mathbf{T}_i, \mathbf{S}]\mathbf{F}\nu(\tau')\right]\right|^2 \right\rangle} \\ &= \sqrt{\tilde{\mathbf{F}}(f) S_\nu^{(k)}(f)} \cdot \left| \mathrm{e}^{-j2\pi f \delta\tau_i} - \mathrm{e}^{-j2\pi(n[k]f_s + f)\delta\tau_i} \right| \\ &= \sqrt{\tilde{\mathbf{F}}(f) S_\nu^{(k)}(f)} \cdot 2\left|\sin(\pi n[k] f_s \delta\tau_i)\right|. \end{aligned} \tag{E.5}$$

This shows $\mathbf{T}_i$ and $\mathbf{S}$ does commute for power below the new Nyquist frequency but does not for all aliased power, i.e., when $k \neq 0$.

Up to here, a constant timer deviation $\delta\tau_i$ was assumed to derive the ASD of the commutator. Our actual timer deviation is time-dependent and almost linear in time over a lab measurement time. Hence, if the timer deviation varies more than $O(1/f_s)$, the sinusoidal factor is averaged because of the phase scanning. In this case, after such an averaging, Eq. (E.4) reduces to,

$$\tilde{Y}^{(k)}(f) \approx \sqrt{\tilde{\mathbf{F}}(f) S_\nu^{(k)}(f)} \cdot \sqrt{2}. \tag{E.6}$$

This model of the aliasing effect can be applied to the three-signal measurement,

$$\begin{aligned}\Delta'_{3PM}(\tau) &= \mathbf{S}\mathbf{F}\nu_{c,2'3'}(\tau') + \mathbf{T}_2^{-1}\mathbf{S}\mathbf{F}\mathbf{T}_2\nu_{c,1'2'}(\tau') + \mathbf{T}_3^{-1}\mathbf{S}\mathbf{F}\mathbf{T}_3\nu_{c,3'1'}(\tau') \\ &= -\mathbf{T}_2^{-1}[\mathbf{T}_2, \mathbf{S}]\mathbf{F}\nu_{c,1'2'}(\tau') - \mathbf{T}_3^{-1}[\mathbf{T}_3, \mathbf{S}]\mathbf{F}\nu_{c,3'1'}(\tau'), \end{aligned} \tag{E.7}$$

where all detailed descriptions of clock synchronizations provided in Section 4.2.2 are omitted and the perfect three-signal test without any additional noise was assumed in the second line, i.e., $\nu_{c,2'3'}(\tau') = -\nu_{c,1'2'}(\tau') - \nu_{c,3'1'}(\tau')$.

Section 4.3 specifically demonstrates the aliasing effect due to the CIC decimation stage mentioned in Section 4.1. The filter operator described in this section corresponds to its integration stage before down-sampling. This is followed by the comb stage, whose transfer function can be applied from the left side of Eq. (E.6).

E.2 LAGRANGE INTERPOLATION ERROR

In post-processing, PM data is interpolated using fractional delay filters to adjust data time stamps. We recall the analytical model of the interpolation error presented in [29]. Time shifts are assumed to be constant in this section.

The interpolation consists of two steps: an integer delay $\mathbf{T}_i^0$ to shift the time stamps to the nearest sample and a fractional delay $\mathbf{T}_i^\epsilon$ implemented by a non-causal FIR filter. To model the interpolation based on this decomposition, the time shift $\delta\tau_i$ is also expanded,

$$\delta\tau_i = \delta\tau_i^0 + \delta\tau_i^\epsilon, \tag{E.8}$$

where $\delta\tau_i^0 = N/f_s$ by definition. f_s is the sampling frequency and N is an integer.

To estimate the error in the frequency domain, the Fourier transform of the following expression needs to be derived,

$$\delta\mathbf{T}_i x(t) = \left[\mathbf{T}_i^\epsilon \mathbf{T}_i^0 - \mathcal{T}_i\right] x(t), \tag{E.9}$$

where $x(t)$ is a given data in time and $\mathcal{T}_i$ is the perfect operator.

The Fourier transform of each operator reads,

$$\mathcal{F}\left[\mathbf{T}_i^0 x(t)\right](\omega) = \mathrm{e}^{j\omega\delta\tau_i^0}\tilde{x}(\omega), \tag{E.10}$$

$$\mathcal{F}\left[\mathbf{T}_i^\epsilon x(t)\right](\omega) = \sum_{k=-p+1}^{p} c_k^\epsilon \mathrm{e}^{j\omega k/f_s}\tilde{x}(\omega), \tag{E.11}$$

$$\mathcal{F}\left[\mathcal{T}_i x(t)\right](\omega) = \mathrm{e}^{j\omega\left(\delta\tau_i^0+\delta\tau_i^\epsilon\right)}\tilde{x}(\omega), \tag{E.12}$$

where $p = (a+1)/2$ with a as the filter order and c_k^ϵ is a filter coefficient.

Combining these equations, the Fourier transform of Eq. (E.9) is derived,

$$\mathcal{F}\left[\delta\mathbf{T}_i x(t)\right](\omega) = \mathrm{e}^{j\omega\delta\tau_i^0}\left[\sum_{k=-p+1}^{p}\left(c_k^\epsilon \mathrm{e}^{j\omega k/f_s}\right) - \mathrm{e}^{j\omega\delta\tau_i^\epsilon}\right]\tilde{x}(\omega). \tag{E.13}$$

After all, the interpolation error in ASD $\delta\tilde{\mathbf{T}}_i(\omega)$ is computed,

$$\delta\tilde{\mathbf{T}}_i(\omega) = \left|\sum_{k=-p+1}^{p}\left(c_k^\epsilon \mathrm{e}^{j\omega k/f_s}\right) - \mathrm{e}^{j\omega\delta\tau_i^\epsilon}\right|. \tag{E.14}$$

E.3 FLEXING-FILTERING COUPLING

The model of the flexing-filtering coupling presented in [80] is adapted to our case where only a single time-stamping operator exists in Eq. (E.4).

The Fourier transform of time-shifted data $\mathbf{T}_i x(t)$ can be generally expressed,

$$\begin{aligned}\mathcal{F}\left[\mathbf{T}_i x(t)\right](\omega) &= \int_{-\infty}^{\infty} x(t-\delta\tau_i(t))\cdot\exp\left(-j\omega t\right)dt \\ &= \frac{1}{1-\dot{q}_i}\exp\left(-j\omega\frac{\delta\tau_{i,0}}{1-\dot{q}_i}\right)\tilde{x}\left(\frac{\omega}{1-\dot{q}_i}\right),\end{aligned} \tag{E.15}$$

where the timer deviation $\delta\tau_i(t)$ was assumed to be a linear function of time, i.e., $\delta\tau_i(t) = \dot{q}_i t + \delta\tau_{i,0}$.

Each term of the commutator between time-stamping and filtering reads,

$$\mathcal{F}\left[\mathbf{T}_i\mathbf{F}x(t)\right](\omega) = \frac{1}{1-\dot{q}_i}\exp\left(-j\omega\frac{\delta\tau_{i,0}}{1-\dot{q}_i}\right)\tilde{x}\left(\frac{\omega}{1-\dot{q}_i}\right)\tilde{\mathbf{F}}(\omega), \tag{E.16}$$

$$\mathcal{F}\left[\mathbf{F}\mathbf{T}_i x(t)\right](\omega) = \frac{1}{1-\dot{q}_i}\exp\left(-j\omega\frac{\delta\tau_{i,0}}{1-\dot{q}_i}\right)\tilde{x}\left(\frac{\omega}{1-\dot{q}_i}\right)\tilde{\mathbf{F}}\left(\frac{\omega}{1-\dot{q}_i}\right). \tag{E.17}$$

Using Eqs. (E.16) and (E.17), the flexing filtering coupling to the first order of $\dot{q}_i$ is derived,

$$\begin{aligned}FF(\omega; x, \mathbf{T}_i, \mathbf{F}) &:= \mathcal{F}\left[[\mathbf{T}_i, \mathbf{F}]x(t)\right](\omega) \\ &\approx \omega\dot{q}_i\exp\left(-j\omega\delta\tau_{i,0}\right)\tilde{x}\left(\omega\right)\frac{d\tilde{\mathbf{F}}(\omega)}{d\omega}.\end{aligned} \tag{E.18}$$

Hence, a filter design couples to a phase measurement via its frequency derivative. This implies that this flexing filtering coupling is dominant close to the Nyquist frequency of a particular decimation stage.

F

LASER LOCK WITH A PHASEMETER

LISA requires the laser transponder lock between local and received beams to maintain all optical beatnote frequencies within the heterodyne beatnote bandwidth from 5 MHz to 25 MHz. Such a laser lock system is based on nested feedback loops [30]; one is a DPLL (see Section 2.2), and the other is a laser control loop. Using an optical beatnote frequency extracted by the former, the latter controls the local laser frequency via piezoelectric transducer (PZT) and crystal temperature actuators. This chapter provides such a nested loop design, analytical formulations, and experimental demonstrations.

Any measurements in Appendix F.2 were conducted by the LISA-like laser lock implemented on the low-budget commercial device, Red Pitaya. Thomas S. Schwarze initiated this implementation, which the author further developed, e.g., the implementation of the injection of the beatnote frequency dynamics in Appendices F.2.2 and F.2.3. The laser lock with Red Pitaya is used for the Hexagon experiment, presented in the main body of this thesis, which features multiple laser sources locked to each other.

F.1 ANALYTICAL FORM

F.1.1 *Block diagram*

A linearized block diagram of the frequency-lock loop is shown in Figure F.1, which consists of optical parts (red), analog electronics (blue), and digital electronics (black). PM DPLL F_{PLL} first extracts the frequency of an input optical beatnote between the local and the received beams. This is then compared to a reference frequency to generate an error signal for the laser lock. After passing through digital servos implemented in FPGA logic, F_{Gain} and F_{Ctrl}, the control signal is converted to an analog electrical signal via DAC F_{DAC}. Lastly, a signal conditioning circuit F_{cond} tailors the signal, based on which an actuator F_{plant} manipulates the local laser frequency. The implicit integration from frequency to phase $F_{\nu 2\phi}$ is inserted before the DPLL.

The laser-lock loop comprises two loops: a fast PZT loop and a slow temperature loop. The former determines the loop bandwidth and is dominant through most of the frequency band, while the latter compensates for a slow and large thermal drift of laser frequencies to keep the system in its operational band.

Notice that each of the PZT and temperature loops has a virtual switch to open or close the loop. For example, the loop must be open during an intersatellite link acquisition. It is achieved with both spatial beam alignments and the beam frequency scan to bring the beatnote frequency to the LISA heterodyne bandwidth. Such a wide-range frequency scanning is possible by sweeping the temperature offset signal over its range.

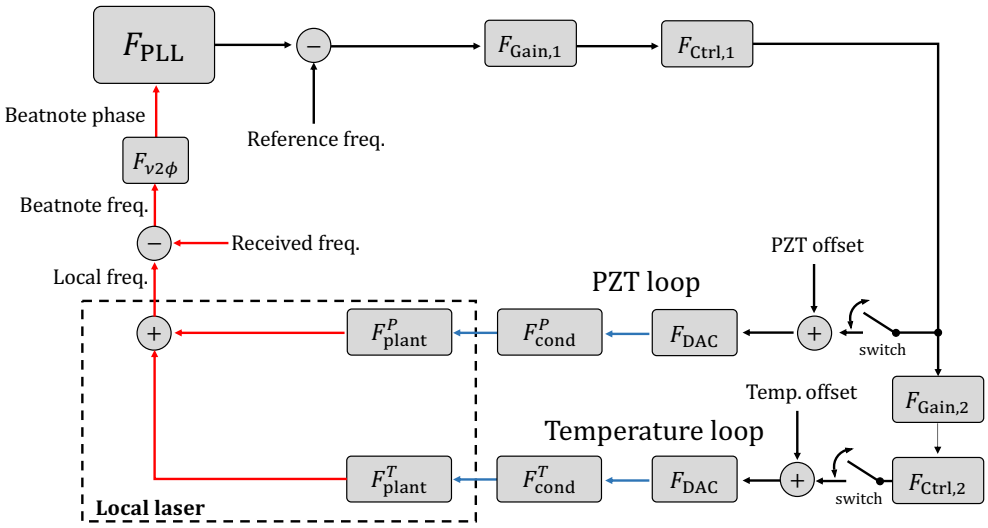

FIGURE F.1: Block diagram of laser lock loop. Red for optical signals, blue for analog electrical signals, and black for digital signals.

F.1.2 *Transfer function*

The laser-lock loop comprises both analog and digital domains. Hence, in the following formulation, the analog components are expressed in the Laplace domain, while the digital components are in the z domain, considering its sampling time. Under the low-frequency approximation against the digital sampling frequency f_s [1], the domains have a simple relation:

$$s \approx (z-1) \cdot f_s, \tag{F.1}$$

which follows by Taylor expansion to the first order from $z = \mathrm{e}^{s/f_s}$.

DPLL (F_{PLL}): The detailed description is provided in Section 2.2.1. Based on its known open-loop transfer function G_{PLL} in Eq. (2.1), its system transfer function F_{PLL} from the perspective of the frequency-lock loop can be expressed,

$$F_{\mathrm{PLL}}(z) = \frac{G_{\mathrm{PLL}}(z)}{1 + G_{\mathrm{PLL}}(z)} \cdot \frac{z-1}{2\pi}, \tag{F.2}$$

where $(z-1)/2\pi$ is the inverse of the product of the phase accumulator and the LUT, according to the fact that a frequency, instead of a phase in radian, is an output.

Digital servo (F_{Gain} and F_{Ctrl}): The gain-reduction stages $F_{\mathrm{Gain},l}$ ($l = 1, 2$) are implemented by adding extra bits to registers from the left. This guarantees enough bits for the fixed-point arithmetic at the following controllers, preventing overflows.

$$F_{\mathrm{Gain},l} = 2^{-C_l}, \tag{F.3}$$

where C_l is the number of bits added from the left.

The controllers $F_{\mathrm{Ctrl},l}$ implement an integrator and a double integrator with dedicated gains,

$$F_{\mathrm{Ctrl},l}(z) = \frac{k_{i,l}}{z-1} + \frac{k_{ii,l}}{(z-1)^2}, \tag{F.4}$$

1 All digital components operate at the PM system clock rate, i.e., 80 MHz in the LISA case.

where $k_{i,l}$ and $k_{ii,l}$ are gains of a single and double integrator, respectively.

DAC (F_{DAC}): This transfer function can be a constant factor depending on the DAC specification. The value represents a conversion from a digital code, which the digital servo provides, to a voltage.

Analog servo (F_{cond}): The signal conditioning circuit in the analog domain F^A_{cond} ($A = P, T$) is nominally composed of a low-pass filter to suppress unwanted high frequencies after the DAC and a gain k^A_c, delivering a signal voltage that fits the operational range of the following actuator,

$$F^A_{\mathrm{cond}}(s) = \frac{k^A_c}{1 + s/\omega^A_c}, \tag{F.5}$$

where $f^A_c (= \omega^A_c / 2\pi)$ is a corner frequency of the low-pass filter.

Actuators (F_{plant}): This represents an actuation efficiency from a signal voltage to a laser frequency. This would be modeled by such an efficiency factor (normally $O(1\,\mathrm{MHz/V})$ for a PZT and $O(1\,\mathrm{GHz/V})$ for a temperature) and a low-pass filter with a particular bandwidth.

Frequency-to-phase conversion ($F_{\nu 2\phi}$): This is an implicit component that stems from the fact that the actuators on a laser control the laser frequency, while the input to DPLL is a phase in radian,

$$F_{\nu 2\phi}(s) = \frac{2\pi}{s}. \tag{F.6}$$

Frequency-lock loop (G_{lock}): The open-loop transfer function of the whole laser frequency-lock loop G_{lock} is given by placing the components introduced above in the way shown in Figure F.1. The entire loop can be decomposed into the PZT loop G^P_{lock} and the temperature loop G^T_{lock}, each of which is a series of the components,

$$G_{\mathrm{loop}}(s,z) = G^P_{\mathrm{loop}}(s,z) + G^T_{\mathrm{loop}}(s,z), \tag{F.7}$$

$$G^P_{\mathrm{loop}}(s,z) = F_{\mathrm{PLL}}(z) \cdot F_{\mathrm{Gain},1} \cdot F_{\mathrm{Ctrl},1}(z) \cdot F_{\mathrm{DAC}} \cdot F^P_{\mathrm{cond}}(s) \cdot F^P_{\mathrm{plant}}(s) \cdot F_{\nu 2\phi}(s), \tag{F.8}$$

$$G^T_{\mathrm{loop}}(s,z) = F_{\mathrm{PLL}}(z) \cdot F_{\mathrm{Gain},1} \cdot F_{\mathrm{Ctrl},1}(z) \cdot F_{\mathrm{Gain},2} \cdot F_{\mathrm{Ctrl},2}(z) \cdot F_{\mathrm{DAC}} \cdot F^T_{\mathrm{cond}}(s) \cdot F^T_{\mathrm{plant}}(s) \cdot F_{\nu 2\phi}(s). \tag{F.9}$$

The PZT, temperature, and combined entire loops are plotted in Figure F.2, based on Eqs. (F.7) to (F.9). In this example, the unity-gain frequency (UGF) of the entire loop and the cross-over frequency between the PZT and temperature loops are 20.8 kHz and 51.7 µHz, respectively. A practical upper bound of the UGF would be determined by a PZT resonance frequency, which is around 50 kHz for Mephisto non-planar ring oscillator (NPRO) laser from COHERENT.

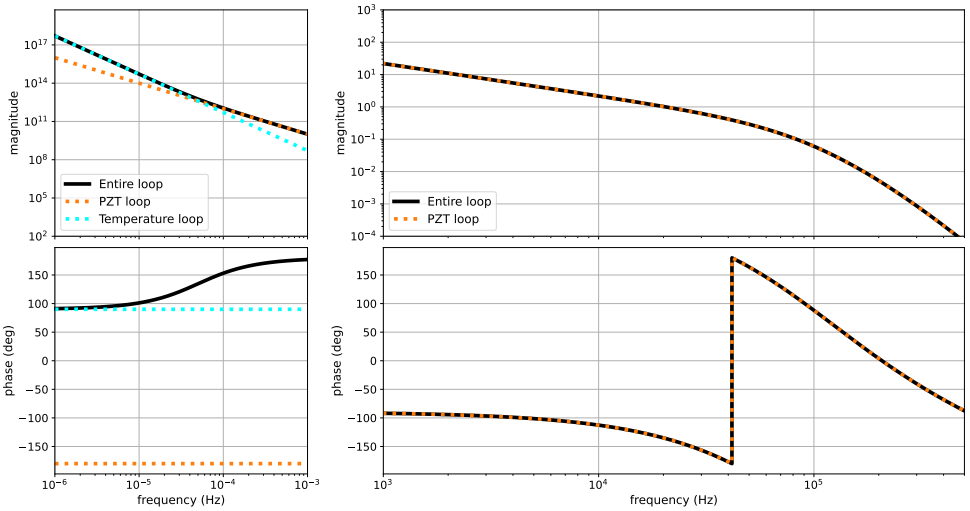

FIGURE F.2: Open-loop transfer functions of the frequency-lock loops. The frequency range around the UGF of the entire loop, 20.8 kHz, is shown on the right, while the range around the cross-over frequency between the PZT and temperature loops, 51.7 µHz, is shown on the left.

F.1.3 *Performance*

The analytical investigation can be wrapped up with the laser-lock performance based on the loop model provided above and laser frequency noise models in Section 1.3.1.1. According to the open-loop transfer function G_{loop} in Eq. (F.7), a local laser frequency $\tilde{\nu}_{l,\text{free}}$ is locked to a received laser frequency $\tilde{\nu}_r$,

$$\tilde{\nu}_{l,\text{lock}}(s) = \frac{1}{1+G_{\text{loop}}}\left(\tilde{\nu}_{l,\text{free}}(s) + G_{\text{loop}}\cdot\tilde{\nu}_r(s)\right). \tag{F.10}$$

The loop error can also be computed by,

$$\begin{aligned}\tilde{\nu}_e(s) &= \tilde{\nu}_{l,\text{lock}}(s) - \tilde{\nu}_r(s)\\ &= \frac{1}{1+G_{\text{loop}}}\left(\tilde{\nu}_{l,\text{free}}(s) - \tilde{\nu}_r(s)\right),\end{aligned} \tag{F.11}$$

which must be compared with the transponder stability requirement $5\,\text{Hz}/\sqrt{\text{Hz}}$.

Figure F.3 shows the results. The local and received laser frequency noises are assumed to be free-running and cavity-stabilized, following Eq. (1.18) and Eq. (1.19), respectively. The local laser is almost freely running above the UGF of the laser lock loop, estimated around 20.8 kHz in Appendix F.1.2. It starts to be locked to the received laser around the UGF, and the lock gets tighter towards low frequencies. The resulting stability of the transponder lock, i.e., the residual loop error, is plotted in red. This meets the aforementioned $5\,\text{Hz}/\sqrt{\text{Hz}}$ requirement below UGF.

F.2 DEMONSTRATION

F.2.1 *Loop transfer function*

The loop model introduced in Appendix F.1 was experimentally verified. The bode plot of the open-loop transfer function measured by Moku:Lab from LIQUID INSTRUMENT is shown in Figure F.4. Blue is the measurement in the lab. Black is the model with the parameters substituted to Eqs. (F.7) to (F.9). The measurement agrees with the model well. The UGF and the phase margin can be estimated around 22 kHz and 50.0°.

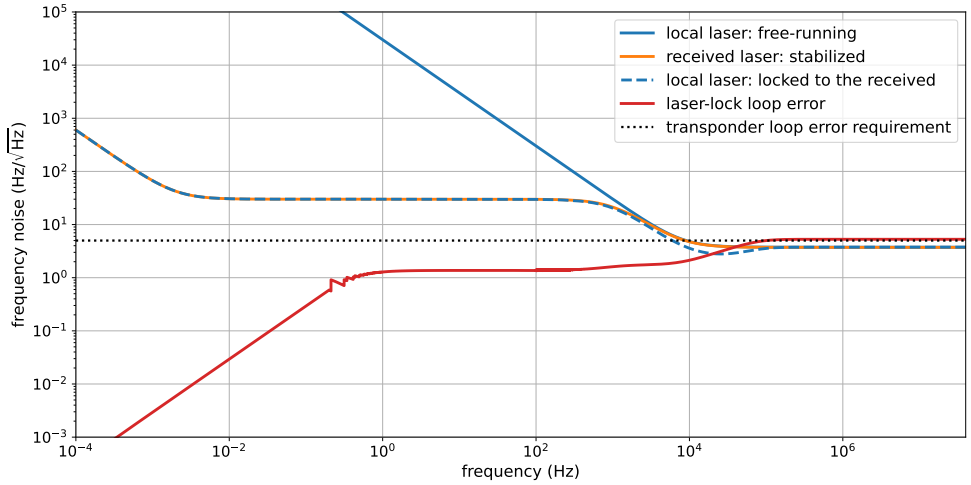

FIGURE F.3: Performance of the laser frequency-lock loop. Solid blue is a free-running local laser noise, orange is a stabilized received laser noise, dashed blue is the local laser noise locked to the received laser, and red is the error of the laser-lock loop. Glitches around 0.1 Hz are artifacts due to numerical errors in simulation.

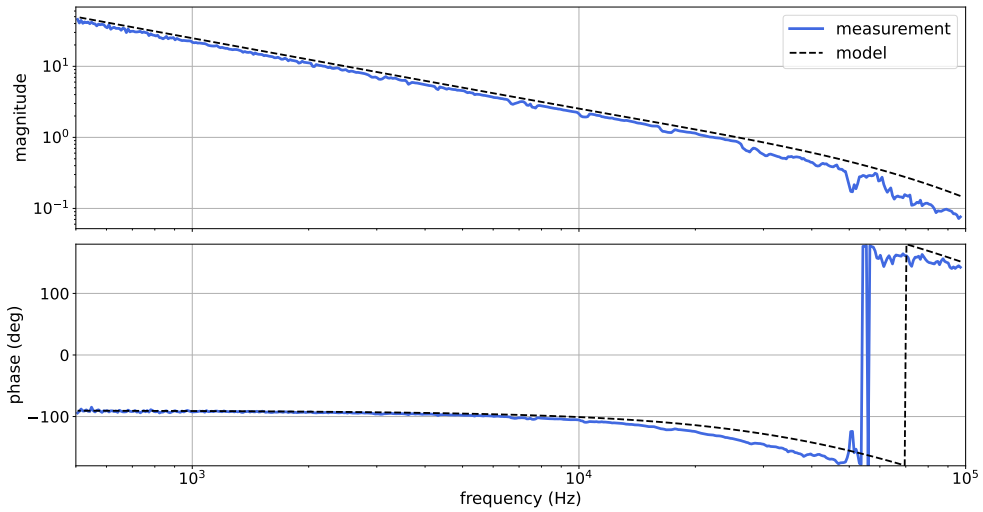

FIGURE F.4: Experimental demonstration of the laser lock system implemented on Red Pitaya, using one of the optical beatnote in the Hexagon.

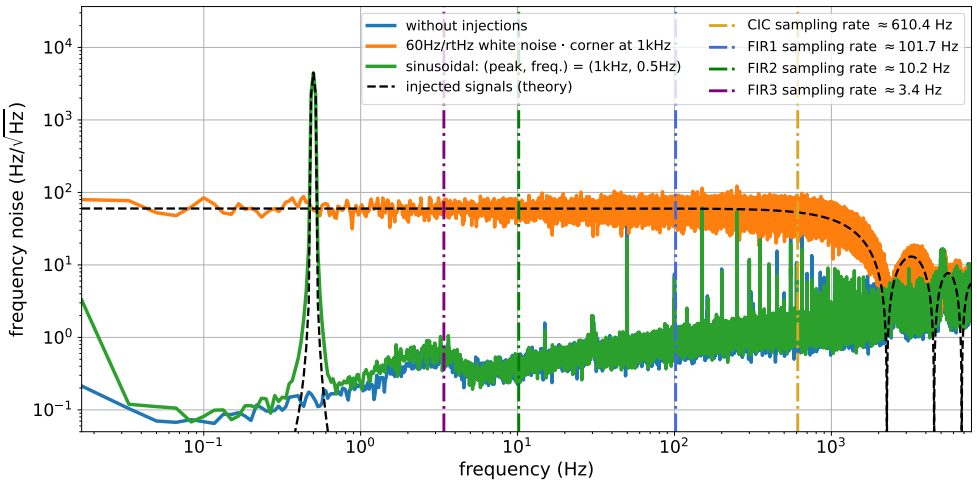

FIGURE F.5: Demonstration of beatnote frequency noise injection. A Moku:Lab PM operation, which has the sampling rate of 15.625 kHz, measures a signal from SEPD on the hexagonal bench for the out-of-loop measurements. Blue is the beatnote frequency without any modulation; Orange is the noise floor of 60 Hz/$\sqrt{\text{Hz}}$ and the corner frequency of 1 kHz; Green is the sinusoidal modulation with the amplitude of 1 kHz at 0.5 Hz; Dashed-black curves are the theoretical curves of the injected signals; Dot-dashed light-color lines show the sampling rates at the decimation stages of PM.

F.2.2 *Frequency noise*

An in-band sinusoidal frequency modulation would be intentionally injected in LISA for the efficient performance characterization of TDI, called tone-assisted TDIR; see Section 4.4. In addition, the injection of the LISA-like noise level (see Section 1.3.1.1) is necessary to produce representative input noises for the PM testing in a lab.

Figure F.5 demonstrates such frequency modulations using one of the beatnotes in the Hexagon. The parameters (a white noise floor, a modulation frequency, a modulation amplitude, etc.) are sent from a client software in Python to a server software in C on the Red Pitaya processor. The server software then numerically generates corresponding noises and sends them to FPGA continuously. The white noise injection (orange) and the sinusoidal modulation (green) both follow the theoretical curves (dashed black) rather well.

Note that the injected noise floor reaches the sampling rate of the CIC decimation stage, i.e., 610.4 Hz. This way, the frequency noise floor of the optical beatnote at the critical frequency can be set deterministically; hence, the investigation of the aliasing effect can be consistently performed, as presented in Chapter 4.

F.2.3 *Frequency drift*

Heterodyne frequencies are not constant due to Doppler shifts caused by a relative motion between SC in LISA. Hence, they keep drifting over the mission duration at the speed of the order in 10 Hz s^{-1}.

Such slow and complicated frequency dynamics can be synthesized on the client software by instantiating an arbitrary function and adding it to the reference frequency. Then, the slowly modulated reference frequency is sent from the client to the server.

Figure F.6 demonstrates three types of frequency drifts over 8 hours: a 700 Hz s^{-1} linear drift (pink), the LISA frequency plan "Keplerian N1c_L1_isc3" (cyan) and the LISA frequency plan "ESA N1a_L1_isc1" (green), together with their models (dashed-black). The LISA frequency plans are intentionally sped up by a factor of 10000 to compress 9 years into 8 hours. Neglecting glitches

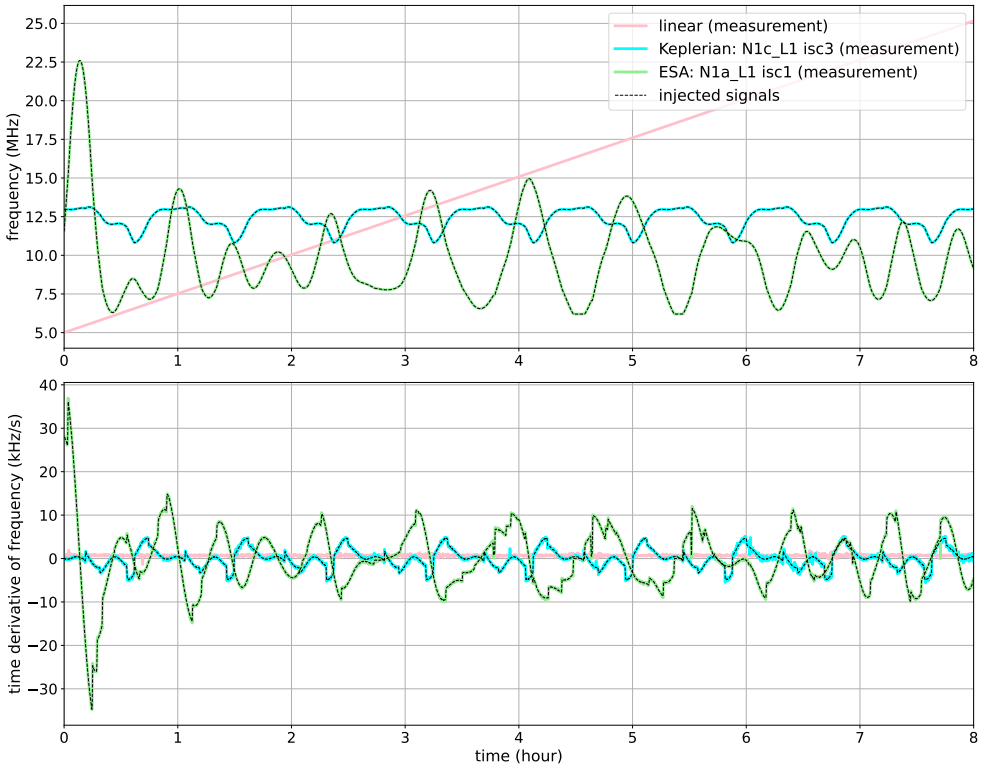

FIGURE F.6: Demonstration of various drifts of beatnote frequencies in absolute frequency (top) and its time derivative (bottom). Pink shows a $700\,\mathrm{Hz\,s^{-1}}$ linear drift. Cyan shows the LISA frequency plan "Keplerian N1c_L1_isc3". Green shows "ESA N1a_L1_isc1". Dashed-black curves are theoretical curves generated in client software. The LISA frequency plans are intentionally sped up by a factor of 10000.

in the bottom panel, the measured beatnote frequencies are modulated by the injected signals as expected.

G

DECIMATION ARTIFACTS

PLLs and DLLs on a PM operate at 80 MHz and the data-bit rate around dozens kHz, respectively. As summarized in Section 2.4, such high-rate loop outputs must be decimated to a few Hz with anti-aliasing filters to suppress aliased noises sufficiently.

A finite number of bits N invested for any digital signal sets a range,

$$0 \leq y[n] \leq 2^N - 1, \tag{G.1}$$

where $y[n]$ is an unsigned integer at a discrete time n. The combination of an anti-aliasing filter and such a finite range becomes a problem when y jumps from the upper bound to zero (or vice versa) due to the signal wrap in this range. This means the signal response to the wrapping gets more sluggish because of the low-pass effect, which causes artifacts at the jump.

Such jumps regularly occur if the signal has a linear ramp. For example, a phase output from PLL ramps almost linearly because of a MHz heterodyne frequency, which changes slowly due to a frequency plan. A received PRNR estimate is another example; it drifts due to a clock bias and SC relative motions.

There would be multiple ways to overcome this artifact at the decimation stages. The method applied to PRNR estimates and PLL phases in this thesis generates an auxiliary signal y_{aux} shifted by half of the range from the raw signal y_{raw},

$$y_{\mathrm{aux}}[n] = \left(y_{\mathrm{raw}}[n] + \frac{M}{2} \right) \mod M + 1, \tag{G.2}$$

$$0 \leq y_{\mathrm{raw}}[n], y_{\mathrm{aux}}[n] \leq M. \tag{G.3}$$

Note that the upper bound of the range is generalized by M because it does not necessarily have to be the bit length that sets the range. Also, only for the simplicity of the following formulation, M is assumed to be an even number.

For example, the upper bound of a PRNR estimate is determined by the number of system clock cycles in a full code; thereby, it corresponds to the maximum of the bit length for the 2^n parameter set from Table 5.1, but it is not the case for the non-2^n parameter set in the table.

Both signals pass through identical decimation stages. Still, jumps occur at different timings because of the half-range offset $\frac{M}{2}$ [1]. The key idea is to switch between the two signals to avoid the jumps and recover the artifact-free signal in post-processing [2]. Signals are switched when the current one gets out of a narrower range from 25 % to 75 % of the original upper bound $\left[\frac{M}{4}, \frac{3M}{4}\right]$ [3],

$$y^F_{1/2}[n] = \begin{cases} y^F_{\mathrm{raw}}[n] & \left(y^F_{\mathrm{raw}}[n] \in \left[\frac{M}{4}, \frac{3M}{4}\right]\right) \\ y^F_{\mathrm{aux}}[n] & \left(y^F_{\mathrm{aux}}[n] \in \left[\frac{M}{4}, \frac{3M}{4}\right]\right) \end{cases} \tag{G.4}$$

The superscript F explicitly shows that these signals are the ones after all decimation stages.

1 This cannot be exactly half if M is an odd number, which is the reason why M is restricted to an even number for the simplicity.

2 This switching method is possible because all anti-aliasing filters have finite impulse response.

3 The bounds would be optimal since only one of the two signals is within the range at a time, and it never occurs that both are out of the range.

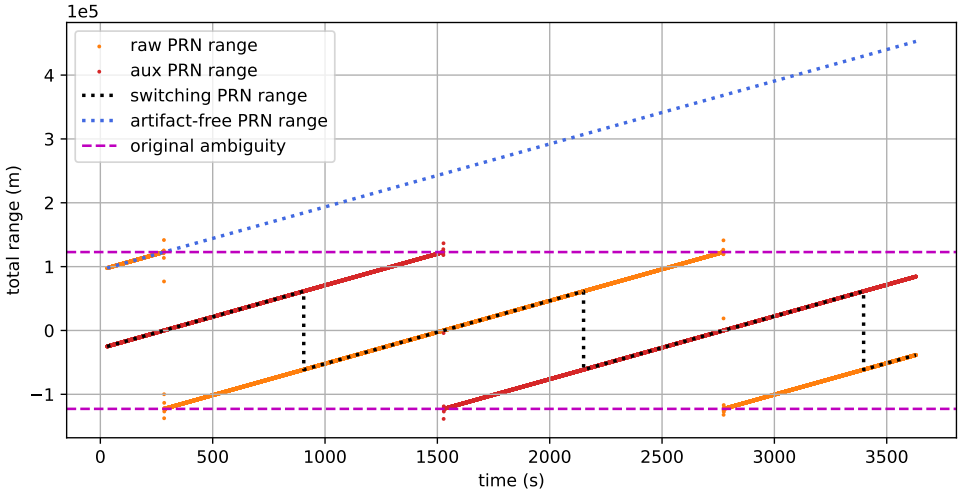

FIGURE G.1: Decimation-artifact-free PRN range. Orange and red markers are the raw and auxiliary ranges, respectively. They show artifacts at jumps. Dot-black has a half ambiguity, switching between the ranges to avoid artifacts. This is unwrapped and shifted to the first segment of the raw range to maintain the original ambiguity (dot-blue).

One should notice that Eq. (G.5) halves the original signal range; $y^F_{1/2} \in \left[\frac{M}{4}, \frac{3M}{4}\right]$. For example, this could be an issue when resolving a PRNR ambiguity. Hence, it is essential to guarantee that a resulting signal starts with y^F_{raw} regardless of its initial value to maintain the original ambiguity,

$$y^F[n] = \begin{cases} y^F_{1/2}[n] + \frac{M}{2} & \left(y^F_{\text{raw}}[0] \in \left[0, \frac{M}{4}\right)\right) \\ y^F_{1/2}[n] & \left(y^F_{\text{raw}}[0] \in \left[\frac{M}{4}, \frac{3M}{4}\right]\right) \\ y^F_{1/2}[n] - \frac{M}{2} & \left(y^F_{\text{raw}}[0] \in \left(\frac{3M}{4}, M\right]\right) \end{cases} \tag{G.5}$$

Figure G.1 shows the experimental demonstration with PRN ranges. The raw and auxiliary ranges show artifacts at jumps due to the filtering as expected. Dot-black corresponds to $y^F_{1/2}[n]$, which has a half ambiguity, while dot-blue is the unwrapped version of $y^F[n]$.

BIBLIOGRAPHY

[1] B. P. Abbott et al. (LIGO Scientific and Virgo Collaborations). Observation of gravitational waves from a binary black hole merger. *Physical Review Letters*, 116(6), 2016.

[2] B. P. Abbott et al. Gw170817: Observation of gravitational waves from a binary neutron star inspiral. *Phys. Rev. Lett.*, 119:161101, Oct 2017.

[3] B. P. Abbott et al. Gw170814: A three-detector observation of gravitational waves from a binary black hole coalescence. *Phys. Rev. Lett.*, 119:141101, Oct 2017.

[4] B. P. Abbott et al. Gw170608: Observation of a 19 solar-mass binary black hole coalescence. *The Astrophysical Journal Letters*, 851(2):L35, dec 2017.

[5] B. P. Abbott et al. Gw151226: Observation of gravitational waves from a 22-solar-mass binary black hole coalescence. *Phys. Rev. Lett.*, 116:241103, Jun 2016.

[6] B. P. Abbott et al. Gw170104: Observation of a 50-solar-mass binary black hole coalescence at redshift 0.2. *Phys. Rev. Lett.*, 118:221101, Jun 2017.

[7] B. P. Abbott et al. Prospects for observing and localizing gravitational-wave transients with advanced ligo, advanced virgo and kagra. *Living Reviews in Relativity*, 21(3), 2018.

[8] P. Amaro-Seoane, J. Andrews, M. Arca Sedda, et al. Astrophysics with the laser interferometer space antenna. *Living Reviews in Relativity*, 26(2), 2023.

[9] Gabriella Agazie, Akash Anumarlapudi, Anne M. Archibald, Zaven Arzoumanian, Paul T. Baker, Bence Bécsy, Laura Blecha, Adam Brazier, Paul R. Brook, Sarah Burke-Spolaor, et al. The NANOGrav 15 yr Data Set: Evidence for a Gravitational-wave Background. *The Astrophysical Journal Letters*, 951(1):L8, jun 2023.

[10] Daniel J. Reardon, Andrew Zic, Ryan M. Shannon, George B. Hobbs, Matthew Bailes, Valentina Di Marco, Agastya Kapur, Axl F. Rogers, Eric Thrane, Jacob Askew, et al. Search for an Isotropic Gravitational-wave Background with the Parkes Pulsar Timing Array. *The Astrophysical Journal Letters*, 951(1):L6, jun 2023.

[11] Heng Xu, Siyuan Chen, Yanjun Guo, Jinchen Jiang, Bojun Wang, Jiangwei Xu, Zihan Xue, R. Nicolas Caballero, Jianping Yuan, Yonghua Xu, et al. Searching for the Nano-Hertz Stochastic Gravitational Wave Background with the Chinese Pulsar Timing Array Data Release I. *Research in Astronomy and Astrophysics*, 23(7):075024, jun 2023.

[12] J. Antoniadis, P. Arumugam, S. Arumugam, S. Babak, M. Bagchi, A.-S. Bak Nielsen, C. G. Bassa, A. Bathula, A. Berthereau, M. Bonetti, et al.

The second data release from the European Pulsar Timing Array III. Search for gravitational wave signals. 2023.

[13] Andrea N. Lommen. Pulsar timing for gravitational wave detection. *Nature Astronomy*, 1(12), 2017.

[14] Karsten Danzmann, Pau Amaro-Seoane, Heather Audley, Stanislav Babak, John Baker, Enrico Barausse, Peter Bender, Emanuele Berti, Pierre Binetruy, Michael Born, et al. Laser interferometer space antenna. Technical report, 2017.

[15] M. Tinto and J. W. Armstrong. Cancellation of laser noise in an unequal-arm interferometer detector of gravitational radiation. *Physical Review D*, 59(10), 1999.

[16] Martin Hewitson, Ewan Fitzsimons, Bill Weber, Daniele Vetrugno, Joseph Martino, Roberta Giusteri, Gudrun Wanner, Michel Lintz, Antoine Petiteau, Olaf Hartwig, Lennart Wissel, and Nam DAM Quang. LISA performance model and error budget (version 2). Technical report, LISA-LCST-INST-TN-003, 2021.

[17] UK Optical Bench Team, LISA instrument group, Martin Gehler, Linda Mondin, and Paul McNamara. LISA Tilt-to-Length and Optical Alignment Analysis. Technical report, LISA-UKOB-INST-TN-004, 2019.

[18] LISA Instrument Group. LISA payload definition document. Technical report, 2018.

[19] Germán Fernández Barranco. *Photodetection in intersatellite laser interferometers*. PhD thesis, Leibniz Universität Hannover, 2018.

[20] Lennart Wissel, Andreas Wittchen, Thomas S. Schwarze, Martin Hewitson, Gerhard Heinzel, and Hubert Halloin. Relative-intensity-noise coupling in heterodyne interferometers. *Phys. Rev. Appl.*, 17:024025, Feb 2022.

[21] SCI-F, LISA Study Team, and L. Mondin. LISA laser system TRL6 demonstrator requirements. Technical report, 2020.

[22] Gerhard Heinzel. LISA frequency planning. Technical report, LISA-AEI-INST-TN-002, 2018.

[23] Olaf Hartwig and Jean-Baptiste Bayle. Clock-jitter reduction in LISA time-delay interferometry. *Physical Review D*, 103(12), 2021.

[24] M. Lilley, E. Savalle, M. C. Angonin, P. Delva, C. Guerlin, C. Le Poncin-Lafitte, F. Meynadier, and P. Wolf. ACES/PHARAO: high-performance space-to-ground and ground-to-ground clock comparison for fundamental physics. *GPS Solutions*, 25(34), 2021.

[25] Thomas S. Schwarze, Christoph Bode, Pascal Grafe, Jose Ogalde, Kohei Yamamoto, Sergio Lozano, Esteban Delgado, Miguel Dovale, and Myles Clark. TRL5 Test Description and Report. Technical report, LISA-AEI-PMS-RP-031, 2023.

[26] Stanislav Babak, Martin Hewitson, and Antoine Petiteau. LISA Sensitivity and SNR Calculations. Technical report, 2021.

[27] M. Armano, H. Audley, G. Auger, J. T. Baird, M. Bassan, P. Binetruy, M. Born, D. Bortoluzzi, N. Brandt, M. Caleno, et al. Sub-femto-g free fall for space-based gravitational wave observatories: Lisa pathfinder results. *Phys. Rev. Lett.*, 116:231101, Jun 2016.

[28] M. Armano, H. Audley, J. Baird, P. Binetruy, M. Born, D. Bortoluzzi, E. Castelli, A. Cavalleri, A. Cesarini, A. M. Cruise, et al. Beyond the required lisa free-fall performance: New lisa pathfinder results down to 20 μHz. *Phys. Rev. Lett.*, 120:061101, Feb 2018.

[29] Olaf Hartwig. *Instrumental Modelling and Noise Reduction Algorithms for the Laser Interferometer Space Antenna*. PhD thesis, Leibniz Universität Hannover, 2021.

[30] Oliver Gerberding. *Phase readout for satellite interferometry*. PhD thesis, Leibniz Universität Hannover, 2014.

[31] Oliver Gerberding, Christian Diekmann, Joachim Kullmann, Michael Tröbs, Iouri Bykov, Simon Barke, Nils Christopher Brause, Juan José Esteban, Thomas S. Schwarze, Jens Reiche, et al. Readout for intersatellite laser interferometry: Measuring low frequency phase fluctuations of high-frequency signals with microradian precision. *Review of Scientific Instruments*, 2015.

[32] Gerhard Heinzel, Juan José Esteban, Simon Barke, Markus Otto, Yan Wang, Antonio F Garcia, and Karsten Danzmann. Auxiliary functions of the LISA laser link: ranging, clock noise transfer and data communication. *Classical and Quantum Gravity*, 28(9):094008, apr 2011.

[33] Juan José Esteban, Antonio F. García, Simon Barke, Antonio M. Peinado, Felipe Guzmán Cervantes, Iouri Bykov, Gerhard Heinzel, and Karsten Danzmann. Experimental demonstration of weak-light laser ranging and data communication for lisa. *Opt. Express*, 19(17):15937–15946, Aug 2011.

[34] Gerhard Heinzel, Miguel Dovale Álvarez, Alvise Pizzella, Nils Brause, and Juan José Esteban Delgado. Tracking length and differential-wavefront-sensing signals from quadrant photodiodes in heterodyne interferometers with digital phase-locked-loop readout. *Phys. Rev. Appl.*, 14:054013, 2020.

[35] Simon Barke, Nils Brause, Iouri Bykov, Juan José Esteban, Andreas Enggaard, Oliver Gerberding, Gerhard Heinzel, Joachim Kullmann, Søren Møller Pedersen, and Torben Rasmussen. LISA metrology system final report. Technical report, 2014.

[36] Simon Barke. *Inter-Spacecraft Frequency Distribution for Future Gravitational Wave Observatories*. PhD thesis, Leibniz Universität Hannover, 2015.

[37] T. S. Schwarze, G. F. Barranco, D. Penkert, O. Gerberding, G. Heinzel, and K. Danzmann. Optical testbed for the LISA phasemeter. In *J. Phys. Conf. Ser.*, 2016.

[38] Thomas S. Schwarze. *Phase extraction for laser interferometry in space: phase readout schemes and optical testing*. PhD thesis, Leibniz Universität Hannover, 2018.

[39] D. Shaddock, B. Ware, P. G. Halverson, R. E. Spero, and B. Klipstein. Overview of the LISA phasemeter. *AIP Conference Proceedings*, 873, 2006.

[40] Oliver Gerberding, Benjamin Sheard, Iouri Bykov, Joachim Kullmann, Juan Jose Esteban Delgado, Karsten Danzmann, and Gerhard Heinzel. Phasemeter core for intersatellite laser heterodyne interferometry: modelling, simulations and experiments. *Classical and Quantum Gravity*, 30(23):235029, nov 2013.

[41] Olaf Hartwig, Jean-Baptiste Bayle, Martin Staab, Aurélien Hees, Marc Lilley, and Peter Wolf. Time-delay interferometry without clock synchronization. *Phys. Rev. D*, 105:122008, Jun 2022.

[42] Katharina-Sophie Isleif, Gerhard Heinzel, Moritz Mehmet, and Oliver Gerberding. Compact multifringe interferometry with subpicometer precision. *Phys. Rev. Applied*, 12:034025, Sep 2019.

[43] T. S. Schwarze, G. F. Barranco, D. Penkert, M. Kaufer, O. Gerberding, and G. Heinzel. Picometer-stable hexagonal optical bench to verify LISA phase extraction linearity and precision. *Physical Review Letters*, 2019.

[44] Kohei Yamamoto, Christoph Vorndamme, Olaf Hartwig, Martin Staab, Thomas S. Schwarze, and Gerhard Heinzel. Experimental verification of intersatellite clock synchronization at lisa performance levels. *Phys. Rev. D*, 105:042009, Feb 2022.

[45] Jean-Baptiste Bayle, Olaf Hartwig, and Martin Staab. Adapting time-delay interferometry for LISA data in frequency. *Physical Review D*, 2021.

[46] M. Tinto, M. Vallisneri, and J. W. Armstrong. Time-delay interferometric ranging for space-borne gravitational-wave detectors. *Physical Review D*, 2005.

[47] Martin Staab, Jean-Baptiste Bayle, and Olaf Hartwig. PyTDI, March 2023.

[48] Shawn J. Mitryk, Guido Mueller, and Josep Sanjuan. Hardware-based demonstration of time-delay interferometry and TDI-ranging with spacecraft motion effects. *Phys. Rev. D*, 86:122006, Dec 2012.

[49] Samuel P. Francis, Daniel A. Shaddock, Andrew J. Sutton, Glenn de Vine, Brent Ware, Robert E. Spero, William M. Klipstein, and Kirk McKenzie. Tone-assisted time delay interferometry on GRACE Follow-On. *Phys. Rev. D*, 92:012005, Jul 2015.

[50] Andrew J Sutton, Kirk McKenzie, Brent Ware, Glenn de Vine, Robert E Spero, W Klipstein, and Daniel A Shaddock. Improved optical ranging for space based gravitational wave detection. *Classical and Quantum Gravity*, 30(7):075008, mar 2013.

[51] Andrew Sutton, Kirk McKenzie, Brent Ware, and Daniel A. Shaddock. Laser ranging and communications for lisa. *Opt. Express*, 18(20):20759–20773, Sep 2010.

[52] Martin Hewitson, Ewan Fitzsimons, and Bill Weber. LISA performance model and error budget. Technical report, LISA-LCST-INST-TN-003, 2018.

[53] Juan José Esteban, Iouri Bykov, Antonio Francisco García Marín, Gerhard Heinzel, and Karsten Danzmann. Optical ranging and data transfer development for lisa. *Journal of Physics: Conference Series*, 154(1):012025, mar 2009.

[54] Juan José Esteban. *Laser Ranging and Data Communication for The Laser Interferometer Space Antenna*. PhD thesis, Leibniz Universität Hannover, 2012.

[55] Andrew Sutton. *Digital Techniques for Coherent Optical Metrology*. PhD thesis, The Australian National University, 2013.

[56] Philipp Euringer, Gerald Hechenblaikner, Francis Soualle, and Walter Fichter. Performance analysis of sequential carrier- and code-tracking receivers in the context of high-precision space-borne metrology systems. 2023.

[57] Jan Niklas Reinhardt, Martin Staab, Kohei Yamamoto, Jean-Baptiste Bayle, Aurélien Hees, Olaf Hartwig, Karsten Wiesner, and Gerhard Heinzel. Ranging sensor fusion in LISA data processing: Treatment of ambiguities, noise, and on-board delays in LISA ranging observables. 2023.

[58] Yan Wang, Gerhard Heinzel, and Karsten Danzmann. First stage of LISA data processing: Clock synchronization and arm-length determination via a hybrid-extended Kalman filter. *Phys. Rev. D*, 90:064016, Sep 2014.

[59] Sebastian Khan, Sascha Husa, Mark Hannam, Frank Ohme, Michael Pürrer, Xisco Jiménez Forteza, and Alejandro Bohé. Frequency-domain gravitational waves from nonprecessing black-hole binaries. ii. a phenomenological model for the advanced detector era. *Phys. Rev. D*, 93:044007, Feb 2016.

[60] Oliver Gerberding. Deep frequency modulation interferometry. *Opt. Express*, 23(11):14753–14762, Jun 2015.

[61] Gerhard Heinzel, Felipe Guzmán Cervantes, Antonio F. García Marín, Joachim Kullmann, Wang Feng, and Karsten Danzmann. Deep phase modulation interferometry. *Opt. Express*, 18(18):19076–19086, Aug 2010.

[62] Katharina-Sophie Isleif, Oliver Gerberding, Thomas S. Schwarze, Moritz Mehmet, Gerhard Heinzel, and Felipe Guzmán Cervantes. Experimental demonstration of deep frequency modulation interferometry. *Opt. Express*, 24(2):1676–1684, Jan 2016.

[63] Yichao Yang, Kohei Yamamoto, Victor Huarcaya, Christoph Vorndamme, Daniel Penkert, Germán Fernández Barranco, Thomas S. Schwarze, Moritz Mehmet, Juan Jose Esteban Delgado, Jianjun Jia, Gerhard Heinzel,

and Miguel Dovale Álvarez. Single-element dual-interferometer for precision inertial sensing. *Sensors*, 20(17), 2020.

[64] Katharina-Sophie Isleif. *Laser Interferometry for LISA and Satellite Geodesy Missions*. PhD thesis, Leibniz Universität Hannover, 2018.

[65] F Gibert, M Nofrarias, N Karnesis, L Gesa, V Martín, I Mateos, A Lobo, R Flatscher, D Gerardi, J Burkhardt, R Gerndt, D I Robertson, H Ward, P W McNamara, F Guzmán, M Hewitson, I Diepholz, J Reiche, G Heinzel, and K Danzmann. Thermo-elastic induced phase noise in the LISA pathfinder spacecraft. *Classical and Quantum Gravity*, 32(4):045014, jan 2015.

[66] Richard P. Kornfeld, Bradford W. Arnold, Michael A. Gross, Neil T. Dahya, William M. Klipstein, Peter F. Gath, and Srinivas Bettadpur. GRACE-FO: The gravity recovery and climate experiment follow-on mission. *Journal of Spacecraft and Rockets*, 56(3):931–951, May 2019.

[67] K. Nicklaus, A. Baatzsch, C. Diekmann, F. Gilles, B. Zender, B. Sheard, G. Heinzel, M. Herding, M. Dehne, K. Voss, B. Guenther, S. Böhme, V. Mueller, D. Schuetze, and G. Stede. Optical bench of the laser ranging interferometer on grace follow-on. In Bruno Cugny, Zoran Sodnik, and Nikos Karafolas, editors, *International Conference on Space Optics — ICSO 2014*. SPIE, November 2017.

[68] Vitali Müller. *Design considerations for future geodesy missions and for space laser interferometry*. PhD thesis, Hannover: Gottfried Wilhelm Leibniz Universität Hannover, 2017.

[69] Oliver Mandel, Alexander Sell, Michael Chwalla, Thilo Schuldt, Jasper Krauser, Dennis Weise, and Claus Braxmaier. Architecture and performance analysis of an optical metrology terminal for satellite-to-satellite laser ranging. *Applied Optics*, 59(3):653, January 2020.

[70] Yichao Yang, Kohei Yamamoto, Miguel Dovale Álvarez, Daikang Wei, Juan José Esteban Delgado, Vitali Müller, Jianjun Jia, and Gerhard Heinzel. On-axis optical bench for laser ranging instruments in future gravity missions. *Sensors*, 22(5), 2022.

[71] Henry Wegener, Vitali Müller, Gerhard Heinzel, and Malte Misfeldt. Tilt-to-length coupling in the GRACE follow-on laser ranging interferometer. *Journal of Spacecraft and Rockets*, 57(6):1362–1372, November 2020.

[72] Hemani Kaushal and Georges Kaddoum. Optical communication in space: Challenges and mitigation techniques. *IEEE Communications Surveys & Tutorials*, 19(1):57–96, 2017.

[73] M. Chwalla, K. Danzmann, M. Dovale Álvarez, J.J. Esteban Delgado, G. Fernández Barranco, E. Fitzsimons, O. Gerberding, G. Heinzel, C.J. Killow, M. Lieser, M. Perreur-Lloyd, D.I. Robertson, J.M. Rohr, S. Schuster, T.S. Schwarze, M. Tröbs, G. Wanner, and H. Ward. Optical suppression of tilt-to-length coupling in the LISA long-arm interferometer. *Physical Review Applied*, 14(1), July 2020.

[74] K Nicklaus, S Cesare, L Massotti, L Bonino, S Mottini, M Pisani, and P Silvestrin. Laser metrology concept consolidation for nggm. *CEAS Space Journal*, 12(3):313–330, 2020.

[75] Schilling, Roland. http://www2.mpq.mpg.de/ ros/optocad/.

[76] Christoph Mahrdt. Laser link acquisition for the grace follow-on laser ranging interferometer, 2014.

[77] Daniel Schütze. *Intersatellite laser interferometry: test environments for GRACE follow-on*. PhD thesis, Hannover: Gottfried Wilhelm Leibniz Universität Hannover, 2015.

[78] Lennart Wissel, Olaf Hartwig, Jean-Baptiste Bayle, Martin Staab, Ewan D. Fitzsimons, Martin Hewitson, and Gerhard Heinzel. The influence of laser relative intensity noise in the Laser Interferometer Space Antenna. 2023.

[79] Martin Staab, Marc Lilley, Jean-Baptiste Bayle, and Olaf Hartwig. Laser noise residuals in LISA form onboard processing and time-delay interferometry. 2023.

[80] Jean-Baptiste Bayle, Marc Lilley, Antoine Petiteau, and Hubert Halloin. Effect of filters on the time-delay interferometry residual laser noise for LISA. *Physical Review D*, 2019.

ACKNOWLEDGEMENTS

First, I thank Prof. Dr. Karsten Danzmann for such an excellent research environment. I cannot imagine a better place for me to be a Ph.D. candidate than this department.

I'm sincerely grateful to Gerhard Heinzel. His broad and deep knowledge and curiosity-based research commitment were always respectable and what I aimed for. The space interferometry group he led is genuinely fantastic and full of enthusiastic researchers. I also want to thank him and his wife for supporting my personal life in Germany.

Thank you, Kiwamu Izumi and Oliver Gerberding, for accepting my request to review this thesis and be a referee for my defense. I also want to thank Kiwamu for his long-term support since before I joined the AEI, especially during my three-month Ph.D. life in Japan. Also, thank you, Professor Milutin Kovacev, for being the chairman of my defense.

Special thanks to Thomas S. Schwarze, who was my mentor for experiments in general, since he showed up with the green GW T-shirt in front of me on my first day in Germany. Discussions with him were always exciting, and his comments were very insightful. I cannot imagine how my life here would have been without him.

With Thomas, I felt like Miguel, Gérman, and Esteban were older brothers in the AEI phasemeter team. Miguel encouraged me in optical simulation, especially in my first two years, from which I learned a lot. For me, Gérman was like a "door" to the electronics world, and he entertained me in the electrical workshop every time. Esteban always encouraged me to keep going and fully supported my research style. In addition, Iouri Bykov patiently instructed me for VHDL coding to implement PRNR-related architecture. Thank you all for everything you have done for me.

Christoph Bode has been one of my closest colleagues in my Ph.D. life. Most of the experiments in this thesis could only happen with phasemeters developed mainly by him. In addition, I'm so much grateful to all the phasemeter team members here. I respect the momentum of this team to head in one direction together. I hope I gave back some support to the team.

Olaf Hartwig was my mentor for analytical modeling and data analysis. Reading his note on LISA models was the start of my life as an instrumental data analyst. He always had a good point; trying to digest his insights was an actual practice in this field. Thanks for willingly spending time on discussions with me.

I also thank colleagues and friends Martin Staab and Jan Niklas Reinhardt. A chat on data analysis with them was always a fun moment. They pulled up many of my poor ideas and questions to the science level.

I'm grateful to the students I "supervised" Narjiss Messied and Sergio Lozano Althammer. I might learn more from you than you did from me. I was always impressed by their passion for research; keep it up!

This thesis was proofread by Thomas, Miguel, Niklas, Martin, Pascal, Narjiss, Olaf, Daikang Wei, Vitali Müller, and Sarah Paczkowski. Thanks a lot for sparing time for it despite such short notice.

I could continue working over the last few months before the thesis submission, thanks to support from Pablo, Malte, Alvise, Kanioar, Yongho, Moritz, Jose Ogalde, Jordina, Jasper, and the many mentioned above. They gave me the energy to reach the last day of the writing; otherwise, I would have even stopped halfway.

Special thanks to my family for fully supporting and encouraging me. My gratitude is beyond description here.

Lastly, I can only wrap up this part by mentioning you. I owe what I am now to you, no doubt. The enormous thanks to you, and I wish you all the best.

COLOPHON

This document was typeset using a modified version of the `classicthesis` LaTeX package developed by André Miede and Ivo Pletikosić.